CHARACTERISATION OF NANOSTRUCTURED LIGHT EMITTERS

A Thesis Submitted to

The Department of Physics

University of Strathclyde

For the Degree of

Doctor of Philosophy

By

Lethy K J

May 2012

Declaration of Author's Rights

This thesis is the result of the author's original research. It has been composed by the author and has not been previously submitted for examination which has led to the award of a degree.

Signed: Date:

Abstract

Group III-nitride semiconductors are the dominant inorganic solid state light emitting materials, spanning the UV to infra-red spectral range. InGaN/GaN based LEDs and lasers are commercially available and intense research is being pursued to improve their efficiency. One practical approach is the development of functionalised and/or improved materials patterned on a nanometre length scale. This thesis presents the optical, morphological and compositional characterisation of III-nitride based nanostructured light emitters.

The III-nitride nanostructures studied are GaN coalesced above arrays of either nanopyramids or nanocolumns, semipolar and nonpolar InGaN QWs on the facets of GaN nanopyramids, and thin epilayers of AlInN and AlInGaN. Spatially resolved optical characterisation of nano-ELOG GaN layers revealed a shift in the exciton-related band edge emission across the coalesced layer. This is related to Si doping and to strain effects. Study of the semipolar {10$\underline{1}$1} InGaN QWs grown on the facets of GaN nanopyramids identified a blue shift in QW emission energy as the sampled region is moved up the pyramid facets. This shift is found to follow the release of the tensile strain towards the top of nanopyramid.

Luminescence properties of nearly lattice matched AlInN epilayers investigated using CL, PL and PLE spectroscopic techniques revealed that the emission and bandgap energy of the AlInN layers are at higher energy than that of GaN. Results obtained from polarisation resolved PL measurements of AlInN epilayers point to two possible implications: the observed higher energy AlInN emission is either related to defects or this emission is due to carrier recombination occurring in InN clusters similar to those of InGaN epilayers.

Optical properties of thin AlInGaN epilayers investigated using PL and PLE spectroscopy revealed a redshift in bandgap energy with increase in InN fraction. The observed spatial intensity fluctuations are discussed in terms of the InN compositional fluctuations and inhomogeneous strain effects.

ACKNOWLEDGEMENTS

I feel very happy to express my deep gratitude to everyone who was by my side through out the period of my research work; three and a half years. At the very beginning, I would like to thank my Heavenly Father, Almighty God, for giving me an opportunity to do my PhD research studies in an excellent and very friendly research group at Department of Physics, University of Strathclyde, UK

I sincerely thank my first supervisor, Prof. Robert W Martin, for sharing his vast knowledge on semiconductor physics and spectroscopy, his genial and excellent guidance, continuous encouragement and many hours spent for the successful completion of my research work. I greatly owe him for his patience and for teaching me how to do research through many levels of discussions on experimental data and results.

I am specially grateful to my second supervisor, Dr Carol Trager-Cowan, for her kind assistance by way of sincere and valuable suggestions throughout my research work, many fruitful discussions on various research topics, and for spending her valuable time for correcting my thesis chapters. Her dedication to research and enthusiasm for science has always fascinated me. Together my two supervisors truly ignited a passion for research and science in me which I hope will always instill and keep me on the research track and maintain my enthusiasm.

I specially wish to thank Dr. Paul R Edwards for his dedicated assistance in familiarizing me with various experimental techniques. His knowledge and skills on experimental techniques of Spectroscopy and Electron microscopy has always amazed me. I cannot proceed without mentioning his patience with my countless questions related to my research work and for never ever getting annoyed for many occasions I approached him to fix the problems I faced while doing SEM-CL and EPMA experiments.

I specially thank Prof Kevin O' Donnell for his valuable suggestions, and giving me an opportunity to do some polarisation resolved spectroscopic measurements with him. I also thankfully remember him for many useful text books on spectroscopy and helping me to clear doubts on semiconductor physics. I would

like to sincerely thank Dr. Benjamine Hourahine for sharing his knowledge on Band structure of III-nitrides and helping me to better understand optical anisotropy in III-nitrides. I hold special thanks to Dave Clark for the very quick fixing of instruments and for his never fading friendly smile.

I sincerely thank many collaborators Dr Duncan Allsopp, Dr Philip Shields, Dr M J Kappers, Dr Wang Wang, Dr. Thomas Sadler and Dr. Lutz Kirste, for providing samples to characterise and Dr Katharina Lorenz for RBS measurements.

I had the privilege of working with very friendly, loving and supportive friends Franzi, Naresh, Yochen and Michael and the joyful memories of their association will remain forever with me.

Finally on a more personal level, I would like to thank my parents for always valuing education, for their understanding, and selfless support for the completion of my research work. My enormous debt of gratitude can hardly be repaid to pastor Saji Samuel and family for helping me morally through my some hard days. Finally and most importantly, I am wholly indebted to my husband and best friend Pradeep Luke Sam for his continuous emotional support, unfailing love and patience. I should also thank my little one Nathaniel for his patience. For those I have not yet mentioned here, I must give my heartfelt thanks and apologies.

I truly thank all, from the bottom of my heart.

Lethy K J

March 2012

List of Abbreviations

BGR	Bandgap renormalisation
CL	Cathodoluminescence
CB/VB	conduction band/valence band
DAP	Donor-Acceptor pair
ELOG	Epitaxial lateral overgrowth
EPMA	Electron probe micro-analyser
FESEM	Field emission gun scanning electron microscopy
FE/BE	Free excitons/bound excitons
HH/LH/CH	Heavy hole/light hole/crystal field split off
HEMT	High electron mobility transistor
HR-XRD	High resolution-X-ray diffraction
LED	Light emitting diodes
LD	Laser diodes
LO	Longitudinal optical
NBE	Near band edge emission
PLE	photoluminescence excitation spectroscopy
PL	Photoluminescence
QW	Quantum well
RBS	Rutherford backscattering spectrometry
SEM	Scanning electron microscopy
TD	Threading dislocation
YB	Yellow band

Table of contents

Chapter 3 Experimental techniques and Principles

Chapter 7 Optical properties of AlInN epilayers

Chapter 8 Optical properties of AlInGaN epilayers

Chapter 9 Conclusions and suggestions for future work

Appendix

Chapter 1
Introduction

1.1 Introduction

Artificial lighting using incandescent and fluorescent lamps is highly inefficient as light is generated only as a by-product of processes which produce heat or plasma. The energy conversion efficiency of incandescent and fluorescent lamps is only 5 and 25 % respectively. If we can replace these inefficient artificial lighting systems with at least 50 % efficient lighting sources, overall electrical energy consumption can be reduced by ~ 25% [1-3]. This would also help to reduce green house gas emission into the atmosphere as the energy consumed to supply lighting throughout the world results in the emission of 1900 megatones (Mt) of CO_2 per year [4].

There is now the great potential of solid state lighting technology (SSL). Solid state lighting is the direct conversion of electrical energy to visible white light using semiconductor materials. It can provide higher efficiency, and thus offers much potential to conserve precious electricity. According to US Department of Energy, if successful, by 2015, solid state lighting can reduce the overall electricity consumption by 25 % [1-2]. However SSL technology is not yet sufficiently developed to replace today's general lighting systems. For that we need white solid state lighting technology that is simultaneously high in efficiency, low in cost, and high in colour-rendering quality. To attain that goal in the near future we require

breakthroughs in solid state lighting technology, stimulated by a fundamental understanding of the science of light-emitting materials. Solid state lighting materials generally belong to three broad categories (a) Inorganic, (b) Organic and (c) Hybrid. The dominant inorganic solid state lighting materials today are group III- nitrides.

1.2 Group III- nitrides

The group III-nitrides (Al,Ga,In)N and their ternary (InGaN, AlInN, AlGaN) and quaternary (AlInGaN) alloys are currently the only commercially available materials class producing light in the green to ultraviolet part of the spectrum [Fig 1 and 2]. They possess direct bandgaps from 0.7 eV for InN to 6.2 eV for AlN, covering the spectral range from infrared to deep ultraviolet (UV). The direct and large bandgap nature, intrinsic high carrier mobility, and the capability of forming heterostructures allow them to dominate photonic and electronic device markets such as ultraviolet, blue, green and white light emitting diodes (LEDs), blue and green laser diodes (LDs) and high speed/high power and high temperature electronic devices [5-8]. The high thermal and chemical stability and physical hardness of GaN give those devices the advantage of operating in hostile environments. The nitride semiconductors also exhibit superior radiation hardness compared to other smaller bandgap counterparts such as Si or GaAs, allowing them to be incorporated into demanding space applications. Because of these widespread applications and properties, group III- nitride semiconductor materials have attracted much attention in both the consumer and defence industries. Detailed discussion of the structural and optical parameters of III-nitrides is given in Chapter 2**.**

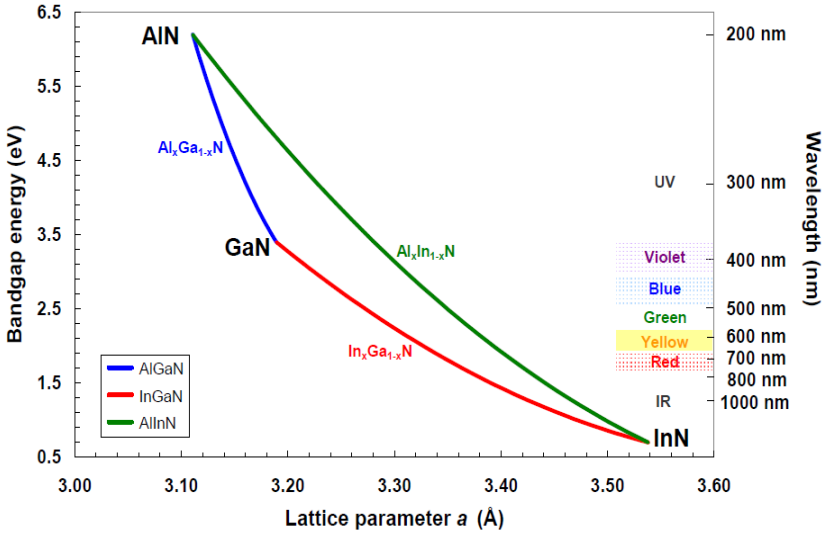

Figure 1.1 Bandgap energy versus lattice constant of III- nitride semiconductors at room temperature [9]

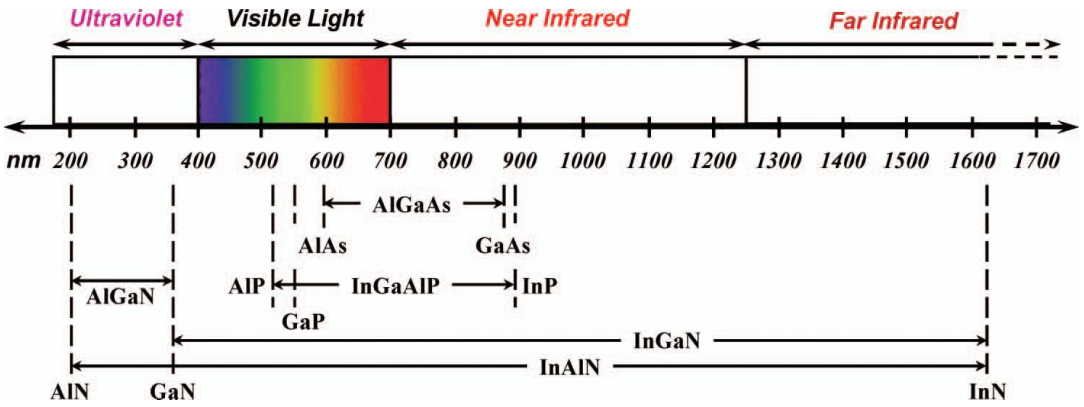

Figure 1.2 Various binary, ternary and quaternary materials used for LEDs with the wavelength ranges indicated [10]

Unlike GaAs and InP based semiconductors, III-nitride based materials have a high density of defects due to very limited availability of lattice matched substrates. Up to now most III-nitride based optoelectronic devices have been fabricated using hetero-epitaxy on substrates such as sapphire (Al_2O_3), silicon carbide (SiC), and in some cases on silicon. Because of lattice mismatch, III-nitrides grown on these substrates often exhibit a high density of threading dislocations, typically of the order

of 10^8- 10^{10}/ cm^2 [11]. These defects are still one of the major limiting factors for the performance of GaN based optoelectronic devices, acting as non-radiative recombination and scattering centres. Achievement of lower defect density would also improve device reliability resulting in a longer lifetime [6, 7]. Various defect reduction process such as epitaxial lateral overgrowth (ELOG), nano-ELOG, coalescence of nanocolumns of III-nitrides etc have been demonstrated and optical characterisation of some of these nanostructures constitute a part of this thesis.

Among the various epitaxial techniques that have been developed for the growth of III-nitride based materials, metal organic chemical vapour deposition (MOCVD) and molecular beam epitaxy (MBE) are the leading technologies. The samples characterised in this thesis were all prepared by MOCVD with the exception of two sets of samples that are grown partially by MBE technique followed by MOCVD.

1.3 Motivation of this work

Semiconductor technology is quickly being driven towards nanoscale dimensions where 'smaller' means better performance e.g., higher efficiency, higher density of integration, faster response and less power consumption. Nanostructures composed of group III-nitride alloys provide the potential for new semiconductor device configurations such as nano-scale optoelectronic devices. Nanostructured light emitters are the building blocks of optoelectronic devices such as LEDs and laser diodes used for lighting and display applications [12]. Both bottom up- and top-down approaches are used in synthesising various group III-nitride nanostructures and there is significant progress in the research areas of fabricating these into light emitting nanostructures. The nano-structural properties of III-nitride semiconductor nanostructures have to be investigated and understood before the device optimisation as the physical properties and ultimate device performance depend strongly on their nano-structures. Therefore to desirably tune the physical properties of semiconductor nanostructures through growth manipulation it is important to understand their fundamental nano-structural and luminescence properties.

1.4 Objectives of the Thesis

Rapid developments of fabrication methods for III-nitride nanostructures have attracted a great deal of interest in their optical and electronic properties for potential applications in optoelectronic devices such as nano-scale light emitting devices. The goal of my project is to understand the optical properties of these III-nitride light emitters relate them to the nanostructures and use the results to enhance devices made from them. For this a combination of a multitude of complimentary techniques on the nanometre scale are needed in order to get insight into the structure-properties interplay within the semiconductor nanostructures. In this project the characterisation of III-nitride based nanostructures is carried out using state-of-the art tools including scanning electron microscopy (SEM) and cathodoluminescence (CL) spectroscopy. These techniques are used to obtain high quality data from nanoscale features in a range of structures. Our CL set-up is attached to a high resolution scanning electron microscope and is capable of obtaining both spatially (< 20 nm) and spectrally (0.2 nm) resolved hyper spectral images from nanostructured light emitters [13]. This permits the optical emission from single, isolated nanostructures to be analysed. PL spectroscopy (He-Cd 325 nm and Xe lamp based excitation) is also used as a complimentary technique to characterise the luminescence properties of these nanostructures. The structures characterised and analysed include semipolar {10$\underline{1}$1} grown InGaN/GaN QWs, nano-epitaxial lateral overgrown (nano-ELOG) GaN, coalesced GaN nanocolumns, AlInN and AlInGaN epitaxial layers grown by MOCVD and MBE. The optical polarisation anisotropy of AlInN samples is studied as a function of InN fraction in order to probe the band structure of the alloy. The cathodoluminescence mapping of quaternary AlInGaN epilayers intended for using as barrier layers in high electron mobility transistors (HEMT) are also a part of this work.

1.5 Thesis overview

This thesis consists of 9 chapters.

(i) The first chapter gives a brief discussion of motivation and the objective of the thesis and outlines its structure.

(ii) The second chapter briefly describes the structural and optical properties of important III-nitrides. A review of recent research and development associated with nano-ELOG GaN, semipolar InGaN QW, nonpolar InGaN QWs, AlInN, and AlInGaN epilayers, which constitute the important light emitting structures described in this thesis, are discussed. Existing research challenges in each of these areas are also pointed out.

(iii) Chapter 3 introduces the working principle and instrument setups of the characterisation techniques used in this thesis to study the nano-structural and optical properties of semiconductor nanostructures. This includes scanning electron microscopy, cathodoluminescence and photoluminescence spectroscopy, Rutherford Backscattering spectrometry (RBS), etc. A brief discussion of MOCVD and MBE growth techniques used for the fabrication of III-nitride heterostructures is also included.

(iv) Chapter 4 presents the optical properties of nanoscale epitaxial lateral overgrown (nano-ELOG) GaN. Spatially and spectrally resolved cathdoluminescence (CL) from such coalesced layers are used to quantify the GaN band edge energy downshift due to bandgap renormalisation effects and due to strain effects.

(v) In Chapter 5, the optical properties of GaN layer coalesced above an array of nanocolumns investigated using plan-view and cross-sectional cathodoluminescence are discussed. Relaxation of tensile strain with increase in thickness of the coalesced layer is observed for GaN layer coalesced over nanocolumns.

(vi) Chapter 6 focuses the optical properties of semipolar (10$\underline{1}$1) InGAN QWs fabricated on the facets of nanopyramids. A blue/red shift in QW emission energy is observed as the electron beam scans from bottom to top of the nanopyramids. An attempt has been made to correlate this QW luminescence emission shift to the strain in underlying GaN template pyramids. A section of this chapter is also devoted to study the optical properties of nonpolar InGaN QWs fabricated on nanofacets of 3D GaN structures.

(vii) In chapter 7 we focus on the luminescence from ternary c-AlInN epilayers. The composition of the epilayers is examined using RBS and X-ray diffraction technique (XRD). The luminescence properties, bandgap energy, Stokes shift etc are discussed as a function of InN molar fraction. An attempt has been made to study the optical polarisation anisotropy in c-plane AlInN emission using PL spectroscopy.

(viii) The optical properties of UV emitting quaternary AlInGaN epilayers are the topic of chapter 8. The spatially resolved luminescence properties of the epilayers are investigated using cathodoluminescence hyperspectral imaging technique and are discussed as a function of InN localisation and strain effects.

(ix) The overall conclusions of the thesis are presented in Chapter 9 and some suggestions for future work are also proposed.

References:

[1] *http://www.sc.doe.gov/bes/reports/files/SSL_rpt.pdf*
(date of access-20-05-2010)

[2] Humphreys C J 2008 *MRS BULLETIN* **33** 459-470

[3] *Solid State Lighting Research and Development: Manufacturing Roadmap* 2009.

[4] www.lrc.rpi.edu (date of access-20-05-2010)

[5] DenBaars S P (*Editors*: Nakamura S and Chichibu S F) 2000 *Introduction to Nitride Semiconductor Blue Lasers and Light Emitting Diodes* (NewYork: CRC PRESS)

[6] Morkoc H 2008 *Handbook of Nitride Semiconductors and Devices* vol. 1& 2 (Germany: Wiley-VCH)

[7] Ruterana P, Albrecht M and Neugebauer J 2003 *Nitride Semiconductors Handbook on Materials and Devices* (Weinheim: Wiley-VCH)

[8] Ng H M, Chowdhuri A 2006 *Ill-Nitride Semiconductor Materials* (*Editor:* Zhe Chuan Feng) (London: Imperial College Press)

[9] Dongwon Yoo PhD Thesis 2007 Georgia Institute of Technology, *Growth and characterization of III-N materials system for photonic and electronic devices by metalorganic chemical vapour deposition*

[10] Morkoc H 2009 *Handbook of Nitride Semiconductors and Devices.* Vol. 3. (Weinheim: Wiley -VCH Verlag)

[11] Rojas Dasilva Y A, Ruterana P, Lahourcade L, Monroy E, Nataf G 2010 *Materials Science Forum* **644** 117

[12] Tang et al 2010 *IEEE Transactions on Electron Devices* **57** 1

[13] Edwards P R and Martin R W 2011 *Semicond. Sci.and Technol*. **26** 064005

Chapter 2

Properties of III-nitrides, Research Background and Objectives

2.1 Introduction

This chapter describes some of the fundamental properties such as crystal structure, band structure and luminescence properties of III-nitrides with emphasis on nanoscale epitaxial lateral overgrowth (nano-ELOG) GaN, coalesced GaN nanocolumns, semipolar and nonpolar InGaN QWs on GaN nanopyramidal facets, AlInN and AlInGaN thin epilayers which form the subject of this thesis. Before proposing the research objectives behind the nano-structural characterisation of each of these structures, it is necessary to summarise the recent research progress and identify the existing research challenges in these structures. Thus the purpose of this chapter is to present the general background of research and to formulate the research aims of this thesis.

2.2 Properties of III-nitrides

2.2.1 Crystal Structure

GaN and its related compounds can crystallise in the following three-crystal structures: (1) wurtzite, (2) zinc-blende and (3) rock-salt. A rock-salt phase occurs at high pressure and the zinc-blende structure is metastable and may be stabilised only by heteroepitaxial growth on substrates like GaAs. At ambient environment, the

thermodynamically stable phase is the wurtzite structure [1]. The wurtzite structure has a hexagonal unit cell containing 6 atoms of each type and has two lattice constants ‘a’ and ‘c’. Further this structure is composed of two hexagonal close-packed (hcp) sub-lattices which are shifted with respect to each other along the c-axis by the amount u=3/8. Each atom of one kind is surrounded by four atoms of the other kind. The unit cell of the wurtzite crystal structure is shown in Fig 2.1.

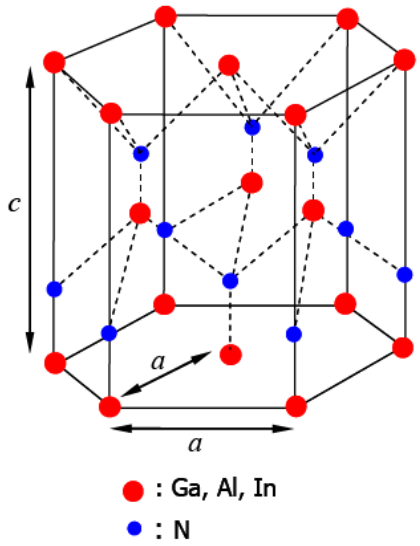

Figure 2.1 Unit cell for the hexagonal wurtzite structure for the III-nitrides [2]

The large electro-negativity of nitrogen atom adds a large ionic bonding component to the III-nitrides and plays a role in forming a tightly bonded crystal structure. In an ideal wurtzite structure, the c/a ratio is 1.633 and the deviation from this ideal value increases as the electro-negativity difference between group III atom and nitrogen atom increases. The bonding energy of AlN is 11.5 eV/atom while that of GaN is 8.9 eV/atom and that of InN 7.7 is eV/atom. The lattice parameters, thermal expansion coefficient and c/a ratio of three binary III-nitrides are listed in Table 2.1. Alloys of GaN, AlN and InN are of special interest as they can form the barriers or the active

layers of nearly all III-nitride based devices. Many properties of the alloys such as energy bandgap, effective mass of the electrons and holes and the dielectric constant depend on the alloy composition. The lattice parameters of the alloys can be estimated using Vegard's law [3] according to which if two binary compounds AC and BC form an alloy $A_xB_{1-x}C$, then the lattice parameter 'a' and 'c' is given by

$$a\ (A_xB_{1-x}C) = xa_{AC} + (1-x)\ a_{BC}$$

$$c\ (A_xB_{1-x}C) = xc_{AC} + (1-x)\ c_{BC}$$

Table 2.1 Material properties of wurtzite AlN, InN and GaN [1, 2]

Property		GaN	AlN	InN
Lattice constant, *a* [Å]		3.189	3.112	3.548
Lattice constant, *c* [Å]		5.185	4.982	5.76
Thermal expansion ($\Delta a/a$) [10^{-6}/K]		5.59	4.2	4
Thermal expansion ($\Delta c/c$) [10^{-6}/K]		3.17	5.3	3
Thermal conductivity (κ) [W/cm·K]		1.3	2	0.8
c/a		1.626	1.601	1.612
Lattice mismatch (%)	sapphire	14.8	12.5	25.4
	SiC	3.3	1	14
	GaN	-	-2.4	10.6

The group III-nitrides lack an inversion plane perpendicular to the c-axis, and thus their surfaces have either a group III- element (Al, Ga, or In) polarity designated as (0001) or a N polarity designated as (000$\underline{1}$). Because of the partial ionic nature of the bonds in (AlN>GaN>InN) III- nitrides, the c/a ratio is always less than the ideal one (Table 2.1) implying that the wurtzite crystal is compressed in the c-direction. Consequently, the centres of positive and negative charges from the metal–N bond are displaced from each other, and electric charges appear at the opposite surfaces of the crystal. This is called spontaneous polarisation. Since, the group III-nitrides are grown by heteroepitaxy, due to the lack of native substrates, a strain induced piezoelectric polarisation also arises. The percentage of lattice mismatch between III-nitride binary and the common substrates such as sapphire, SiC and GaN is shown in Table 2.1. This polarisation causes an in-built internal electric field which can adversely affect the III-nitride based optoelectronic devices. The polarisation induced internal electric field effects in III-nitride QW heterostructures are discussed in detail in section 2.2.2.

In order to overcome the problems relating to intense in-built fields, III-nitride heterostructures and QWs can be grown along crystallographic directions where the piezoelectric field is small or zero. This opens up the potential of semipolar and non-polar planes or directions of III-nitride for QW fabrication. Nonpolar orientations are planes perpendicular to the *c* -plane like the (1$\underline{1}$00) plane (*m*-plane) and the (11$\underline{2}$0) plane (*a*-plane) of wurtzite crystal structure and utilise $\cos\theta = 0$, where θ is the inclination angle from the c-plane. Semipolar orientations are any plane having a tilt angle between $0^{\circ}$and 90° relative to the [0001] direction. The important nonpolar and semipolar planes are shown in Fig 2.2 [4].

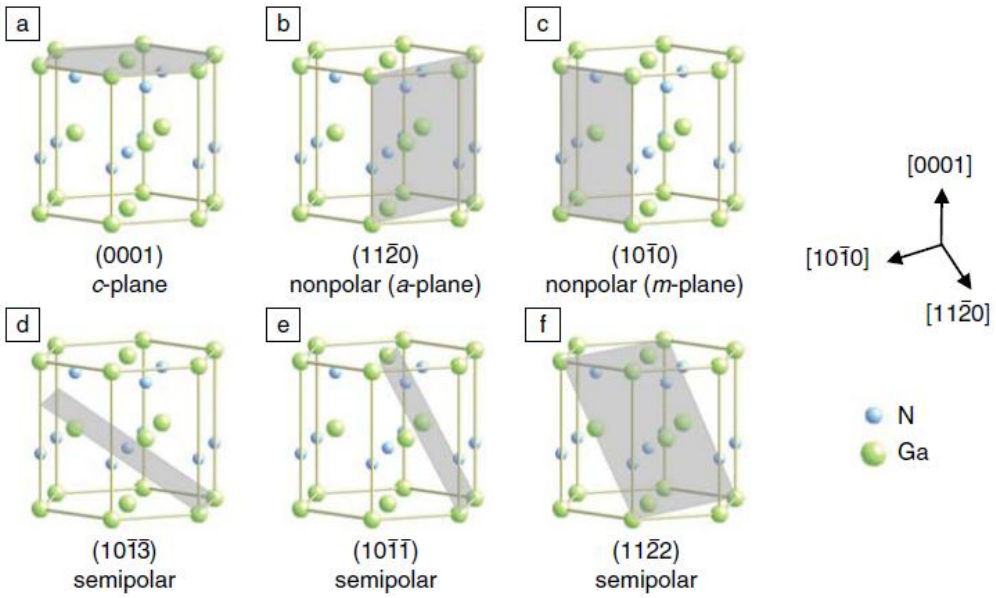

Figure 2.2 The schematic illustrations of major directions and planes in the hexagonal GaN system (a) the polar c-plane (0001) (b) the nonpolar a-plane (11$\underline{2}$0) (c) the m-plane (1$\underline{1}$00) (d-f) semipolar planes (10$\underline{1}$3), (10$\underline{1}$1) and (11$\underline{2}$2) respectively [4]

2.2.2 Polarisation induced electric field in III-nitride QWs

The origin of spontaneous and piezoelectric polarisation in III-nitrides was introduced in section 2.2.1. The piezoelectric polarisation has two components; (a) due to lattice mismatch (misfit) strain while the other due to (b) thermal strain caused by thermal expansion coefficient difference between the substrate and the material. Also piezoelectric coefficients in III-nitrides are almost an order of magnitude larger than in many of the traditional III-V semiconductors, as high as ~30% of the values for classical proper ferroelectrics such as $BaTiO_3$ (i.e., P_s = –0.081 C/m^2, –0.029 C/m^2, –0.032 C/m^2 for AlN, GaN, and InN, respectively) [1]. Electric fields induced by spontaneous/piezoelectric polarisation are irrelevant in large homogeneous materials. However, in heterostructures, this is not the case. There will be polarisation-charge discontinuities at the interfaces, and net polarisation charges induce internal electric field [5]. This internal electric field is large in small size heterostructures, such as QWs and is of the order of 1-2 MV/cm [6]. The effect of

this internal electric field in QW structures (the active region in most of the light emitting devices) is to spatially separate the electrons and hole wave function to opposite sides of the QW. This is known as Quantum Confined Stark Effect (QCSE) [Fig 2.3]. This results in reduced radiative recombination efficiency (reducing the internal quantum efficiency), redshift in emission energy, and blueshift in emission energy under high carrier injection. This internal electric field significantly contributes to the widely discussed low efficiency of green InGaN LEDs ('green-yellow gap'), carrier leakage and efficiency droop in LEDs [7, 8].

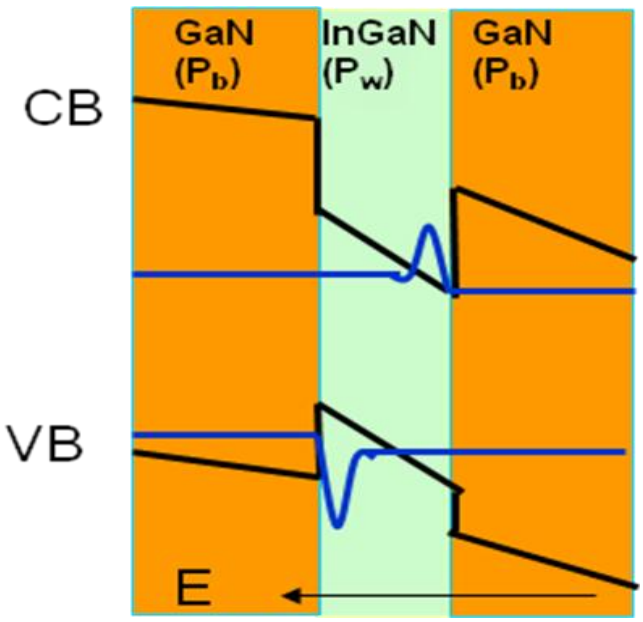

Figure 2.3 Quantum confined stark effect in InGaN/GaN QW structures [6]. P_b and P_w represent the Polarisation within the barrier and quantum well layer respectively.

The strength of the internal electric field is determined by the projection (i.e., cos θ) of the polarisation vector onto the plane of interest [Fig 2.4 (a)]. Since the InGaN QWs grown along semipolar and nonpolar directions experience small or zero built-in field related adversities, the heterostructures grown along such planes are of significant research interest.

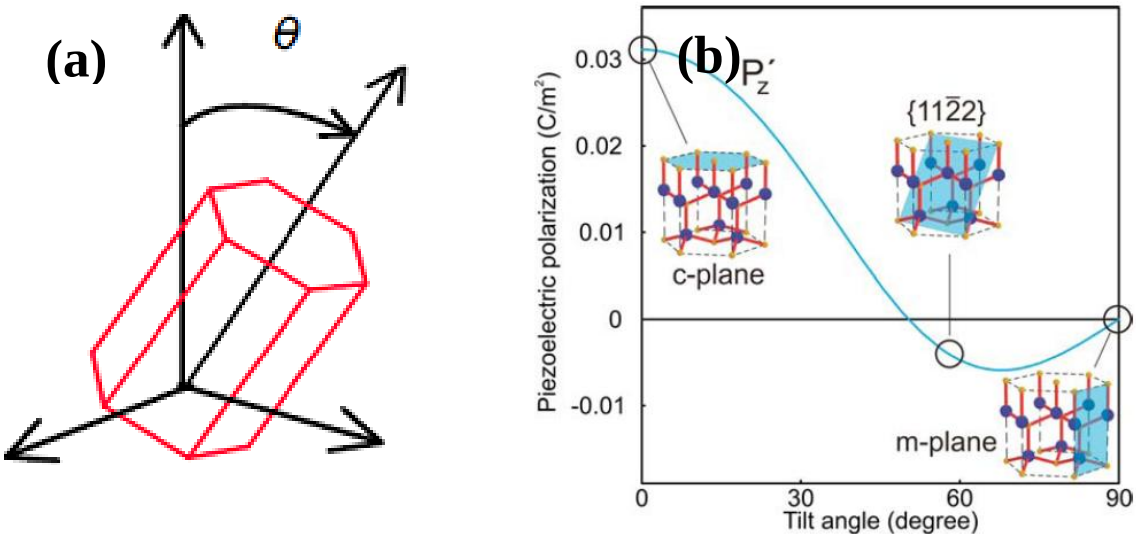

Figure 2.4 (a) The inclination angle θ from the c- plane (b) piezoelectric polarisation of an $In_xGa_{1-x}N$ quantum well grown pseudomorphically between relaxed GaN barriers. The lattice planes of particular polar, semipolar, and nonpolar orientations are shown as insets. P'z is the polarisation perpendicular to the growth plane [9]

It was pointed out by Park and Chuang [10] that the piezoelectric field can be cancelled out for certain oblique crystal orientations of semipolar planes [Fig 2.4 (b)]. Though there is still a debate concerning the semipolar orientation for which the field vanishes, a reduction in piezoelectric field strength has been experimentally verified for III-nitride heterostructures grown along {10$\underline{1}$1}, {10$\underline{1}$3} and {11$\underline{2}$2} crystalline facets inclined respectively at angles 62, 32 and 58^0 with respect to the polar c-axis [7]. Furthermore the epitaxial growth and InN incorporation along these semipolar directions appear to be much easier to control [11] and the InN incorporation in InGaN semipolar quantum wells may be comparable to, or greater than that of the c-plane one. Therefore, it may be possible to overcome the green-yellow gap with semipolar InGaN quantum wells [12].

2.2.3 Band structure of III-nitrides

The III-nitride hexagonal crystals all have direct- transition bandgap structure whereas the cubic structures of AlN and BN exhibit indirect bandgaps. InN was initially reported to have an energy gap of 2 eV, but values from 0.67 (low temperature) to 0.63 eV (room temperature) have been accepted based on the optical properties of high quality hexagonal InN epitaxial layers with low background electron densities grown by MBE [1]. Fig 2.5 shows the band structure of the wurtzite and zincblende III-nitrides near the Γ- point. The conduction band (CB) is formed of highly symmetric s-orbitals and valence band (VB) is composed of highly asymmetric p-orbitals.

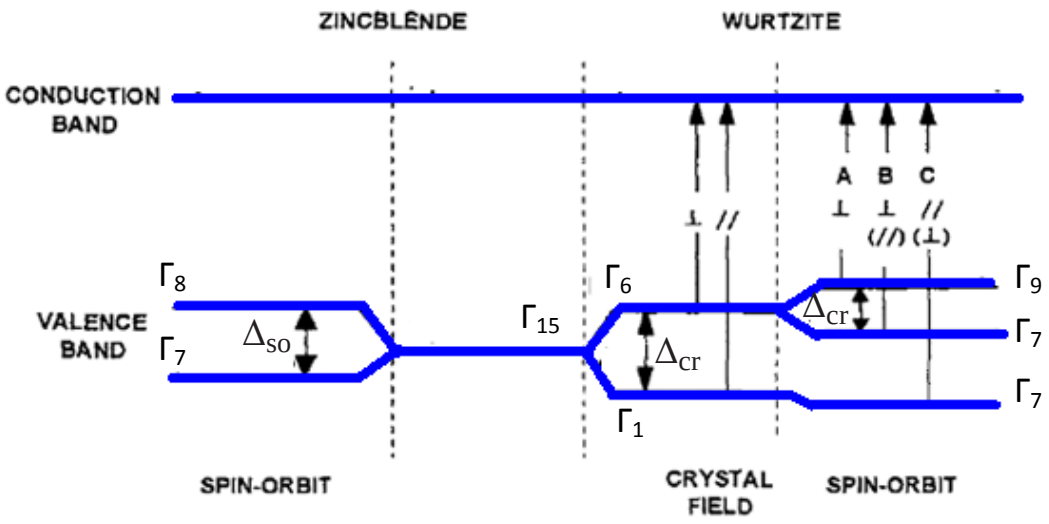

Figure 2.5 Relationships between the VB splitting at the Γ point in the zinc-blende and wurtzite lattices and the irreducible representations of the CB and VB in these lattices. The indications ⊥ and ∥ show that, the optical transition is allowed for the light polarisation perpendicular and parallel to the c-axis respectively. Brackets indicate the partially allowed transition. The symbols Δ_{so} and Δ_{cr} are the spin-orbit and crystal field splitting respectively [13].

For wurtzite, the energy at the Γ-point, Γ_{15}, corresponds to the valence band and split into three levels through the action of crystal field and spin–orbit coupling. The crystal field splitting arises due to the hexagonal symmetry of the wurtzite crystal structure and this splits the valence band into Γ_6 state (two fold degenerate) and Γ_1

state (non-degenerate). Spin-orbit interaction further splits the Γ_6 state into Γ_9 and Γ_7 states. The three resulting bands in wurtzite III-nitrides are called heavy hole [HH (Γ_9), A band], light hole [LH (Γ_7), B band), and crystal field [CH (Γ_7), C band], respectively. On the other hand, the zincblende valence band is divided into the doubly degenerate Γ_8 (HH, LH) and Γ_7 (CH) because of spin–orbit splitting. For wurtzite GaN and InN, the crystal field splitting parameter Δ_{cr} is small and positive and Γ_6 is always higher than that of Γ_1 state. Thus the top of the valence band is mainly constituted by HH band and the valence band ordering of wurtzite GaN is similar to as shown in Fig. 2.5. On the other hand, AlN has a large *negative* crystal-field splitting energy due to its smaller ratio of the c- and a-lattice constants (c/a=1.601 compared to 1.625 for GaN). Hence the energy level of Γ_1 state is higher than Γ_6 state. Consequently the top of the valence band is constituted by CH band [13, 14]. The more details on band structure of AlN and GaN is given in Chapter 7.

The electronic energy band parameters of semiconductor alloys and their dependence on alloy composition are very important. The bandgap energy exhibits nonlinearity as a function of alloy composition. The bandgap energies of $A_xB_{1-x}C$ alloys (from *AC* and *BC*) can be expressed as follows:

$$E_g\,(A_xB_{1-x}C) = x\,E_{g\,AC} + (1-x)\,E_{g\,BC} - bx(1-x)$$

where *b* denotes the bowing parameter accounting for the deviation from a linear interpolation between the two binaries *AC* and *BC*. For $In_xGa_{1-x}N$, recent bandgap data give a relatively small bowing parameter of 1.43 eV [17]. For $Al_{1-x}In_xN$ alloys, the bowing parameter as large as 10 eV and a dependence on InN composition are also observed [18].

2.2.4 Optical properties of III-nitrides

The typical radiative recombination processes occurring in III-nitrides semiconductors are summarised in Fig 2.6 [13]. Intrinsic optical transitions take place between the electrons in the CB and holes in the VB including excitonic effects due to the Coulomb interaction. Free excitons (FE) and their excited states transition can be seen in high quality samples with low impurity concentration. Excitons could be bound to neutral or charged donors and acceptors. The two important bound

excitons (BE) in III-nitrides are neutral shallow donor bound excitons (DBE) and neutral shallow acceptor bound (ABE) excitons. The transition energy of bound excitons associated with neutral impurities is lower than that of FE by their localisation energy E_{loc}. The bandgap energy of GaN can be accurately determined from luminescence measurements of exciton transitions. The actual bandgap is recovered by adding the estimated binding energy to the observed exciton transition energy. Extrinsic properties are related to dopants or defects. The defect related transition seen in optical spectra are free to bound, bound to free and bound to bound (donor-acceptor) and yellow band luminescence. Photoluminescence and cathodoluminescence spectroscopic techniques are employed to study the radiative recombination of optical properties of various III- nitride based nanostructures and epitaxial layers as discussed in this thesis.

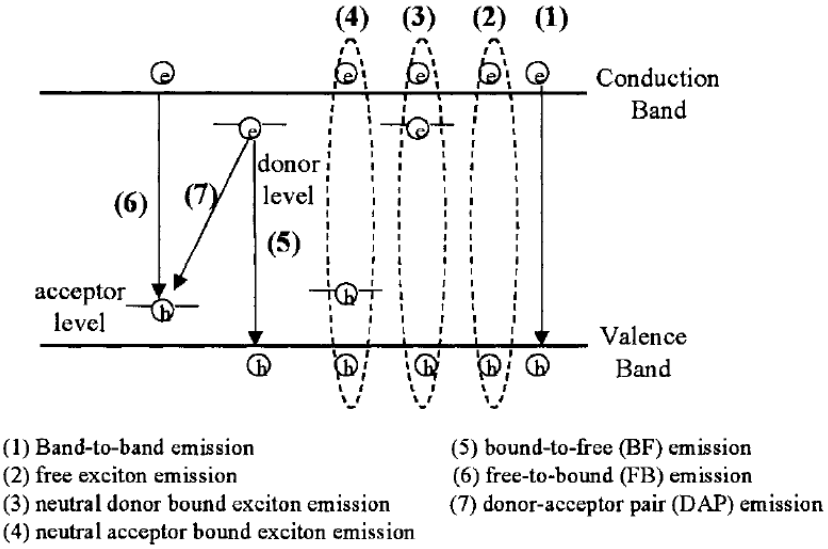

Figure 2.6 Schematic drawing of radiative recombination processes in III-nitride semiconductors preferably at low temperature where the excitonic and impurity-related emission occur [13]

Excitons couple with several kinds of phonons. Phonons are quanta of the collective lattice vibrations. They play an important role in the luminescence spectrum because in the exciton recombination process, the energy distributed is not only given to the photon but also to the lattice, leading to the so called phonon sidebands. The interaction of carriers with phonons is known to strongly affect the optical properties of semiconductors. A noticeable feature of the PL spectrum of GaN at low

temperature is the appearance of longitudinal (LO) optical phonon replica of FE and BE [1, 13, 19].

As the investigated samples include epilayers of ternary and quaternary alloys it is necessary to consider another important optical property of exciton localisation. The localised exciton transition takes place in alloy semiconductors with potential fluctuations (inhomogeneity) at low temperature. Potential fluctuation causes a difference between absorption (occurs at higher energy) and emission (at lower energy) which is referred to as the Stokes shift. Localisation and potential fluctuation can affect intensity dependent excitation and temperature dependent PL intensity by opening the channels of nonradiative recombination as the temperature is increased. The amplitude of the fluctuating potential at the bandedge caused by alloy disorder is strongly correlated to the energy bandgap difference between the two binaries constituting the alloy. The factors constituting the localisation are indium segregation, compositional fluctuations, quantum well width variation, and strain inhomogenities. Fig 2.7 gives a schematic of exciton localisation in InGaN epilayers [1].

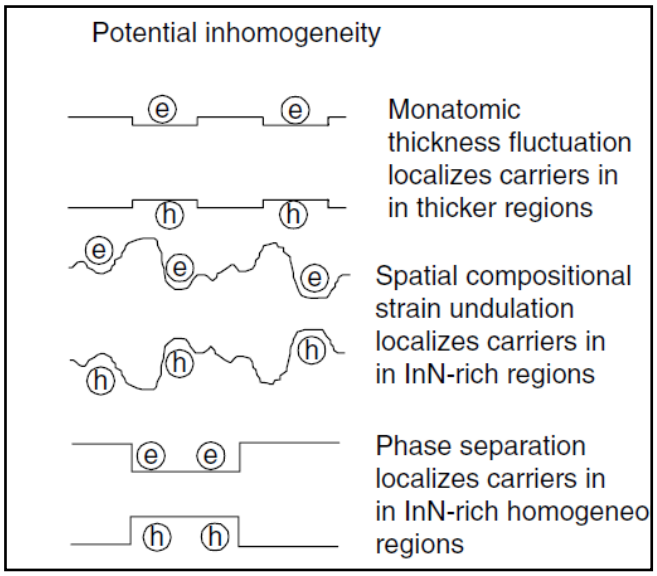

Figure 2.7 Schematic representation of the origin of potential fluctuations causing localisation and Stokes shift in InGaN epilayers [1]

2.2.5 Factors causing the optical anisotropy in III-nitrides

Since the polarisation resolved optical properties of AlInN and GaN are discussed in chapter 7 of this thesis, it is worth to discuss the factors that cause the optical anisotropy in wurtzite III-nitrides. Optical polarisation anisotropy can arise from the structural properties of the semiconductor material as well as due to external factors. The symmetry of the lattice of crystalline III-nitride semiconductors can affect the polarisation properties of the system. The wurtzite crystals have low symmetry. The lattice arrangement in wurtzite unit cell, having a hexagonal base with a unique c-axis normal to this hexagonal base, introduces anisotropy between directions parallel and perpendicular to the c-axis. This can influence the electronic band structure which in turn results in a difference in the responses of the system for light polarised relative to the c-axis.

Lattice mismatch and thermal expansion coefficient mismatch between the substrate and the epitaxial material result in the growth of strained epilayers. Anisotropic strain manifests as a deformation of the lattice structure of the semiconductor film and can modify the electronic band structure and can cause the anisotropy in optical properties. Thus for a bulk semiconductor which is isotropic when unstrained, the presence of anisotropic strain can reduce the symmetry of the crystal and introduce polarisation anisotropy in its optical responses [20, 21]. Even for crystal structures which are essentially asymmetric, the anisotropic strain can further modify the electronic band structure and can alter the polarisation dependence of the optical response of the system [22, 23].

The next section gives the description of various III-nitride heterostructures whose optical properties are investigated in this thesis. Research background and challenges in each of the sample structure is discussed in separate sections.

2.3 Research Background and Objectives

2.3.1 Epitaxial Lateral Overgrowth (ELOG) GaN

Most of the technological development of GaN based devices relies on heteroepitaxy because of the absence of bulk GaN substrates. This generates huge densities of dislocations (10^9 to 10^{11} cm^{-2}) due to lattice parameter and thermal

expansion coefficient differences. Using appropriate buffer layers allows the dislocation density to be reduced into the low 10^8 cm^{-2} ranges. An important method of reducing the defect density is epitaxial lateral overgrowth technology (ELOG) [24]. In ELOG, parts of a highly dislocated GaN layer are masked with a dielectric mask after which the growth is restarted. At the beginning of the second step deposition only occurs within the openings while no deposition is observed on the mask. This is referred to as selective area epitaxy (SAE) or selective area growth (SAG). The basic idea of ELOG is the filtering and blocking of the defects [1,25].

The ELOG depends on growth anisotropy in the form of different growth rates on different crystallographic planes. The lateral overgrowth rates and the equilibrium facets developed in the process are strong functions of both crystallographic orientation of the stripe openings and the growth parameters, such as the temperature, V/III ratio in the vapour phase, reactor pressure, composition of the carrier gas (H_2- N_2) and the fill factor (definend as the ratio of the stripe opening and the pattern period) [1, 25]. In the pyramidal structures formed by selective area epitaxy, the bending mechanism of threading dislocation causes a sizable reduction in threading dislocation (TD) density. The threading dislocations bend at 90 degrees when they reach the {1$\underline{1}$01} facets and minimise the free energy of the system by bending towards the free surface. Chapter 6 of this thesis investigates the optical properties of QWs fabricated on pyramidal structures of nanodimension. These samples constitute different sets based on the QW thickness and pyramid shape and are prepared at University of Bath. Modulation of the V/III ratio can also be employed to control the morphology of overgrown structures. This can be implemented by introducing controlled interruptions of the NH_3 flow in the growth process. The lateral growth increases with the duration of the flow interruption. By tuning the growth conditions it is possible to enhance the lateral growth and to get full coalescence [1].

There are some disadvantages with ELOG as follows; in ELOG threading dislocations originating from the interface in the window regions can propagate to the surface and very thick GaN layers (of the order of tens of microns) are needed in comparison to nano-ELOG method (discussed below) to greatly reducing TD

density. Moreover, the processing of efficient devices is possible only above the ELO wings and thereby reduces the area available for device fabrication.

2.3.1 (a) Nanoheteroepitaxy and nano-ELOG

Nanoheteroepitaxy can eliminate defects more efficiently than other ELOG techniques. Here the coalescence takes place in the realm of nano dimension with resulting overall strain relaxation for minimal defect propagations. This approach starts with patterning of a substrate into a two-dimensional array of 10-300 nm sized nucleation islands. This is then followed by selectively growing epitaxial material on the islands. These processes are followed by lateral overgrowth to get coalescence. The nanoscale patterning permits strain partitioning as in planar compliant structures and stress in these nanostructured sample decays exponentially away from the heterointerface with a characteristic decay length proportional to the diameter of the island. These factors can lower the strain energy in nanostructured lattice mismatched material systems. According to nanoheteroepitaxy theory, mismatch dislocation formation can be avoided from material systems with a lattice mismatch in the range 0-4 %, though unavoidable in material systems with larger lattice mismatch (e.g., the 20 % mismatch for GaN on Si). Also this nanostructuring can effectively prevent defect propagation owing to the large surface to volume ratio [1, 25].

Nano-ELOG process is a cross between nanoheteroepitaxy and ELOG processes. Following the formation of nanosized patterns (stripe or dot) the nanosized growth windows allow for prismatic GaN growth with thicknesses at the top below the critical thickness for extended defect free material to be achieved. The prismatic GaN grown in nano-ELOG should be defect free because of its small thickness and three dimensional strain minimising shape. This is in contrast to conventional ELOG where the base for selective area growth is large and (11$\underline{2}$01) prismatic planes require a layer thickness greater than the coherence limit to reach the tip and therefore the prismatic GaN is defect loaded. Following prismatic growth, the growth temperature can be changed as in conventional ELOG for enhanced lateral epitaxial growth for coalescence. The various steps of nano-ELOG are shown in Fig 2.8 [26]. Preliminary investigations showed threading dislocation densities as

low as 10^7 cm^{-2} in GaN coalesced films on Si substrate. This is notable considering a thickness of 2 µm for the coalesced GaN film [27].

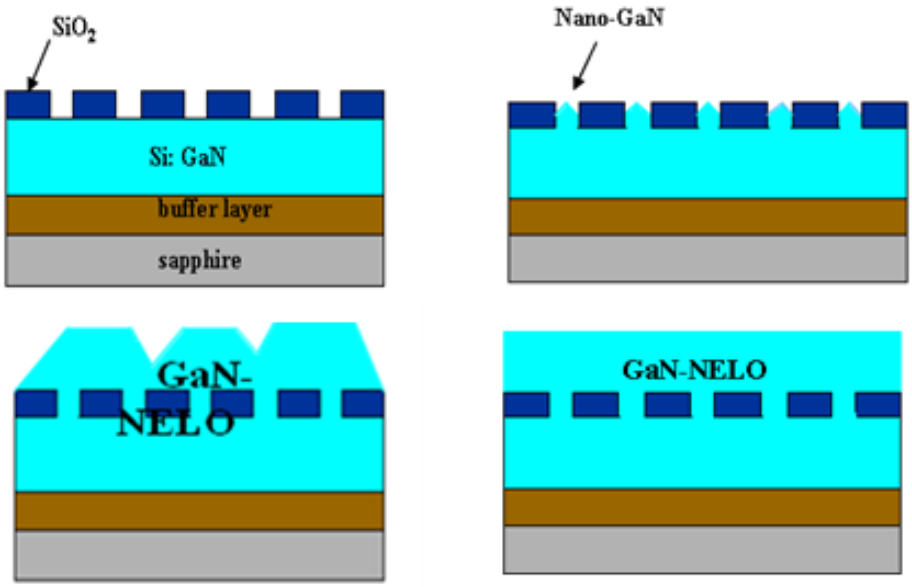

Figure 2.8 Different stages of nano-ELOG GaN growth [26]. (NELO stands for nano-ELOG)

The previous reports on nano-ELOG suggest that it is a promising method to improve the quality of GaN semiconductor materials for the commercialisation of GaN devices on Si/sapphire substrates [28, 29]. New additions on these achievements are the following two reports. The fabrication of phosphor free white light InGaN/GaN MQW based LED structures on nano-ELOG GaN has recently been reported by Soh et al [30]. The nanopatterning with embedded SiO_2 mask enhanced the light extraction efficiency due to multiple scattering. Very recently Fong et al [31] reported improved performance of the InGaN/GaN MQW LED structures fabricated on nano-ELOG layers. The nano-ELOG layer contributes to a twofold improvement in the LED performance, (i) by increasing the internal quantum efficiency due to reduction of threading dislocations and (ii) by increasing the extraction efficiency. The threading dislocation density estimated from (transmission electron microscopy) TEM measurements was 7.5 x $10^7 cm^{-2}$.

However, most publications on the subject focus on the threading dislocation densities (TDDs) and there are only a few that analyse the optical properties of the

nano-ELOG GaN especially the spatial distribution of radiative recombination emission across such a coalesced layer. Hence a part of this thesis is devoted to the investigation of optical properties of a series of nano-ELOG GaN layers using high spatial and spectral resolution CL hyperspectral imaging technique.

2.3.2 Coalescence of GaN nanocolumns

Nanocolumns are self-organised one dimensional nanocrystals. GaN nanocolumns were first demonstrated in 1996 by Yoshizawa et al [32]. Following this several related researches on the growth of nanocolumns on Si, sapphire and SiC by RF-MBE, hydride vapour phase epitaxy (HVPE), MOCVD and the characterisation of their structural and optical properties were reported. The GaN nanocolumn layers showed very intense luminescence emission with intensity many times higher than that of standard MOCVD grown GaN layers. This can be mainly attributed to their nanocolumn character. Their almost dislocation free nature introduces higher internal quantum efficiencies and the one dimensional nanostructure enhances the light extraction efficiency. Thus GaN nanocolumns are expected to be key technologies for realising nanometre scale photonic and electronic devices. [33].

Because of the very high structural and optical quality of GaN nanocolumns, it is possible to obtain a GaN epitaxial layer with potentially little or no stress and very few dislocations if the tops of such relaxed and dislocation-free GaN nanocolumns are coalesced by lateral growth. Nano-ELOG based on nanocolumns was first described by Luryi and Suhir [34]. Three approaches have so far been reported for the coalescence of GaN nanocolumns: (a) an all MBE route, involving coalescence overgrowth of MBE grown GaN nanocolumns by switching from N-rich to Ga-rich conditions [35]; (b) an all MOCVD route [28], involving coalescence overgrowth of GaN nanocolumns fabricated using a nano-imprint lithographic patterning and (c) growth of GaN nanocolumns by MBE following by an MOCVD overgrowth [36].

Tang et al reported the coalescence overgrowth of GaN nanocolumns on a Si (111) substrate with MOCVD. The cross-sectional CL spectroscopy revealed the

more efficient radiative emission from the coalesced layer than from the nano-column layer, showing the high optical quality of the coalesced layer [37]. The TD density of the coalesced GaN layer over the nanocolumns of ~ 10^8 cm^{-2} and the improvement in crystal quality of the coalesced layer with increase in thickness of the layer is also reported [38].

The coalesced GaN nanocolumn layers on Si substrates described in chapter 5 of this thesis are obtained by combining MBE and MOCVD approach, i.e utilising the third method mentioned above and their optical properties are investigated. These samples were prepared at the University of Bath. Self-assembled GaN nanocolumns are produced by MBE on a Si [111] substrate, and then serve as seeds for nano-ELOG by MOCVD. The optical properties of the coalesced GaN nanocolumn layers using high spatial resolution cathodoluminescence hyperspectral imaging technique is discussed in detail in Chapter 5.

2.3.3 Semipolar/nonpolar InGaN/GaN QWs

The significance and advantages of semipolar/nonpolar III-nitride semiconductor heterostructure growth have already been discussed in section 2.2. Advantages of using nonpolar or semipolar LEDs are not only reducing quantum confined stark effect related effects but also making a polarised light source which is important in applications such as LD and liquid crystal display (LCD) back light module [39]. There are three main approaches for the fabrication of semipolar InGaN/GaN QWs. These include the growth of a GaN epilayer on spinel ($MgAl_2O_4$) substrates [40], on bulk GaN substrates [41], and on the sidewalls of pyramidal or ridge GaN structures created on planar polar GaN surfaces using selective area epitaxy [42]. GaN grown on spinel substrates suffer from high density of threading dislocations and stacking faults. The use of bulk semipolar GaN substrates is prohibited by high wafer cost and small substrate size. On the other hand, the SAE technique can create semipolar planes on polar GaN surfaces and is a promising technique for creating high quality semipolar ($10\underline{1}1$), ($11\underline{2}2$) or nonpolar ($11\underline{2}0$) facets on (0001) GaN [1, 25].

Most of the reports on faceted GaN microstructures are on the micron-scale, with the minimum mask window openings in the range 1– 6 μm with a spacing of 5 to 20 μm.

But as far as any large area LED application of light emission from QWs grown on semi- or non-polar facets is considered, there is a need to maximise the emissive area by reducing the separation between the growth islands, i.e by fabricating QWs on nanopyramids. The semipolar {10$\underline{1}$1} InGaN/GaN QWs described in this thesis [Chapter 6] are all fabricated on facets of GaN nanopyramids. The advantages of faceted geometry are (i) reduced piezoelectric fields (ii) increase in the effective area (iii) good light output etc. Experimental and theoretical study demonstrated that the low dimensional structures contain low defect density, thus reducing the nonradiative recombination centres and increasing internal quantum efficiency of GaN based light emitting diodes. Nanostructures i.e. nanopyramid arrays offer additional strain relaxation afforded by the presence of the additional free surface. This strain relaxation should enable more indium to be incorporated into the active layers, therefore expanding emission spectrum of GaN based LEDs [25]. Thus, fabrication of GaN based nanostructures is important for improving the semiconductor device performance.

There are only a few reports for the semipolar InGaN/GaN QWs fabricated on the nanofacets of hexagonal pyramids. The available literature is summarised below. Keyan et al fabricated the {10$\underline{1}$1} InGaN/GaN MQWs on the nanofacets of hexagonal nanopyramid formed on top of the GaN nanorods of ~ 60 nm diameter. Higher InN incorporation and higher PL emission intensity is observed in comparison to c-plane grown InGaN/GaN QWs and is attributed to the strain relaxation effects in nanostructures, reduced dislocation density and high light extraction efficiency due to nano-patterning [43]. Yu et al reported the fabrication and optical properties of semipolar InGaN/GaN MQW deposited on the facets of high density self assembled nanostructured semipolar GaN pyramids, based on c-plane GaN template. InGaN/GaN MQWs were fabricated on the facets of self-formed nanopyramids having the dimension of 100-200 nm and with two types of semipolar planes (10$\underline{1}$1) and (11$\underline{2}$2). The analysis of optical properties by PL spectroscopy revealed a remarkably reduced internal electric field and higher internal quantum efficiency (>30 %) from these nanostructured semipolar MQWs [44]. In both these cases, though the very high density of nanostructures were realised, they were not quite uniform and resulted in broad PL emission which would affect the

device performance adversely. Kim et al [45] reported the InGaN MQWs emitting in the yellow region fabricated on (11$\underline{2}$2) facets of nanoscale GaN hexagonal pyramids. Effective suppression of InN localisation (absence of S-shape as a function of temperature) and piezoelectric field is attributed mainly to the nanosize and semipolar nature respectively. But the report lacks a spatial distribution analysis of QW emission to verify how InN incorporation and well width varies across the nanopyramids compared to their micron scale-dimensions. Though (11$\underline{2}$2) plane is remarkable in terms of InN incorporation, they are not thermodynamically stable under the InGaN growth conditions and QWs grown on these planes can be quite non- uniform. On the other hand the semipolar (10$\underline{1}$1) facets making an angle of 62^0 with respect to the c-plane have reduced quantum confined stark effect and thermodynamically stable for MOCVD growth conditions.

The InGaN QWs investigated in this thesis are all fabricated on {10$\underline{1}$1} facets of nanopyramids which are uniformly patterned in size and shape and the obtained emission spectral width is better than the published reports mentioned above. The growth details of the samples are described in Chapter 6. A detailed analysis of nonpolar and semipolar QWs fabricated on such nanopyramid facets is challenging because of their small dimension. However we have obtained spectrally and highly spatially resolved (~15 nm) luminescence information from these nanostructures. This yields information such as which facets emit in a particular wavelength region, how the indium incorporation in these nanopyramids can be compared to that of micron scale pyramids and how the strain on the GaN template pyramids affects the indium incorporation in the QW layer etc. This information is important to realise white light generation from the InGaN/GaN LEDs fabricated on these nanofacets as this would allow growers to modify the growth conditions of these nanopyramids without the use of phosphors which is the most efficient method to efficient white light generation.

2.3.4 AlInN epilayers

AlInN is the least explored ternary compared to AlGaN and InGaN, mainly because of the difficulty in the growth of high quality AlInN alloy epilayers. This is due to the spinodal phase separation phenomenon caused by the difference of lattice

parameters, bonding energy and the optimum growth temperature between InN and AlN [46]. The first growth of AlInN was done by Starosta and a linear relation between the composition and the lattice constant was reported [47]. Presently AlGaN is the standard material for optical engineering of GaN devices and deep-UV emitters are currently being developed using AlGaN as active layer. However, because of the cracking issues and strain relaxation issues most of the reports on AlGaN/GaN distributed Bragg reflectors (DBRs) and LDs use AlN contents below 30 %. In contrast, pure AlN layers cannot be employed effectively because of the lack of an appropriate barrier material for carrier confinement. GaN based optoelectronics need a high-index contrast and high-bandgap lattice matched material. AlInN alloys with indium content between 14-22 % which are within a $\pm$0.5 % lattice mismatch to GaN are of special interest if they prove to exhibit a sufficiently high bandgap and refractive index contrast with GaN, so that these alloys can be employed as the active and cladding layers with no strain in the light emitting diodes and laser diode structures operating from the deep UV region to an infrared region [46, 48].

Lattice matched AlInN/GaN heterostructure based highly reflective (>99 %) DBRs and high electron mobility transistors with high two-dimensional electron gas (2DEG) sheet carrier density and mobility of upto 1760 cm^2/Vs are reported [49-51]. Senda et al reported that AlInN is more suitable than AlGaN for UV photodiodes with a cut-off wavelength in the UV-C range [52]. Despite the numerous applications of AlInN, the luminescence characteristics are not widely investigated compared to InGaN and AlGaN. Therefore it is worth investigating the optical properties of AlInN alloys. Understanding the compositional dependence of the bandgap is necessary in order to fabricate AlInN/GaN based optoelectronic devices as carrier confinement largely depends on the bandgap values.

Kubota et al reported for the first time the bandgap energy of the ternary AlInN and demonstrated that lattice matched AlInN has a bandgap energy of 3.34 eV [53]. Onuma et al reported recombination dynamics of localised excitons in AlInN epitaxial films on GaN templates grown by MOCVD. The integrated PL intensity at 300 K was as strong as 29 % of that at low temperature, showing the potential use of AlInN alloys as infrared to UV light emitters [54]. Wang et al reported the

composition dependent emission and absorption energies for AlInN with InN fraction varying from 0.13 to 0.24. A very large bowing parameter of 6 eV and Stokes shift of 0.4 to 0.8 eV were observed. The estimated bandgap using photoluminescence excitation spectroscopy is 3.9 to 4.5 eV [55]. Seppanen et al reported the highest value of luminescence emission of 5 eV from lattice matched AlInN grown on $Ti_{0.2}Zr_{0.8}N$ on single crystal MgO (111) substrates by Magnetron Sputter Epitaxy [56]. Sakalauskas et al reported a detailed discussion on band structure and valence band ordering in Al rich AlInN alloys pseudomorphically grown on GaN for the InN molar fraction of 0.143 to 0.242 [57]. Preparation of a-plane AlInN and their polarisation resolved emission and absorption measurements were recently reported by Laskar et al [58].

As a part of this thesis, the optical properties of a set of c-plane AlInN epilayers with InN molar fraction ranging from 14-20 % is investigated using the non-imaging mode CL set up and Xe-lamp based PL spectroscopy. Along with emission characteristics, the bandgap and bowing parameter of the epilayers are obtained using photoluminescence excitation (PLE) spectroscopy. The sample structure and the experimental results are discussed in detail in Chapter 7. The thin (~100 nm) epilayers of c-plane AlInN described in this thesis were prepared at University of Cambridge.

2.3.5 AlInGaN epilayers

Deep-UV LDs and LEDs are useful for realising large capacity optical memory or long-life time fluorescent light. Moreover they are important in biochemical and medical fields. However there are some technical problems that prevent the realisation of UV devices. The most severe problems are: difficulty in obtaining efficient UV emission at room temperature (RT) from AlGaN QWs compared with InGaN QWs; difficulty in achieving p-type doping in high Al content AlGaN; and the lack of efficient exciton localisation which makes carriers very sensitive to the non-radiative recombination centres.

However AlInGaN alloys are very important materials for the UV and deep UV range where Al rich AlGaN alloys have problems with low quantum efficiency and cracks due in part to lattice mismatch with GaN. The quaternary AlInGaN alloys

have the advantages such as strong spontaneous emission due to an enhanced radiative recombination of localised excitons / carriers at band tail states and better lattice match to AlN [59, 60]. The very intense UV emission at RT from AlInGaN has been utilised in fabricating efficient UV LEDs and LDs in the wavelength range 340- 375 nm with InN content varying from 0.02- 0.05. Light output powers of greater than 80 mW under pulsed current injection and power of 3.8 mW cw operation is also reported [61]. The application of AlInGaN quaternary for barrier layers in High Electron Mobility Transistor (HEMT) devices is also demonstrated [62]. It has been reported that introduction of InN ~ 5 % in AlGaN to form AlInGaN can considerably enhance the UV emission due to In segregation effects [63].

With all these successful implementations of AlInGaN -based devices, the spatial distribution analysis of AlInGaN intrinsic emission has not been widely investigated. This is partly limited by the spatial resolution of the CL experimental set up. However such an analysis is worth undertaking as it would provide experimental support to the proposition of InN localisation effect in AlInGaN similar to InGaN epilayers. As a part of this thesis, the spatial distribution of emission characteristics of a set of c-plane AlInGaN epilayers with InN molar fraction ranging from 1.8 to 4.3 % is investigated using high spatial resolution CL set up. Large area luminescence emission measurements such as PL and PLE are also employed to study their optical properties. These samples were prepared at Fraunhofer Institute for Applied Solid State Physics (IAF), Germany. Thus the study on AlInGaN epilayers involves two main objectives: (1) to study the light emission and bandgap energy as a function of InN in AlInGaN; and (2) to investigate the spatial distribution of light emission from AlInGaN to see any effect of InN localisation.

2.4 Summary

The fundamental properties of III-nitrides relevant to the study discussed in this thesis are described. Previous reports on various III-nitride nanostructures such as nano-ELOG GaN, coalesced GaN nanocolumn, semipolar and nonpolar InGaN/GaN QWs fabricated on nanofacets, epilayers of AlInN and AlInGaN,- which are the heterostructures studied in this thesis – are reviewed. The main research challenges

and research objectives in each of these III-nitride heterostructures are discussed and stated.

References:

[1] Morkoc H 2008 *Handbook of Nitride Semiconductors and Devices Vol. 1* (Weinheim: Wiley-VCH)

[2] Piprek J 2007 *Nitride Semiconductor Devices Principles and Simulation* (Weinheim: Wiley-VCH)

[3] Vegard L 1921 *Z. Phys.* **5** 17

[4] Paskova T 2008 *Phys. Status Solidi B* **245** 1011

[5] Mishra U K and Singh J 2008 *Semiconductor Device Physics and Design* (Netherlands: Springer-Verlag)

[6] Speck J S and Chichibu S F 2009 MRS Bulletin **34** 304

[7] Masui H, Nakamura S, DenBaars S P and Mishra U K 2010 *IEEE TRANSACTIONS ON ELECTRON DEVICES* **57** 88

[8] Bernardini F 2007 *Nitride Semiconductor Devices Principles and Simulation* Piprek J Editor (Weinheim: Wiley-VCH)

[9] Schwarz U T and Kneissl M 2007 *Phys.Stat.Sol. (RRL)* **1** A44

[10] Park S H and Chuang S L 1999 *Phys. Rev. B* **59** 4725

[11] Chakraborty A, Baker T J, Haskell B A, Wu F, Speck J S, DenBaars S P, Nakamura S, and Mishra U K 2005 *Jpn.J. Appl. Phys.* **44** L945

[12] Wunderer T et al 2011 *Phys. Status Solidi B* **248** 549

[13] Chichibu S F, Kawakami Y and Sota T 1999 *Introduction to nitride semiconductor blue lasers and light emitting diode* Edited by Nakamura S and Chichibu S F (New York : CRC Press)

[14] Vurgaftman I and Meyer J R 2007 *Nitride Semiconductor Devices Principles and Simulation* Piprek J Editor (Weinheim: Wiley-VCH)

[15] Taniyasu Y and Kasu M 2011 *Appl. Phys.Lett.* **98** 131910

[16] Suzuki M, Uenoyama T and Yansae A 1995 *Phys.Rev.B* **52** 8133

[17] Wu J and Walukiewicz W 2003 *Superlatt. Microstruct.* **34** 63

[18] LayTheng Tan 2009 PhD Thesis, University of Strathclyde *Nanometric characterisation of III-Nitride semiconductors*

[19] Shionoya S 1998 *Luminescence of Solids* [Edited by D R Vij] (New York : Plenum Press)

[20] Chuang S L 1995 Physics of Optoelectronic Devices (USA: Wiley Interscience)

[21] Bhattacharya J 2008 PhD Thesis, Tata Institute of Fundamental Physics, *Optical Polarisation anisotropy in Semiconductor Heterostructures*

[22] Alemu A, Gil B, Julier M and Nakamura S 1998 *Phys. Rev.B* **57** 3761

[23] Ghosh S, Waltereit P, Brandt O, Grahn H T, Ploog K H, 2002 *Phys. Rev. B* **65** 075202

[24] Nakamura S, Senoh M, Nagahama S, Iwasa N, Yamada T, Matsushita T, Kiyoku H, Sugimoto Y, Kozaki T, Umemoto H, Sano M and Chocho K 1998 *Appl. Phys. Lett*. **72** 211

[25] Gibart P, Beaumont B and Vennegues P 2003 *Nitride Semiconductors handbook on materials and devices* Edited by Ruterana P, Albrecht M, J. Neugebauer (Weinheim: Wiley-VCH)

[26] Zang K Y, Wang Y D and Chua S J 2005 *Appl. Phys. Lett*. **87** 193106

[27] Zubia D, Zaidi S H, Brueck S R J and Hersee S D 2000 *Appl. Phys. Lett*. **76** 858

[28] Wang Y D, Zang K Y, Chua S J, Tripathy S, Zhou H L and Fonstad C G 2006 *Appl. Phys. Lett*. **88** 211908

[29] Wang L S, Tripathy S, Wang B Z, Teng J H, Chow S Y and Chua S J 2006 *Appl. Phys. Lett*. **89** 011901

[30] Soh et al 2010 *Phys. Stat. solidi A* **207** 1400

[31] Fong W K, Leung K K and Surya C 2011 *Crystal Growth Design* **11** 2091

[32] Yoshizawa M, Kikuchi A, Mori M, Fujita N and Kishino K 1997 *Institute of Physics Conference Series* **155** 187

[33] Kumano H and Suemune I 2007 *Wide Bandgap Semiconductors Fundamental properties and modern photonic and electronic devices* (Heidelberg: Springer –Verlag)

[34] Luryi S and Suhir E 1986 *Appl. Phys. Lett.* **49** 140

[35] Cherns D, Meshi L, Griffiths I, Khongphetsak S, Novikov S V, Farley N, Campion R P and Foxton C T 2008 *Appl. Phys. Lett.* **92** 121902

[36] Bougrioua Z, Gibart P, Calleja E, Jahn U, Trampert A, Ristic J, Utrera M and Nataf G 2007 *J. Cryst. Growth* **309** 113

[37] Tang T Y, Averett K L, Albrecht J D, Shiao W Y, Chen Y S, Yang C C, Hsu C W and Chen L C 2007 *Nanotechnology* **18** 445601

[38] Meshi L 2008 *Phys Stat solidi c* **5** 1645

[39] Kubota M, Okamoto K, Tanaka T and Ohta H 2008 *Appl. Phys. Lett.* **92** 011920

[40] Baker T J et al. 2005 *Jpn. J. Appl. Phys. part 2 Lett. Expr. Lett.* **44** L920

[41] Anurag T et al 2007 *Jpn. J. Appl. Phys. part 2 Lett. Expr. Lett.* **46** L444

[42] Cho C Y 2008 *Appl. Phys. Lett.* **93** 241109

[43] Keyan Z, Yadong W and Jin C S 2009 *phys. Stat. Sol. (c)* **6** S514–S518

[44] Yu H, Jung T and Ku P C 2008 *phys. Stat. Sol. (c)* **5** 1618

[45] Kim T, Kim J, Yang M S, Lee S, Park Y, Chung U-ln and Cho Y 2010 *Appl. Phys. Lett.* **97** 241111

[46] Butte R et al 2007 *J. Phys. D: Appl. Phys*. **40** 6328

[47] Starosta A 1981 *Phys. Stat. solidi A* **68** K55

[48] Carlin J-F, Zellweger C, Dorsaz J, Nicolay S, Christmann G, Feltin E, Butte R and Grandjean N 2005 ´ *Phys. Stat. Solidi b* **242** 2326

[49] Carlin J F, Dorsaz J, Feltin E, Butte R, Grandjean N, Ilegems M and Laugt M 2005 *Appl. Phys. Lett* **86** 031107

[50] Kuzmık J 2001 *IEEE Electron Device Lett*. **22** 510

[51] Xie J, Ni X, Wu M, Leach J H, Ozgur U and Morkoc H *Appl. Phys. Lett* **91** 13 132116

[52] Senda S, Jiang H and Egwa T 2008 *Appl. Phys. Lett* **92** 203507

[53] Kubota K, Kobayashi Y and Fujimoto K 1981 *J. Appl. Phys.* **66** 2984

[54] Onuma T, Chichibu S F, Uchinuma Y, Sota T, Yamaguchi S, Kamiyama S, Amano H and Akasaki I 2003 *J. Appl. Phys.* **94** 2449

[55] Wang K, Martin R W, Amabile D, Edwards P R, Hernandez S, Nogales E, O'Donnell K P, Lorenz K, Alves E, Matias V, Vantomme A, Wolverson D and Watson I M 2008 *J Appl. Phys*. **103** 073510

[56] Seppanen T, Hultman L and Birch J 2006 *Appl. Phys. Lett* **89** 181928

[57] Sakalauskas E et al 2010 *Journal of Physics D: Applied Physics* **43** 365102

[58] Laskar M R, Ganguly T, Rahman A A, Arora A, Hatui N, Gokhale M R, Ghosh S and Bhattacharya A 2011 *Appl. Phys. Lett* **98** 181108

[59] Hirayama H 2005 *J Appl. Phys*. **91** 091101

[60] Bedair S M, McIntosh F G, Roberts J C, Piner E L, Boutros K S and El-Masry N A 1997 *Journal of Crystal Growth* **178** 32

[61] Hirayama H, Akita K, Kyono T, Nakamura T and Ishibashi K 2004 *Jpn J of Appl Phys* **43** 1241

[62] Manuel J M, Morales F M, Garcia R, Lim T, Kirste L, Aidam R and Ambacher O 2011 Crystal Growth and Design **11** 2588

[63] Hirayama H, Kinoshita A, Yamabi T, Enomoto Y, Hirata A, Araki T, Nanishi Y and Aoyagi Y 2002 *Appl. Phys. Lett* **80** 1433162

Chapter 3

Experimental techniques and principles

3.1 Introduction

Research on semiconductor materials requires various kinds of characterisation techniques for proper understanding of the material with a view to improving performance of devices and increasing the yield. This chapter gives the details of the characterisation techniques used in this thesis. The techniques used are photoluminescence (PL) and PL excitation (PLE) spectroscopy for investigating the luminescence properties; cathodoluminescence (CL) spectroscopy and CL hyperspectral imaging for spatially resolved luminescence characterisation, secondary electron microscopy (SEM) for visualisation of the surface morphology; and Rutherford backscattering spectrometry (RBS) to study the compositional properties.

3.2 Optical characterisation

The main objective of this thesis is the characterisation of nanostructured III-nitride light emitting structures. To explore the optical properties of these structures, the luminescence properties and excitation mechanisms are studied using PL and CL hyperspectral imaging technique. Luminescence in solids is a non-equilibrium process in which the electronic states of solids are excited by some energy from an external source and the excitation energy is released as light. When the excitation source is optical, the process is termed as photoluminescence. Electron beam induced

luminescence is called cathodoluminescence. Through the process of carrier recombination excited carriers return to their ground state after a given life time. In the process of radiative carrier recombination, light is emitted with energy equal to the difference between the ground and excited states and non-radiative carrier recombination process occurs through dissipation of thermal energy [1]. By analysing the spectral intensity and wavelength position in respective luminescence methods, important properties such as the bandgap energy, bound exciton emission energy and defect emission bands can be determined. The comparison of these optical properties with the measured compositional and morphological properties can yield important properties of the material under investigation.

3.2.1 Photoluminescence spectroscopy

Photoluminescence from semiconductors is the most commonly used spectroscopic technique. PL spectroscopy is useful for providing information on: (1) optical emission efficiencies, (2) composition of the material (i.e. alloy composition), (3) impurity content, and (4) layer thicknesses (i.e. quantum well thicknesses), etc [2]. Two setups are used to measure PL and PL excitation (PLE) spectra of the samples. One PL setup uses a 325 nm Helium-Cadmium (He-Cd) laser line and the other PL/PLE setup uses a 1000 W Xenon lamp as the excitation source. Details of these setups are described in the following sections.

3.2.1 (a) PL experimental setup

A schematic representation of the PL setup using the 325 nm He-Cd laser is shown in Figure 3.1. A narrow band-pass interference filter near 325 nm is employed to remove plasma lines. The laser is focused onto the sample using a Schwarzschild-type reflecting objective, which also collects the emitted luminescence. The PL signals from the samples are detected using a combination of a spectrograph (Oriel Instruments MS125^{TM}, Model No. 77400, with an f-number of 3.7) and a 1024 x 255 pixel silicon charge-coupled detector (CCD; Andor front illuminated Model DV420 OE). The luminescence from the sample is focused on the 26 μm entrance slit of the spectrograph and reflected by two mirrors inside onto the surface of a diffraction grating which disperses the collected luminescence onto the CCD detector. A Schott

WG345 long-pass filter placed in front of the entrance slit of the spectrograph blocks any remaining 325 nm laser. The detector is cooled using a thermoelectric cooler to about -50 °C in order to reduce thermal noise. During the PL measurements, the signal from each vertical column of pixels in the CCD is integrated to obtain the PL intensity at a particular wavelength. Thus each column of the CCD acts as the output slit and detects the light dispersed at a particular angle from the diffraction grating. The width of each column in the CCD is 26 μm, which is matched to the entrance slit and helps to obtain signals with high signal to noise ratio.

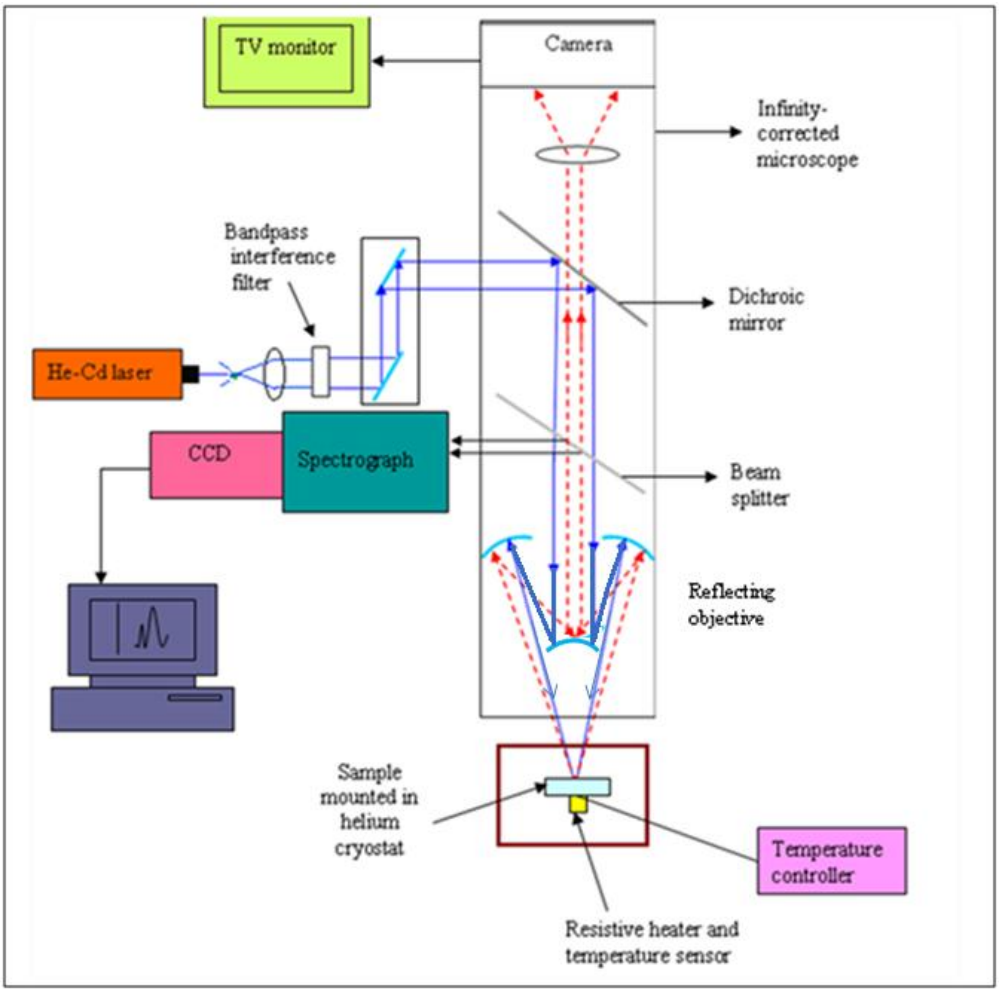

Figure 3.1 325 nm He-Cd laser PL spectroscopy setup. The blue lines show the excitation light path, the red lines represent the luminescence from the sample, part of which goes to the camera to check the position of the luminescence spot.

All samples were mounted on sample holder made of aluminium inside a closed cycle helium cryostat. An oil based diffusion pump backed by a rotary pump creates the required vacuum. A Cryogenics CT1 helium compressor permits the

cryostat to be cooled down to around 15 K. In combination, the helium cryogenerator and a film heater which is connected to a temperature controller (Oxford Instruments ITC-4) control the temperature around the sample. A temperature sensor is used to monitor the temperature in the cryostat and provides feedback to the temperature controller. In this way, the temperature of the samples can be controlled in the range from 15 K up to 300 K. During the experiment, the position of the PL spot (~ 15 μm) was fixed on a certain location on the sample as the temperature was increased in several steps up to room temperature. The spectral resolution depends on the wavelength and diffraction grating selected [3, 4]. Table 3.1 summarises some parameters of each grating used in this thesis.

Table 3.1 Important parameters of the gratings used in the spectrograph. The spectral resolution data are obtained using a 26 μm entrance slit and 1024 element CCD array. The blaze wavelength is the wavelength at which the grating efficiency is maximum [5]

Line Density (lines/mm)	Blaze wavelength (nm)	Type	Spectral resolution (nm)	Wavelength Range (nm)
400	350/500	Ruled	1.2	200-800
1200	350	Ruled	0.4	200-1000
2400	400	Holographic	0.2	230-650

3.2.1 (b) Photoluminescence excitation (PLE)/PL experimental setup

Photoluminescence excitation measurements are a widely used spectroscopic tool for the characterisation of optical transition in semiconductors. This technique is especially useful for studying the bandgap of epilayers grown on opaque substrates and thin epilayers, and is less dependent on the thickness of the material than direct absorption measurements. A typical spontaneous light emission process (luminescence) involves mainly three processes; (1) excitation of the valence band electrons to the conduction band (2) relaxation of non-equilibrium electrons and holes to their ground state (3) recombination of e-h pairs to produce luminescence.

In PLE spectroscopy, the spontaneous emission from the sample is detected at fixed photon energy, typically at the lowest excitonic resonance. The intensity of this signal is then recorded as a function of the excitation frequency. When the excitation photon energy is less than the bandgap, the intensity of the luminescence is negligible, but it increases rapidly as the absorption edge is approached. The equivalence between PLE and absorption signals strongly depends on the assumption that the recombination times are much larger than the intraband relaxation times, i.e., the excited electrons and holes have enough time to relax completely into quasi-equilibrium before recombining radiatively. In this case, the emission intensity at the lowest exciton becomes independent of the relaxation rate, and the PLE spectrum is approximated to the absorption signal [2, 6]. The difference between the excitonic peak positions in PL and PLE is known as the Stokes shift.

To measure the PLE spectra and selectively-excited PL spectra, a wavelength adjustable excitation source is needed. The excitation source used is a short arc 1000 W Xenon lamp with a quartz envelope and with output wavelength covering the deep ultraviolet of 220 nm to the visible wavelength range. The variation of excitation wavelength is achieved by scanning the excitation monochromator whereas the detection monochromator remains fixed at the desired position. The quartz envelope totally blocks the emission shorter than 220 nm, providing a short wavelength limit.

A schematic representation of the PLE setup using Xe-lamp is shown in Figure 3.3. Light from the Xe-lamp is focused by a quartz lens onto the slit of a Jobin Yvon 0.25 m monochromator (excitation monochromator) that consists of a UV grating of 1200 lines/mm. Slit width determines the band-pass of the quasi-monochromatic light from the excitation source. A narrow slit improves the band-pass and hence the excitation spectral resolution; however this would lower the intensity of the output light. Hence, to make a trade off between the resolution and the excitation intensity, a slit width of 2 mm is selected, giving a band-pass of approximately 6 nm at 300 nm. The output from the excitation monochromator passes through a chopper (chopping frequency ~ 36.5 Hz) and is focused on the sample surface to a spot size of approximately 2 x 5 mm^2. The sample is mounted on the cold head of a closed-cycle helium refrigerator on a moveable stage. An Oxford

Instruments ITC-4 Temperature Controller in conjunction with a heater and sensor inside the cryostat is used to measure and change the temperature.

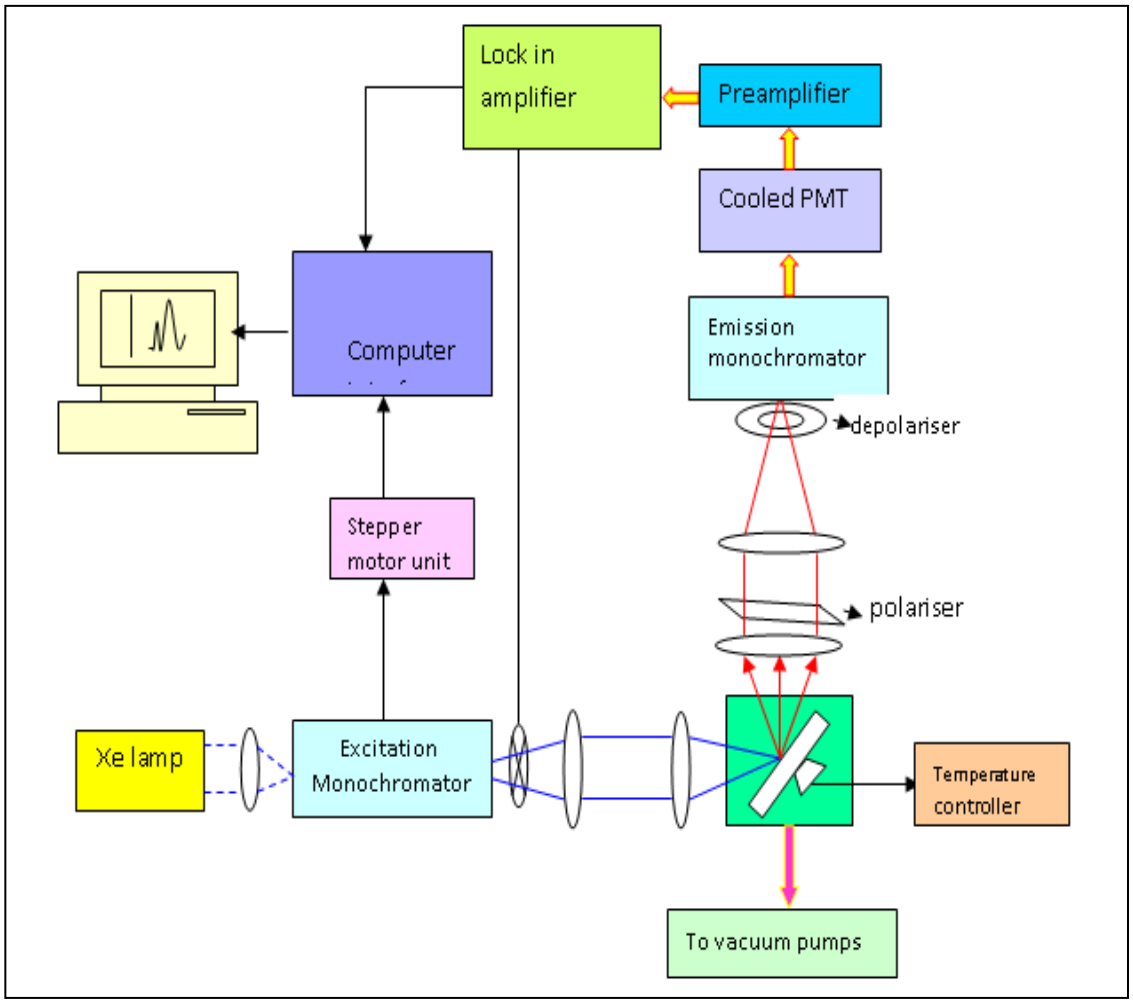

Figure 3.2 Schematic diagram of PLE/PL spectroscopy set-up using Xe lamp. The blue lines are the excitation light path and the red lines represent the luminescence from the sample.

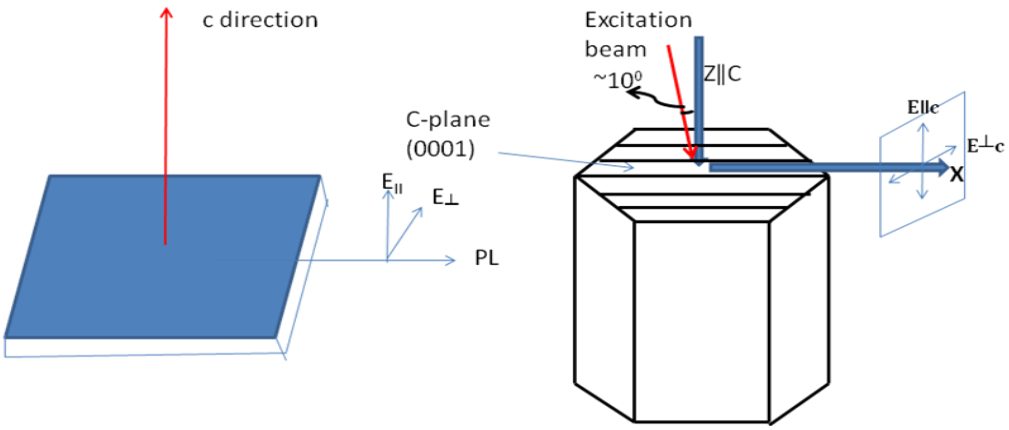

Figure 3.3 Geometrical arrangement of the experimental setup for the polarisation resolved PL measurements

Two quartz lenses are arranged in series to collect and collimate the luminescence from the sample and focus it onto the entrance slit of a McPherson 0.67 m detection monochromator with 1800 lines/mm UV/visible grating (blazed at 400 nm and working from 200-800 nm). The lenses are adjusted to maximise the amount of PL collected into the slit. The sample is mounted at an angle of 60° to the excitation beam to minimise the amount of specularly reflected excitation light entering the detection monochromator. A cooled photomultiplier tube (PMT) (Thorn EMI Gencom Inc. 3365) is used to detect the light dispersed by the detection monochromator. The PMT is connected via a Stanford SR570 current preamplifier to a Stanford SR810 DSP lock-in amplifier. The PL and PLE measurements are recorded using in-house software written by Dr. Paul Edwards, a colleague from our research group.

All PLE spectra presented in this thesis have been corrected for the combined throughput of lamp and the excitation monochromator. This was performed by using a UV sensitive photodiode placed at the sample position. The spectral response of the photodiode was obtained from the supplier. Dividing the measured intensity by the sensitivity function, the excitation intensity as a function of wavelength could be obtained. This Xe-lamp setup is also used to perform PL measurements. In a PL measurement, the setup is the same, the only difference being that the stepper motor is now used to drive the detection monochromator whilst the excitation wavelength remains unchanged. Prior to acquisition of a PLE spectrum, a PL spectrum is

acquired in order to determine the detection energy at which the emission monochromator should be set. This setup is further modified to measure the luminescence anisotropy of c-plane AlInN epilayers. Figure 3.3 shows the measurement geometry for the polarised PL measurements, with PL being collected in a direction close to the c-plane of the sample (near edge luminescence is measured). Xe lamp is used as the excitation source and the excitation wavelengths used range from 260- 290 nm. The PL from the AlInN epilayers collimated using UV lenses is passed through a rectangular sheet of UV polariser [50 x 50 mm, transmission range: 280-450 nm, 01 WL 50 Comar systems] to resolve the emitted photons with electric field vector parallel to c-direction (E∥c) and perpendicular to c-direction (E$^{\perp}$c). A depolariser is inserted before the entrance slit of the emission monochromator to eliminate the polarisation dependence of monochromator sensitivity as shown in in Fig 3.2.

3.3 Spatially resolved characterisation/luminescence

Although PL/PLE spectroscopy is ideal for analysing light emission/absorption properties on a large area, in-depth optical characterisation of III-nitride nanostructures essentially demands the spatially resolved luminescence information as well. The spatial resolution achievable with far field optical techniques is diffraction limited to ~ 250-500 nm. This diffraction limit can be overcome by two methods; (1) reduction of wavelength of the probing source (2) employment of near field detection techniques. Moving to shorter photon wavelengths is difficult due to the lack of versatile lenses and mirrors beyond the ultraviolet. Near field scanning optical microscopy (NSOM) exploits near field detection technique to push the spatial resolution down to tens of nanometers ($\leq$ 30 nm) depending on the tip aperture size. The use of electrons as the probing source rather than photons, permits one to achieve much improved and higher spatial resolution of < 1 Å, since the de Broglie wavelength of electrons is well below 0.1 Å at electron beam energies above 20 keV. Thus electron microscopes are one of the the best choice for spatially resolved characterisation of nanostructures. In this thesis, the field emission gun scanning electron microscope (FESEM) and electron probe

microanalyser (EPMA) are used to obtain spatially resolved information on surface features, luminescence and composition of III-V heterostructures [**7**].

When an energetic electron beam is incident on a target solid, the electrons interact elastically and inelastically with the specimen creating an interaction volume (depending on beam conditions) from which various types of radiation emerges. The generated signals include backscattered, secondary, and Auger electrons, characteristic and continuous X-rays, cathodoluminescence (long wavelength photons in the ultraviolet, visible, and infrared ranges) and beam induced currents in certain type of materials [8, 9]. By recording the magnitude of these signals with suitable detectors, a measure of certain properties of the specimen such as topography, composition, and luminescence can be studied from any area of interest of the specimen. Most commonly electron microscopes are used for imaging nanosized features using secondary electrons, but nowadays electron microscopes are modified to collect and analyse other inelastically scattered electrons as well to extract material information contained in them. In this thesis electron beam generated secondary electrons, and cathodoluminescence from III-nitride heterostructures are respectively exploited to study the surface morphology and optical properties. Figure 3.4(a) and (b) show the various signals resulting from electron beam interaction with the solid and the depth from which the respective signals are generated.

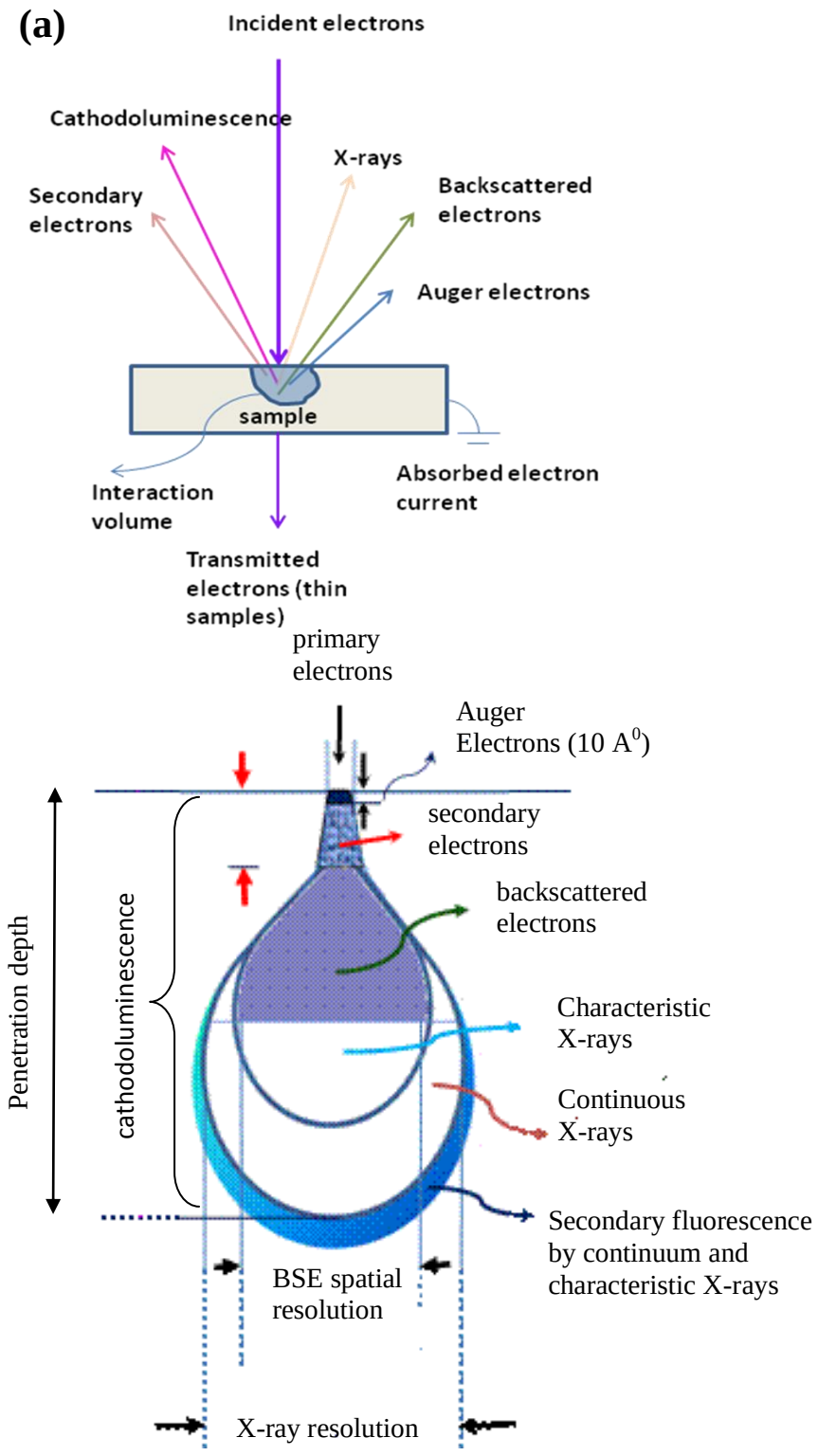

Figure 3.4(a) Generalised illustration of various signals arising for electron – specimen interaction and (b) the interaction volumes from which respective signals arise [10]

3.3.1 Field emission gun scanning electron microscopy (FESEM)

An FESEM is used to visualise very small topographic details on the surface and hence ideal for studying the surface features/topography of III-nitride nanostructured light emitters. In standard electron microscopes, electrons are mostly generated by heating a tungsten filament by means of a current to a temperature of about 2800°C. In FESEM no heating source is employed. An extremely thin and sharp tungsten needle (tip diameter 10^{-7}–10^{-8} m) functions as a cathode in front of a primary and secondary anode. The voltage between cathode and anode is in the order of magnitude of 0.5 to 30 kV. Because the electron beam radius produced by the field emission source is about 1000 times smaller than in a standard microscope, the image quality and spatial resolution is markedly better. Electrons are liberated from a field emission source and accelerated in a high electrical field gradient. Within the high vacuum column these so-called primary electrons are focussed and deflected by magnetic lenses to produce a narrow scan beam that bombards the object. As a result secondary electrons are emitted from each spot on the object. The angle and velocity of these secondary electrons relates to the surface structure of the object. A detector catches the secondary electrons and produces an electronic signal. This signal is amplified and transformed to a video scan-image that can be seen on a monitor or to a digital image that can be saved and processed further [11, 12]. Four main components combine to produce the images from the sample: an electron gun, a demagnification unit, a scan unit and a detection unit. The electron gun, which is the source emitter, is already described above. The electron beam emitted by the electron gun is focused by the electro-magnetic lenses (condenser lens, scan coils, stigmator coils and objective lens) and the apertures in the column to a tiny sharp spot.

3.3.2 Cathodoluminescence spectroscopy and hyperspectral imaging

Since the most extensively used luminescence characterisation method employed in this thesis is the phenomenon of cathodoluminescence, this is described in detail in the following section. Cathodoluminescence is the phenomenon of emission of light (commonly wavelength ranges for λ = 200 nm to 2500 nm) by a solid material due to irradiation by an energetic electron beam. The mechanism of (electron-hole) e-h pair generation in CL is impact ionisation, a typical non-

equilibrium process where one energetic charge carrier loses energy by the creation of other charge carriers [9, 13, 14].

CL spectroscopy is the study of the spectral distribution of the emitted CL light signals. When the intensity of light emission is mapped in 2D space, this is termed as CL microscopy. Changes in CL spectra or intensity contrast in maps can lead to information about the alloy composition, intrinsic emission and/or defects distribution. Thus in combination, CL spectroscopy and microscopy are indispensable tools for the study of light emission from materials and the factors that improve or degrade it in the semiconductor and optoelectronic industries. The most common and versatile way to perform CL experiments is within a scanning electron microscope, specially equipped with some form of light collection and detection apparatus. In this thesis, CL measurements are performed using two custom built (by Dr Paul Edwards from our research group) high resolution CL setups: one attached to a field emission scanning electron microscope and a second lower resolution CL setup attached to a electron probe microanalyser.

CL spectroscopy is also performed as a function of sample temperature in non-imaging mode in a vacuum chamber equipped with an electron source and an optical spectrometer. This CL setup is developed by Dr Carol Trager-Cowan from our research group. In all the cases, prior to CL measurements, computational technique of Monte Carlo (MC) simulation is performed using CASINO software to get an insight into the electron beam interaction volume [15]. The electron beam injected into the sample undergoes a series of elastic and inelastic scattering processes as discussed above. The trajectory as well as the angle of scattering is random, described by a computable statistical distribution. The MC simulation never represents the exact electron path taken by electrons in a sample but by averaging thousands or millions of simulated paths, a representation of the experimental interaction volume is obtained computationally. The interaction volume and simulated trajectories of electrons in 2 μm thickness GaN layer for electron beam voltage of 1, 3 and 5 kV are shown in Fig 3.5.

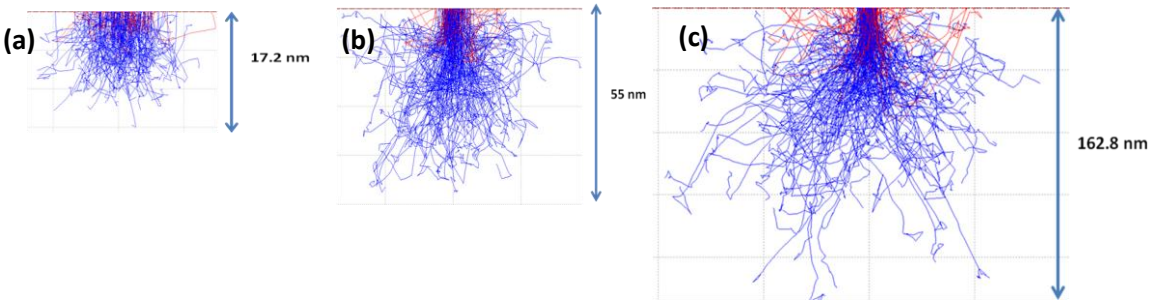

Figure 3.5 The electron beam trajectories in 2 µm thick GaN layer simulated by CASINO software for electron beam acceleration voltages of (1) 1 (b) 3 and (c) 5 kV.

3.3.2 (a) Types of CL experiments

In addition to the highly spatially resolved 2D maps, other different types of CL measurements are also performed to study the uniformity of composition across different layers of the ternary and quaternary III-nitride alloys, to discern the nature of a particular transition in observed CL spectra and also to study the strain variation and the localisation effects.

3.3.2 (a).1 CL as a function of electron beam energy

The electron beam acceleration voltage or energy is the most obvious operating parameter that can be controlled to cause variation in the CL response. The lower electron beam energy CL experiments excite parts of the sample closer to the surface. With increase in electron beam energy more e-h pairs are injected into the deeper layer of sample and thus it is possible to depth profile the CL emission characteristics [14]. Figure 3.6 shows the electron beam energy deposition profile (using Monte Carlo simulation) for a GaN epilayer of thickness 800 nm for different electron beam energies. In this thesis, depth resolved CL measurements are performed for GaN epilayers coalesced above a nanocolumn and nanopyramid array to study the strain variation across the coalesced layer and also for AlInN/GaN heterostructures to track the compositional homogeneity and to differentiate the origin of different luminescence peaks. These voltage-resolved CL measurements are further verified by the complimentary technique of cross sectional CL spectroscopy and mapping, wherever possible.

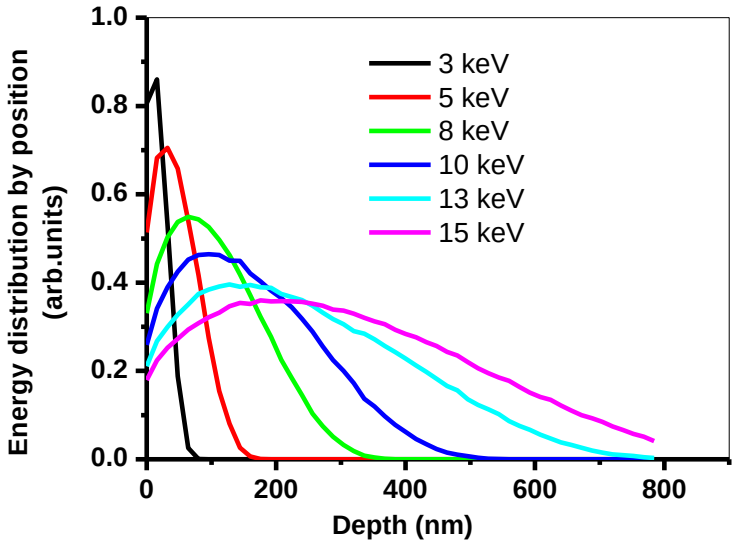

Figure 3.6 Electron beam energy deposition profile vs depth as a function of different electron beam energies. GaN layer of thickness 800 nm is considered as the sample.

3.3.2 (a).2 CL as a function of electron beam current

In current-resolved CL, the beam voltage is kept constant and beam current I_b is varied to reveal information about the physics of recombination processes. The theory of current-resolved CL originates from excitation power dependent PL measurements. Current-resolved CL measurements are performed for AlInN/GaN epilayers to study any band filling effects and also for semipolar and nonpolar InGaN QWs. For the InGaN QWs grown along polar c-direction, there exists an internal electric field of the order of MV/cm leading to QW emission red shift and decrease in radiative efficiency (QCSE) as discussed in chapter 2. With increase in excitation current, more e-h pairs are created and induce an electric field screening the built-in field, and hence the QW emission gets blue shifted. The amount of blue shift is a measure of the polarisation induced electric field experienced by the QWs. The peak energy shifts in InGaN QW emission due to changes in excitation current density are analysed to compare the polarisation induced electric field effects for QWs fabricated on different crystal orientations of facetted 3D GaN structures.

3.3.2 (a).3 CL hyperspectral imaging

CL hyperspectral imaging is a uniquely valuable tool enabling the acquisition and storage of an entire CL spectrum from each imaging point of the sample under investigation [16]. A pixel in a conventional colour image typically contains information on the intensities of three colour channels: red, green, and blue. In hyperspectral imaging each sampled pixel contains an entire spectrum of data – the intensities of hundreds or thousands of individual wavelength channels. In more detail, hyperspectral image is a three dimensional data cube which contains both spatial and spectral information I (x,y,λ); the two spatial axes x and y corresponds to the co-ordinates of electron beam injection and scanning on the sample plane and the third a spectral axis corresponding to CL emission wavelength. The hyperspectral image is also known as a spectrum image, or a spectrum map [14, 17]. A typical image size in hyperspectral imaging is 256 x 256 pixels. In this thesis the hyperspectral images of III-nitride nanostructures are acquired using CHIMP software developed by Dr Paul Edwards.

The hyperspectral image is formed by scanning the sample surface with a focussed electron beam and simultaneously recording the light emission spectrum from each pixel of the sampled region. Alternatively, larger area scans can be acquired by scanning the sample under a fixed electron beam. To be capable of acquiring a full spectrum from each pixel of an SEM image, fast electronics and detectors are necessary in hyperspectral imaging technique. Hence the detector side is setup by parallel spectroscopy using a CCD array which requires only tens or hundreds of milliseconds of dwell time to acquire each spectrum. Moreover, since the complete spectroscopic information is collected in a single electron beam scan, the parallel detection minimises the effects of electron-beam damage that could hamper the CL studies of nanostructures. In this thesis, the CL hyperspectral images are acquired by the CL setups attached to the EPMA and to the FESEM. The CCD on the EPMA has 1024 pixels and each pixel is of 26 µm wide, whereas the CCD on the SEM has 1600 pixel with each pixel width of 16 µm. The number of wavelength channels can be selected by binning (adding pixel columns together). In CL hyperspectral imaging measurements described in this thesis, the dwell time varies for 0.05 s to 0.1 s, depending on the brightness of the samples under investigation. In conventional

spectrally resolved (monochromatic) imaging, a narrow wavelength band pass is used to obtain a CL image and most of the spectral response is lost inside the monochromator. The information in such monochromatic CL maps is limited to the intensity of a single wavelength band. Hyperspectral imaging technique allows one to perform advanced data analysis methods such as multivariate statistical analysis, and nonlinear least squares (NLLS) fitting pixel by pixel yielding valuable information such as 2D distribution of peak intensity, peak energy and line width across a region of interest of the sample corresponding to each CL emission spectral band [18]. The principle of hyperspectral image acquisition is shown below in Figure 3.7.

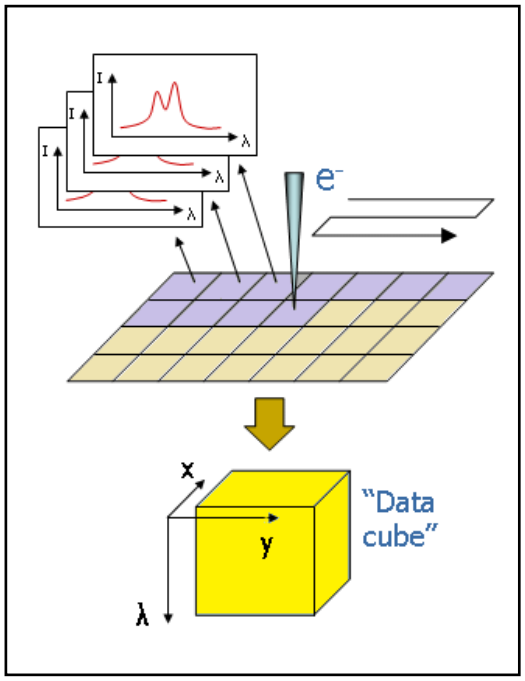

Figure 3.7 The working principle of hyperspectral imaging [19] technique.

3.3.3 EPMA- CL hyperspectral imaging setup

The schematic of the CL setup attached to Cameca SX 100 EPMA is shown in Figure 3.8. Here, the exciting electron beam and the light collection geometry are normal to the sample surface. The CL signals from the sample, collected and collimated by a reflecting objective is focussed onto the entrance slit of a 12.5 cm spectrometer [Oriel MS125] which disperses the CL signal to a cooled Si CCD

detector [Andor DU420 –BU]. A built-in optical microscope coaxial and confocal with the electron beam allows optical monitoring of the samples during measurements. This system is capable of simultaneous mapping of composition distribution by wavelength dispersive X-ray spectroscopy (WDX) and CL signals, permitting the correlation of composition and luminescence over dimensions ranging from µm to cm. Depth-resolved CL spectroscopy and hyperspectral imaging for a coalesced GaN layer ~ (2 µm thickness) above an array of nanocolumns (Chapter 4) and nanopyramids (chapter 5) are performed using this CL set-up. Since the excitation beam current can be precisely varied from pA to µA, this setup is of special interest in experiments requiring exciting electron beam current resolution. In chapter 6 where the spatially resolved optical properties of InGaN QWs fabricated on the nanofacets of 3D GaN structures of specific crystal orientation are discussed, the excitation current density resolved measurements are performed using this CL setup to investigate the screening effect in QW emission peak shift due to electric field induced by excited charge carriers.

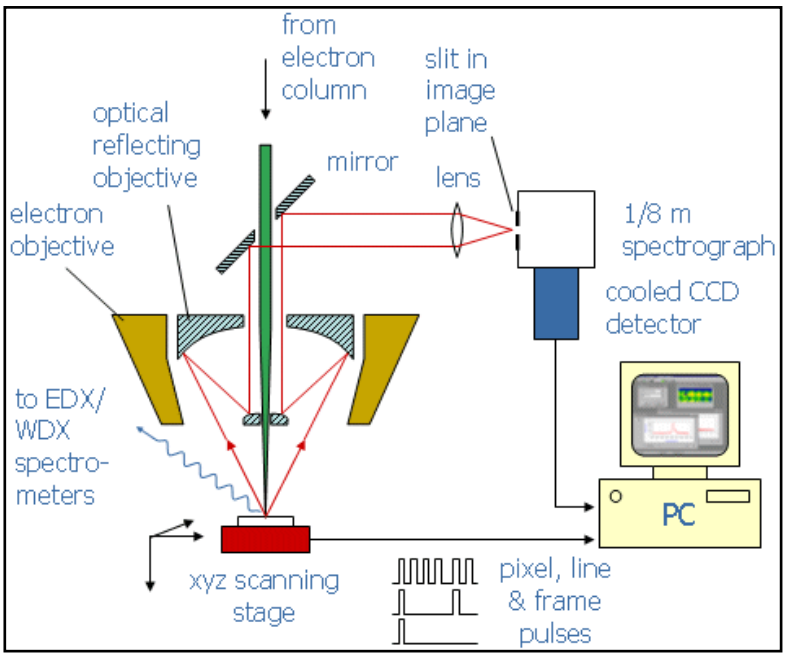

Figure 3.8 Schematic of the CL setup attached to the Cameca SX 100 EPMA system [19].

3.3.4. SEM CL hyperspectral imaging setup

The schematic of the CL setup attached to the FESEM is shown below in Figure 3.9. Here the geometry of CL setup is different from that attached to EPMA. The normal to the sample surface is inclined (45^{o}) to electron beam excitation direction and the horizontal axis of the reflecting objective (NA 0.28) which collects and collimates the CL signals to a 90° off-axis paraboloidal shaped aluminium mirror through a quartz window. The reflecting objective is of Schwarzchild type which is useful in correcting the astigmatism, aberration and coma, whilst also having a long working distance and zero chromatic aberration. The off-axis metal mirror directs and focuses the collimated CL to the entrance slit (100 µm or 25 µm) of 12.5 cm spectrograph (Oriel MS125). This disperses the luminescence to a 1 inch length electron multiplied CCD (EMCCD, Andor Newton) camera which forms the CL hyperspectral image described above. The electron multiplication (EM) technology implemented in the CCD chip allows for the magnification of the captured electron signal, resulting in the reduction of the effective readout noise. Thus EMCCD technology essentially enables to obtain high quality CL hyperspectral images and spectra from nanostructured light emitting heterostructures. The detector array used in our FESEM CL setup has the provision to be used both as a conventional CCD and as an EMCCD.

The spatial resolution achievable with the CL setup attached to electron microscope is determined by 3 factors: (a) the electron beam size on the sample surface; (b) the interaction volume; and (c) the diffusion length of the minority carriers [18]. The electron beam size depends on the acceleration voltage, working distance and the beam current. In order to have small beam size, the acceleration voltage should be large, with a small working distance and low beam current. However, high value of acceleration voltage would degrade the spatial resolution. Hence to maximise the spatial resolution that can be achieved with the instrument, a trade off can be made between the acceleration voltage and the beam current to obtain good CL signal at a small possible beam size. Since the FESEM is capable of producing electron beams having spot size of ~ 1 nm the spatial resolution of CL hyperspectral images acquired on the FESEM CL setup is far better than that

attached to EPMA where the thermionic tungsten filament acts as the electron source. Moreover, the FESEM can perform well at low electron beam voltages compared to EPMA.

With the EPMA CL setup the size limit of the features that can be resolved is > 100 nm whereas FESEM has been demonstrated to be able to resolve features as small as ~ 10 nm [20]. Furthermore, the objective electron lens in the FESEM is aberration corrected helping it to achieve a small spot at low electron voltages. A comparison of the Monte-Carlo simulation for electron trajectories in GaN for different acceleration beam voltages suggest that the lateral spread and penetration depth are approximately the same for a given beam voltage. Hence while mapping the CL signals from QWs, QDs, and thin epilayers of ternary and quaternary alloys, a lower beam voltage is selected to limit the interaction volume to the near-surface region. Donolato et al [21] has experimentally confirmed that the diffusion of the minority carriers do not significantly affect the resolution of CL image as the density of e-h pairs falls off rapidly as one moves away from the generation region.

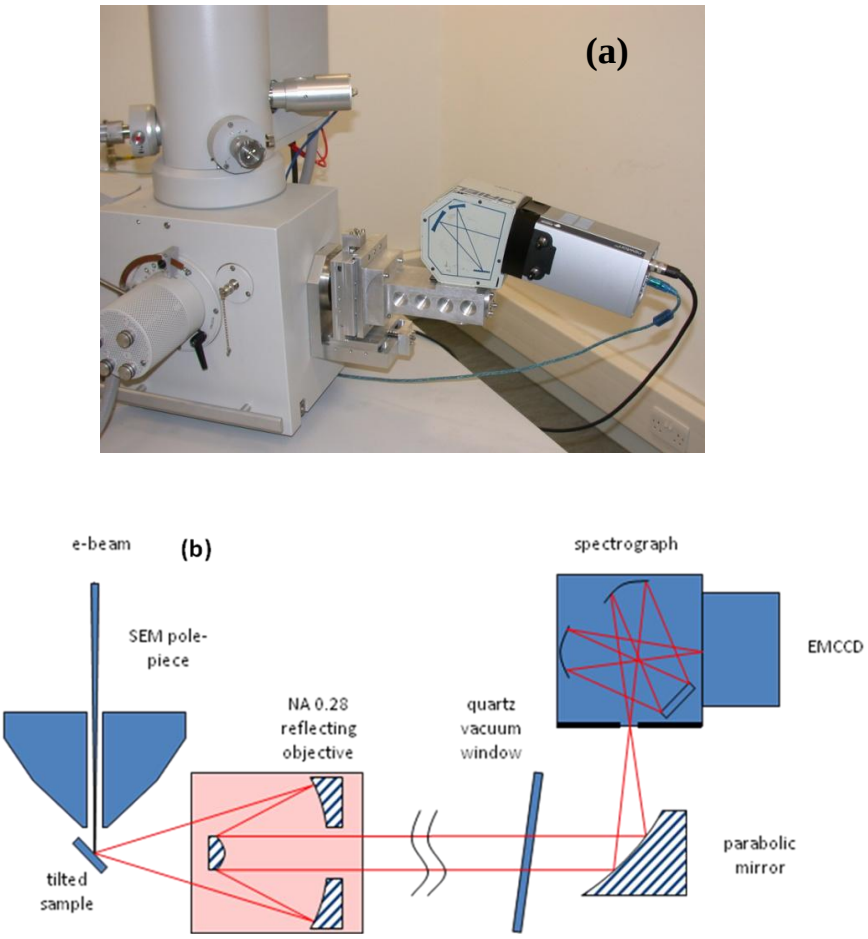

Figure 3.9 (a) Photograph of the CL se up attached to FESEM system and (b) its schematic arrangements of the optical components. EMCCD is the electron multiplying CCD camera.

3.4 Composition Analysis

Composition analysis is of significant interest especially that of alloys as the nano-structural and optical properties are directly dependent on the composition. This section focuses on Rutherford backscattering spectrometry (RBS) and high resolution X-ray diffraction techniques (HR-XRD) used to investigate the composition of the ternary III-nitride alloys. The RBS measurements described in this thesis were performed by Dr. Katharina Lorenz together with her PhD student Sérgio Magalhães at the Instituto Tecnologico e Nuclea (ITN), Sacavém, Portugal. HR-XRD

measurements were performed by Dr Thomas Sadler at University of Cambridge and Dr. Lutz Kirste of Fraunhofer Institute for Appied Solid State Physics.

3.4.1 Rutherford backscattering spectrometry

Rutherford Backscattering Spectrometry (RBS) is a widely used nuclear method for the quantitative determination of the composition of a material and depth profiling of individual elements. RBS can perform quantitative measurements without the need for reference samples. It is a non-destructive technique, having good depth resolution of the order of several nm, and a very good sensitivity for heavy elements of the order of parts-per-million (ppm). During an RBS measurement, high energy [MeV] He++ ions are directed onto a sample and the energy distribution and the yield of the backscattered He++ ions at a given angle of the sample are recorded. The energies of the backscattered ions depend on the mass of the atoms from which they scatter (kinematic factor) as well as the depth at which the collision occurs (energy loss factor). The number of backscattered ions is proportional to the concentration of a given element. Since the backscattering crosssection is known for all elements, it is possible to derive quantitative depth profiles from the RBS spectra for thin films that are less than 1 µm thick [22]. Usually silicon solid state detectors are used in RBS measurements for the determination of the energy of backscattered particles. The ions create electron-hole pairs in the detector, which are separated by an applied electric field and create a charge pulse. The number of electron-hole pairs in this pulse is proportional to the ion energy [23]. RBS includes all types of elastic ion scattering with incident ion energies in the range 500 keV to several MeV. Usually protons, ^{4}He, and sometimes lithium ions are used as projectiles at backscattering angles of typically 150- 170$^{0.}$ Different angles or different projectiles are used in special cases.

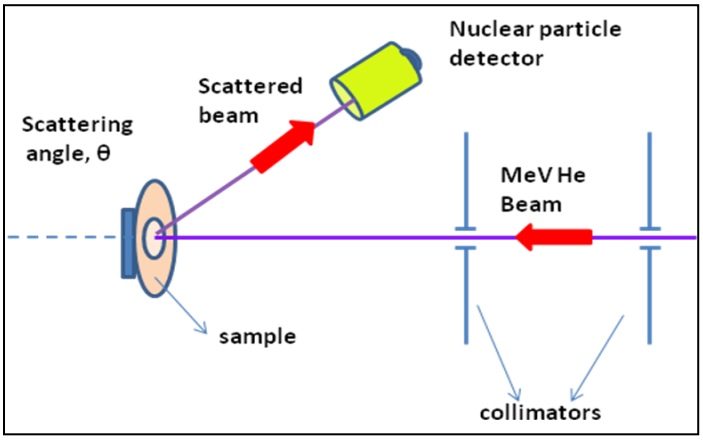

Figure 3.10 Schematic of an RBS setup [24]

Figure 3.10 shows a schematic of an RBS technique. A computer program is used to fit the data to obtain both compositional and thickness information. The crystalline quality of a target sample can be determined by the RBS channelling technique. Target ions which are incident on the sample at an angle which corresponds to a particular crystal plane travel along the channel between the atomic rows and penetrate much further before backscattering. This effect is known as channelling [25, 26] and the corresponding spectrum is known as the channelling or aligned spectrum. This is then compared with the spectrum obtained when the ions are incident at an angle which does not correspond to any of the crystal planes, the so-called random spectrum, as used above to obtain composition and thickness information. If the atoms within the target are displaced from their crystalline lattice site this will result in a higher backscattering yield in relation to a perfect crystal. The ratio of the backscattered yields from the two spectra gives a value for the crystalline quality denoted as $\chi_{\min}$ and is usually quoted as a percentage. The lower the $\chi_{\min}$ value, the better the crystalline quality. State of the art values of $\chi_{\min}$ for GaN are around 2 % [27].

3.4.2 High resolution X-ray diffraction (HR-XRD)

X-ray diffraction is an important structural characterisation technique for crystalline material due to their periodic nature. The existence of Bragg diffraction peaks in the XRD spectrum is used to confirm the structure of the crystal. This non-destructive

characterisation technique can provide information on alloy composition, uniformity of epitaxial layers, thickness, built-in strain (tilt, twist stress), crystalline perfection, dislocation density and interface quality [28]. In this thesis, the XRD measurement is performed with the purpose of determining alloy composition and thickness of AlInN and AlInGaN epilayers. These are respectively discussed in chapter 7 and chapter 8.

3.5 Surface roughness analysis

Surface roughness values of thin AlInGaN epilayers are discussed in Chapter 8. These values were estimated using the method of X-ray reflectometry (XRR). XRR measurements were performed by Dr Lutz Kirste of IAF.

3.5.1 X-ray reflectometry (XRR)

This is a non-destructive and non-contact technique for measuring the surface topography/surface roughness of epilayers at sub-micron scales. This technique is also useful for thickness determination between 20-200 nm with a precision of about 1-3 A^0. The principle of XRR is, a short wavelength radiation is scattered effectively by a small-scale surface roughness [29]. The angular dependence of the scattered radiation intensities contains the information about the average geometric characteristic of roughness. For very flat surfaces with root mean square roughness in the range of several angstroms, XRR and Atomic Force Microscopy (AFM, the most commonly used technique for surface roughness determination) give similar roughness values [30].

3.6 Growth of III-nitride heterostructures

3.6.1 MOCVD

It is very difficult to grow III-nitrides from their stoichiometric melts using techniques such as the Czochralsky or Bridgman technique commonly used for typical semiconductors. Because of the high bonding energy of the N_2 molecule, the III-V semiconducting nitrides, especially GaN and InN, require high N_2 pressures to be stable at the high temperatures necessary for the growth of high quality single layers. The typical melting conditions of binary III-nitride materials are shown in

table 3.2 below. Because of these extreme conditions they have to be crystallised by a method that allows bulk growth at low temperatures and pressures. With metal organic chemical vapour deposition and molecular beam epitaxy technique it is possible to grow high crystalline quality epilayers of binary and alloys of III-nitride compounds [28].

Table 3.1 Melting temperatures of GaN, InN and AlN [28, 29]

Binary compound	Melting temperature (^{o}C)
GaN	2500
InN	1900
AlN	3200

Metal organic chemical vapour deposition (MOCVD), also known as metal organic or organo- metallic vapour phase epitaxy (MOVPE, OMVPE) is the growth of thin layers of compound semiconducting materials by co-pyrolysis of various combinations of organometallic compounds and hydrides. This is the most widely used growth technology for III-nitrides, both for research and for commercial production of LEDs and LDs. MOCVD growth of epitaxial layers results in high material quality, interfacial abruptness between layers, luminescence efficiency, uniformity and throughput. Sources that are used in MOCVD for both major film constituents and dopants are various combinations of organometallic compounds and hydrides. The group III metal organics typically used are trymethyl aluminium (TMAl), trymethyl gallium (TMGa) and trymethyl indium (TMIn). The commonly used group V precursor is ammonia (NH_3). The high bond energy of NH_3 requires a higher growth temperature of about 1100°C for GaN. The sources are introduced as vapour phase constituents into a reaction chamber at approximately room temperature and are thermally decomposed at elevated temperatures by a hot susceptor and substrate to form the desired film in the reaction chamber. In order to prevent the growing III-nitrides from dissociating, very high V-III ratios and a high

flow rate of NH_3 are necessary. The thermal decomposition of most metal organic precursors typically involves the sequential release of the methyl ligands by cleavage of the metal carbon bonds. The majority of NH_3 is decomposed catalytically on the growing surface through dissociative adsorption in conjunction with adsorbed group-III compounds. The chamber walls are not deliberately heated (a 'cold wall' process) and do not directly influence the chemical reactions that occur in the chamber [29, 30].

A schematic of an MOCVD growth system is given in Figure 3.11. The growth of nitride semiconductors by MOCVD relies on the transport of organometallic precursor gases, hydrides for nitrogen source and reacting them on or near the surface of a heated substrate. The underlying chemical mechanisms are complex and involve a set of gas phase and surface reactions. The deposition of epitaxial nitride layers by MOCVD involves the reaction of metal-containing In, Ga or Al gases with ammonia.

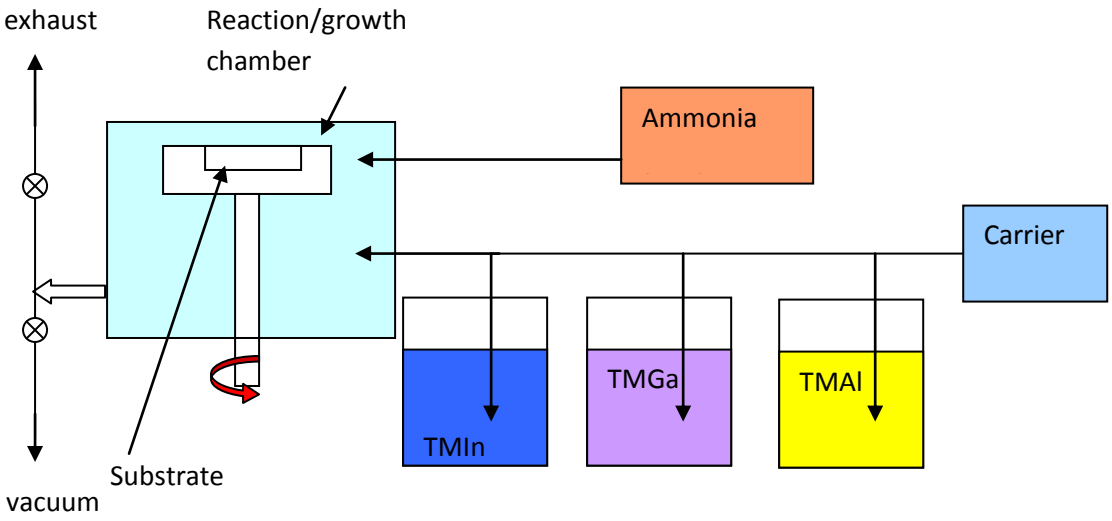

Figure 3.11 Schematic of MOCVD technique

The overall chemical reaction in MOCVD,

$$R_nM(v) + ER'_n \xrightarrow{v} ME(s) + nRR'(v)$$

Where R_n - methyl or ethyl radical

R' - Hydrogen

M - Group III metal

E - Group V element

n - 3 for III-V growth

For the GaN, $Al_{(1-x)}In_xN$ and $Al_xGa_{(1-x)}N$ growth,

$Ga(CH_3)_3 + NH_3 \longrightarrow GaN + 3CH_4$

$xIn(CH_3)_3 + (1-x)\ Al_2(CH_3)_6 + NH_3 \longrightarrow In_xAl_{(1-x)}N + 9CH_4$

$xAl_2(CH_3)_6 + Ga(CH_3)_3 \longrightarrow Al_xGa_{(1-x)}N + 9CH_4$

The vapour phase reactants R_nM and ER_n' are thermally decomposed at elevated temperatures to form the non-volatile product ME which is desposited on the substrate and the susceptor while the volatile product RR' is carried away by the H_2 flush gas to the exhaust. The above equation describes a simplified overall reaction and ignores any side reaction and intermediate steps [29].

3.6.2 MBE

MBE offers the possibility to grow epitaxial films on crystalline substrates with atomic layer precision. In MBE technique, thin films are formed in ultra-high vacuum (approximately ~ 10^{-10} Torr) on a heated substrate through various reactions between thermal molecular beams of the constituent elements and the surface species on the substrate. The composition of the epilayer and its doping level depend on the arrival rates of the constituent elements and dopants, respectively. The typical growth rate is ~ 1 μmh^{-1}, or slightly more than one monolayer per second (MLs^{-1}). As MBE growth occurs under conditions that are governed primarily by the kinetics, rather than by mass transfer, this allows the preparation of many different structures that are otherwise not possible to attain. Figure 3.12 shows a schematic of the MBE technique.

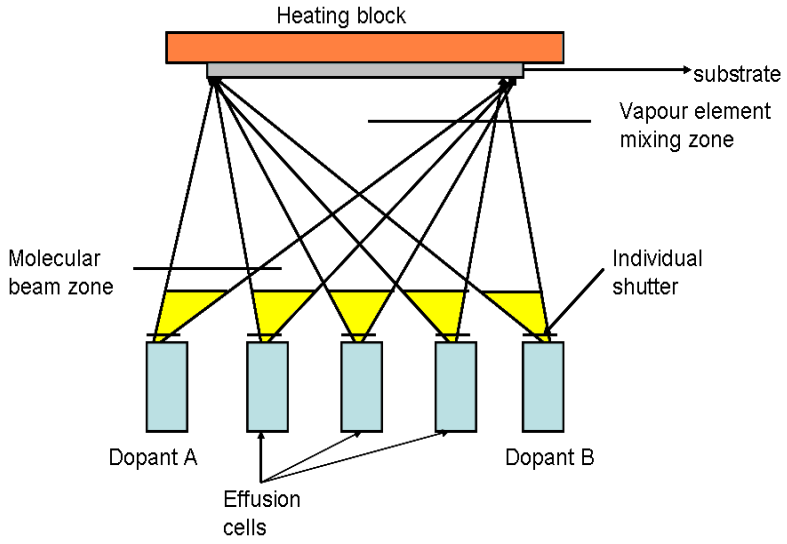

Figure.3.12 Schematic of the MBE setup

In III-nitride growth by MBE, the metal species are provided by Ga, In, and Al metal sources, the dopants are provided by pure Si for n-type and Mg for p-type using conventional Knudsen effusion cells that are heated to sufficient temperatures for the desired growth rate, composition, and doping levels [30]. These Knudsen-effusion-cells forms the "molecular beam" by thermal evaporation (for the group-III elements). Several approaches have been investigated for supplying an atomic source of nitrogen. RF plasma and electron cyclotron resonance (ECR) microwave plasma sources are the two most successful techniques. In these RF plasma MBE systems, the plasma source is used to crack molecular nitrogen. These plasma sources use cylindrical cavity geometry to efficiently pump microwave energy into the nitrogen discharge area. When using ECR sources, a tradeoff between growth rate and ion damage occurs. Under normal ECR use, the flux of the low energy reactive N species is so low that only low growth rates of 500 Å/hr can be achieved. At higher microwave powers, higher growth rates can be achieved, but ion damage leading to deep levels and semi-insulating electrical properties occurs. A major advantage of MBE for III-nitride growth is the low growth temperature that can be achieved because of the atomic nitrogen source. This is in contrast to MOCVD, which must employ high growth temperatures (>1000°C) to crack the ammonia molecules [31]. The lower growth temperatures should result in lower thermal stress upon cooling,

less diffusion, and reduced alloy segregation. The low growth temperature also allows the system to grow abrupt heterostructures and superlattices with reduced solid-state diffusion, and there is additional flexibility in creating novel structures. However, MBE has several inherent drawbacks. The ultra-high vacuum requires multi-stage cryogenic vacuum systems. Deposition rates for MBE are relatively low compared to MOCVD. Furthermore, source material replacement and maintenance inside the ultra-high vacuum chamber is tedious and time consuming. This thesis includes two sets of samples that are prepared partly using MBE technique. In chapter 4 the optical properties of coalesced GaN nanocolumns are discussed and the GaN nanocolumns are realised by MBE technique. In addition, the AlInGaN quaternary layers described in chapter 7 were also prepared by the MBE technique.

3.7 Summary

The various characterisation techniques used in this thesis for obtaining high quality data from various III-nitride nanostructures are discussed. The basic principle and the experimental setup corresponding to photoluminescence, cathodoluminescence, CL hyperspectral imaging, Scanning electron microscopy, Rutherford-backscattering spectrometry etc were discussed in detail. A brief description of the growth techniques such as MOCVD and MBE used for the growth of samples studied in this thesis were also included.

References:

[1] Shionoya S 1998 *Luminescence of Solids* [Edited by D R Vij] (New York : Plenum Press)

[2] Klingshirn C 2005 *Semiconductor Optics* (Berlin: Springer)

[3] Lerner J M and Thevenon A *'The optics of spectroscopy'* http://www.jobinyvon.co.uk/ukdivisions/OOS/oos1.htm#11[date date of access -23-06-2009]

[4] Robinson J W, Skelly Frame E M and Frame G M 2005 *Undergraduate Instrument Analysis* (New York : Marcel Dekker)

[5] Palmer C 2002 *Diffraction grating handbook* (Edited by Loewen E) www.gratingslab.com [date of access- 28-07-2009]

[6] Yu P Y and Cardona M 1999 *Fundamentals of Semiconductors* (Berlin: Springer)

[7] Garcia F J, Abajo D 2010 *Reviews of Modern Physics* **82** 209

[8] Garcia J S, Bausa L E and Jaque D 2003 *An introduction to the optical spectroscopy of inorganic solids* (Weinheim: Wiley-VCH)

[9] Yacobi B G and Holt D B 1990 *Cathodoluminescence microscopy of inorganic solids* (New York: Plenum press)

[10] http://materialsworld.utep.edu/Background/SCANNING ELECTRON%20MICROSCOPY/SccaningElectronMicroscopy.htm [date of access -16-02-2010]

[11] http://www.fei.com/uploadedFiles/Documents/Content/Introduction to_EM_booklet_July_10.pdf [date of access- 13-06-2009]

[12] http://www.vcbio.sci.kun.nl/public/pdf/fesem_info_eng.pdf [date of access 13-06-2009]

[13] Philips M R 2006 *Microchim. Acta* **155** 51

[14] Parish C M and Russell P E 2007 *Advances in imaging and electron physics* **147** Elsevier

[15] Hovington P, Drouin D and Gauvin R 1997 Scanning **19** 1

[16] Christen J, Grundmann M and Bimberg D 1991 *J. Vac. Sci.Technol.* B **9** 2358

[17] Martin R W, Edwards P R, O'Donnell K P, Dawson M D, Jeon C –W, Liu C, Rice G R and Watson I M 2004 *Phys. Stat. Sol. (A)*) **201** 665

[18] Edwards P R and Martin R W 2011 *Semicond. Sci.and Technol*. **26** 064005

[19] http://ssd.phys.strath.ac.uk/index.php/Cathodoluminescence(CL)hyperspectral imaging [date of access 13-04-2009]

[20] Bruckbauer J, Edwards P R, Wang T and Martin R W 2011 *Appl.Phys.Lett.* **98** 141908

[21] Donolato C 1979 *Appl. Phys. Lett.* **34** 80

[22] http://www.eaglabs.com/files/techniquenote/TN107.pdf. [date of access- 21-09-2011]

[23] Lectures given at the Workshop on Nuclear Data for Science and Technology: Materials Analysis Trieste, 19-30 May 2003 [date of access- 05-07-2010] http://users.ictp.it/~pub_off/lectures/lns022/Mayer_1/Mayer_1.pdf

[24] http://jack.pixe.lth.se/kfgu/ApplSubatomicPhys/Material-kurs/RBS/RBS-01-Principle.pdf [date of access- 31-12-2011]

[25] Yakushev M V 2003 Lecture Notes, *Ion Beam Techniques*, Class 12-902, University of Strathclyde

[26] Feldman L C, Mayer J W and Picraux S T 1982 *Materials Analysis by Ion Channeling* (NewYork : Academic Press)

[27] Lorenz K and Martin R W Private communication

[28] Krost A, Bauer G, and Woitok J,1995 *Optical Characterization of Epitaxial Semiconductor Layers*, (*Editors:* G. Bauer and W. Richter) (Berlin: Springer)

[29] Stoev K and Sakurai K 1997 *The Rigaku Journal* **14** 22

[30] Mironov V L, Udalov O G, Gribkov B A and Fraerman A A 2008 *J.Appl.Phys*.**104** 064301

[31] Ruterana P, Albrecht M and Neugebauer J 2003 *Nitride Semiconductors Handbook on Materials and Devices* (Weinheim: Wiley-VCH)

[32] Zilko J L 2002 *Handbook of Thin film deposition Processes and Techniques-Principles, Methods, Equipment and Applications* Edited by Seshan K (USA: NoYes publications)

[33] Morkoc H 2008 *Handbook of Nitride Semiconductors and Devices Vol. 1* (Weinheim: Wiley-VCH)

[34] http://itri2.org/ttec/hte_j/report/03.pdf [date of access 28-12-2011]

Chapter 4

Cathodoluminescence studies of GaN coalesced from selectively grown nanopyramids

4.1 Introduction

GaN-based light emitting diodes (LEDs) and laser diodes (LDs) in the UV/blue/green wavelength range are necessary for applications like full colour displays, solid state lighting, short-haul optical communications, back lights for liquid crystal displays, laser printers and read-write laser sources for high density information storage [1, 2]. For the realisation of GaN-based next generation opto-electronic devices with improved optical power, quantum efficiency and operating lifetime, reductions in threading dislocation density (TDD) are essential. The conventional technique of epitaxial lateral overgrowth (ELOG) used for reducing TDDs in GaN layers were already discussed in section 2.3.1 of chapter 2. The ELOG technique had reduced the TDDs on GaN-on-sapphire to ~10^6 cm^{-2} [3, 4]. This micron-scale ELOG technique has attracted extensive attention since Nakamura *et al.* demonstrated blue laser diodes with lifetimes exceeding 10,000 hours on ELOG GaN in the 1990s [4, 5]. Theoretical and experimental studies show that further reductions in the TDD are possible if the ELOG technique is extended to the nanoscale, which is referred to as nano-ELOG [6,7] as discussed in section 2.3.1(a) of chapter 2.

Zang *et al.* [8] have reported dislocation densities down to 10^8 cm^{-2} for a 2.5 μm thick nano-ELOG GaN layer grown on a Si substrate by MOCVD. Wang *et al* [9] reported a TDD as low as ~ 10^7 cm^{-2} for a 4 μm nano-ELOG GaN layer grown over a nanoporous SiO_2 mask. A high light extraction efficiency as well as

dislocation reduction for nano-ELOG GaN grown on a sapphire substrate has been reported by Chiu *et al* [10]. However there are not many reports that investigate in detail the optical properties of the nano-ELOG GaN layers. This chapter investigates the optical properties of a series of nano-ELOG GaN layers using high spatial and spectral resolution CL hyperspectral imaging. .

4.2 Sample specifications and Experimental details

The GaN layers were grown by MOCVD in an Aixtron AIX 200/4HT RF-S reactor, using both conventional and pulsed growth modes. A nanopatterned growth mask was fabricated from 100 nm SiO_2 by nanoimprint lithography (NIL) on GaN templates grown on c-plane sapphire substrates. The nanopatterns are hexagonal arrays of circular pores with a diameter of about 200 nm and a pitch of about 450 nm, giving a pattern fill-factor of ~ 50 %. In the conventional growth mode, gallium (group III) and nitrogen (group V) precursors are switched into the growth chamber simultaneously, whereas in pulsed growth mode the group V sources are intermittently supplied while the group III sources are supplied continuously. Pulsed mode MOCVD enhances the migration length of the group III species and promotes lateral growth [11, 12]. The results described in this chapter were obtained from three samples, A, B and C. Samples A and B are grown with 40 pulses to give a thickness of approximately 300 nm for the coalesced GaN layer, whilst twice as many pulses were used for sample C to give a thicker coalesced layer (~ 700 nm) of GaN. Samples B and C were grown with growth interruptions during the pulsed growth conditions [11].

The light emitting properties of the samples were studied by room temperature CL hyperspectral imaging technique using two different set ups as described in section 3.3.2 of chapter 3. High spatial resolution spectrum images were collected using the field emission gun SEM and lower spatial resolution spectrum images were obtained in plan-view using the electron probe micro-analyser. A focussed electron beam is scanned across the sample surface and a room temperature CL spectrum is recorded at each pixel in a 2D map, using a 1/8 m spectrograph and cooled charge coupled device array. Voltage resolved CL spectroscopy was also performed using the CL set up attached to the electron probe micro-analyser.

4.3 Results and Discussion

4.3.1 Surface morphology

Figure 4.1(a) shows a representative cross-sectional secondary electron image of sample B. The cross-sectional images together with large area secondary electron images of partially coalesced regions (Figure 4.7(b)) indicate that the initial GaN deposition forms nanopyramids in the window regions [13]. The subsequent changes in the growth conditions favour the lateral growth and coalescence of these nanopyramids over the SiO_2 mask, giving the formation of a thick continuous GaN layer [11]. Figure 4.1(b) shows planar secondary electron images of samples A, B and C. The surface of sample C appears to have more features than the others, with the presence of many closed loop like features having dark contrast and extending over the surface.

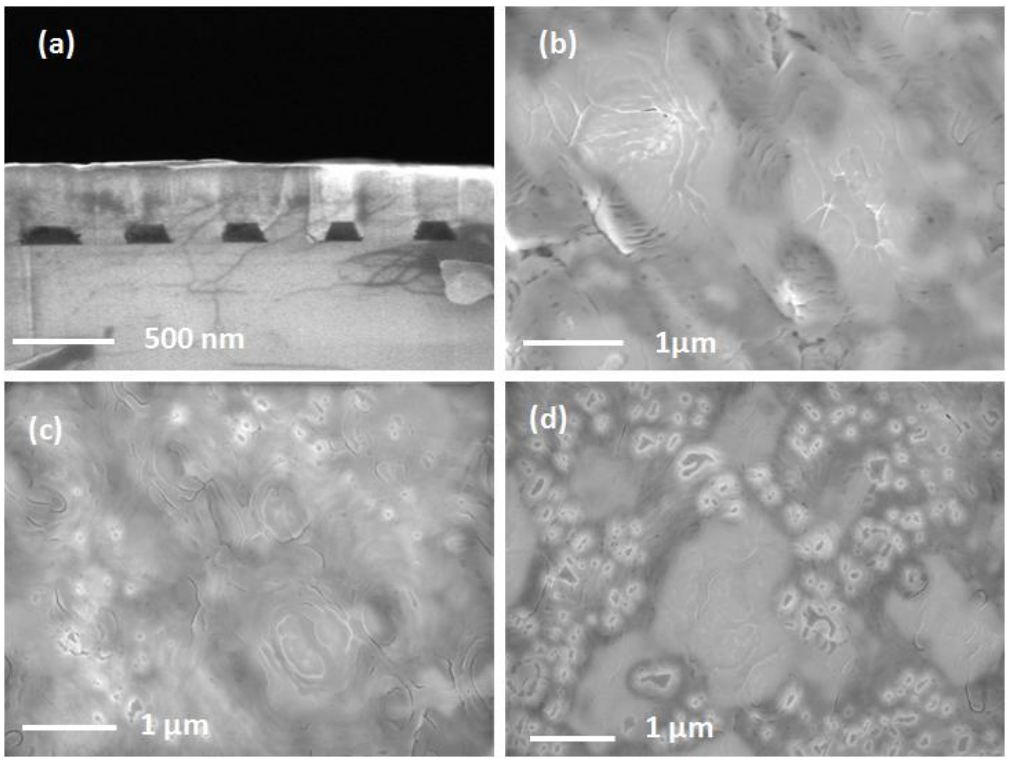

Figure 4.1. (a) Cross-sectional SEM image for sample B, and SEM images of coalesced layer of GaN for samples (b) A, (c) B and (d) C.

4.3.2 Optical properties

Depth resolved CL spectra from the samples are obtained by exciting the samples with different electron beam acceleration voltages varying from 3 to 15 kV. The electron beam energy deposition profile in a thick GaN epilayer is shown in Fig. 4.2 (a) as a function of electron beam acceleration voltage. This is obtained by Monte-Carlo simulation for a fixed range parameter for the electron beam trajectories [14]. The peak of the electron beam energy distribution profile, for each electron beam energy voltage shown in Fig. 4.2(a) corresponds to the maximum energy loss within the GaN epilayer and can be associated with the formation of the maximum number of e-h pairs and hence the maximum CL signal generation. The depth corresponding to this maximum electron beam energy loss will be used for the depth scale in this chapter. Figure 4.2(b) shows the depths for the maximum CL emission as a function of beam acceleration voltage. The error bars represent the depth range within which 85 % of the maximum energy loss of the incident exciting electron beam occurs. The increase in size of these error bars with increase in acceleration voltage is commensurate with the broad nature of the electron energy loss profile [Fig 4.2(a)] within the GaN epilayer at higher electron beam voltages.

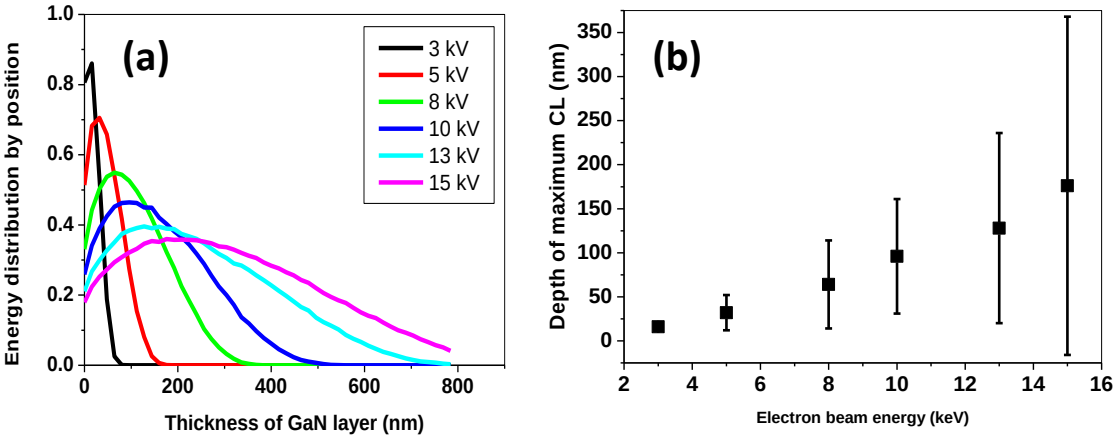

Figure 4.2(a) Electron beam energy deposition estimated using Monte-Carlo simulation of the electron trajectories in a thick GaN layer (b) depth of maximum CL vs electron beam acceleration voltage with the error bars representing the range within which 85 % of the maximum electron beam energy loss occurs within the GaN epilayers.

Depth resolved CL spectra from sample B are shown in Fig. 4.3(a), revealing a red-shift of the GaN near bandedge (NBE) emission peak with increasing electron beam penetration. The peak positions of the GaN peaks are fitted using Gaussian functions and plotted as a function of the depth of maximum CL for all three samples in Fig. 4.3(b). As the depth of maximum CL increases, the peak energy is observed to redshift from the bandgap energy for bulk unstrained wurtzite GaN (3.42 eV) [15].

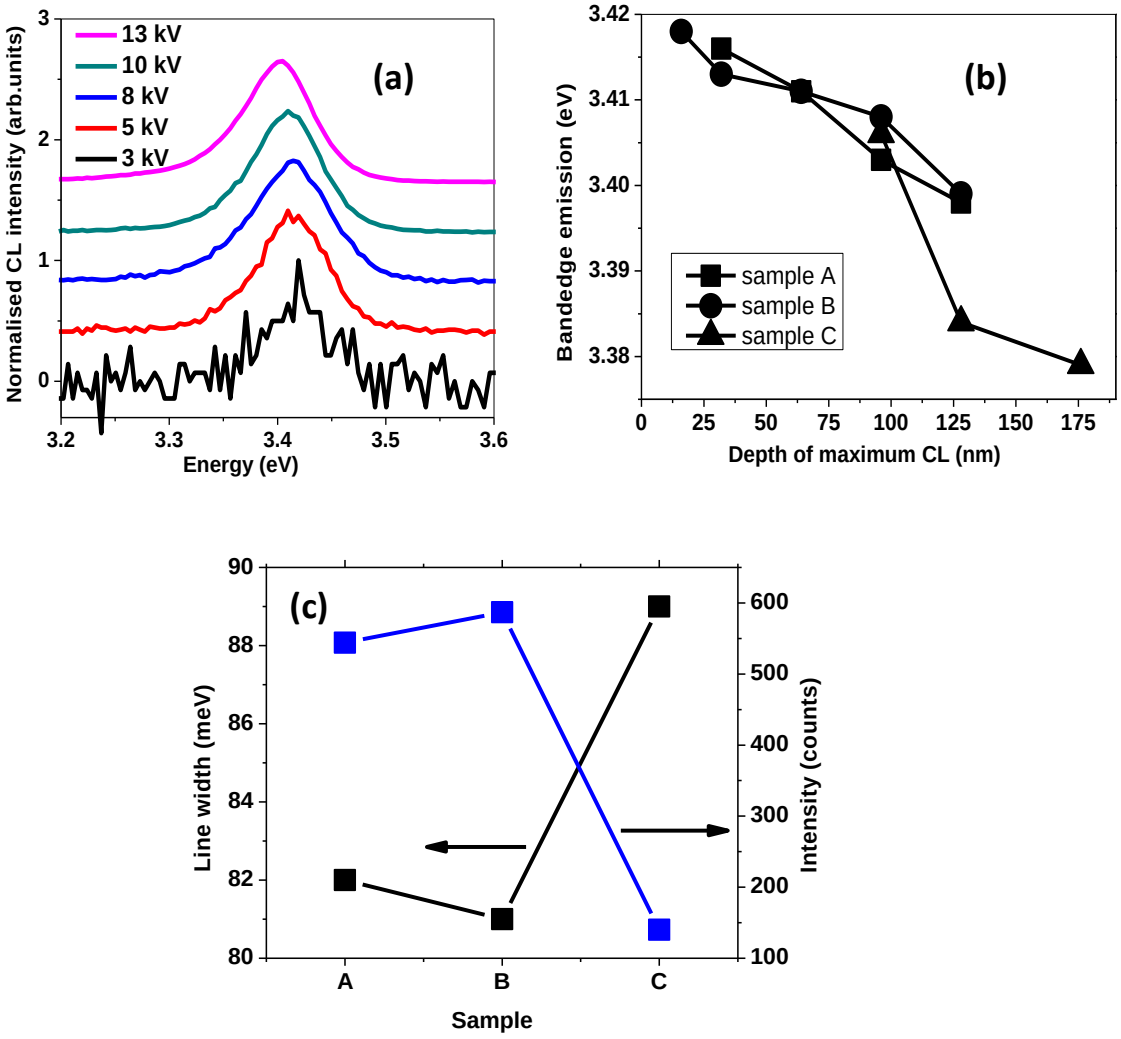

Figure 4.3 (a) CL spectra as a function of electron beam voltage for Sample B (b)peak emission energy vs depth of maximum CL for all three samples (c) line width and intensity of the CL emission peak for all three samples at an accelerating voltage of 10 kV.

It might be supposed that this indicates a reduction in tensile stress within the GaN layers towards their top surface, but later in this chapter we will show that energy shifts due to doping must also be considered. With sample C it was necessary to excite with a higher voltage electron beam (corresponding to greater depth) to generate a CL signal. The secondary electron image in Fig.4.1(d) indicates that sample C has a higher density of surface features, which may be causing a higher rate of non-radiative recombination in its near-surface layer. However, despite the lower radiative efficiency of the sub-surface layer in sample C all three samples show a very similar shift of peak energy with depth within the sample. A comparison of the CL emission intensity and line width for all the samples is shown in Fig.4.3(c) for electron beam energy of 10 keV. The maximum luminescence intensity and minimum line width are obtained for sample B, suggesting that this layer has the best crystal quality. The interpretation of the excitation energy dependent CL is confirmed by measurement of CL spectra from a cross-section of sample B (Fig. 4.4(a) and (b)). The CL peak measured from below the mask region is red-shifted, by approximately 18 meV, compared to that from the coalesced region. It is noteworthy that the CL peak emission wavelength and FWHM are both very similar for the wing and seed regions. This observation is in contrast to the GaN NBE behaviour in micron-scale patterned lateral epitaxial growth, where the peak energy and FWHM of GaN NBE emission from wing and seed region differs [16]. Monte-Carlo simulations show that at 5 kV the CL comes from a volume approximately 120 nm in diameter, which limits the ability to compare intensities for the cross-sectional CL spectra from the different regions.

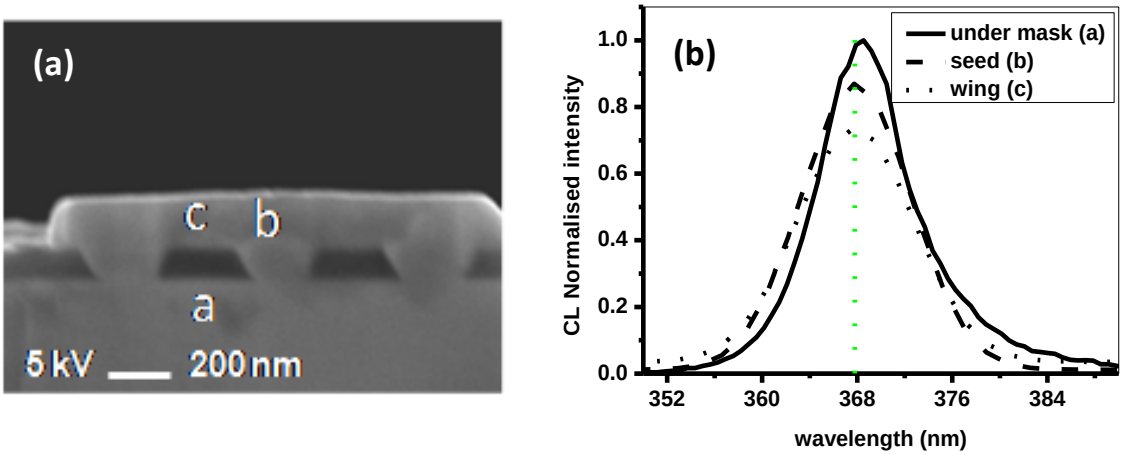

Figure 4.4(a) Cross-sectional SEM and (b) RT CL spectra for sample B excited using 5 keV electron beam

The values of the NBE exciton energies are known to depend on the built-in strain within the GaN layer, with GaN grown on sapphire generally under in-plane compressive strain. Although the stress due to the lattice mismatch between GaN and sapphire can be relaxed at a film thickness of less than several nanometers, a significant compressive strain builds up in the GaN layer during cool down from the growth temperature due to the difference in thermal expansion coefficients between the GaN and sapphire. As the film thickness increases the residual compressive strain in the GaN layer will decrease due to the formation of dislocations [17]. This compressive strain blueshifts the NBE energy compared to the value for bulk GaN and this shift is expected to increase with depth (from the surface) in a GaN-on-sapphire sample. The observed redshift in band edge emission peak with increasing the depth of maximum CL in the samples in this study is therefore unexpected. Possible causes are discussed below.

To obtain spatially resolved luminescence information across the coalesced layers hyperspectral CL maps are acquired for all samples, using different electron beam energies to provide information as a function of depth. These hyperspectral CL maps, composed of 100 × 100 pixels are acquired from 20 × 20 μm areas using a scan step size of 200 nm. Figure 4.5(b) shows the integrated intensity CL map of the

coalesced layer from sample C obtained for an electron beam voltage of 15 kV. The mapped region is shown by the white box on the secondary electron image [Fig.4.5(a)] and the intensity map reveals regions of intensity contrast of micron scale size. The bright spots have average diameters of 2-5 μm, which indicates the size of the defect free regions in the coalesced layer.

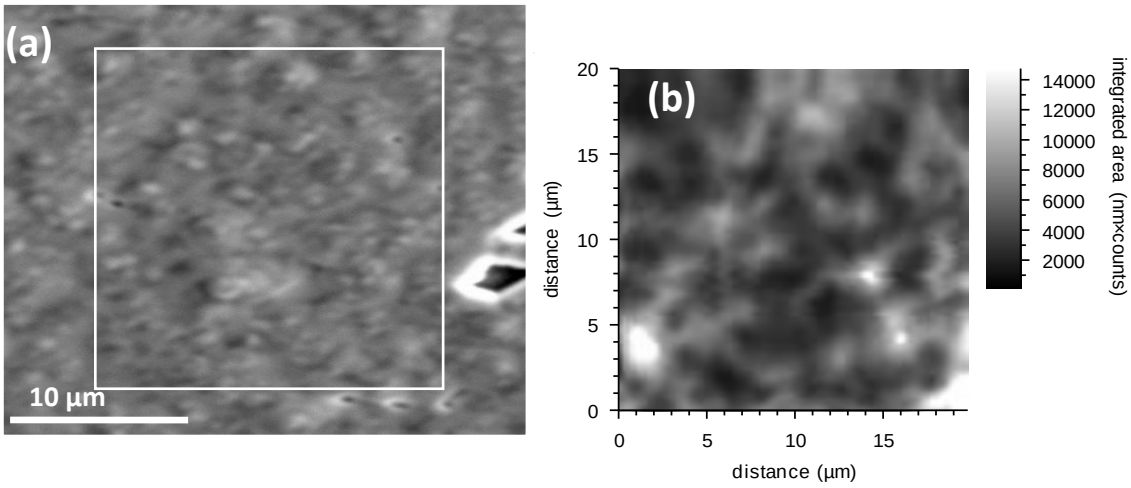

Figure 4.5 (a) Secondary electron image of the coalesced layer for sample C, (b) integrated intensity CL map of the coalesced layer shown in the white box in (a).

The spatially averaged CL spectra collected from the mapped region show a single peak similar to those in Fig. 4.3(a) and Gaussian peak fitting using a non-linear least squares algorithm is used to generate maps showing the distribution of the peak height, centre energy and FWHM for the GaN NBE. Figure 4.6 shows depth resolved centre energy CL maps for sample A (8 kV and 10 kV) and a 13 kV map for sample C. The depth of maximum CL in GaN for electron beam acceleration voltages of 8, 10 and 13 kV are approximately 60, 100 and 130 nm, respectively, ensuring the excitation volume is confined, or nearly confined (considering the error bars as well in Fig 4.2(b)), within the coalesced GaN layers of the respective samples. Moreover, the depth range within which the maximum number of e-h pair formation occurs within the GaN epilayers as shown in Figure 4.2 (b) must also be considered.

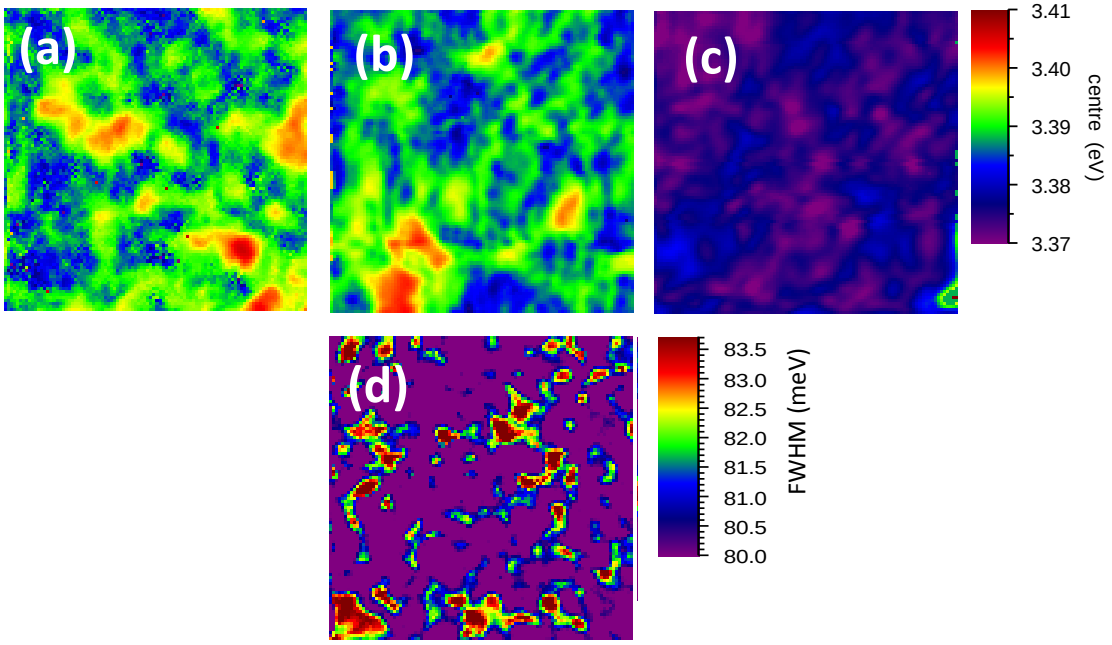

Figure 4.6 Curve fitted centre energy maps of the GaN band edge CL emission at RT for the samples A (at 8 and 10 kV) and C (10 kV) for (a), (b) and (c) respectively. To make the energy shift clearer the same energy scales are used. (d) CL map showing the FWHM distribution for sample A for 10 keV electron beam energy. All images are 20 x 20 µm

The CL maps reveal domain-like variations in peak energy ranging from 3.37 to 3.41 eV, which can most likely be attributed to the effects of local strain. These can be related to the coalescence of GaN seeded from quite widely separated GaN nanopyramids [11]. This may also be a reflection of microstructure within the template below the mask region [18]. No significant variation in domain size with depth is observed for samples A and B. The corresponding integrated CL intensity maps also show micron-scale random variations in intensity which might be due to the random distribution of defects. It is worth noting that the FWHM maps corresponding to the GaN NBE emission show a variation of only 3-6 meV across the mapped 20 x 20 μm area of the coalesced layer, with an example shown in Fig 4.6(d).

To study the effect of individual nanoholes in the selective growth mask on the luminescence properties, higher spatial resolution hyperspectral CL maps were acquired from sample A. The CL intensity map (acquired using an 8 kV electron beam) for the GaN near bandedge emission shows a hexagonal pattern (Fig.4.7(a)),

which likely corresponds to the hexagonal symmetry of the nanohole lattice arrangement. To correlate the features in this map with the underlying mask, a secondary electron image of a different region of the nanostructured sample, where the coalescence was incomplete, is compared to the band edge intensity map. The alignment indicates that the intensity of the bandedge emission is relatively higher for the regions of coalesced GaN above the growth mask compared to that from the regions directly above the growth window. Enhanced emission intensity from the regions above the growth mask would correlate with an improved crystal quality of GaN in the laterally overgrown wing region along with an intensity enhancement due to reflection of backward travelling light at the interface of the GaN and buried SiO_2 layer.

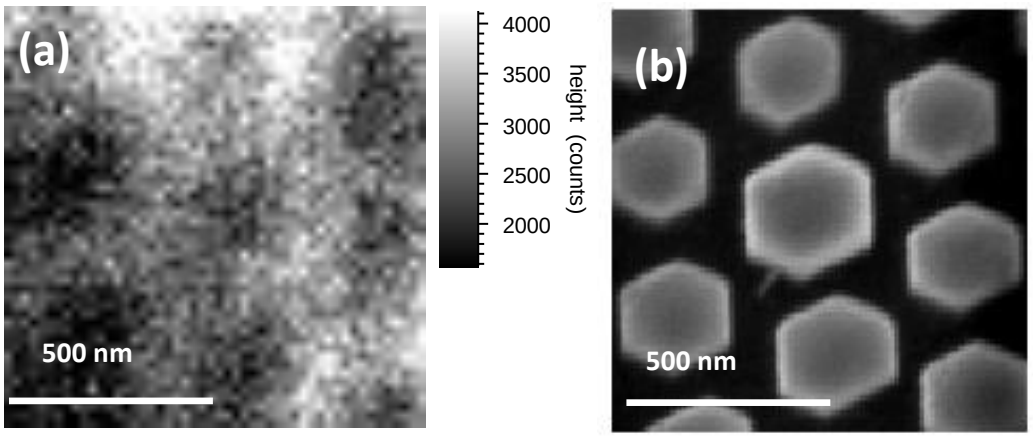

Figure 4.7.(a) Bandedge CL emission intensity map for the sample A acquired using an 8 kV electron beam in a FESEM (b) secondary electron image from a different region of the nanopyramid array where the coalescence is incomplete,

In addition to the effect of built-in-strain, the band edge emission peaks are affected by temperature, carrier concentration and the energy of the incident electron beam. The influence of the electron beam energy on the band edge emission peak can have two origins; one related to the penetration depth of the electron beam in the coalesced layer, which increases with beam energy, and second an excitation power induced peak shift. Since low injection conditions are maintained for the CL mapping, the effect of excitation power on bandedge emission peak position is expected to be negligible in comparison to depth effects. With increase in depth from

the sample surface, the possible factors contributing to strain variation are: (1) lattice and thermal expansion coefficient mismatch between the substrate and GaN, resulting in a residual compressive strain, (2) tensile strain due to the presence of Si, and (3) any stress arising due to coalescence effects. The presence of high concentrations of silicon, possibly from the mask or n-GaN template, can influence both strain and carrier concentration in a GaN lattice and can contribute to a redshift of the NBE emission through bandgap renormalization (BGR). This is a reduction in the fundamental bandgap energy caused by doping densities in excess of about 10^{18} cm^{-3} within GaN [19, 20]. Another direct effect of Si doping in GaN is the broadening of the PL/CL line width of the near band edge emission [19, 21].

Substitution of Si in place of Ga in the GaN lattice might be expected to lead to tensile strain and a net contraction of the lattice as the Si atoms (~ 100 pm) are smaller than the Ga atoms (130 pm). Dadger et al [22] and Lee et al [23] have previously observed tensile strain in Si doped GaN layers. However, according to Romano et al [24], the tensile stress due to Si doping is not related to the change in lattice constant of GaN rather it is due to an increase in surface roughness (which increases with decrease in effective crystallite size) and crystallite coalescence. Since our nanopyramids (which coalesce to form the GaN epilayers) are of ~ 200 nm, size-related effects could be significant.

The observed shift in bandedge emission peak (ΔE) is treated as a sum of the shifts due to strain, including that induced by Si, (ΔE_{strain}) and to the carrier concentration induced by the Si donors ($\Delta E_{carrier}$) :

$$\Delta E = E_{CL} - E_{bulk} = \Delta E_{strain} + \Delta E_{carrier} \qquad [4.1]$$

Hence, estimation of $\Delta E_{carrier}$ enables an estimation of the strain induced GaN peak shift in the coalesced layers.

The carrier concentration in these layers can be estimated using data for the PL FWHM of Si-doped GaN published by Yoshikawa et al. [25], Lee et al. [19] and Schubert *et al.* [26]. The following power law dependence is generated by combining the FWHM and Si concentration data in these three reports:

$$FWHM(meV) = 49 + 8.4 \times 10^{-12} n^{2/3} \qquad [4.2]$$

where n is the carrier density. This expression does not include any strain dependence of the GaN CL line width, which is expected to be very small [21, 27]. This is supported by the CL maps of these samples, where the GaN FWHM varies by only ~ 3 meV whilst the corresponding peak energy shifts by about 30-35 meV [Fig.4.6(d)].

Figure 4.8(a) shows the variation of the FWHM estimated from the CL spectra for the three samples as a function of depth of maximum CL. Equation 4. 2 is used to estimate carrier concentrations from these FWHMs, with values varying from 9.6×10^{17} to 7.6×10^{18} cm^{-3}. The carrier densities increase with the depth of maximum CL up to a depth of about of 70 nm (corresponding to an electron beam voltage of ~ 8 kV). When the depth range of CL excitation is considered, the 85 % range in Figure 2(b), it is seen that this corresponds to the region of excitation approaching the SiO_2 mask. Beyond this the carrier densities reach a plateau. These carrier concentrations are sufficient to shift the GaN bandgap energy via BGR. The bandgap reduction due to BGR can be estimated using the following relation,

$$\Delta E_{carrier} = Kn^{1/3} \qquad [4.3]$$

where K is the BGR coefficient and n the electron density. Lee *et al* [19] have reported BGR coefficients of -1.38×10^{-8} and -2.1×10^{-8} eV cm for moderately and heavily compensated Si doped GaN layers, respectively. Based on the estimates of the Si doping density in the coalesced layers in the region just above the growth mask, the BGR coefficients for samples A, B and C are calculated to be -2.27, -2.05 and -2.31×10^{-8} eV cm, respectively. Figure 4.8 (b) shows the BGR redshift in band edge CL peak position due to the raised carrier concentrations and the measured redshift ΔE (from Fig.4.3(b)) as a function of depth. In all samples the shifts reach values close to, or exceeding, 40 meV as the excited region reaches depths close to the SiO_2 masks. Thus bandgap renormalisation will account for a large proportion of the observed redshift. Moreover, a comparison of the measured shift and BGR shift

reveals that at each depth of maximum CL, the corresponding biaxial strain shift (ΔE_{strain} in Equation 4.1) in bandgap energy should be positive; implying prevailing compressive strain at each depth from the sample surface. The obtained BGR redshift values are comparable to the values reported previously for Si doped GaN [19, 25].

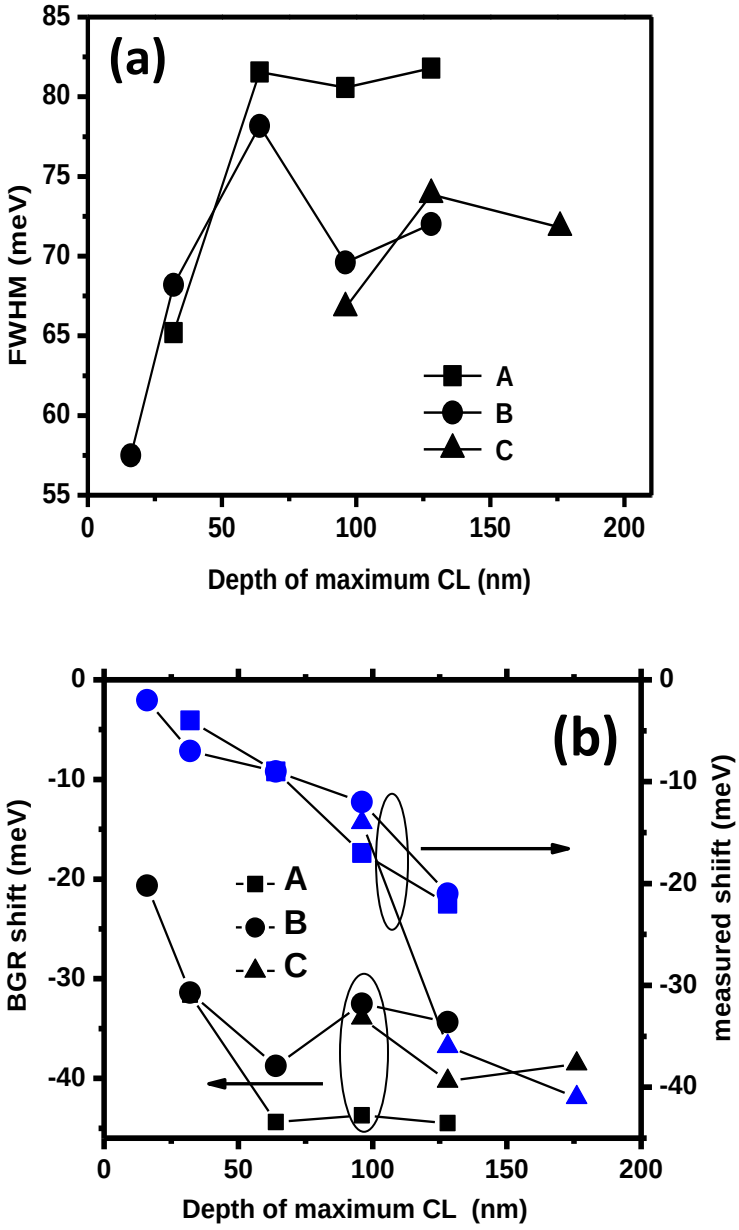

Figure 4.8(a) Room temperature band edge CL linewidth and (b) bandgap narrowing shift and measured shift vs depth of maximum CL for the three samples.

These BGR shift values are then used to quantify the CL band edge emission peak shift due to biaxial strain by subtracting the estimated BGR shifts from the total shift. The resulting shifts due to biaxial strain are plotted in Fig.4.9. For the thinner samples there is a peak in the strain induced shift at the excitation energy that corresponds to a depth of maximum CL reaching down to the buried mask, when the 85% range is taken into account. The positive strain shifts, corresponding to compressive strain, decrease for lower penetration depths giving the expected strain relaxation towards the surface. Further, the observed positive strain shifts imply that the residual compressive strain dominates the tensile strain due to the presence of Si.

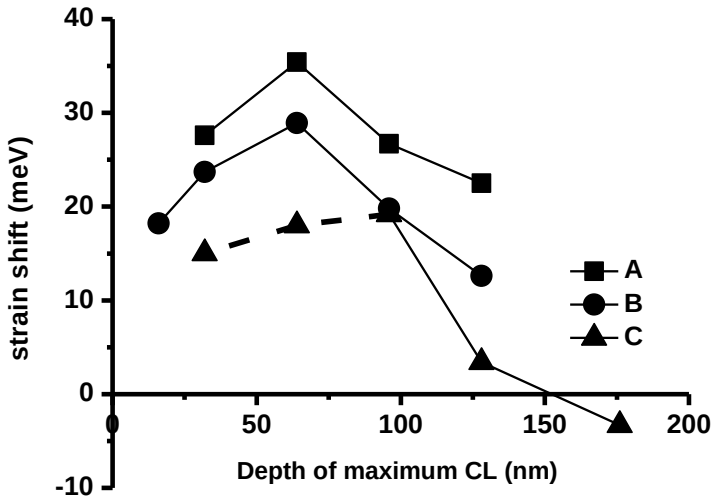

Figure 4.9 Biaxial strain shifts for the three samples as a function of depth of maximum CL. The dashed line extends the plot for sample C to the two simulated data points, as described in the text.

For the thickest coalesced layer (sample C) the behaviour appears somewhat different, although anticipating a reducing carrier shift for lower excitation volumes and continuing the trend in Fig.4.3(b) would produce a peak in compressive strain at a penetration depth somewhat deeper than in samples A and B. Thus two extra points have been simulated for sample C, corresponding to low excitation depths, by

continuing the trend of $E_{CL} - E_{bulk}$ vs depth of maximum CL and assuming a similar drop of $\Delta E_{carrier}$ towards the surface as in samples A and B. The result is a strain shift plot of similar overall shape to the thinner samples but with a peak occurring at a greater depth, as might be expected in the thicker sample.

4.4 Summary

Nanoscale epitaxial lateral overgrowth of GaN has been carried out on a GaN sapphire template by MOCVD using nanopatterned SiO_2 as the mask material. The room temperature depth-resolved CL bandedge emission spectra from coalesced GaN layers are redshifted from the bandgap energy for bulk unstrained GaN. Analysis of the FWHM of the GaN bandedge emission provides estimates of carrier induced red-shifts, which are found to have maxima (near 40 meV) at the point where the extent of the excited region approaches the SiO_2 mask region. This suggests that this effect is due to the diffusion of Si from the mask material into the GaN. The energy shifts due to strain are estimated and the expected positive values, reducing towards the surface, are recovered. Spatially resolved CL maps show micron-scale domain-like variations possibly reflecting the microstructure of the template below the growth mask.

References:

[1] Khan A, Balakrishnan K and Katona T 2008 *Nature Photonics* **2** 77

[2] Nakamura S 2009 *Mater. Res. Bull*. **34** 101

[3] Zheleva T S, Nam O-H, Bremser M D and Davis R F 1997 *Appl. Phys.Lett.* **71** 2472

[4] Nakamura S, Senoh M, Nagahama S, Iwasa N, Yamada T, Matsushita T, Kiyoku H, Sugimoto Y, Kozaki T, Umemoto H, Sano M and Chocho K 1998 *Appl. Phys. Lett.* **72** 211

[5] Nakamura S, Senoh M, Nagahama S, Iwasa N, T. Yamada T, Matsushita T, Kiyoku H, Sugimoto Y, Kozaki T, Umemoto H, Sano M and Chocho K 1998 *J. Cryst. Growth* **189/190** 820

[6] Alizadeh A, Sharma P, Ganti S, LeBoeuf S F and Tsakalakos L 2004 *J. Appl. Phys.* **95** 8199

[7] Tsakalakos L, Alizadeh A, Huber W, Malenfant P, Stein J, Seker F, Reitz J, Ganti S and Sharma P 2004 *Methods of defect reduction in wide bandgap thin films using nanolithography, US20040077156*

[8] Zang K Y and Chua S J 2008 *Phys. Stat. Sol. C* **5** 1585

[9] Wang Y D, Zang K Y, Chua S J, Tripathy S, Zhou H L and Fonstad C G, 2006 *Appl. Phys. Lett*. **88** 211908

[10] Chiu C H et al 2008 *Appl. Phys. Lett*. **93** 081108

[11] Liu C, Shields P A, Chen Q, Allsopp D W E, Wang W N, Bowen CR, Phan T L and Cherns D 2010 *Phys. Status Solidi C* **7** 32

[12] Ren D W, Zhou W and Dapkus P D 2005 *Appl. Phys.Lett.* **86** 111901

[13] Liu C, Satka A, Lethy K J, Edwards P R, Allsopp D, Martin R W, Shields P, Kovac J, Uherek F and Wang W 2009 *Appl. Phys. Exp.* **2** 121002

[14] Hovington P, Drouin D and Gauvin R 1997 Scanning **19** 1

[15] Lee W S 2009 *Appl. Phys. Lett.* **94** 082105

[16] Roskowski A M, Preble E A, Einfeldt S, Miraglia P M, and Davis R F 2002 *IEEE J. Quantum Electronics* **38** 1006

[17] Kim C, Robinson I K, Myoung J, Shim K, Cheol Yoo M and Kim K 1996 *Appl. Phys. Lett.* **69** 2358

[18] Shields P A, Liu C, Šatka A, Trampert A, Zúñiga-Pérez J, Alloing B, Haško D, Uherek F, Wang W, Causa F and Allsopp D 2011 *Phys. Status Solidi C* **8** 2334

[19] Lee I H, Lee J J, Kung P, Sanchez F J and Razeghi M 1999 *Appl. Phys. Lett.* **74** 102

[20] Chine Z, Rebey A, Touati H, Goovaerts E, Oueslati M, El Jani B and Laugt S 2006 *Phys. Status Solidi A* **203** 1954

[21] Koh E K, Woo Park I, Choi H, Yoon M, Choh S H, Kim H S, Cho Y M, Kim S and Park S S 2005 *J. of Crystal Growth* **276** 37

[22] Dadgar A, Schulze F, Zettler T, Haberland K, Clos R, Straßburger G, Bläsing J, Diez A and Krost A 2004 *J. Cryst. Growth* **272** 72

[23] Lee I H, Choi I H, Lee C R, Shin E, Kim D, Noh S K, Son S J, Lim K Y and Lee H J 1998 *J. Appl. Phys.* **83** 5787

[24] Romano L T, Van de Walle C G, Ager J W, Götz W and Kern R S 2000 *J. Appl. Phys.* **87** 7745

[25] Yoshikawa M, Kunzer M, Wagner J, Obloh H, Schlotter P, Schmidt R, Herres N, and Kaufmann U 1999 *J. Appl. Phys.* **86** 4400

[26] Schubert E F, Goepfert I D, and Grieshaber W 1997 *Appl. Phys. Lett.* **71** 921

[27] Kudrawiec R, Rudziski M, Serafinczuk J, Zajc M and Misiewicz J 2009 *J. Appl. Phys.* **105** 093541

Chapter 5

Cross-sectional and plan-view cathodoluminescence of GaN partially coalesced above a nanocolumn array

5.1 Introduction

A brief introduction to the GaN nanocolumns and their epitaxial overgrowth was given in Chapter 2. This chapter describes the study of optical properties of such a coalesced GaN layer above an array of GaN nanocolumns. The high quality optical data on these samples are obtained using CL hyperspectral imaging as described in Chapter 3. The growth of GaN on Si substrates is of significant interest because of the potential for use of large area substrates and integration with electronic devices along with advantages such as low cost, wide availability and high thermal conductivity [1, 2]. GaN-on-sapphire and GaN-on-SiC are currently the leading combinations for commercial high brightness blue/green/white LEDs and III-nitride wireless/RF products. GaN-on-silicon has yet to really make its mark on either of these industries, but is the most promising material combination for achieving high device performance from growth on a low cost, large diameter platform. However, the growth of high quality GaN on Si is challenged by the large lattice (16.9 %) and thermal expansion coefficient (56 %) mismatches, which result in high densities of threading dislocations and tensile stress in GaN epilayers. GaN substrates with fewer

threading dislocations are highly desirable for fabricating high-performance III-nitride devices and also for next generation laser diodes (LDs). Growth processes utilizing epitaxial lateral overgrowth (ELOG) have proved significant in reducing dislocation densities and improving optical and electrical properties [3] as described in section 2.3.1 of Chapter 2. However, TD densities < $10^{-6}cm^{-2}$ have not been achieved so far using this technique and high performance devices are fabricated only on the ELOG "wings".

Nano-ELOG involving lateral overgrowth at the nanometer scale, developed to overcome the limitations of the conventional ELOG techniques and to reduce the dislocation density to below $10^{-6}cm^{-2}$ was already described in section 2.3.1(a) of Chapter 2. GaN nanocolumns are one dimensional columnar nanostructures with high crystal quality and can possess improved optical properties due to their dislocation-free nature [4]. If the tops of such relaxed and dislocation-free GaN nanocolumns are coalesced by lateral growth, a GaN epitaxial layer with potentially little or no stress and very few dislocations can be obtained. This chapter discusses the optical properties of partially coalesced GaN nanocolumns on a Si substrate. Self-assembled GaN nanocolumns are produced by MBE on a Si [111] substrate, and then serve as seeds for nano-ELOG by MOCVD. The optical properties of the partially coalesced layers are investigated using high spatial resolution cathodoluminescence hyperspectral imaging to provide visualisation of the microstructure, information on the local luminescence and tracking of the strain variation across the coalesced layers. Collecting such data from cross-sections provides information as a function of depth within the grown layers.

5.2 Sample specifications and Experimental details

Growth of GaN nanocolumns on Si was carried out in an RF-MBE systems having two Ga sources configured with different angles towards the growth substrate. NH_3 was used as the nitrogen source to grow layers of GaN and AlN. Prior to growth the Si (111) substrate was heated to 950^{o}C for 60 minute for thermal cleaning, followed by a 60 minute surface nitridation at 1023^{o}C. The AlN buffer was deposited for 30 minutes at 850^{o}C. The substrate temperature was then raised to

900^{o}C and the GaN nanocolumn structures were grown for 2 hours using the two Ga sources.

Coalescence of the GaN nanocolumns was conducted in an Aixtron 200/4HT RF-S MOCVD reactor. The combined conventional growth mode, i.e. when gallium and nitrogen precursors are switched into the growth chamber simultaneously, and pulsed growth mode was applied [5]. Under the conventional growth mode, a growth temperature of 1150 ºC, reactor pressure 100 mbar, V/III ratio in the range of 500-10000, and the growth time corresponding to nominal planar growth for 2 µm GaN were used. The pulsed growth was employed to achieve the fast lateral growth in the early stage of coalescence. H_2 was used as carrier gas in all the growth experiments.

The surface and cross-sectional morphology of the partially coalesced nanocolumns were studied by field emission gun scanning electron microscopy (FESEM) as described in chapter 3. The light emitting properties were investigated by spatially and spectrally resolved room temperature CL setups attached to two different electron microscopy systems. High spatial resolution CL maps were collected from an angled sample using the FESEM and lower spatial resolution CL maps were obtained in plan-view using the CL setup attached to a Cameca SX100 electron probe micro-analyser (EPMA). Detailed descriptions of these two set ups were given in chapter 3. The application of appropriate mathematical methods to CL hyperspectral, three dimensional data set I (λ, x, y), was used to extract the spatial distribution of peak intensity, peak energy and FWHM across the mapped region.

5.3. Results and Discussion

5.3.1 Surface morphology

The plan-view secondary electron image (Fig. 5.1(a)) of the top GaN layer reveals that the surface of the overgrown epilayer is not continuous, rather constituted by a number of sub-µm scale domain structures with distinct grain boundaries. The misalignment of adjacent GaN nanocolumns with respect to each other can possibly account for this incomplete coalescence with distinct grain boundaries. The cross-section SEM image, in Fig.5.1(b), shows the layer of GaN

nanocolumns, approximately 500 nm in height, which then merge into larger columns giving an overgrown layer of partially coalesced GaN, about 2 μm in thickness.

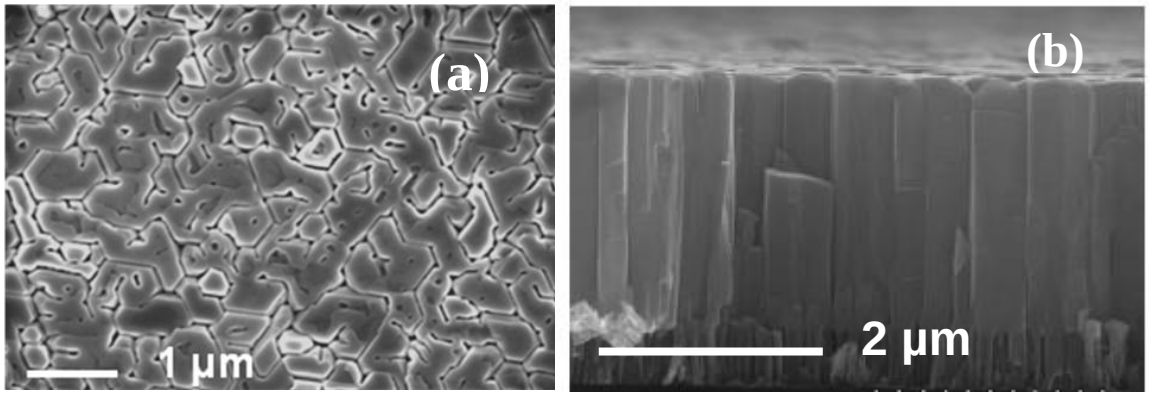

Figure 5.1(a) Plan-view and (b) cross-sectional SEM images of the partially coalesced GaN nanocolumns.

5.3.2 Plan view CL hyperspectral imaging

A plan-view integrated intensity CL map from the partially coalesced nanocolumns acquired with an electron beam energy of 10 keV using the CL setup attached to the EPMA is shown in Fig.5.2. The penetration depth (the depth at which the energy density of the incident electron beam has reduced by 90%) estimated using Monte-Carlo simulation is 370 nm for this electron beam energy and is thus confined well within the partially coalesced layer. The CL emission intensity [Fig 5.2 (b)] is not uniform across the partially coalesced layer and shows strong contrast between dark and bright regions. Figure 5.2(c) shows the mean CL spectrum for the mapped region in Fig. 5.2(a) and presents two peaks at 3.41 eV and 3.19 eV. The 3.41 eV peak corresponds to near band edge (NBE) emission and indicates a slight tensile strain in the partially coalesced GaN layer, by comparison with the NBE of bulk unstrained wurtzite GaN bandedge emission of 3.42 eV [6].

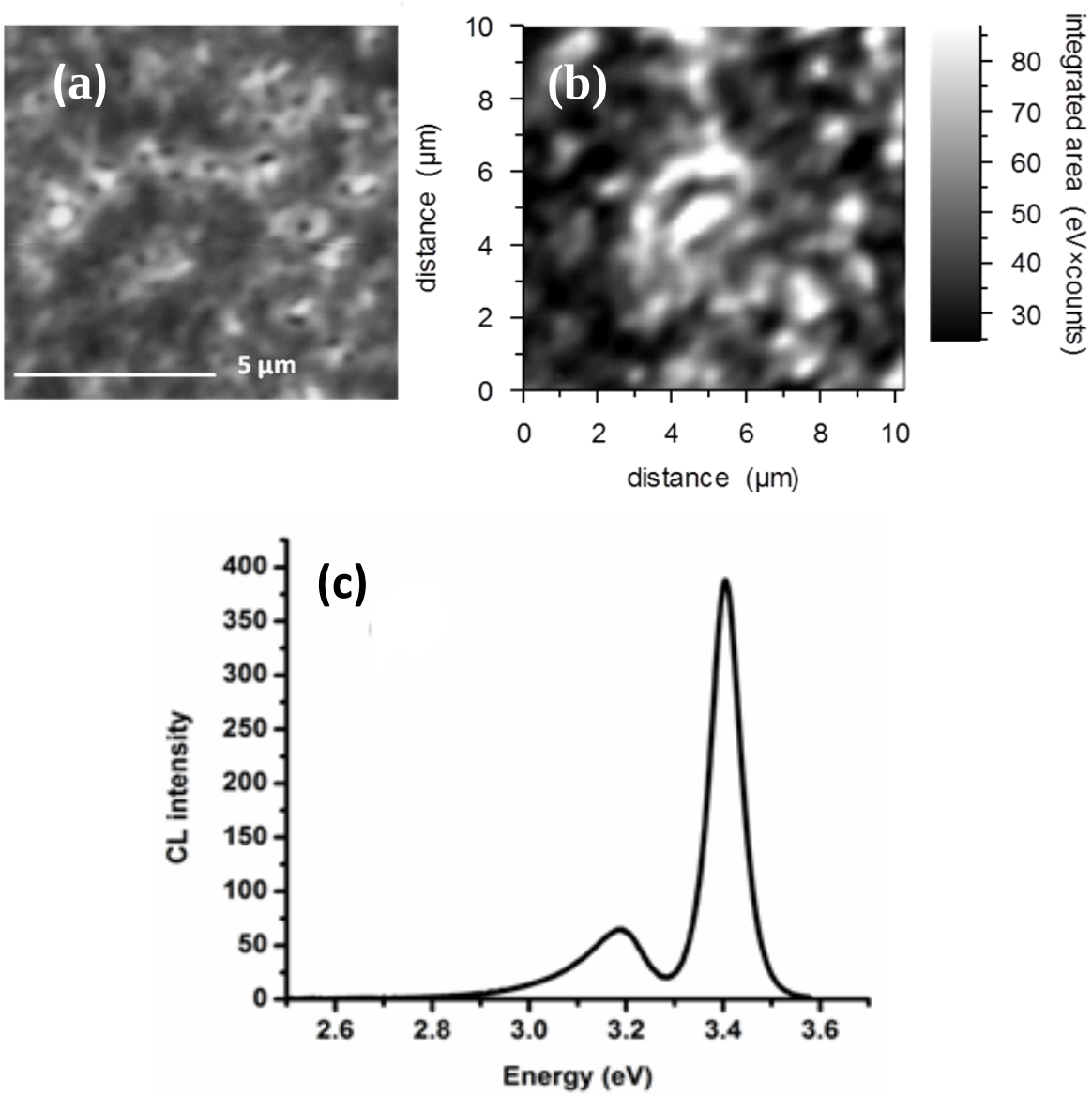

Figure 5.2(a) Secondary electron image of the partially coalesced GaN layer. (b) plan-view integrated intensity CL map from the partially coalesced GaN nanocolumns layer (b) mean CL spectrum from the mapped region.

The peak appearing at 3.19 eV is most likely related to donor-acceptor pair (DAP) recombination. The most common donor species in GaN are O and Si, behaving as shallow donors. Although oxygen is not a usual contaminant in MBE growth, Si contamination is possible when using a Si substrate and Si-based mask material. In both MOCVD and MBE techniques, carbon is the most common residual acceptor

contaminant [4]. However, since the nanocolumn growth occurs under nitrogen rich conditions, the formation of Ga vacancies acting as acceptors is also likely.

Gaussian peak fitting to the individual CL spectra from each pixel, using a non-linear least squares (NLLS) algorithm, is used to generate maps showing the distribution of peak height, centre energy and FWHM for both GaN near band edge emission and the DAP emission, as shown in Fig. 5.3. The CL intensity maps [Fig. 5. 3(a) and (d)] show the distribution of the NBE and DAP emission respectively. Both are localised and randomly distributed and, importantly, these variations occur on a length scale much larger than that of the nanocolumn array. The spatial variation of the DAP emission indicates an inhomogeneous distribution of impurities across the partially coalesced surface and it is noteworthy that there is a contrast difference between the domain centre and boundaries.

The GaN bandedge centre energy CL map (Figure 5.3(b)) reveals micron-scale domain-like variations in peak energy, which can be attributed to the effects of the micron sized domain structures seen on the plan- view SEM. The effects of strain and/or doping can have a contribution to this variation in NBE CL emission. The thickening of GaN nanocolumns occurs by the merging of neighbours during the MOCVD overgrowth process and, together with minor misalignments between the adjacent coalesced regions, can cause strain in the partially coalesced layer. CL maps taken at different electron beam energy, to provide some depth resolution, indicate that there is no significant variation in domain pattern with depth, for either intensity contrast or peak energy. The CL maps showing the spatial distribution of GaN NBE and DAP emission peak FWHM [Fig 5.3(c) and (f)] also reveal μm-scale range variations similar to that of intensity and peak energy spatial distribution.

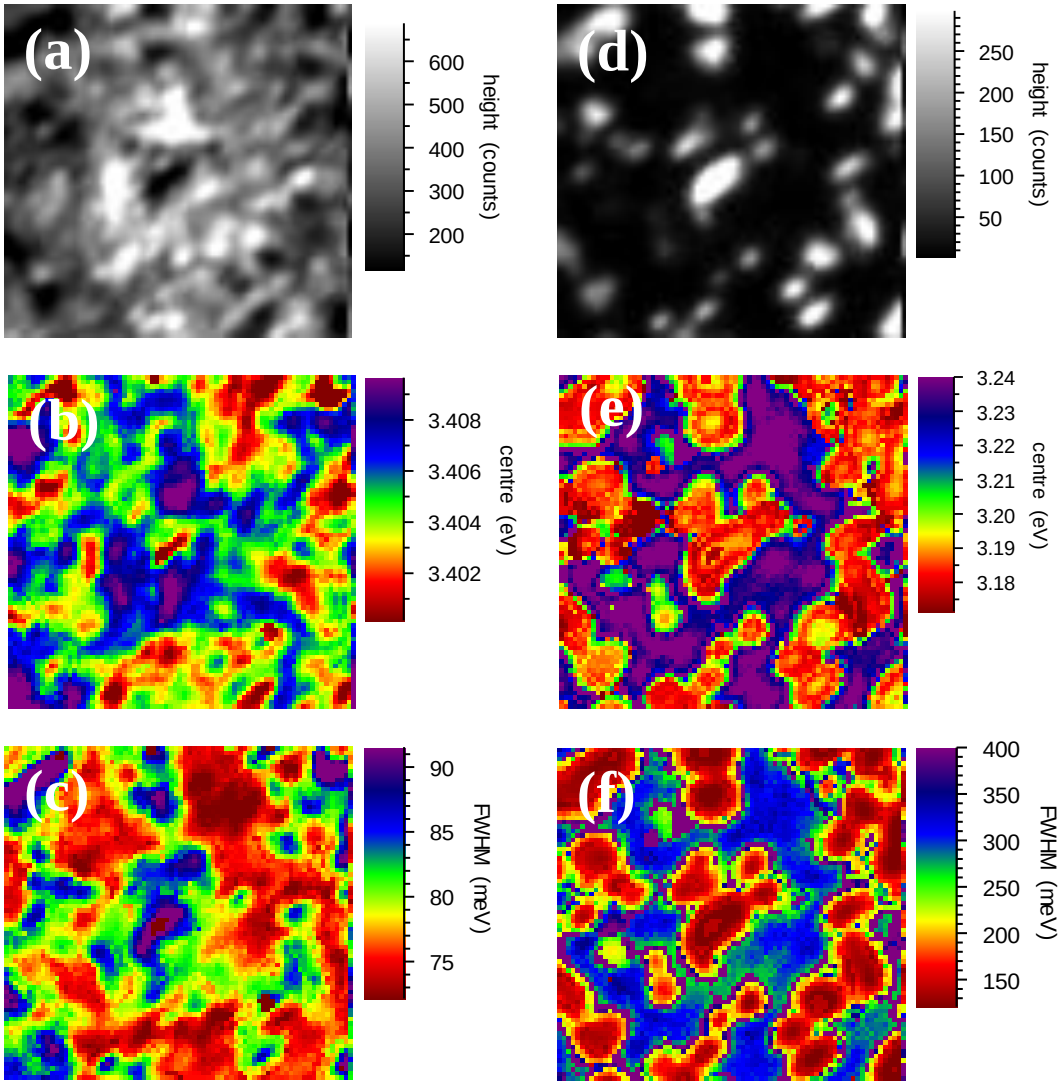

Figure 5.3 The CL maps showing the distribution of peak intensity, centre energy and line width for the GaN near bandedge (a,b and c respectively) and DAP emission (d, e and f respectively). Images (a)-(f) are 10 x 10 µm.

To study the spatial distribution of strain across the partially coalesced GaN layer, high resolution plan-view CL hyperspectral maps are acquired from a 2 x 2 μm^2 area of the sample using the FESEM CL set up. Figure 4 shows the CL peak energy map of GaN NBE emission overlaid on the secondary electron image. The grain boundaries are generally seen to match the higher energy (blue) regions, indicating higher compressive strain at these points. The merging of adjacent crystal domains,

arising from non-perfectly aligned nanocolumns can account for the strain at the grain boundaries [7].

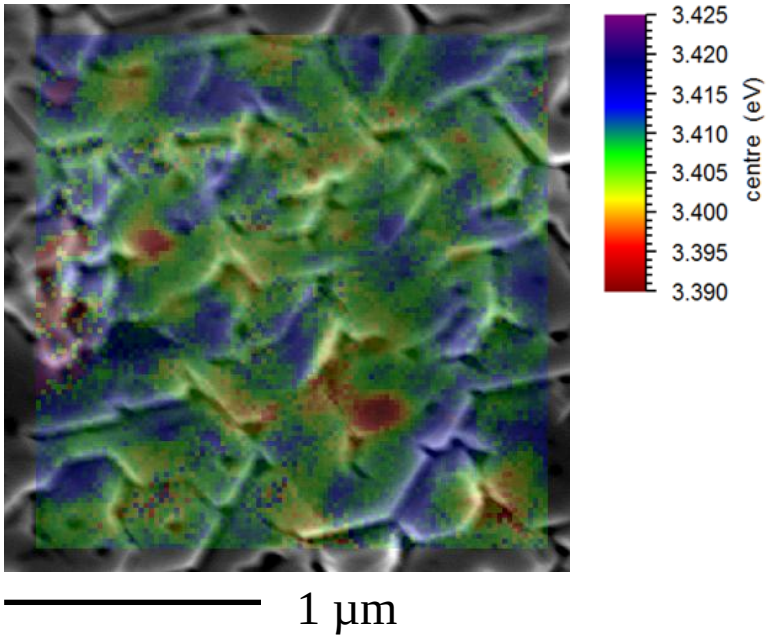

Figure 5.4 The CL peak energy map of GaN NBE emission overlaid on the corresponding secondary electron image. The scale bar corresponding to the CL peak energy distribution map is also shown.

5.3.3 Cross-sectional CL hyperspectral imaging

Cross-sectional CL hyperspectral imaging is performed using the CL set up attached to FESEM**.** Figure 5.5(a) shows a secondary electron image of a cross-section, which was then mapped using CL hyperspectral imaging in the FESEM. The mapped area was 0.75 x 3 μm^2 with a step size of 50 nm and a dwell time of 500 ms per pixel. The mapped area is indicated by the box, and includes both the partially coalesced and nanocolumn layers. Figure 5.5(b) shows the integrated intensity CL map across the cross-section with lines separating the emission from the partially coalesced and nanocolumn regions. The vertical scale of Fig 5.5(b) has been corrected for the tilt of the sample. The CL emission is brighter from the nanocolumn layer relative to the partially coalesced layer indicating the higher optical quality of nanocolumn layer which can be attributed to its lower dislocation density [4, 8]. This

can also be due to the improved light extraction efficiency of one dimensional nanocolumns.

The dislocation density reduction in the nanocolumns is partially due to the dislocation bending in the nanocolumns and dislocation blocking effect of the SiO_2 mask and partially due to strain relaxation in the nanometer sized nucleation and growth [9]. A similar observation of brighter CL from the nanocolumn layer has been reported by Tang et al [10] from samples fabricated using nano-imprint lithography and MOVPE, although the same authors have reported the opposite behaviour for coalescence above MBE nanocolumns grown from an AlN nucleation layer [11].

The spectra from the full height of Fig. 5.5(b), averaged across the fifteen pixels of the map are plotted as a CL line scan in Fig. 5.5(d). The analysis of this cross-section map reveals a blue shift of ~ 25 meV in the GaN near bandedge CL peak as the sampled region moves upward from the nanocolumn layer, through the partially coalesced layer of thickness ~ 2μm. This shift in the GaN band-edge emission can be related to the release of tensile strain through the partially coalesced layer. This is in agreement with the observation by Shiao et al [7] where the strain across an overgrown GaN layer of similar thickness decreases with an increase in thickness of the coalescence layer. Similarly Tang et al [10] observed a rebuilding of compressive strain (~0.66 GPa) in a GaN coalesced layer over strain free nanocolumns grown on nanopatterned sapphire substrate. Bougrioua et al [12] also reported the incorporation of strain in an MOCVD overgrown GaN layer using PL spectroscopy, with coalescence started from strain–free nanopillars grown by MBE, although in this case the sense was tensile.

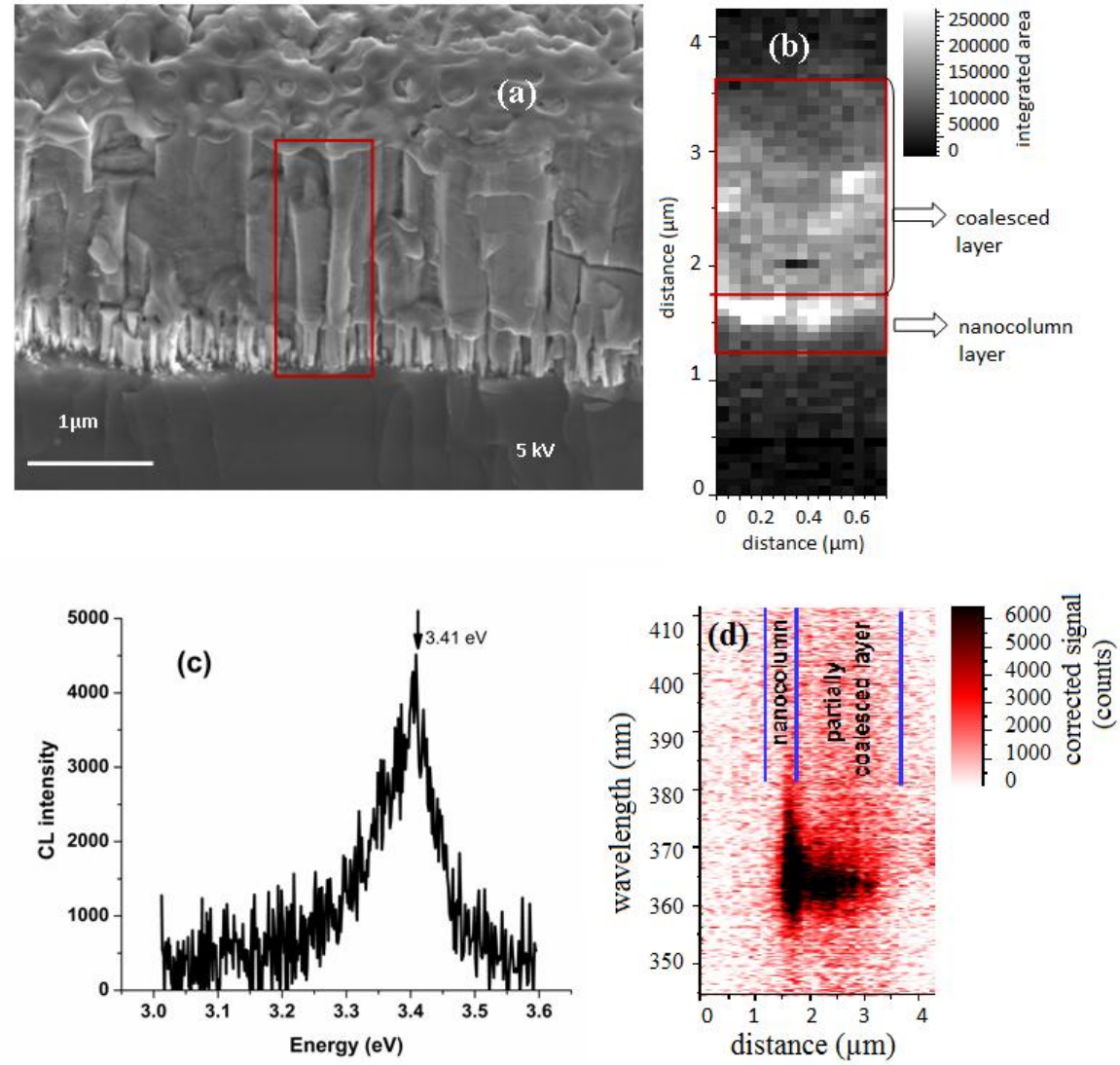

Figure 5.5(a) Secondary electron image showing the mapped region in a box (b) Cross-sectional CL integrated intensity map (c) mean spectrum from the cross-section CL map (d) line spectrum corresponding to CL line scan analysis.

A comparison of the averaged CL spectra obtained from line scan analysis of 15 pixels across the nanocolumn layer and the top part of the partially coalesced layer reveals that the GaN bandedge emission from the nanocolumn layer is broader [Fig.5.6] (by approximately 50 meV) and hence this layer is more tensile strained than the partially coalesced GaN layer. The small dimensions of the nanocolumns allow for local strain relaxation, permitting the lattice parameter to approach its bulk value. Hence the GaN nanocolumns are expected to grow strain-free and defect-free

with a single hexagonal crystal structure, as has been experimentally observed by several research groups [4, 13]. This leads to an expectation that the GaN layer structure realised by coalescence of these strain free nanocolumns should be completely strain relaxed. However the tensile strain from the nanocolumn layer observed in the present case could be due to high residual doping. Liu et al [14] also observed a tensile stress for micron scale pyramid facets near the base of epitaxial lateral overgrowth (ELOG) GaN grown over a SiO_2 mask.

Figure 5.7 clarifies how the blueshift and narrowing of the GaN bandedge emission develop as the electron beam scans from the nanocolumn layer to the top layers of partially coalesced overgrowth GaN. Each data point on these plots are obtained by Gaussian peak fitting to the individual CL spectra, averaged across 15 pixels on a line spectrum. The tensile strain from doping arises due to Si from the substrate or mask diffusing to the nanocolumn layer. Si doping effects in the GaN lattice were discussed in Chapter 4. The FWHM analysis of the PL spectra for bandedge emission from GaN as a function of Si doping by Schubert et al [15] and Lee et al [16] revealed an increase in FWHM of the bandedge emission with increase in Si doping concentration. Tang et al [10] also observed a similar broadening effect for the GaN bandedge emission from regularly patterned GaN nanocolumns on sapphire substrate. However the nanocolumns in the present case are not uniformly patterned or well ordered arrays as reported by Tang et al. The MBE grown nanocolumns have slight dispersions in their height, width and orientation, as shown in Figure 5.1, which can contribute to the broadening of the FWHM of the GaN bandedge emission.

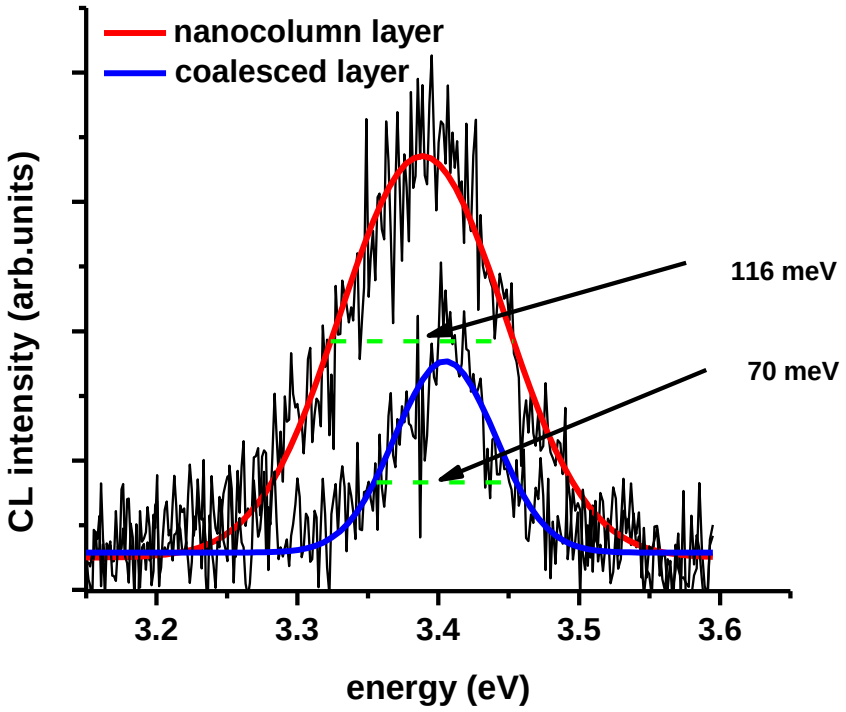

Figure 5.6. Comparison of the FWHM of the mean CL spectra collected from the nanocolumn layer and the top partially coalesced layer

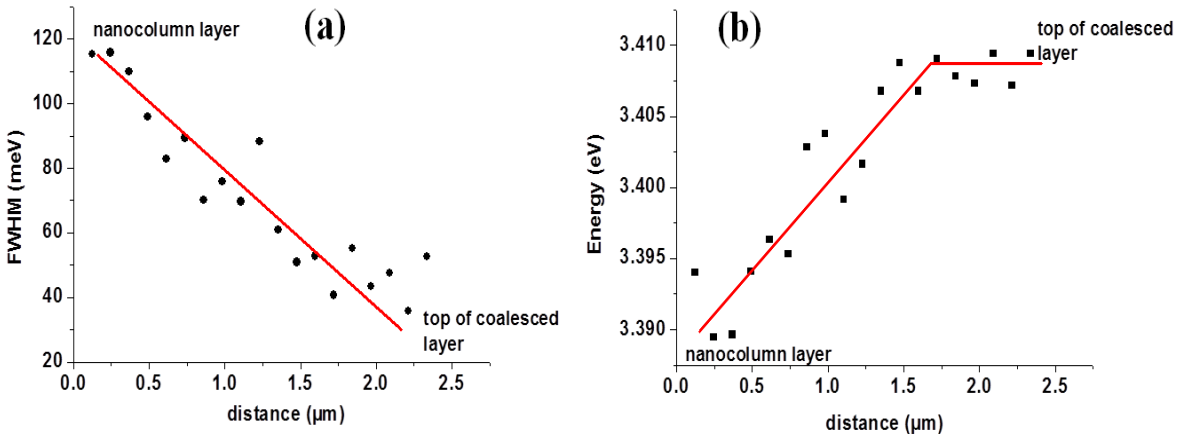

Figure 5.7(a) FWHM and (b) energy variation of the GaN NBE emission as the electron beam scans from the nanocolumn layer to the top of the coalesced layer. The lines are guides to the eye.

The peak of the mean band edge CL emission (~3.41 eV) from the plan-view map is comparable to that collected from the top partially coalesced layers in the cross-sectional CL map (~3.41 eV), but shifted from that of unstrained bulk GaN emission (3.42 eV) implying that the partially coalesced layer is not fully relaxed and under a slight tensile strain. The absence of a continuous crystal surface and the presence of distinct domain structure as seen in the SEM image, and a possible epitaxial misalignment due to random orientation of the growth facets between adjacent domains as suggested by plan-view CL map, can result in a build up of compressive strain in the GaN overgrown layer, reducing the tensile strain.

Investigation of a similar region further along the cross-section revealed a slightly different strain situation. Starting from the top of the nanocolumns, a slight redshift of ~ 20 meV for GaN bandedge emission is observed across the partially coalesced GaN layer, indicating a build up of tensile strain as the coalescence overgrowth proceeds. Analysis of individual CL spectra averaged across 15 pixels obtained from line scan analysis along the partially coalesced layer further revealed that the initial layers of the overgrowth layer are tensile strain relaxed.

It is worth mentioning that the mean CL spectrum collected from some regions of the cross-section has a shoulder emission at 3.35 eV in addition to the bandedge emission peak. There are two different views about the origin of this peak. Bunea et al [17] attributed this shoulder emission to re-absorption where as Chen et al.[18] reported this emission at 3.35 eV to be related to localised or extended defects, such as stacking faults and dislocations or shallow levels in the bandgap. The presence of this shoulder emission peak in the coalesced overgrown GaN layer on sapphire and Si substrates are reported by Tang et al [10, 11]. An intensity comparison of the emission at 3.35 eV to the NBE emission across the nanocolumn and partially coalesced layers was performed using the mean CL spectra collected from the respective layers. No consistent behaviour exists for the ratio $I_{3.35}/I_{NBE}$ across the nanocolumn layer and partially coalesced layer, implying that the defects, if they are the cause of this emission, are randomly distributed across the nanocolumn layer and coalesced layer.

5.4. Summary

The optical properties of a GaN layer coalesced by MOCVD starting from MBE grown nanocolumns on Si substrate have been studied using CL hyperspectral imaging. The overgrown GaN layer is partially coalesced with distinct grain boundaries, with plan-view CL hyperspectral imaging revealing micron-scale domain like spatial variations of the GaN NBE emission energy and FWHM. Higher resolution plan-view CL mapping indicated that the grain boundaries associated with this partially coalesced GaN are under strain. Cross-sectional CL hyperspectral imaging identified a blue shift of ~ 25 meV, and a narrowing of the GaN bandedge emission peak, as the electron beam sampled region moves upward from the nanocolumn layer. This energy shift is possibly associated with the release of tensile strain through the partially coalesced GaN layer.

References:

[1] Semond F, Cordier Y, Grandjean N, Natali F, Damilano B, Ve´zian S and Massies J 2001 *phys. stat. sol. (a)* **188** 501-10

[2] Krost A and Dadgar A 2002 *phys. stat. sol. (a)* **194** 361-75

[3] Chichibu S F et al 1999 *Appl. Phys. Lett*. **74** 1460-2

[4] Calleja E, Sanchez-Garcia M A, Sanchez F J, Naranjo F B, Munoz E, Jahn U and Ploog K 2000 *Phys. Rev. B* **62** 16826-34

[5] Liu C, Shields P A, Denchitcharoen S, Stepanov S, Gott A, and Wang W N 2007 *J. Cryst. Growth* **300**, 104-9

[6] Lee W S et al 2009 *Appl. Phys. Lett.* **94** 082105-3

[7] Shiao W Y, Tang T Y, Chen Y S, Averett K L, Albrecht J D, Yang C C 2008 *J. Cryst. Growth* **310** 3159-62

[8] Hersee S D, Sun X and Wang X 2006 *Nano Lett.* **6** 1808-11

[9] Keyan Z, Yadong W, and Jin C S 2009 *phys. stat. sol.(c)* **6** S514-8

[10] Tsung-Yi Tang et al. 2009 *J. Appl. Phys*. **105** 023501-8

[11] Tang T Y, Averett K L, Albrecht J D, Shiao W Y, Chen Y S, Yang C C, Hsu C W and Chen L C 2007 *Nanotechnology* **18** 445601-4

[12] Bougrioua Z, Gibart P, Calleja E, Jahn U, Trampert A, Ristic J, Utrera M and Nataf G 2007 *J. Cryst. Growth* **309** 113-20

[13] Cerutti L, Ristic J, Garrido F S, Calleja E, Trampert A, Ploog K H, Lazic S, and Calleja J M 2006 *Appl. Phys. Lett.* **88** 213114-7

[14] Liu Q K K, Hoffmann A, Siegle H, Kaschner A, Thomsen C, Christen J and Bertram F 1999 *Appl. Phys. Lett.* **74** 3122-4

[15] Schubert E F, Goepfert I D and Grieshaber W 1997 *Appl. Phys. Lett.* **71** 921-3

[16] Lee I H, Lee J J, Kung P, Sanchez F J and Razeghi M 1999 *Appl. Phys. Lett.* **74** 102-4

[17] Bunea G E, Herzog W D, Unlu M S and Goldberg B B and Molnar R J 1999 *Appl. Phys. Lett.* **75** 838-40

[18] Chen G D, Smith M, Lin J Y, Jiang H X, Salvador A, Sverdlov B N, Botchkarv A and Morkoc H 1996 *J. Appl.Phys*. **79** 2675-83

Chapter 6

Cathodoluminescence imaging of semipolar and nonpolar InGaN/GaN single quantum wells

6.1 Introduction

This chapter discusses spatially resolved optical properties of semipolar {10$\underline{1}$1} and nonpolar {1$\underline{1}$00} InGaN /GaN single quantum wells probed using high resolution CL hyperspectral imaging. The significance of these specific crystal orientations for InGaN QW fabrication was already described in Chapter 2. The non-polar and/or semipolar InGaN/GaN QW based LEDs and laser diodes are expected to exhibit enhanced efficiency and performance compared to their polar counterparts. In order to realize efficient non-and semipolar III-nitride LEDs and lasers, high quality QWs in the respective crystal orientations are required. These can be fabricated using selective area epitaxy where GaN pyramidal facets grown on c-plane GaN act as the template for semipolar/nonpolar QW growth. Selective area epitaxy on the nanoscale offers advantages such as an increase of light emitting area, improved light extraction efficiency, 3D stress relief, low defect density, efficient means for precise control of position and homogeneous size distribution of QDs (on the apex of nanopyramids) [1, 2]. There are only a very few reports [discussed in section 2.3.3 of Chapter 2] on semipolar {10$\underline{1}$1} and nonpolar InGaN QWs fabricated on GaN nanofacets and detailed investigation on their spatially resolved luminescence properties are seldom reported.

This chapter investigates the optical properties of three different sets of semipolar {10$\underline{1}$1} InGaN QWs fabricated on the facets of GaN nanopyramids. In addition to

these, the optical properties of InGaN QWs grown along the nonpolar m-plane {1$\underline{1}$00} nanofacets of 3D GaN structures are also discussed. The purpose of present study is to explore the nanoscale spatial variation of InGaN/GaN QW emission properties across the nanofacets of 3D GaN structures using high resolution cathodoluminescence hyperspectral imaging.

6.2 Sample specifications and Experimental details

The three sets of semipolar {10$\underline{1}$1} InGaN QW samples [Table 6.1] described in this chapter were grown by Dr Philip Shields and Dr Duncan Allsopp at the University of Bath. These InGaN QWs were fabricated on the nanofacets of GaN pyramids selectively grown on c-plane sapphire (Fig 6.1). A brief discussion of the selective area growth (SAG) of GaN can be seen in section 2.3 of Chapter 2. The selective area grown template consisted of a patterned SiO_2 layer on a c-plane GaN on c-sapphire substrate realised by nanoimprint lithography and CHF_3 plasma etching [3]. The pores or openings in the mask are quasi-hexagonal in shape arranged in a hexagonal lattice of 450 nm. The GaN nanopyramids in the first set of sample (1969 SQW) are non-intentionally doped while those for second (2135-2138) and third (2321-2344) sets of samples are Si doped with dopant concentration as given in Table 6.1. The nominal thicknesses of the InGaN QW and GaN cap layer for the first two sets are 2.8 and 10 nm based on equivalent c-plane growth at 865 ^{0}C and 200 mbar. For the third set, the QWs have double the thickness compared to first two sets, as the growth time was doubled. Moreover for the third set, the thin GaN cap layer is followed by a high temperature grown thick (~110 nm) p-type GaN layer. The SiO_2 mask is 100 nm thick for the first set and 40 nm for the other two sets. The pore dimensions are ~200 X 400 nm^2, for the first set of sample, the elongation deriving from the nanoimprint master (hence the GaN nanopyramids are slightly elongated). For the other two sets of samples (II and III), the pores are circular with a diameter of 200-250 nm. The QW growth temperature in each set is given in Table 6.1.

The fourth set comprises one sample having InGaN QWs on nonpolar m-plane {1$\underline{1}$00} facets of 3D GaN structures, which are grown on nano patterned a-plane GaN templates on r-plane sapphire substrates. The nonpolar templates were grown

by Dr Menno Kappers at the University of Cambridge and the overgrowth was performed by Dr Philip Shields and Dr Duncan Allsopp at University of Bath. A 19 nm thick SiN_x layer constitutes the mask layer and the pores are circular in shape with diameters in the range 200-250 nm on a hexagonal lattice of 600 nm. The GaN 3D nanostructures are grown by MOCVD at a reactor temperature of 1000 ^{0}C and pressure of 200 mbar. The size, shape and the crystal orientation of different facets of 3D GaN nanostructures realized on a-plane GaN templates depends on the growth anisotropy in different directions. Once the growth of 3D GaN nanostructures is complete, the reactor conditions were changed for the growth of a single InGaN QW on their facets.

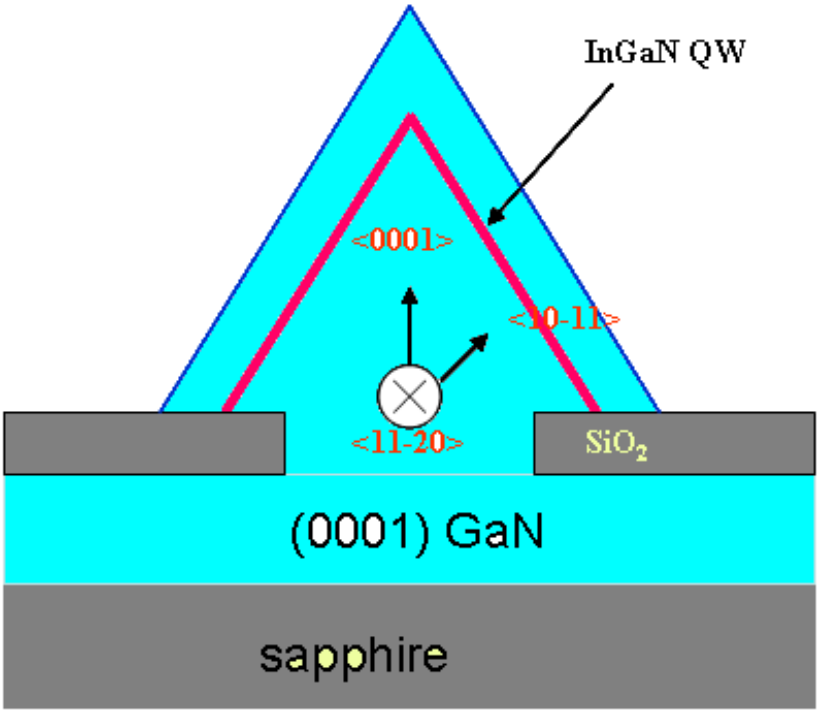

Figure 6.1. General sample structure for semipolar InGaN QWs on nanofacets of GaN pyramids

Table 6.1 Sample specifications for semipolar and nonpolar InGaN QWs

Sample name	InGaN Growth temperature (^oC)	Mask material and thickness (nm)	Pore size and shape (nm)	Pitch (nm)	Si doping to GaN nanopyramid
Set 1					
1969 SQW	865	SiO_2/100	200 x 400 Quasi-hexagonal	450	Non-intentionally doped
Set II					$5 \times 10^{18} cm^{-3}$
2136 SQW	815	SiO_2/40	200-250 circular		
2137 SQW	825				
2135 SQW	835				
2138 SQW	845				
Set III					
2335 SQW	825				
2321 SQW	845				
2344 SQW	865				
Set IV					
2458 SQW	865	SiNx/19	200-250 circular	600	Non-intentionally doped

The PL spectra of the samples are obtained using the 325 nm line of He-Cd laser as the excitation source. The experimental setup and component details are as described in Chapter 3. The detailed description of the custom built hyperspectral CL setup attached to FESEM and EPMA used for CL measurements are also given in Chapter 3. The hyperspectral CL maps are obtained using the FESEM CL set up using an electron beam voltage of 5 kV and a beam current of 1.6 nA. For the set III samples, 7 kV beam voltage is used because of the thick p-type GaN layer on top of the QWs. The CL maps thus obtained were treated mathematically to extract the spatial

dependence of GaN NBE and InGaN QW luminescence. The depth resolved luminescence properties of both the QWs and GaN nanostructures were obtained by FESEM CL measurements as a function of electron beam voltages. Electron beam voltages of 2, 5 and 7 kV (with probe currents of 3.4, 1.6 and 1 nA respectively) were the beam conditions used this measurements. Excitation current dependent measurements were performed on selected samples using the CL set up attached to the EPMA. For this measurement, the electron beam is defocused to 2 μm and the excitation current is varied from 0.5 nA to 200 nA corresponding to a current density of 0.01 to 5 A/cm^2.

6.3 Results and Discussion

6.3.1 Spatial mapping of array of nanopyramids

6.3.1(a) Set I : 1969 SQW (non-intentionally doped GaN nanopyramids)

The surface morphology of the sample is studied by scanning electron microscopy [Fig 6.2]. The areal density of the GaN pyramidal structures estimated from the SEM image is ~1×10^{9}cm^{-2}. Growth on the SiO_2 mask is not entirely suppressed, possibly because of residual contamination from the imprint resist. Detailed CL imaging revealed that the debris on the growth mask did not contribute to the luminescence. The CL from an area encompassing several nano-pyramids [Fig 6.2(b)] comprises (i) a sharp emission peak at a wavelength of ~365 nm associated with GaN near band-edge emission (ii) a somewhat broader peak at a wavelength of ~420 nm associated with the InGaN QW and (iii) a broad defect band centred near 550 nm. Figure 6.3 shows maps of the peak intensity of the QW CL peak and yellow band (YB), obtained by curve fitting to the 5 kV CL data obtained using EPMA CL set up. The maps in Figure 6.3 clearly show that the ~420 nm QW emission comes only from the nanopyramids whilst the defect band emission emanates predominantly from under the growth mask.

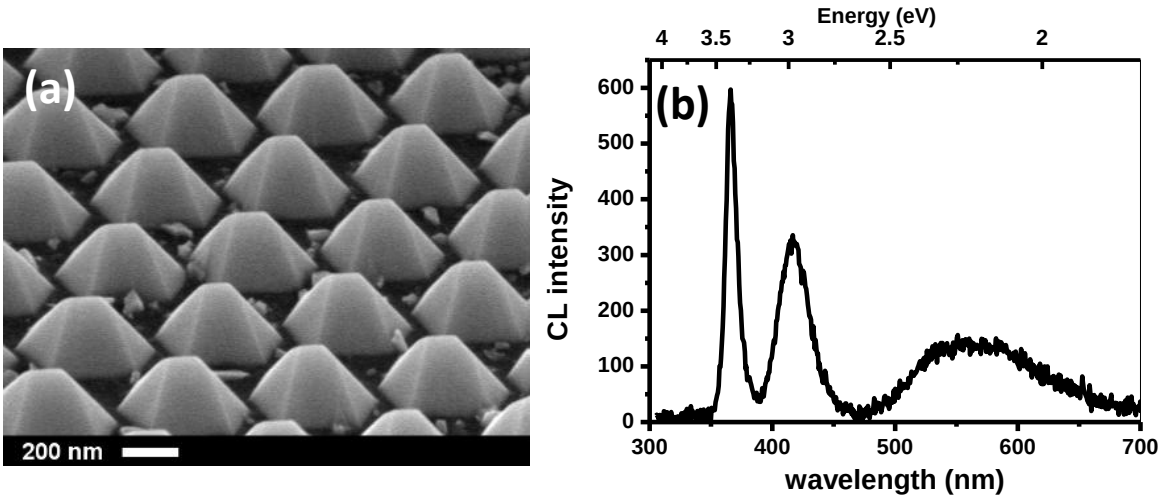

Figure 6.2 (a) GaN nano-pyramids formed by selective area growth with InGaN/GaN quantum wells on the facets (b) mean CL spectrum from a set of nanopyramids showing the different luminescence peaks

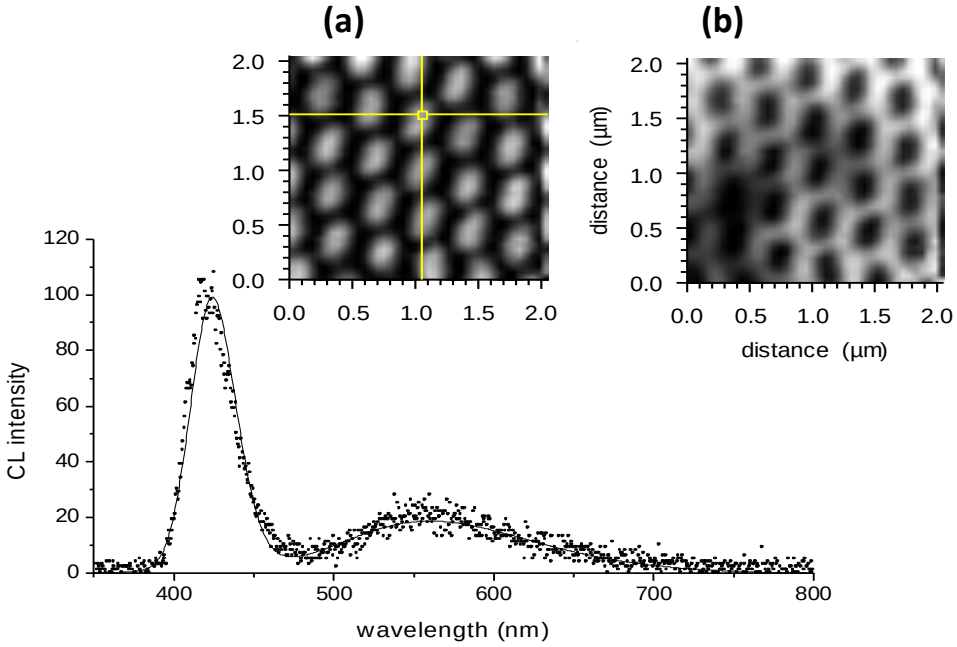

Figure 6.3 Maps of the room temperature CL intensity at 5 kV electron beam voltage for (a) the QW peak and (b) the long wavelength YB. Also shown is a spectrum measured on a nanopyramid facet.

By combining the scanning mode yielding 2D CL maps with the electron beam voltage variation, 3D details of the samples can be obtained. Voltage resolved

monochromatic CL mapping measurements had been performed on this sample by A. Šatka at International Laser Center and Slovak University of Technology, Slovakia, using their SEM-CL setup employing a photomultiplier tube as the detector. The obtained CL maps for 375, 425 and 525 nm emissions excited by electron beam voltages of 10, 5 and 3 kV are shown in Figure 6.4.

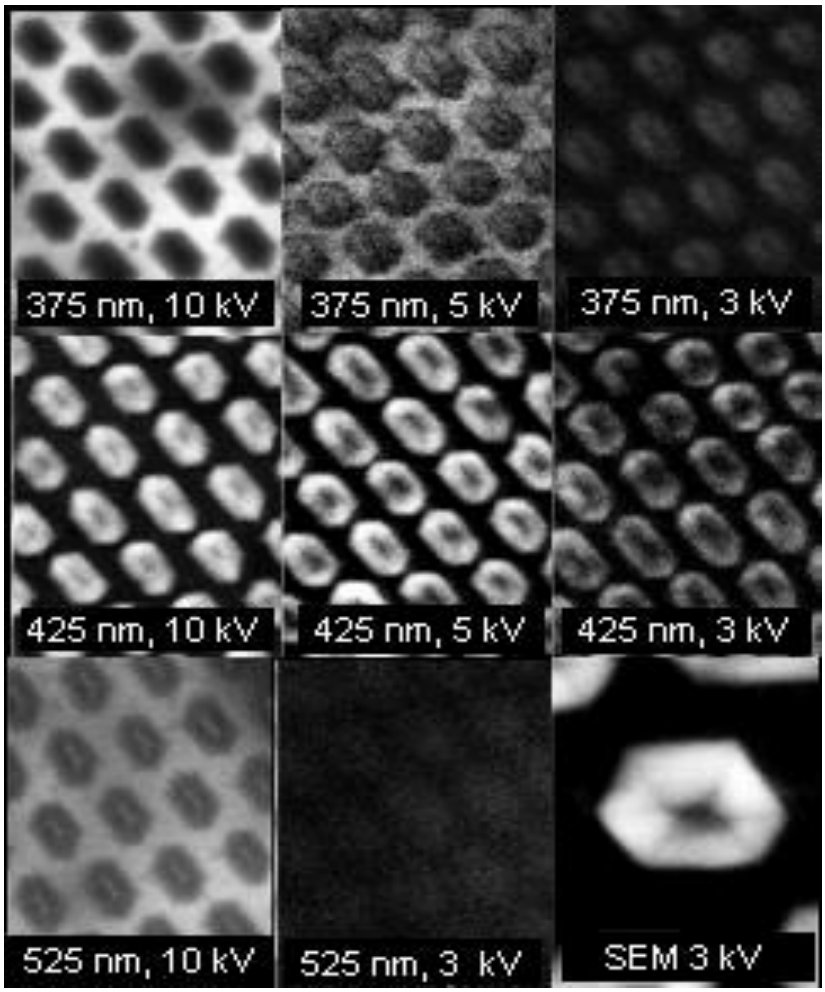

Figure 6.4 Room temperature monochromatic CL images at wavelengths of 375 nm and 425 nm for beam voltages of 10 kV (left), 5 kV (centre) and 3 kV (right)

The upper rank of Fig. 6.4 shows monochromatic CL images obtained at wavelengths of 375 nm (GaN NBE) for accelerating voltages of 10, 5, and 3 kV (left to right), the middle rank shows the 425 nm wavelength QW emission whilst the bottom row shows the defect related 525 nm emission distribution for the same beam

conditions. Monte Carlo simulations of the electron beam interaction with the sample reveal that for the 10 kV beam a majority of the electron–hole (e–h) pair generation occurs at depths beyond 100 nm in the nanopyramids and below the 100-nm-thick SiO_2 mask in the regions between pyramids. The dominant NBE and defect related emission from beneath the mask indicates carrier diffusion lengths in the GaN seed layer are shorter than the distance between the nanopyramids, i.e., <200 nm. The defect emission band has been associated with silicon [4] and possibly with oxygen related defects [5] in this case associated with the SiO_2 growth mask. Since the single QW is too thin to absorb much NBE, the low intensity of the latter clearly indicates that e–h pairs generated deep within the pyramid cores predominantly diffuse to the QW before recombining radiatively. Since this behaviour was observed for a range of beam penetration depths (accelerating voltages), this implies that the carrier diffusion lengths in the nanopyramid cores are long, i.e., the nanopyramids are formed from high quality GaN. This is confirmed by the low intensity of the defect band emission from the nanopyramids apart from a small region at their tips.

At 5 kV, the depth of the peak energy loss of the beam electrons determined from Monte Carlo simulation is <50 nm below the inclined facets of the nano-pyramids and just below the oxide in the mask regions. As a result of the significantly decreased number of e–h pairs generated in GaN beneath the mask, the overall NBE and defect-related CL intensity is lower. Also the contrast between the NBE from the nanopyramids and from beneath the mask is greatly reduced. Consequently, the QW emission still dominates the CL from the nanopyramids at this beam voltage. At 3 kV, the integrated CL from the nanopyramids is weaker still, owing to a further decrease in the injection level; however the QW emission is still clearly dominant. The electron beam now barely penetrates the mask and NBE and defect related CL is no longer observed from beneath the growth mask. No NBE or QW emission could be detected from the nanopyramid tips under any of the excitation conditions used.

The bottom rank of Figure 6.4 shows monochromatic maps of the 525 nm CL at 10 and 3 kV beam voltages and an SEM image of a single nanopyramid measured at 3 kV. The nano-pyramids contain few if any of the defects that cause the broad band emission, apart from at the tips. This emission band has been associated with

silicon [6] and possibly with oxygen related defects[13]. Both species could diffuse from the SiO_2 growth mask into the underlying GaN buffer layer. The image of the integrated CL from a typical nano-pyramid reveals there is little emission from the interfaces between the facets, yet the only evidence of any defects in the nano-pyramids is at their tips. Since QW emission dominates the luminescence from the nano-pyramids, this implies that either the structure of the QW varies or the QW is depleted of carriers towards the interfaces between facets.

Figure 6.5 maps the distribution of peak intensity and peak energy of the InGaN QW luminescence, obtained by Gaussian peak fitting to each component spectrum measured using a 5 kV electron beam. A line scan analysis performed over four adjacent nanopyramids as shown in Fig 6.5(b) shows that the QW emission energy shifts to the blue by ~60-80 meV as the beam traverses from the bottom to the top of the sampled nanopyramid facets. Given the absence of QW emission from the nanopyramid tips [Fig 6.5 (a)], a monotonic reduction in the InN fraction is thought to be the cause of the variation in QW emission energy with distance up the nanopyramids. Also, their small size is thought to limit well width variations. The alloy variation is remarkably consistent from pyramid to pyramid, confirming that the nanoscale self-assembly growth process produces dense, uniform arrays of semi-polar oriented QWs that efficiently emit light. More discussion on this QW energy variation is given in the following sections. The FWHM distribution of the QW emission is uniform across individual pyramids and also from pyramid to pyramid with values in the range 200-220 meV. This FWHM is comparable to that reported for semipolar InGaN QWs emitting in the similar wavelength region and fabricated on micron scale sized GaN pyramids [7-9]. Keyan et al and Yu et al reported semipolar InGaN QWs on the nanofacets of GaN pyramids having base lengths of 200-250 nm and 60 nm respectively. The linewidth of QW emission from these structures were respectively 300 and 430 meV [10, 11]. The lower FWHM of the QW emission from the 1969 SQW sample imply their better quality and the alloy homogeneity.

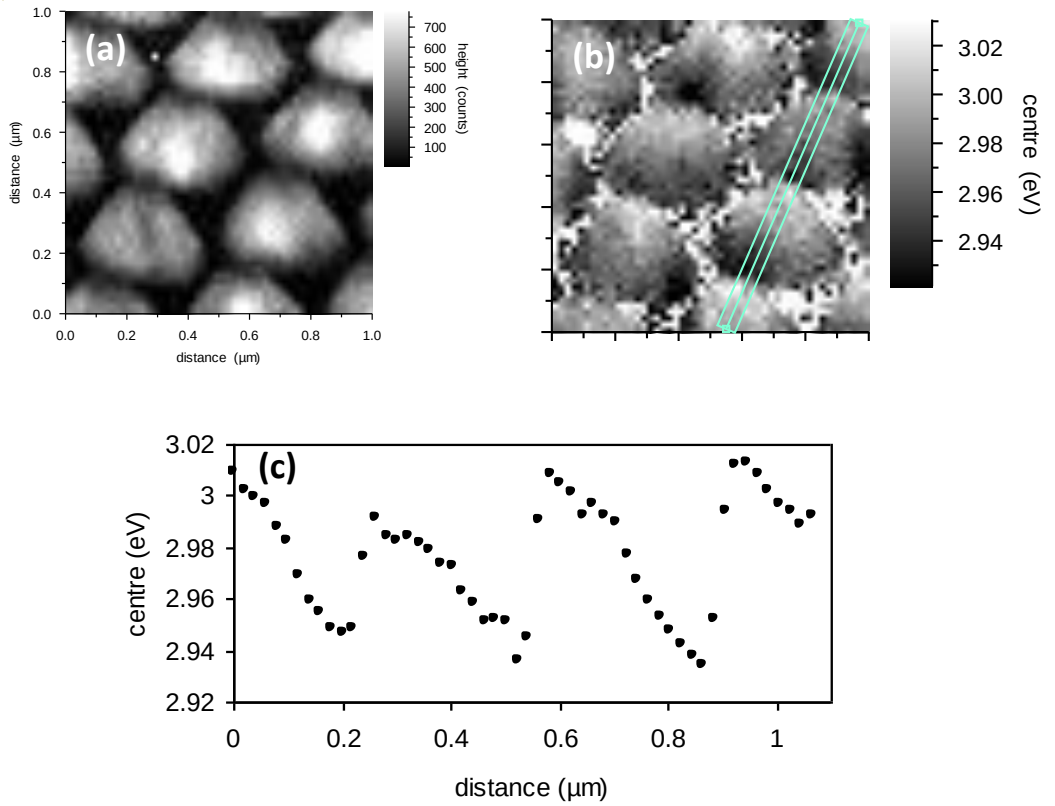

Figure 6.5 InGaN QW (a) emission intensity and (b) peak energy CL maps obtained by nonlinear least square Gaussian fitting to individual CL spectra from 5 kV hyperspectral CL map (c) QW emission energy variation across the nanopyramids for the line scan shown in Fig 6.5 (b).

6.3.1(b) Set II: (2135-2138 SQW) : Si-doped GaN nanopyramids

The nanopyramids in this series are not elongated as that of 1969 SQW sample as discussed in section 6.3.1(a). Fig 6.6 shows the secondary electron image of a typical thin capped QW sample (2138 SQW) fabricated on the GaN nanofacets. The areal density of SAG GaN nanopyramids is $7x10^8/cm^2$. The facets of the GaN nanopyramids are smooth, similar to that of 1969 sample. Debris on the SiO_2 mask is hardly seen for these samples and thus growth on mask has been effectively suppressed. The pyramidal tops are pointed for this series of samples in contrast to the elongated tops for the 1969 SQW sample.

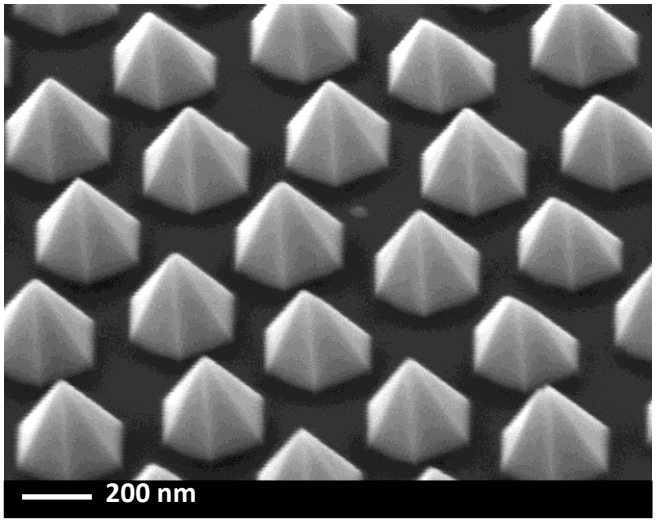

Figure 6.6 Typical SEM image of GaN nano-pyramids formed by SAG self-assembly with InGaN/GaN quantum wells on the facets grown at temperature of 845^0C (2138 SQW)

Fig 6.7(a) shows the low temperature (LT) (16 K) PL spectra of the samples as a function of their growth temperature. The room temperature as well as low temperature PL spectra collected from an area comprising a large number of nanopyramids have three main peaks similar to that of 1969 SQW sample, (1) peak at ~ 360 nm corresponding to GaN NBE (2) peaks in the wavelength range 400-480 nm originating from the InGaN QWs and (3) a peak at ~570 nm corresponding to yellow band emission. LT PL spectra also resolve peaks at 378 nm (3.28 eV) corresponding to GaN donor- acceptor pair emission and its first longitudinal optical phonon emission at 387 nm (3.2 eV) appearing as a shoulder emission. Fig 6.7(b) shows the spatially averaged CL spectra collected from a 2 x 2 μm^2 area of the samples. Multiple QW emission peaks are observed for the lower temperature (815 and 825 ^{0}C) grown samples. These features are not resolved in the QW PL spectra, where the luminescence signals are collected from a larger area of the sample (~ 15 µm spot size). The spatial distribution analysis of the QW emission across the nanopyramids is performed on these samples using the high spatial resolution CL setup (described later on) in order to assess the spatial origin of these multiple peaks in the QW emission region. The behaviour of QW emission wavelength as a function

of growth temperature can be seen in Fig 6.8. The blueshift in QW emission peak with increase in growth temperature is consistent with the decreasing InN composition in the InGaN QWs.

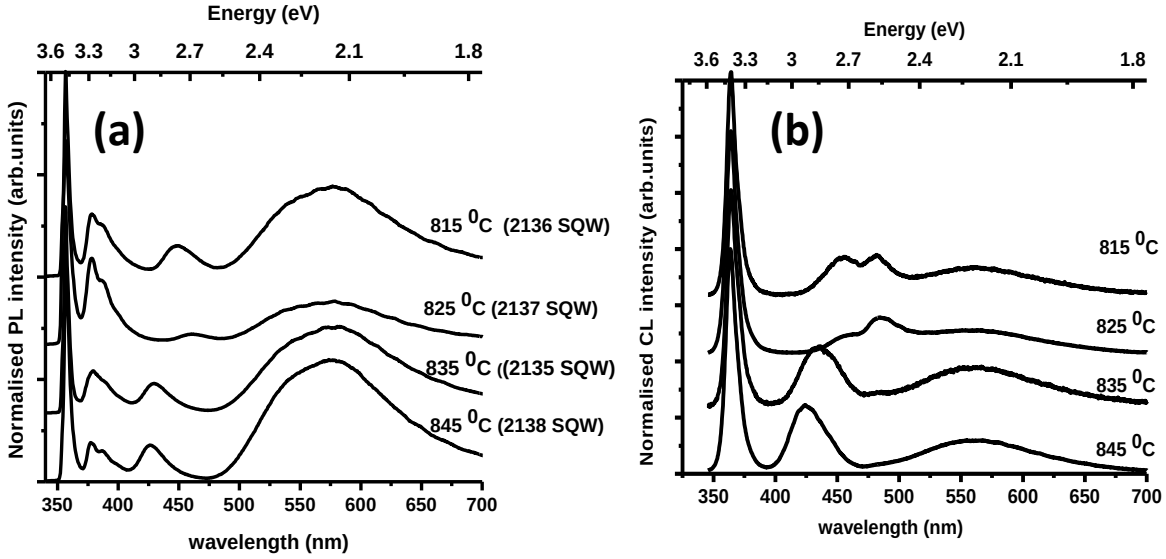

Figure 6.7(a) Low temperature (16 K) PL spectra and (b) spatially averaged normalized RT CL spectra of set II semipolar InGaN QW samples at room temperature as a function of QW growth temperature

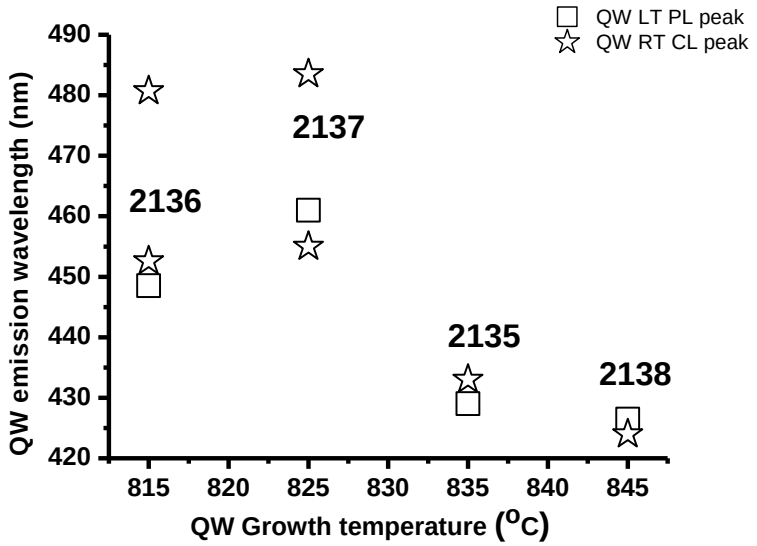

Figure 6.8 Growth temperature dependence of QW emission wavelength of the samples under optical (PL) and electron (CL) beam excitation

Nonlinear least square curve fitting of the individual InGaN QW CL emission peak by Gaussian function is carried out to obtain the emission intensity, energy and FWHM spatial distribution. Fig 6.9 shows such a spatial distribution of different peak parameters for QW emission from a 1.5 x 1.5 μm^2 area of the 2138 SQW sample. The QW emission at ~ 425 nm is observed only from the pyramid facets implying its selective growth [Fig.6.9 (a)]. The QW peak energy distribution map [Fig 6.9 (b)] reveals that the InGaN QW emission energy blueshifts as the electron beam scans the nanopyramids from bottom to top and this observation is similar to that of 1969 SQW sample. The FWHM of the QW emission is ~ 230 meV [Fig 6.9(c)]. The behaviour of the CL emission is the same for the other three samples in this series as well. The amount of blueshift in QW emission energy as the electron beam scans from bottom to top of the nanopyramid ranges from 50-110 meV and the FWHM of the QW emission from 190-240 meV for this sample series [Table 6.2]. This QW emission energy shift and FWHM distribution is found to be consistent from pyramid to pyramid for CL mapping carried out from different regions of the sample and demonstrate the uniformity of the self assembly process. Similar nonlinear least squares fitting procedure applied to GaN NBE emission using Voigt functions reveals that the FWHM of the GaN nanopyramid is smaller than from the GaN template layer implying the high material quality of the nanopyramids. Intensity spatial distribution maps for YB emission shows a lower intensity from the pyramidal structures compared to the underlying GaN nucleation layer implying reduced defect concentration in the pyramidal structures.

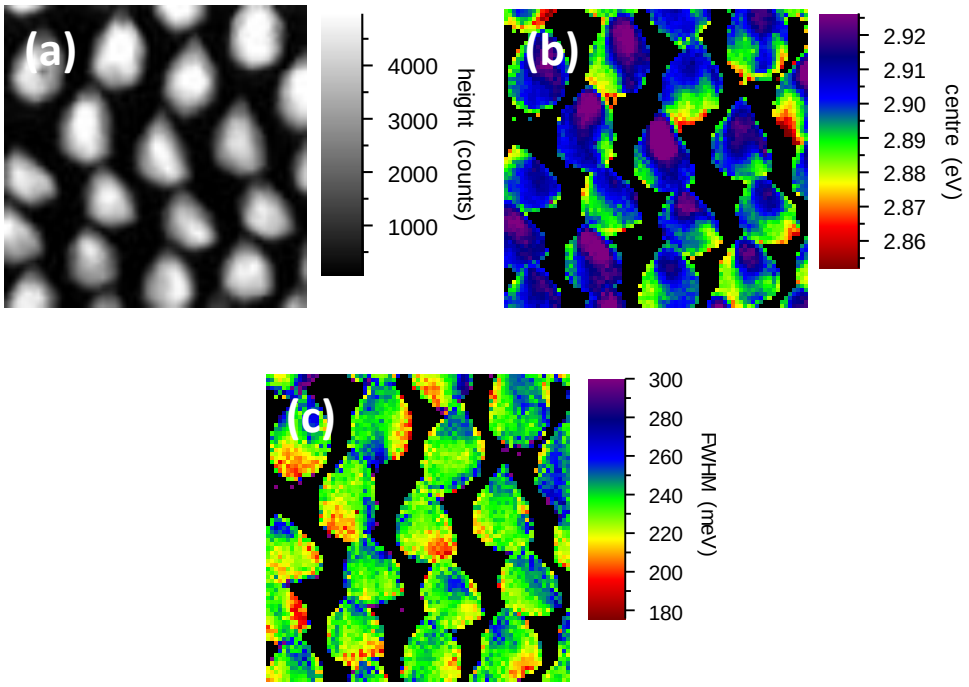

Figure 6.9 InGaN QW (a) peak emission intensity, (b) peak energy and (c) FWHM CL maps obtained by nonlinear least square Gaussian fitting to individual CL spectra from 5 kV hyperspectral CL map. All images are 1.5 x 1.5 µm.

The spatial origin of the double peaks in the wavelength range 430- 500 nm for the samples 2136 SQW and 2137 SQW is obtained by Gaussian nonlinear curve fitting of the individual peaks from their CL hyperspectral data. For both samples their intensity distribution CL maps [Figure 6.10 (a)-(d)] show that these emissions come from nanopyramids and the spatial distribution is different for different peaks. While the intensity spatial distribution of emission at ~ 450 nm (2.8 eV) is uniformly distributed across the pyramid facets, the emission at 484 nm (2.6 eV) shows variation in spatial distribution with lesser intensity towards the top region of the pyramidal structures. This multiple emission from QWs can be due to QW potential variation due to InN composition fluctuation or thickness variation.

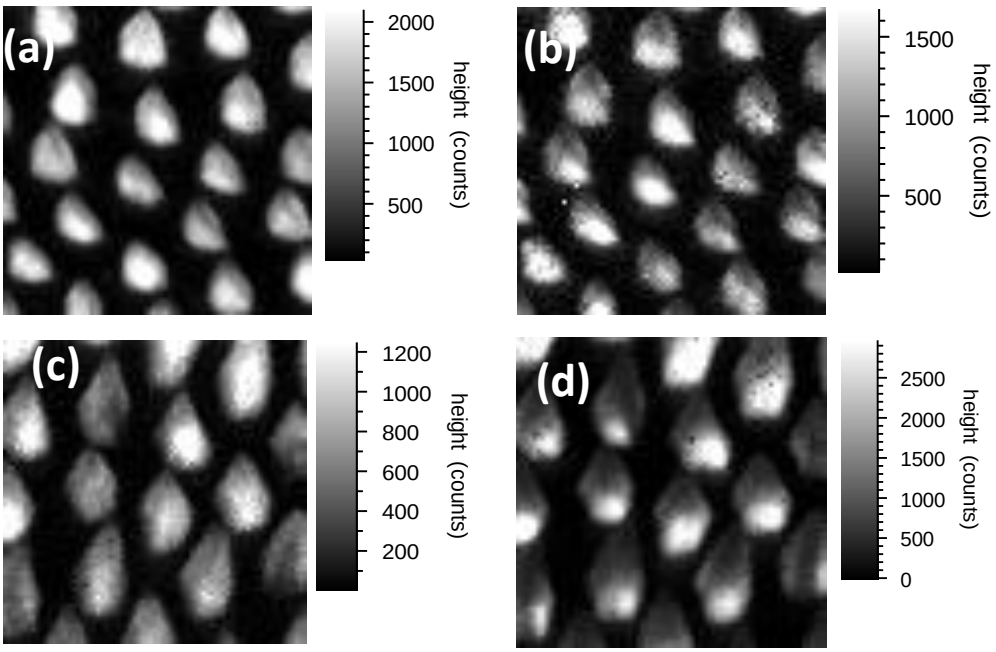

Figure 6.10 Spatial distribution of multiple QW emission intensity for the samples (a) 2136 @ 451 nm (b) 2136 @ 484 nm (c) 2137 @ 452 nm and (d) 2137 @ 484 nm. All images are 1.5 x 1.5 µm.

6.3.1(c) Set III: (2321-2344 SQW): Si-doped GaN nanopyramid

This sample series is similar to that of set II with the exception of a thicker p-type GaN cap layer (~110 nm) and double thickness QWs compared to set II of samples. Hence to extend the electron beam interaction volume to the QW region, these samples are probed by a slightly higher electron beam voltage than used for the previous set of samples. Fig 6.11 shows the secondary electron image of the sample 2344 SQW obtained for 6 kV electron beam voltage. The nanopyramids are slightly larger for this series compared to set II and smaller than set I. The nanopyramids are uniform in size and shape with the growth on the mask region effectively suppressed and with smooth facets. The areal density of the nanopyramids is 8 x $10^8$$cm^{-2}$.

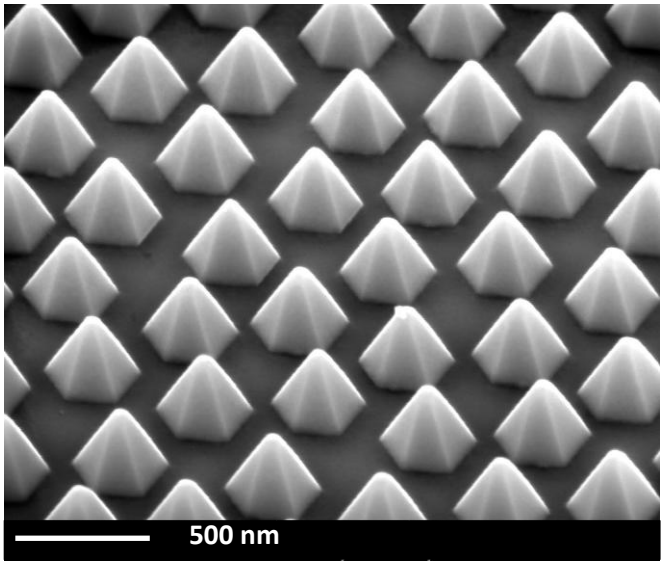

Figure 6.11 Secondary electron image of the 2344 SQW nanopyramid sample

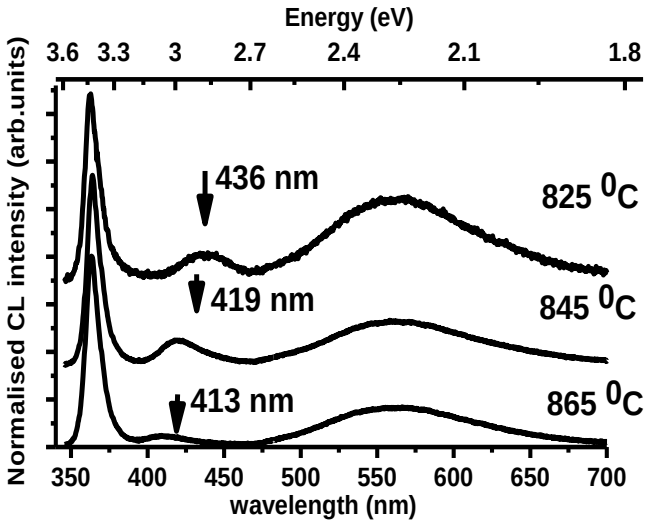

Figure 6.12 Spatially averaged RT CL spectra as a function of InGaN QW growth temperature

Figure 6.12 shows the spatially averaged CL spectra from an array of nanopyramids. In addition to the QW emission peaks around 400-450 nm, the GaN NBE and yellow band emissions can be seen. The spectral position of the QW emission obtained in PL and CL spectroscopic measurements match well and no additional QW peaks are resolved in CL measurements as in 2136 and 2137 SQW of

set II. Though the QWs are twice as thick compared to set II, their lower intensity may be due to the thick p-GaN cap absorbing the incident exciting beam or the high growth temperature of the p-GaN cap might have deteriorated the quality of the QWs. The CL maps corresponding to the intensity of NBE, QW and YB emissions are found to be similar to set I and set II. Defect related YB emission is observed from the tips of the nanopyramids in addition to its intense emission from the GaN nucleation layer.

Depth resolved CL measurements are performed for these samples using electron beam acceleration voltages 2, 5 and 7 kV respectively. The electron beam voltage dependent luminescence behaviour of each of the emission peaks (GaN NBE, InGaN QW, and YB) is similar to that obtained for the 1969 SQW series and can be explained by similar arguments. Nonlinear least squares Gaussian fitting is applied to the QW luminescence to study the spatial distribution of peak intensity, peak energy and FWHM. Considering the QW emission energy variation, the samples 2321 and 2335 SQW exhibit a blueshift as the electron beam scans from bottom to top of the nanopyramid, similar to the behaviour shown by the set I and set II samples. However the sample 2344 SQW with the QWs grown at a higher temperature of 865^0 C shows a redshift in QW emission energy as the electron beam scans from bottom to top of the nanopyramid [Fig 6.13(a)]. This is further evidenced by a line scan analysis across the nanopyramids as shown in Fig 6.13 (b). The exact reason for the QW emission redshift for this sample is not known at this point.

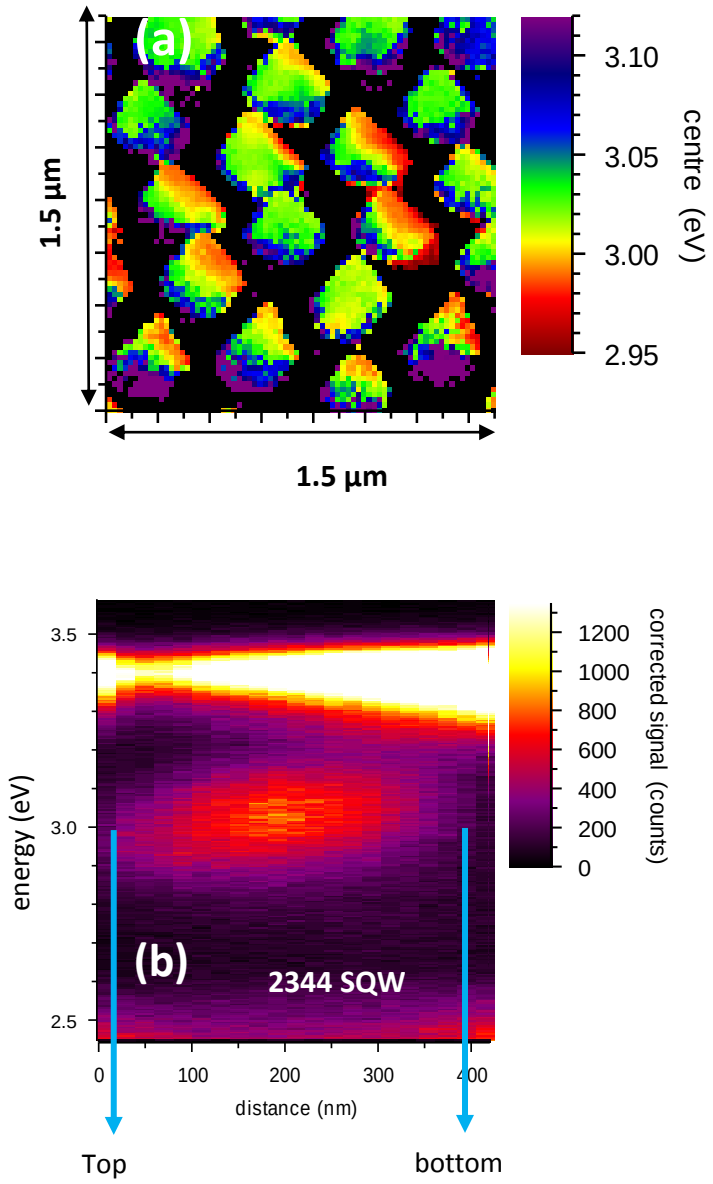

Figure 6.13 (a) Spatial distribution of InGaN QW emission peak energy for the 2344 SQW (b) The line spectra of QW emission energy obtained from line scan analysis across a single nanopyramid for sample 2344 SQW.

6.3.2 Spatial mapping of single nanopyramid

The high spatial resolution of the SEM-CL set up and the intense InGaN QW emission from the samples permit the mapping of QW emission from a single nanopyramid. Figure 6.14(a)-(d) show typical images from such a CL hyperspectral

imaging and the corresponding secondary electron image. The mean CL spectrum [Figure 6.15(a)] collected from a single nanopyramid consists of three emission bands corresponding to GaN NBE, InGaN QW and yellow band, similar to that of array of nanopyramids. The intensity spatial distribution maps [Fig 6.14(b)-(d)] show that the QW emission mainly originates from the nanopyramids while the GaN NBE and the yellow band emission from the area between the nanopyramids. Yellow band emission can also be observed from the tip of the nanopyramid as mentioned above. The blueshift in QW emission peak energy as the electron beam scans from bottom to top of the nanopyramid is shown in the line spectrum analysis given in Fig. 6.15(b). Table 6.2 summarises the QW emission characteristics such as emission energy, FWHM and peak energy shift from bottom to top of nanopyramid for all the three sets of semipolar InGaN QW samples.

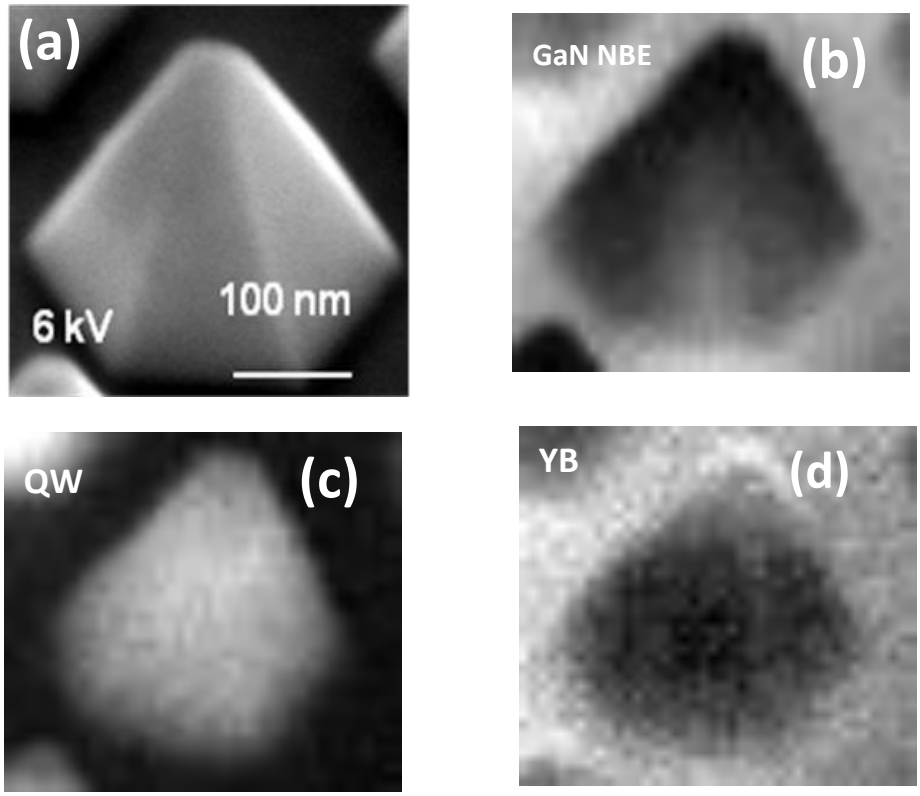

Figure 6.14 (a) Scanning electron image of a single nanopyramid [2335 SQW] (b) integrated intensity of GaN NBE emission (c) integrated intensity of QW emission (d) integrated intensity of YB emission from the single nanopyramid. Images b, c,d are 0.35 μm x 0.40 μm

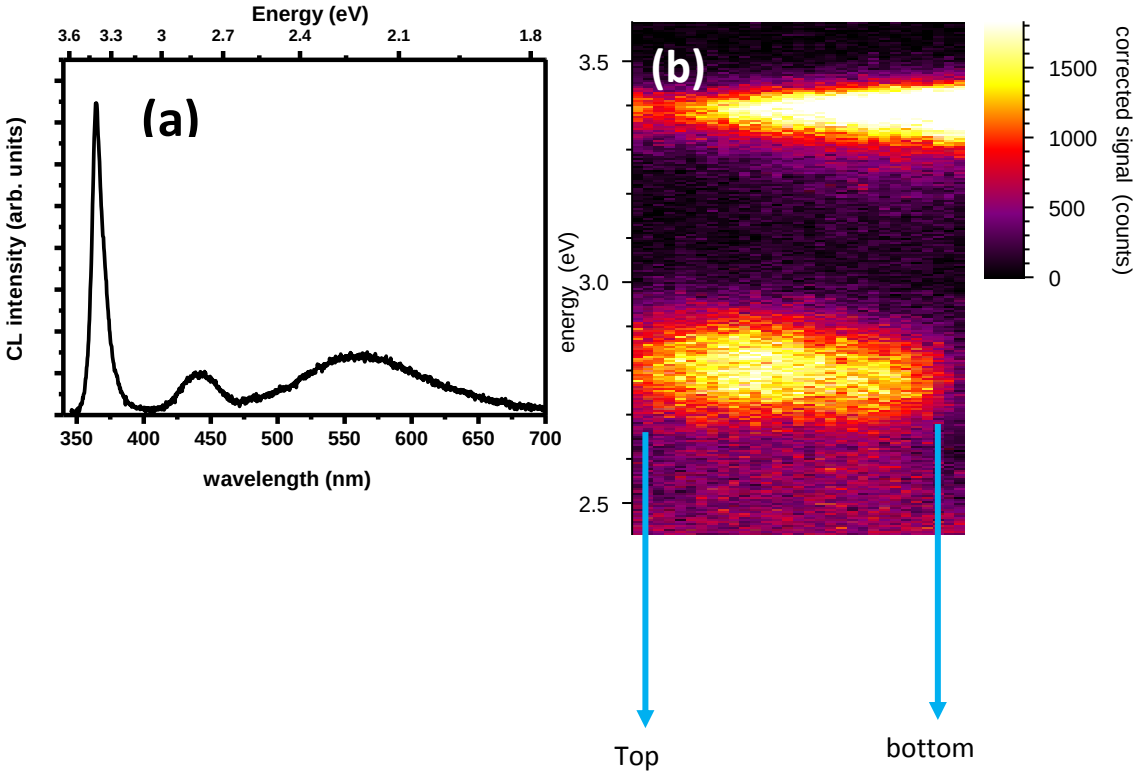

Figure 6.15(a) Mean CL spectrum from a single nanopyramid (b) the line spectra of QW emission energy obtained from line scan analysis across a single nanopyramid for sample 2335 SQW.

According to previous reports of InGaN QW fabrication on the facets of GaN micro-pyramidal structures, a red shift in QW emission energy is observed as the electron beam scans from bottom to top of the pyramid [12-14]. However in the present case of QWs on GaN nanofacets, all of the samples except 2344 SQW exhibit a blueshift in emission energy as the electron beam traverses from bottom to top of the nanopyramids. Contrary to micron-scale pyramids, the small size of the nanopyramids is thought to limit the temperature gradient effects (which may affect InN incorporation and QW thickness) across the nanopyramid facets. These observations provide clear evidence that the rate of InN incorporation into the InGaN QWs grown on closely separated nano-pyramids of the type described in this work differs from that observed on micro-pyramidal structures [14-17]. With closely packing of the pyramids, differences in the adatom diffusion lengths will have little effect on InN incorporation into the QW. Instead, the reactor ambient conditions will govern the InN mole fraction. This will impact on applications of luminescent, semi-

polar pyramidal structures in light emitting devices [18]. Unlike earlier work [12, 13] on larger, widely spaced pyramidal structures, there is no clear evidence of quantum dot (or wire) formation.

Table 6.2 Summary of semipolar InGaN/GaN QW emission characteristics

sample	main QW peak energy	main QW FWHM (meV)	Blue vs redshift + size of shift (meV) (bottom to top of nanopyramid	Nanopyramid GaN NBE FWHM (meV)
Set I				
1969 SQW	2.95	200	Blueshift ~60-80	75-85
Set II				
2136 SQW	2.74	230	Blueshift ~60	65-75
2137 SQW	2.73	190	Blueshift ~60	80-90
2135 SQW	2.85	240	Blueshift ~70	70-80
2138 SQW	2.94	240	Blueshift ~ 50	85-95
Set III				
2335 SQW	2.8	240	Blueshift ~70	80-90
2321 SQW	2.93	250	Shift not clear. Blue shift for a few pyramids	70-75
2344 SQW	3.02	300	Redshift ~110	80-86

6.3.3 CL emission as a function of excitation current

The excitation current dependence of the InGaN QW CL emission is studied using the CL set up attached to the EPMA [Fig.6.16(a)-(c)]. For this measurement, the electron beam is defocused to 2 μm and in order to check there is no damage caused by the electron beam on the CL spectra of the QW structures, spectra measured at the same spot are compared with those spectra measured at different spots located a

certain distance away. The electron beam voltage used is 5 kV and the excitation current is varied from 0.5 nA to 120 nA.

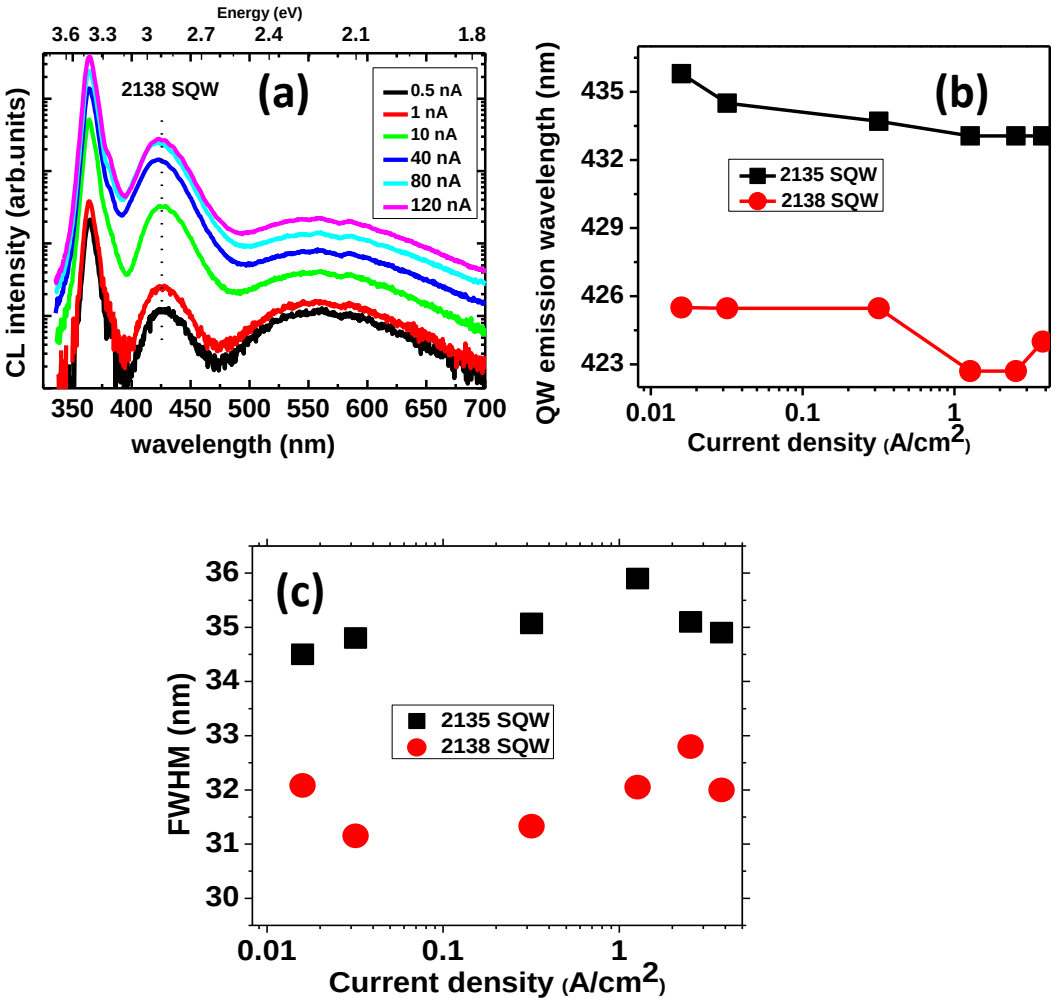

Figure 6.16 (a) CL emission spectra of the sample 2138 SQW as a function of electron beam current (b) QW emission wavelength as a function of excitation current density for samples 2135 and 2138 SQW (c) FWHM of the InGaN QW emission as a function of excitation current density

As shown in Fig.6.16(b) & (c), the variation in both QW emission peak energy shift and the FWHM are very small (< 2-3 nm). A similar small QW peak shift has been previously reported for {10$\underline{1}$2} and {10$\underline{1}$1} semipolar InGaN QWs [1, 7] fabricated on the microfacets of GaN pyramidal stripes and mixed [{10$\underline{1}$1} and {10$\underline{1}$2}] semipolar InGaN QWs [11] fabricated on the nanofacets of GaN pyramids. The

characteristic blueshift of emission from InGaN QWs fabricated in the polar c-direction is attributed to the screening of piezoelectric field caused by the increased carriers accumulated in the wells with increasing excitation power and is a measure of the internal electric field existing due to spontaneous and piezoelectric polarization effects as discussed in Chapter 2. The very small QW emission blueshift and only a slight increase in FWHM with increase in excitation current indicate the reduced in-built electric field experienced by these QWs on the semipolar nanofacets of GaN. The slight redshift in QW emission wavelength for the sample 2138 SQW at high excitation current density can be due to electron beam induced heating effects. A similar excitation current dependent QW emission shift investigation for 2335 and 2344 SQW samples yielded similar results.

6.3.5 PL spectroscopy

Temperature dependent PL emission properties of InGaN QWs are investigated for all the three sets of semipolar samples for temperatures ranging from 16 to 300 K. Figure 6.17 (a) and (b) show the temperature dependence of the PL spectra for the sample 1969 SQW along with its QW peak energy shift as a function of temperature. Similar plots of QW emission energy as a function of temperature for 2321 SQW and 2138 SQW for the temperature range of 15 to 300 K are shown in Fig. 6.17 (c) and 6.17 (d). The QW emission peak energies in these plots are obtained by fitting the QW emission spectra with Gaussian functions. As seen, a monotonic decrease of InGaN QW emission enegy with temperature is observed for all samples. No S-shape energy variation with temperature is seen as usually reported for c-plane grown InGaN QWs. This suggests the absence of significant carrier localisation effects on the QW emission properties. A similar observation of the absence of S-shape dependence of InGaN QW emission energy on temperature for the semipolar {10$\underline{1}$1} InGaN QWs fabricated on GaN micropyramid facets are reported by Yu et al [7].

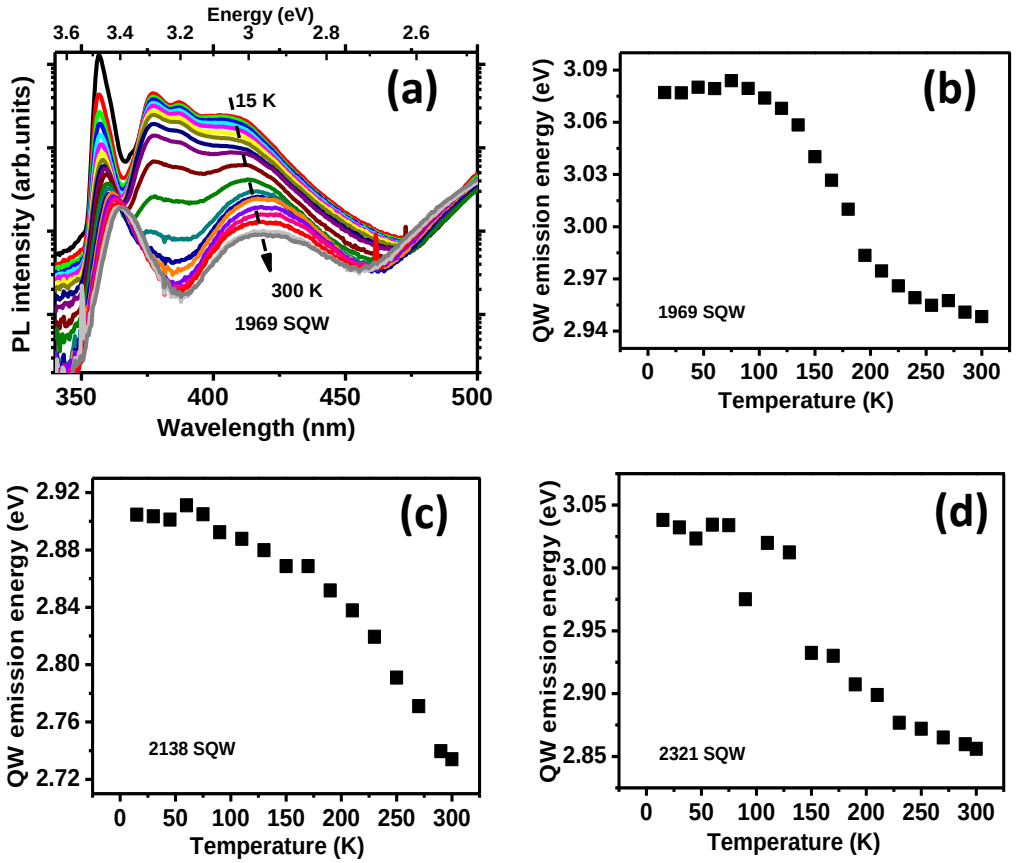

Figure 6.17 PL spectra of 1969 SQW as a function of temperature (from 15 K to 300 K in steps of 15 K). The temperature dependent InGaN QW peak position for the sample (b)1969 SQW (c) 2138 SQW and (d) 2321 SQW

In the case of polar c-plane grown InGaN QWs, the anomalous blueshift in QW emission energy in the temperature range of 100- 150 K is believed to originate from localised tail states induced by inhomogeneous distribution of indium in InGaN layers [19] or from the QCSE induced by a large in-built electric field [20] or from the combination of both effects [21]. Since for the semipolar {10$\underline{1}$1} orientations which makes an angle of 62^0 with polar c-direction have reduced in-built electric field which is further confirmed by the above mentioned excitation current dependent studies, the result shown in Fig 6.17 (b)-(d) possibly indicate a dominant contribution of QCSE in the S-shape behaviour of polar c-plane InGaN QWs. Now considering the InN incorporation and ad-atom mobility in different crystallographic orientations of GaN such as {10$\underline{1}$1} and {0001}, it is reported that the {10$\underline{1}$1} semipolar plane

is the thermodynamically most stable plane in terms of InGaN MOCVD growth conditions [22] and hence the absence of anomalous blueshift might also indicate the absence of localisation effect induced by inhomogeneous distribution of InN.

6.3.6 Effect of strain in GaN on InGaN QW emission shift

An attempt has been made to investigate the effect of the strain in the GaN on the InGaN QW emission peak energy shifts as the probing electron beam scans the nanopyramids from bottom to top. The basis of this analysis is the CL maps showing the distribution of peak energy of GaN NBE and InGaN QW emission. These are obtained by Voigt (for GaN NBE) and Gaussian (for QW emission) curve fitting to the CL hyperspectral data. At the start, a line scan is performed on intensity distribution maps, scanning from base to top of nanopyramids and including the appropriate pixels. Then the same pixel coordinates are loaded onto their energy distribution maps. A line scan of 4 pixel width is employed in this analysis. Samples from set I and II are mainly included in this study as the thick p-type GaN cap layer in set III samples makes them more complex to investigate. Figure 6.18(a) and (b) show the fitted centre energy CL maps for the QW and GaN NBE emissions with the numbers over the investigated pyramids. GaN NBE energy distribution CL map and line scan analysis across the nanopyramid revealed that the GaN pyramids are under tensile strain. This can be due to the Si doping of the GaN nanopyramids as described in the sample specification section. Figure 6.18(c) and (d) show two typical line scan analyses for the GaN NBE and QW emission energies and represents the typical behaviour. The InGaN QW peak energy appears to follow that of the GaN NBE emission which is simply related to the GaN strain state. The blueshift of the InGaN QW emission peak and the decrease of tensile strain in GaN, though small, is evident from the plots of Fig 6.18 (c) and (d). The InGaN layer is under compressive strain. In the case of samples in set II, the tensile strain in the GaN resulting from intentional Si doping might be reducing the compressive strain in InGaN, thus permitting more InN to be incorporated. Towards the base of the GaN nanopyramids, there is a possibility of enhanced Si doping accelerated by the unintentional Si doping from the SiO_2 mask materials leading to more InN content in the InGaN QW towards the bottom.

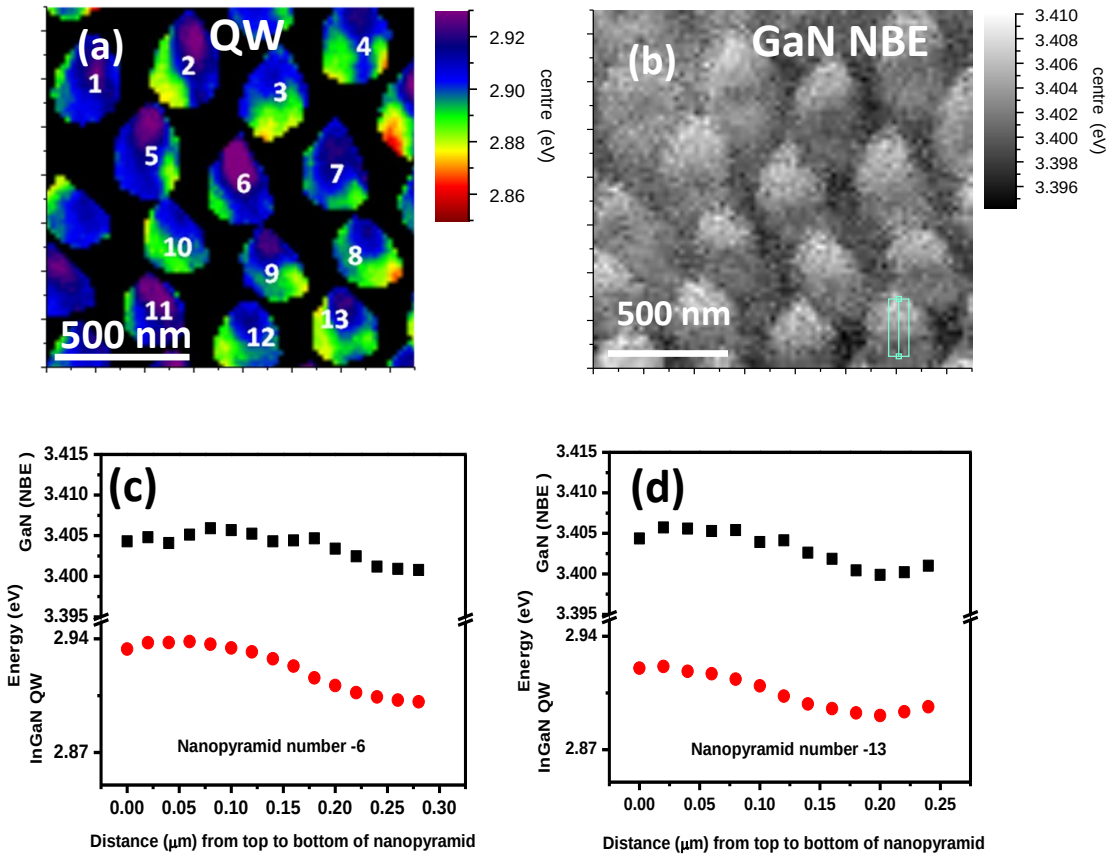

Figure 6.18 (a) QW energy distribution map and (b) GaN NBE energy distribution map for the sample 2335 SQW (c) Energy variation of QW and NBE emission as a function of distance from top to bottom of the nanopyramids numbered 6 and 13.

For the 1969 SQW sample, the energy variation of InGaN QW emission and GaN NBE emission follows the same pattern as the electron beam scans the nanopyramid from bottom to top [Fig 6.19]. The source of the increase of tensile strain within the GaN nanopyramids towards the bottom is possibly the Si doping from the SiO_2 mask material.

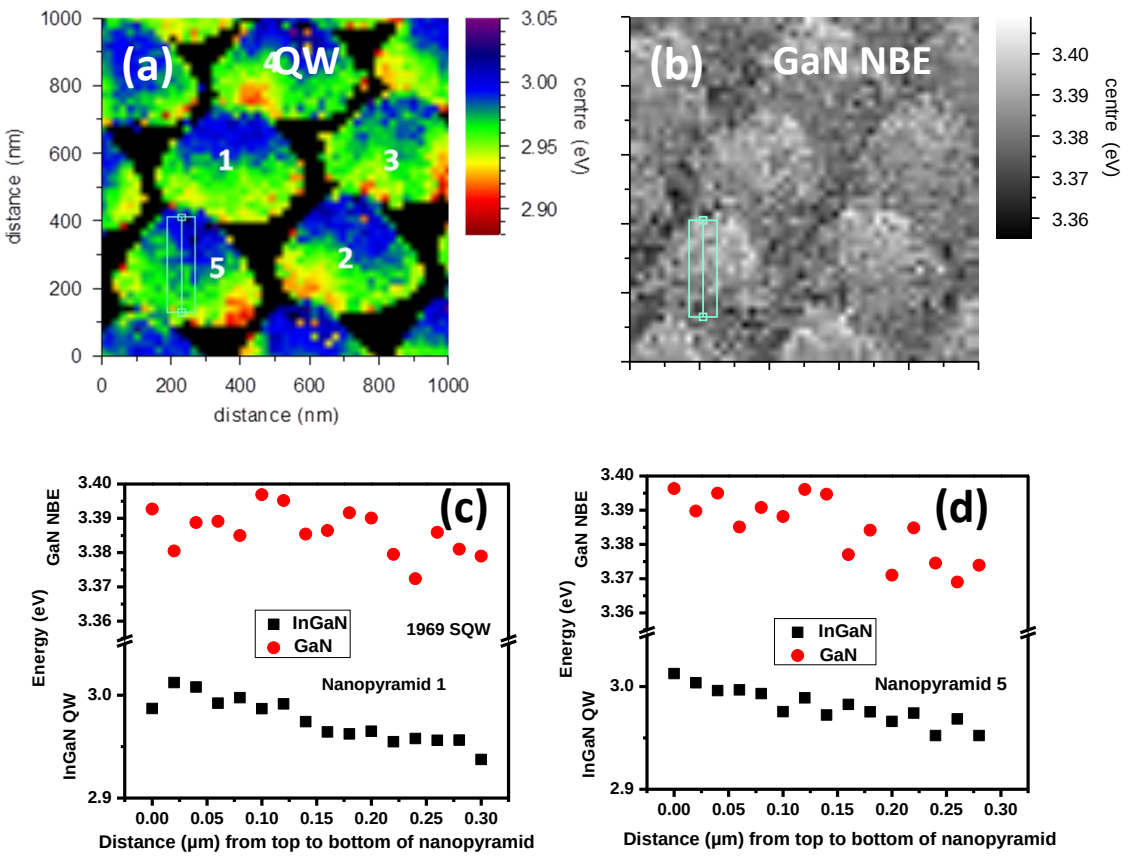

Figure 6.19 (a) QW energy distribution CL map and (b) GaN NBE energy distribution CL map for the sample 1969 SQW (c) Energy variation of QW and NBE emission as a function of distance from top to bottom of the nanopyramids numbered 1 and 5. Image (b) has the same scale as (a).

In the case of InGaN QWs fabricated on the facets of micron scale sized pyramids, the redshift in QW emission energy towards the top of the nanopyramid is thought to be due to the temperature gradient effects leading to QW well width and increased InN incorporation towards the top and these large size effects may be dominating the Si incorporation effects to the GaN pyramids from the SiO_2 mask if any. However, in the case of the GaN nanopyramids, their small size makes the temperature gradient effects to the QWs negligible and the reactor ambient conditions governing the InN mole fraction and the Si incorporation effects from the SiO_2 masks, the predominant factors affecting the InGaN QW properties.

6.3.7 2458 SQW sample

So far the the semipolar InGaN QWs fabricated on the nanofacets of GaN pyramids have been discussed. It would be advantageous if nanoscale selective area growth technique could be applied to nonpolar III-nitrides as well. There are not many reports on nonpolar InGaN QWs fabricated on nanometre scale 3D GaN templates. Fichtenbaum et al have reported the fabrication of nonpolar/semipolar InGaN/GaN QWs on nano-patterned 3D GaN templates. Their study was mainly focused on structural characterisation and there was no detailed discussion of their optical properties [23]. Here, we report the optical properties of nonpolar m-plane InGaN SQWs on the facets of 3D GaN nanostructures realised by selective area growth. The novelty of the approach lies in the nanoscale selective area growth on a-plane GaN. Figure 6.20 gives orientation of GaN 3D structures with respect to sapphire (1$\underline{1}$02) r- plane.

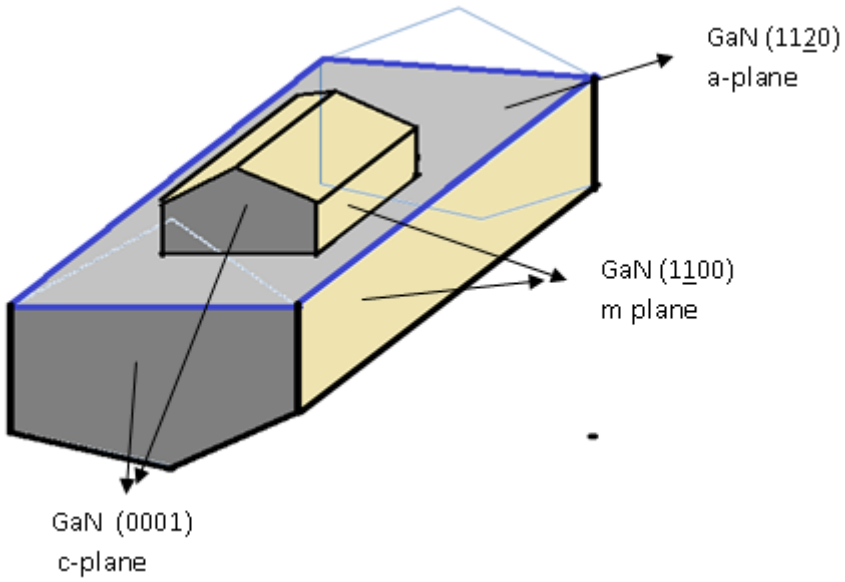

Figure 6.20 Orientation of a-plane GaN 3D structures on a-plane GaN template

The secondary electron image of the facetted 3D GaN nanoscale structures used for the growth of nonpolar InGaN QWs is shown in Figure 6.21(a). The formation of the different shapes and specific facets of the 3D GaN structures can be accounted for by the different growth rates and surface migration of adatoms in *a*, *m* and c- directions,

influenced by MOCVD growth conditions (determined by growth temperature and pressure) and the mask design [22, 24]. Based on the previous experimental reports on micron scale structures, the InN incorporation in InGaN QWs would take place at different rates depending on the facet type [22, 25]; however there are no such reports on nanoscale structures. The spatially averaged RT CL spectrum [Fig. 6.21 (b)] collected from an array of 3D nanoscale structures from an area of 1.5 x 1.5 μm^2 of the sample clearly shows intense QW emission in the blue wavelength region.

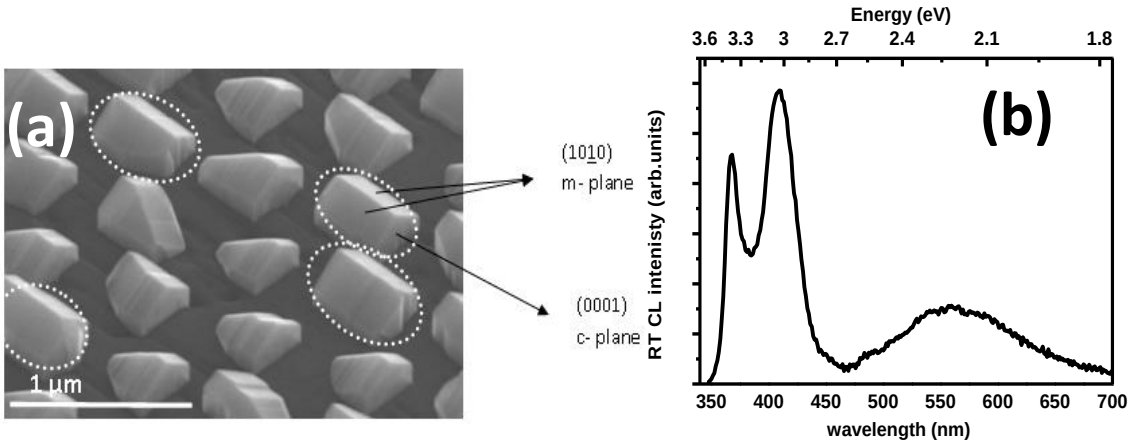

Figure 6.21 (a) Secondary electron image of the nanoscale 3D GaN templates used for the fabrication of InGaN/GaN SQW (b) spatially averaged CL spectrum from a 1.5 x 1.5 μm^2 area of the sample.

High resolution SEM-CL measurements are performed on a single 3D nanostructure to get locally resolved information on the QW emission properties. Figure 6.22(a) and (b) show the secondary electron image of a single 3D facetted structure and its integrated intensity CL map respectively. Figure 6.22 (b) indicates that the corners of the structures give brighter luminescence compared to other regions. The integrated intensity CL map for QW emission [Fig 6.22 (c)] revealed that the brighter corners are solely associated with QW luminescence. This can be due to the light escape cone of the QW emission from the 3D GaN nanostructures after undergoing multiple reflections inside it, resulting in more emission at the corners. The suggestion is based on the geometry of 3D GaN structures having smooth facets permitting total internal reflection and the possibility of existence of optical modes inside the 3D nano-cavities [26].

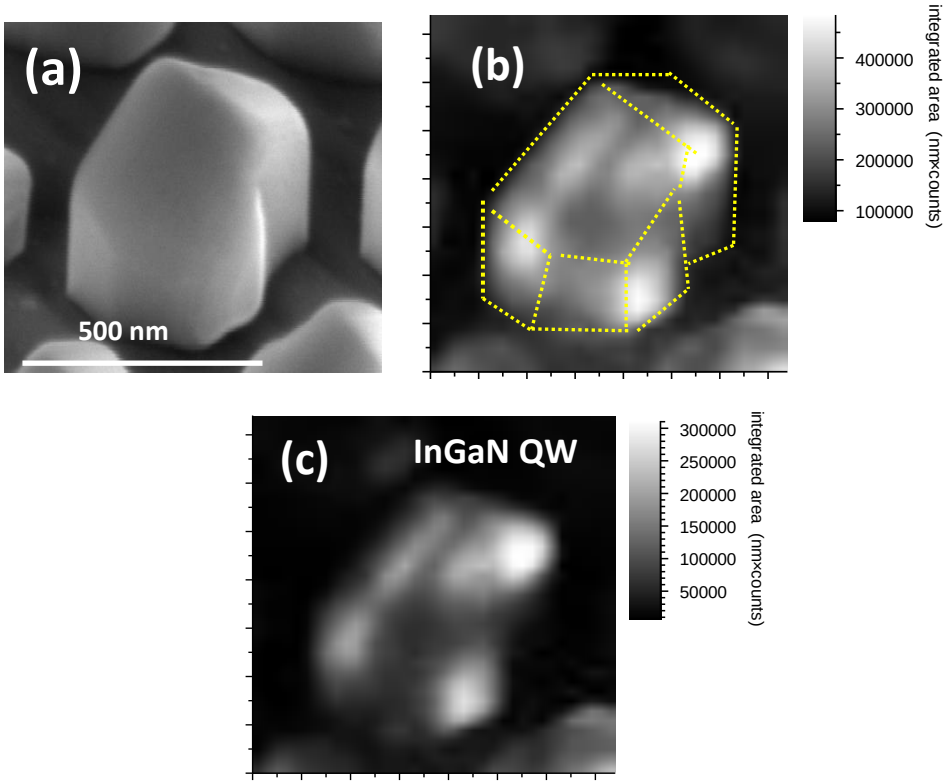

Figure 6.22 (a) Secondary electron image of a single 3D facetted structure (6 keV electron beam energy) (b) the corresponding integrated intensity CL map (c) InGaN QW emission intensity distribution CL map. Images (b) and (c) are 0.75 x 0.75 µm.

The CL emission of the sample is studied as a function of excitation current density [from 0.004 to 5 A/cm^2] using the CL set up attached to the EPMA [Fig. 6.23]. Since the CL excitation and light collection geometry are in plan-view mode in EPMA CL set-up, the QWs fabricated on the top facets (the *m*-plane and the inclined semipolar planes) of 3D nanostructures contributes more to the measured CL spectra. A very small and negligible blueshift (1 nm) in QW emission energy is observed on raising the excitation current density to 5 A/cm^2 and implies that the polarisation related internal electric fields are minimal in QWs fabricated on these facetted structures. No significant change in QW emission line width is observed with increase in current. Negligible broadening of the QW line width [Fig. 6.23 (b)] and emission wavelength with increasing excitation current, point to the flat quantum well (implying less built-in field) nature [27].

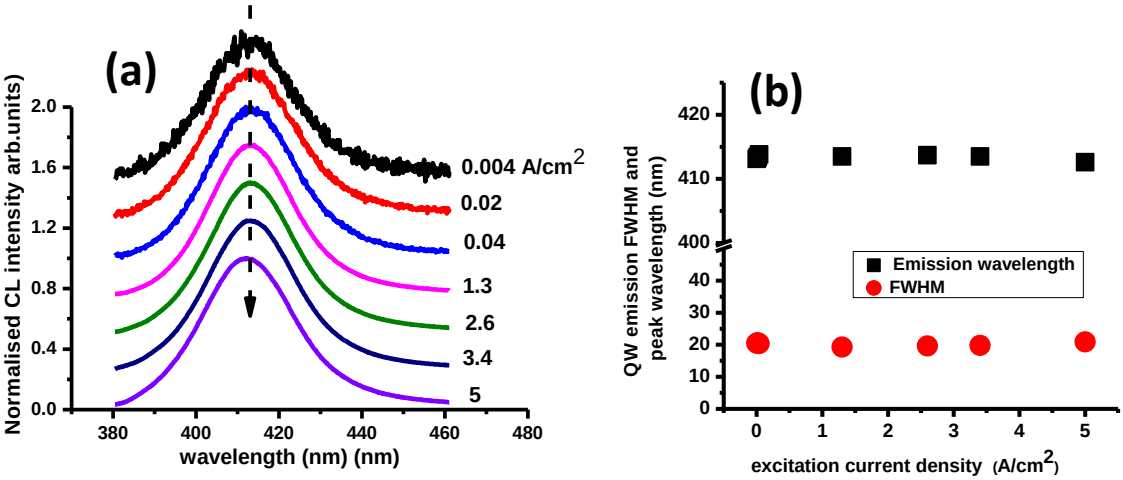

Figure 6.23 (a) QW CL emission spectra as a function of excitation current density (b) QW peak position and FWHM as a function of excitation current density

6.4 Summary

The spatially resolved optical properties of high density arrays of semipolar {10$\underline{1}$1} InGaN QWs fabricated on the nanofacets of GaN pyramids were studied using high resolution hyperspectral CL mapping technique. The QW emission energy blueshifts in most of the samples as the electron beam scans from bottom to top of the nanopyramid. The InN incorporation in these InGaN QWs fabricated on the nanofacets of GaN pyramids is thought to be governed by reactor ambient conditions rather than the adatom diffusion lengths. This QW energy blueshift from bottom to top of the nanopyramid is found to follow the release of the tensile strain in GaN towards the top of nanopyramid. The spectral position of InGaN QW emission studied as a function of excitation current density and temperature revealed negligible polarisation induced internal electric field in these structures. The optical properties of nonpolar InGaN QWs fabricated on nanofacets of GaN 3D structures on a-plane GaN template are also studied. The possibility of the existence of optical modes within the 3D GaN structures is shown by high resolution QW emission CL map from a single 3D nanostructure. In summary, these high radiative efficient InGaN QWs deposited on nanofacets of GaN with semipolar and nonpolar orientation realised by nano-SAG technique demonstrate their potential to form the basis of a low cost technique for fabricating InGaN LEDs.

References:

[1] Cho C Y, Han S H, Lee S J, Park S C, and Park S J 2010. *J. Electrochem. Soc.* **157** H86-H89

[2] Chiu C, Lee C, Lo M, Huang H, Lu T, Kuo H and Wang S 2008 *Japanese J. Appl. Physics* **47** 2954

[3] Liu C, Shields P A, Chen Q, Allsopp D W E, Wang W N, Bowen C R, Phan T L and Cherns D 2010 *Phys.Stat. Sol. (c)* 7 32

[4] Hwan I, Choi I, Lee C R and Noh S K 1997 *Appl. Phys. Lett.* **71** 1359

[5] Slack G A, Schowalter L J, Morellic D and Freitas J A et al 2002 *J. Cryst. Growth* **246** 287.

[6] Song D Y, Chandolu A, Stojanovic N, Nikishin S A and Holtz M 2008 *J. Appl. Phys.* **104** 064309

[7] Yu H, Lee L K, Jung T, and Ku P C 2007 *Appl. Phys. Lett.* **90** 141906

[8] Wunderer T, Brückner P, Neubert B and Scholz F, Feneberg M, Lipski F, Schirra M, and Thonke K 2006 *Appl. Phys. Lett.* **89** 041121

[9] Ueda M, Kojima K, Funato M and Kawakami Y, Narukawa Y and Mukai T 2006 *Appl. Phys. Lett.* **89** 211907

[10] Keyan Z, Yadong W and Jin C S 2009 *phys. Stat. Sol. (c)* **6** S514–S518

[11] Yu H, Jung T and Ku P C 2008 *phys. Stat. Sol. (c)* **5** 1618

[12] Edwards P R, Martin R W, Watson I M, Liu C, Taylor R A, Rice J H, Na J H, Robinson J W and Smith J D 2004 *Appl. Phys. Lett* **85** 4281.

[13] Pe´rez-Solo´rzano V Gröning A, Jetter M, Riemann T and Christen J 2005 *Appl. Phys. Lett* **87** 163121

[14] Feng W, Kuryatkov V V, Chandolu A, Song D Y, Pandikunta M, Nikishin S A and Holtz M 2008 *J. Appl. Phys.* **104** 103530

[15] Neubert B, Bruckner P, Habel F, Scholz F, Riemann T, Christen J, Beer M and Zweck J et al 2005 *Appl. Phys. Lett*. **87** 182111.

[16] Nishizuka K, Funato M, Kawakami Y, Narukawa Y and Mukai T 2005 *Appl. Phys. Lett.* **87** 231901.

[17] Funato M, Kotani T, Kondou T, Kawakami Y, Narukawa Y and Mukai T 2006 *Appl. Phys. Lett.* **88** 261920.

[18] Liu C, Satka A S, Lethy K J, Edwards P R, Allsopp D W E, Martin R W, Shields P, Kovac J, Uherek F and Wang W 2009 *Appl. Phys. Express* **2** 121002

[19] Cho Y H, Gainer G H, Fischer A J, Song J J, Keller S, Mishra U K, and DenBaars S P 1998 *Appl. Phys. Lett*. **73** 1370

[20] Riblet P, Hirayama H, Kinoshita A, Hirata A, Sugano T, and Aoyagi Y 1999 *Appl. Phys. Lett.* **75** 2241

[21] Kuokstis E, Yang J W, Simin G, Asif Khan M, Gaska R, and Shur M S 2002 *Appl. Phys. Lett.* **80** 977

[22] Wunderer T et al 2011 *Phys. Status Solidi B* **248** 549

[23] Fichtenbaum N A et al 2007 *Jap. J. Appl. Physics* **46** L230

[24] Fang H, Yang Z J, Wang Y, Dai T, Sang L W, Zhao L B, Yu T J, and Zhang G Y 2008 *J. Appl. Phys.* **103** 014908

[25] Hiramatsu H, Nishiyama K, Motogaito A, Miyake H, Iyechika Y, and Maeda T 1999 *Phys. Status Solidi* A **176** 535

[26] Jiang H X, Lin J Y, Zeng K C, and Yang W 1999 *Appl. Phys. Lett.* **75** 763

[27] Kim K C, Schmidt M C, Sato H, Wu F, Fellows N, Fujito K, Speck J S, Nakamura S and DenBaars S P 2007 *Phy Stat. Sol. (RRL)* **1** 125– 127

Chapter 7

Optical properties of AlInN epilayers

7.1 Introduction

The ternary AlInN material system possesses the widest bandgap range from 0.7 (InN) to 6.2 eV (AlN) amongst all the III-nitrides and hence holds great potential for applications in light emitting diodes (LEDs), laser diodes (LDs) and solar cells operating from the UV to the near infrared [1, 2]. Lattice matching of AlInN to fully relaxed GaN is of benefit to AlInN/GaN based high electron mobility transistors, highly reflective distributed bragg reflectors (DBRs) and in confinement layers in GaN based UV optoelectronic devices [3]. AlInN/AlN/GaN structures are a promising alternative to AlGaN barrier GaN- channel heterostructure field effect transistors (HFET) as the former provides more engineering freedom over the high 2 dimensional electron gas (2DEG) density (~ $2.7x10^{13}$ cm^{-2}) at the interface, circumventing strain and supporting high power operation of HFETs with higher cut-off frequency [4, 5]. Despite this potential AlInN alloys are the least explored ternary III-nitrides in terms of fundamental and applied research mainly because of the difficulty in the growth of high quality AlInN alloys. Section 2.3.4 of Chapter 2 described in detail the properties and applications of AlInN ternary system and addressed the existing research challenges especially for the fundamental material properties like bandgap, luminescence properties etc.

This chapter presents the study of composition, surface morphology and optical properties of AlInN epilayers with InN molar fraction ranging from 0.14 to

0.20. Optical emission and absorption have been studied using photoluminescence, cathodoluminescence and PL excitation (PLE) spectroscopy, and values for the band gap energy and luminescence properties are discussed in relation to InN fraction. Polarisation resolved PL emission of AlInN/GaN heterostructures is also studied in order to investigate the electronic band structure of AlInN ternary alloys and assess the nature of the observed luminescence emission from the AlInN. In III-nitride wurtzite semiconductor heterostructures, their low symmetry crystal structure, highly asymmetric and anisotropic *p*-orbitals constituting the valence band and the anisotropic strain [3, 4] can contribute to the different optical response measured in directions parallel and perpendicular to the polar-c axis.

7.2 Sample specification and Experimental Details

The AlInN epilayers under investigation were grown by metal-organic chemical vapour deposition (MOCVD). Sample growth was performed by Thomas Sadler, Dr. Menno Kappers and Dr. Rachel Oliver in the Department of Materials Science and Metallurgy, University of Cambridge. All the AlInN epilayers were grown on c-plane sapphire substrates. Trimethylaluminium (TMAl), trimethylindium (TMIn), trimethylgallium (TMGa) and ammonia (NH_3) were used as precursors for Al, In, Ga and N respectively. Each run began with the growth of a low temperature GaN nucleation layer followed by the growth of a 6 μm thick GaN buffer layer. Figure 7.1 shows the schematic structure of these samples. Table 7.1 summarises the sample code, growth temperature and nominal thickness of the AlInN epilayers. These samples vary in growth temperature and hence consist of different InN fractions varying from ~ 0.14 to 0.20.

PL, PLE and polarisation resolved PL measurements were performed at low temperature (~20 K) in a closed-cycle helium cryostat. A 1000 W short arc Xenon lamp combined with a 0.25 m focal length monochromator, as described in Chapter 3, was used as the excitation source. In all of the PL and PLE measurements using the Xe-lamp, the excitation area on the sample was about 2 x 5 mm^2. More details of the Xe lamp based PL/PLE experimental setup is given in Chapter 3. Figure 3.2 and 3.3 show the measurement geometry for the polarized PL measurements, with the PL being collected in a direction almost parallel to the c-

plane of the sample. Near edge luminescence (the angle between the normal to the sample surface and incident exciting beam is very small $\leq 10^0$) and the PL signals are collected nearly parallel to one of the sample edges as shown in the experimental geometry.

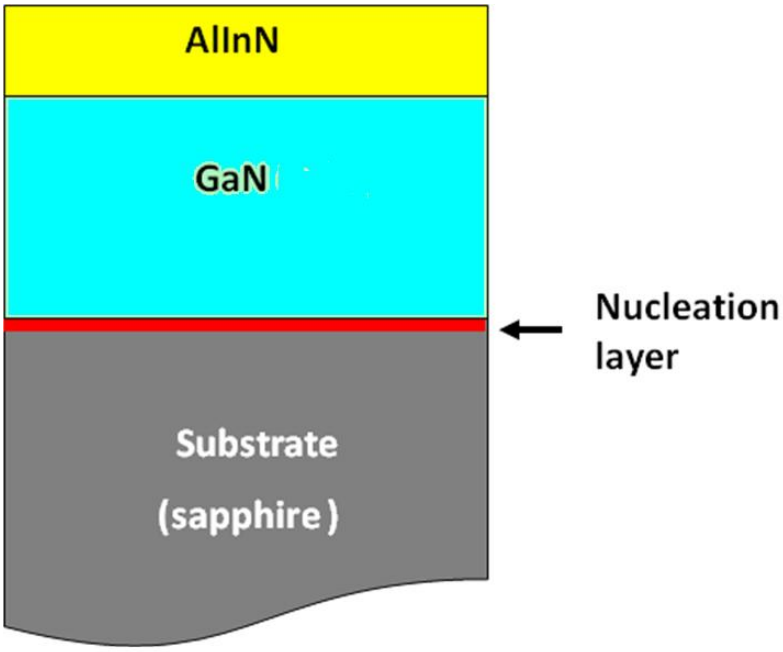

Figure 7.1 Schematic diagram of AlInN epilayer samples on *c*-plane sapphire substrate (not to scale).

Table 7.1 Sample code, growth temperature and thickness of AlInN layers

Sample name	substrate	Growth temperature (^{0}C)	AlInN layer thickness (nm) (from XRD)
C3042 A	c-plane sapphire	800	97 ± 6
C3043 A		800	93 ± 6
C3303 A		790	90± 6
C3305 A		790	52 ± 6
C3622 A		760	106 ± 3

The sample surface quality was examined by SEM at an electron beam energy of 5 keV, the crystal quality and compositions were determined by RBS and HR-XRD. Composition measurement by wavelength dispersive X-ray spectrometry (WDX) is not possible for these AlInN epilayers, since their thicknesses are less than the probing depth of the electron beam at beam energy of 5 keV which has been estimated to be ~120 nm using Monte Carlo simulation [6] as discussed in Chapter 3. The 5 keV is the minimum electron beam energy required to excite X-ray emission lines from InN. This will result in a large penetration into the underlying GaN buffer layer and can give high inaccuracies in the ratio of In/Al content if using the WDX technique. Variable temperature, variable energy cathodoluminescence spectra were acquired at low temperature (~ 20 K) using a home-built electron beam excitation system. The electron beam excitation spot was focussed to a diameter of ~200 µm. The electron beam voltages varying from 0.75 to 5 kV and beam current of 0.1 to 5 µA were used for the CL spectroscopy measurements described in this thesis. Spectra were acquired using an Oriel InstaSpecTM cooled 2-dimensional CCD array mounted at the output focal plane of a Chromex 0.5M monochromator. The sample temperature was varied between 20 and 300 K using a Leybold closed cycle helium cryo-refigerator and temperature controller.

7.3 Results and Discussion

7.3.1 Composition and Crystalline Quality

The RBS measurements were performed by Dr. Katharina Lorenz together with her PhD student Sérgio Magalhães at the Instituto Tecnologico e Nuclea (ITN), Sacavém, Portugal. The measurements were performed with a 1 mm diameter beam of 1.6 or 2 MeV He+ ions using silicon surface barrier detectors. The InN composition and AlInN layer thickness values from the RBS spectrum are obtained through fitting using a simulation program. To improve the depth resolution, the samples were tilted to $\Theta = 70^0$; where Θ is the angle between the beam and the normal to the sample surface. The χ_{min} parameter is measured from the data as the ratio of the backscattered yield in an aligned (or channelled) spectrum to that in a random spectrum. It is used as a measure of the crystalline quality of the AlInN epilayers. Low values of χ_{min} correspond to good crystalline quality and high values

correspond to relatively bad crystalline quality. State of the art values of χ_{min} for GaN are around 2 % [7].

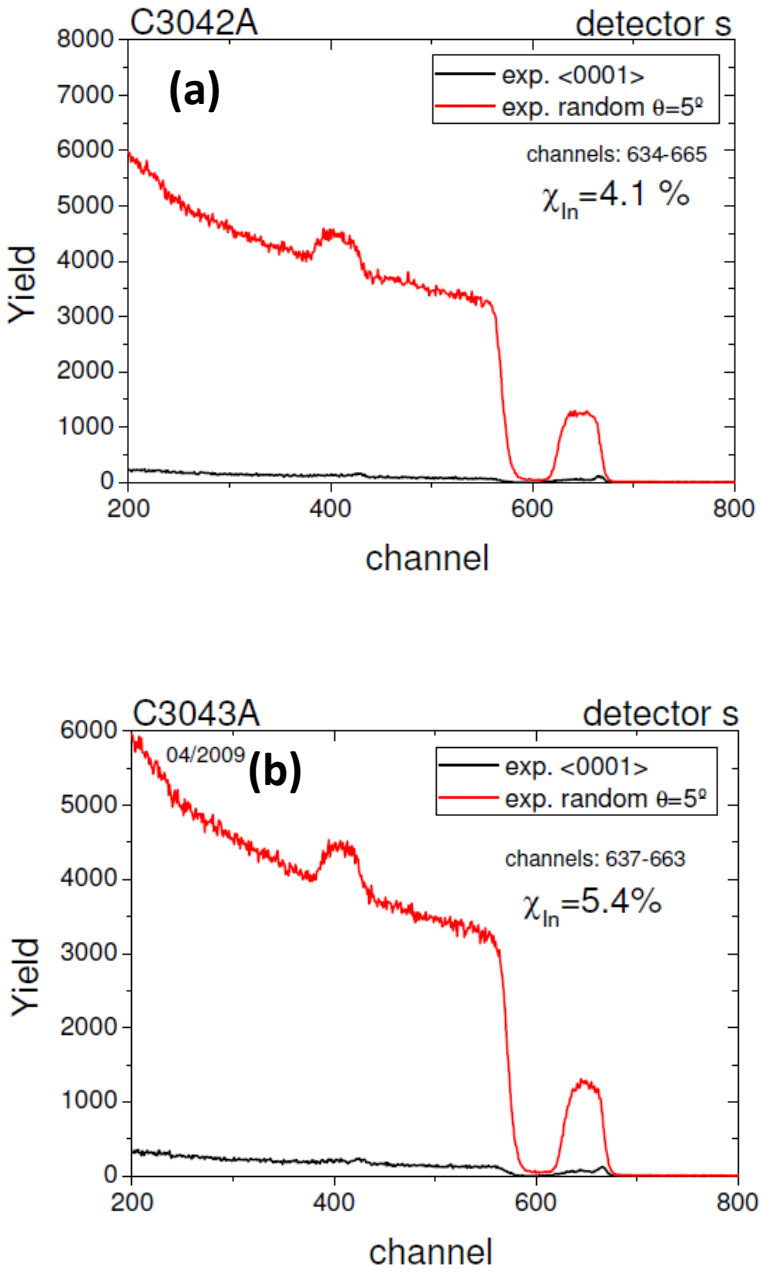

Figure 7.2 RBS/C random and <0001>-aligned spectra taken with a 1.6 MeV He+ beam for (a) C3042 A and (b) C3043 A respectively.

Figure 7.2(a) and 7.2(b) show the random and <0001> aligned RBS/C spectra measured from samples C3042 A and C3043 A respectively. It is observed from these figures that the channelled spectrum shows much lower backscattering yield than that of the random spectrum. The channelled spectrum of C3043 A has a higher

backscattering yield than that of C3042 A. This indicates that the former has poorer crystalline quality as compared to the latter. This is further reflected in the higher χ_{min} value of C3043 A. The InN molar fractions, layer thickness and χ_{min} parameters derived from the RBS/C spectra are summarised in Table 7.2. The fractional errors for InN molar fraction, epilayer thickness and χ_{min} parameters are ± 5 %, ± 5 % and ± 10 %, respectively.

The crystalline quality of the AlInN epilayers was also assessed by high resolution XRD measurements by Dr. Thomas Sadler. The thickness and InN content of the Cambridge series of samples measured using XRD techniques are also listed in Table 7.2. A comparison of the InN fraction and thickness determined by XRD and RBS shows that there exists a slight deviation in their values. From the RBS method, the compositional value is obtained through fitting of the RBS spectrum using a simulation program. Thus the results depend on the model and the values of the parameters used during fitting procedures. The XRD measurements require accurate lattice constants of the binary constituents of the alloy. For both AlN and InN, scattered values appear in the literature [8, 9]. Furthermore, XRD depends on the validity of Vegard's Law for the lattice constants of the fully relaxed alloys. Lorenz et al have observed a deviation from Vegard's Law for AlInN using InN contents obtained from RBS and lattice constants obtained from HR-XRD reciprocal space mapping [10]. This deviation will lead to further uncertainty in the compositional measurements. The presence of strain in the AlInN epilayers would also lead to additional errors as it is not considered during analysis. Moreover, the different region of the samples from which data is collected for RBS and XRD may also result in a variation in the compositional percentage determined. The slight differences in the thickness values measured by XRD and RBS may again be due to the differences in principles employed. In HR-XRD the thickness of the epilayers is estimated from the thickness fringes of the XRD-Rocking curve while the RBS technique of thickness measurement is very sensitive to the surface roughens.

Low chi-min (χ_{min}) values of 3 to 5 % (see Table 7.2) for AlInN reveal relatively good single crystalline quality, although they are slightly higher than for the GaN buffer layer (2.9 %). Minimum χ_{min} values of 3.8 and 4.1 % are obtained for the samples C3303 A and C3042 A for which the InN fraction is near lattice matched to GaN buffer layer according to XRD measurements.

Table 7.2 InN molar fraction, χ_{min} and thickness of AlInN epilayers determined by RBS at ITN, Portugal and by XRD at Cambridge.

Sample name	InN molar fraction (RBS)	InN molar fractions (XRD)	AlInN layer thickness (nm) (From RBS)	AlInN layer thickness (nm) (From XRD)	χ_{min} (%) (From RBS)
C3042 A	0.127	0.143	95	97 ± 6	4.1
C3043 A	0.126	0.139	90.8	93 ± 6	5.4
C3303 A	0.152	0.175	89.6	90± 6	3.8
C3305 A	0.146	0.175	49.7	52 ± 6	4.9
C3622 A		0.196		106 ± 3	

7.3.2 Surface morphology

A crack free and relatively smooth surface with small pits and a few extended dark regions distributed across the surface are seen for the samples. The typical surface morphology of the AlInN epilayers is shown in Figure 7.2. Pits are often observed on the surface of indium containing nitrides and have been proposed as a preferential migration path for Indium ad-atoms during the growth of InGaN and AlInN alloys causing the accumulation of In atoms within and around the pits [11, 12]. These v-pits are not generally formed during the growth of the AlInN epilayer rather the epilayers often reproduce the morphology of the underlying GaN buffer layers [13]. In a similar manner to InGaN, the origin of v-pits in AlInN alloys can be linked to the threading dislocations in the underlying GaN buffer layer.

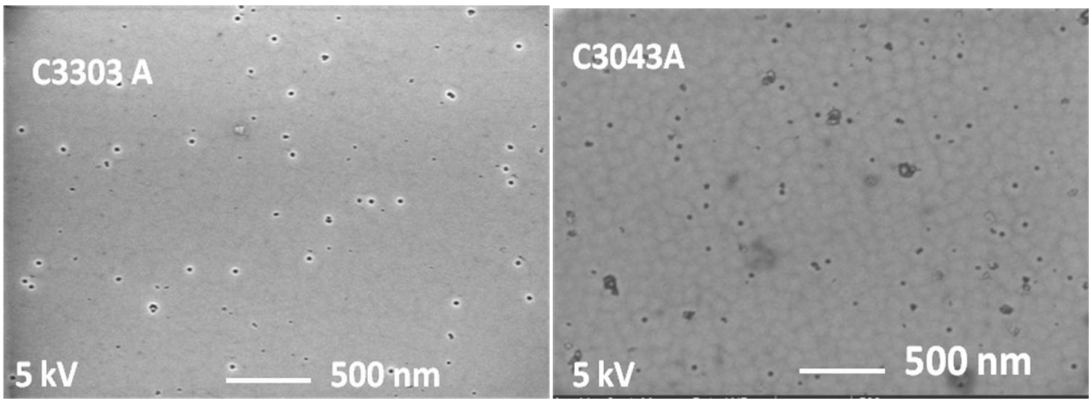

Figure.7.3 FESEM surface morphology images of AlInN epilayers samples for two different InN molar fraction (a) ~ 0.18 (C3303A) and (b) ~0.14 (C3043 A)

7.3.3 PL/PLE spectroscopy

The PL and PLE spectroscopic study of the AlInN epilayers are discussed in this section. The luminescence and luminescence excitation properties are discussed in terms of their InN content, surface and crystalline quality. The low temperature (~20 K) PL spectra of the AlInN epilayers excited using the Xe lamp is shown in Figure 7.4. There are two emission regions in each PL spectrum: transitions relating to the GaN buffer layer and a broad higher energy peak attributed to the AlInN emission. GaN band edge emission (~ 3.48 eV), GaN-related defect emission (3.42 eV), donor-acceptor pair (DAP) emission (3.29 eV) and its first LO phonon replicas are observed on the low energy side [7-9]. Although high absorption of the exciting light by the AlInN epilayers at high excitation energy is expected, the GaN buffer layers have also been excited either by the light penetrating the ternary or by diffused excess carriers. The broad emission bands at higher energy are observed to show a redshift from 308 nm (4.03 eV) to 338.5 nm (3.67 eV) as the InN molar fraction increases from 0.14 to 0.20. They are attributed to emission from the AlInN epilayers. The high energy PL emission bands of C3303A, C3042 A and C3043 A exhibit a double structure, which could be related to the existence of regions with different AlInN alloy compositions.

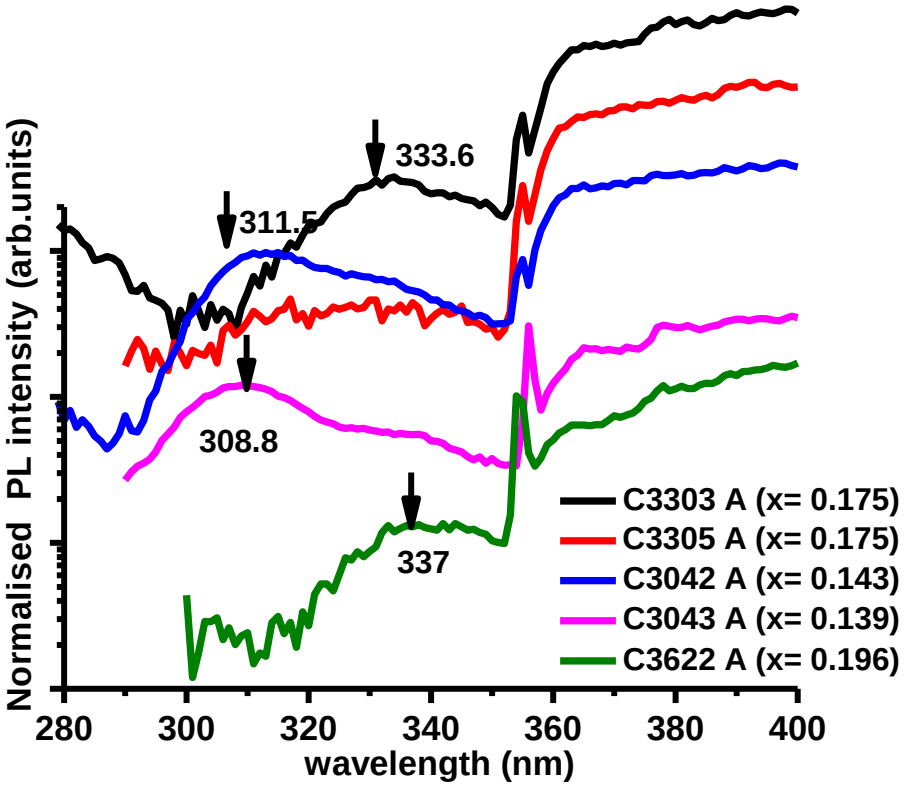

Figure 7.4 Low temperature PL spectra of AlInN epilayers with InN molar fraction (x) from 0.14 to 0.20 excited by the Xe-lamp. C33042 and C33043 A are excited using 260 nm and others with 280 nm radiation.

Figure 7.5 plots the energies of the AlInN luminescence peak in the PL spectra from the epilayers studied in this work as a function of InN fraction. The emission energy displays roughly a linear dependence on the InN fraction in the studied composition range. The peak energy of the AlInN PL peak blue shifts from 3.67 eV to 4.03 eV as the InN fraction decreases from 0.20 to 0.14. Figure 7.5 also compares the current work with the previous reported works [14-16].

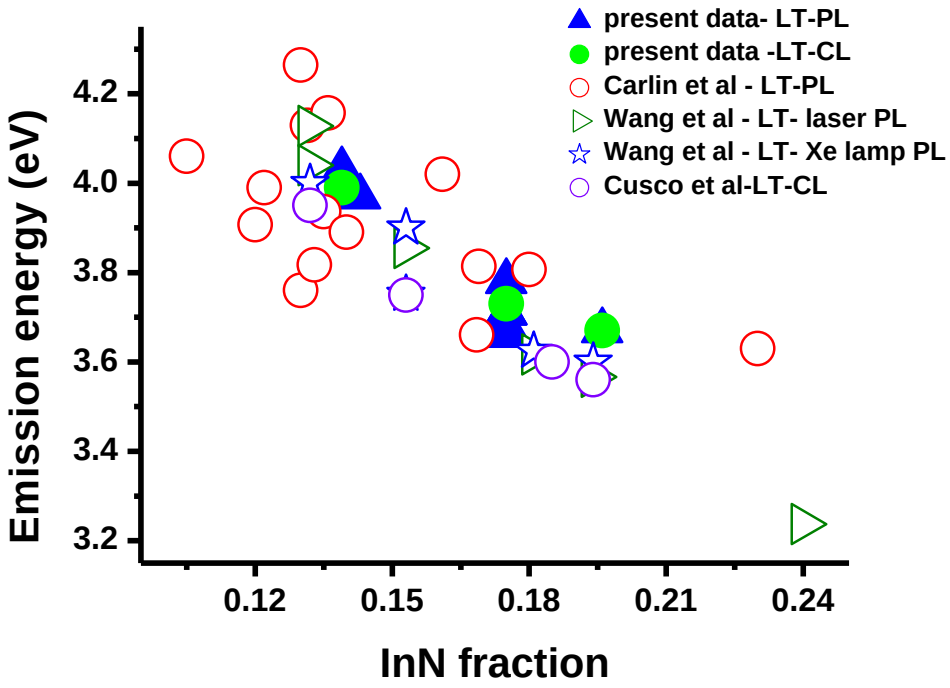

Figure 7.5 Luminescence emissions of AlInN epilayers as a function of InN molar fraction using PL and CL spectroscopy (described later). Filled symbols are current work all done at LT ~ 20 K. Open symbols are literature data from Wang *et. al.* [15], Carlin *et. al.* [14] and Cusco et al [16].

7.3.4 PLE spectroscopy

The principle of PLE spectroscopy is described in detail in Chapter 3. The assumed equivalence between absorption and PLE spectra is used to estimate the bandgap energy of AlInN epilayers. Low temperature PLE spectra excited by the Xe-lamp and detected at the AlInN emission peak from each of the samples are shown in Figure 7.6. The PLE spectra were acquired by fixing the detection wavelength at the maximum of the respective PL emission bands. A clear absorption edge can be seen in each of the PLE spectra and is attributed to the band gap absorption in the AlInN layer. The absorption edge revealed by the PLE spectra displays a redshift as the InN fraction increases. Each of the PLE spectra has been cut off on the low energy side at the point where the PLE intensity rises again towards the detection emission energy.

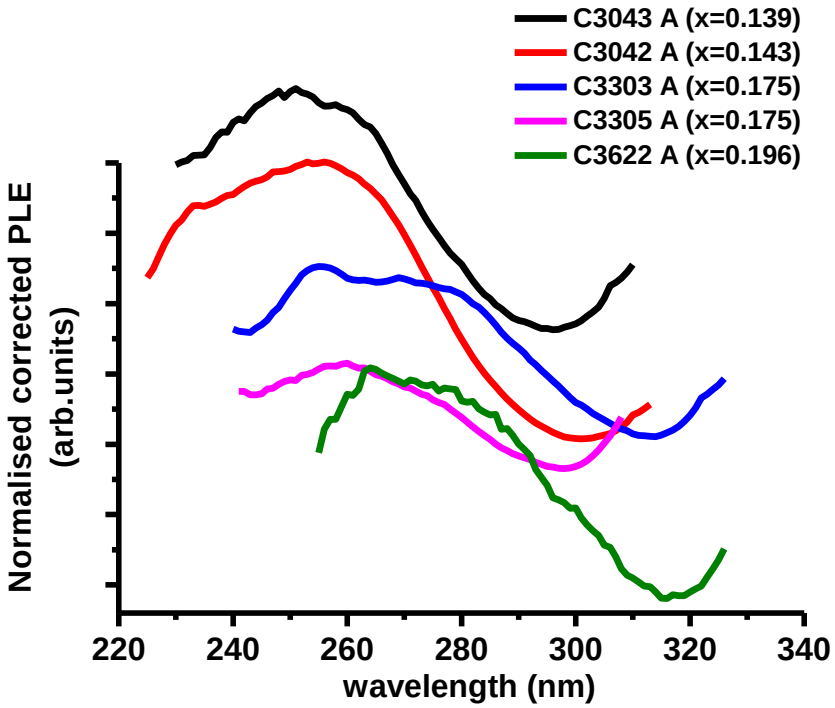

Figure 7.6 PLE spectra of AlInN epilayers as a function of InN fraction

The positions of the absorption peaks give an estimate of the band gap of the samples. The effective energy gap is evaluated by fitting the low energy side of the PLE spectrum to a sigmoidal function [17]:

$$\alpha = a_0 + \frac{\alpha_0}{1 + \exp\left(\frac{E_g - E}{\Delta E}\right)} \tag{7.1}$$

where a_0 is the offset correction, E_g is defined as an effective band gap energy, ΔE(eV) is a broadening parameter, α_0 is a constant and E(eV) is the excitation energy at which the intensity α is recorded. A representative sigmoidal fitting is given in Fig 7.7 for the PLE spectrum from C3042 A.

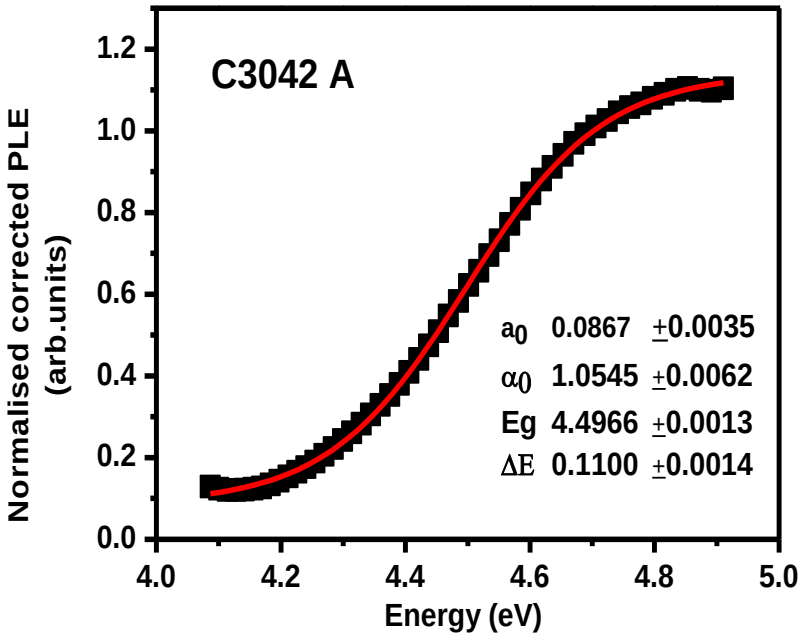

Figure 7.7 Typical representation of sigmoidal fitting (red line) to a PLE spectrum for sample C3042 A. E_g is the effective band gap

Table 7.3 summarises the effective band gap energies, broadening parameters and the emission energies of AlInN epilayers in this work. Figure 7.8 presents the experimental dependence of the estimated band gap of the AlInN epilayers studied in this work determined by the sigmoidal fitting of the PLE spectra as a function of InN fraction. The band gap energy is observed to display a linear dependence on the InN fraction in the restricted composition range studied. This behaviour is similar to that observed for InGaN epilayers [17] and the AlInN emission energy shown earlier in Figure 7.5. Figure 7.8 also includes the literature data for comparison. It is observed that the band gap energies agree reasonably well with the literature values [Iliopoulos *et. al.* [18], Wang *et. al.* [15] and Carlin *et. al.* [14], Oh et al [19], Yeh [20] et al] in the similar InN fraction range.

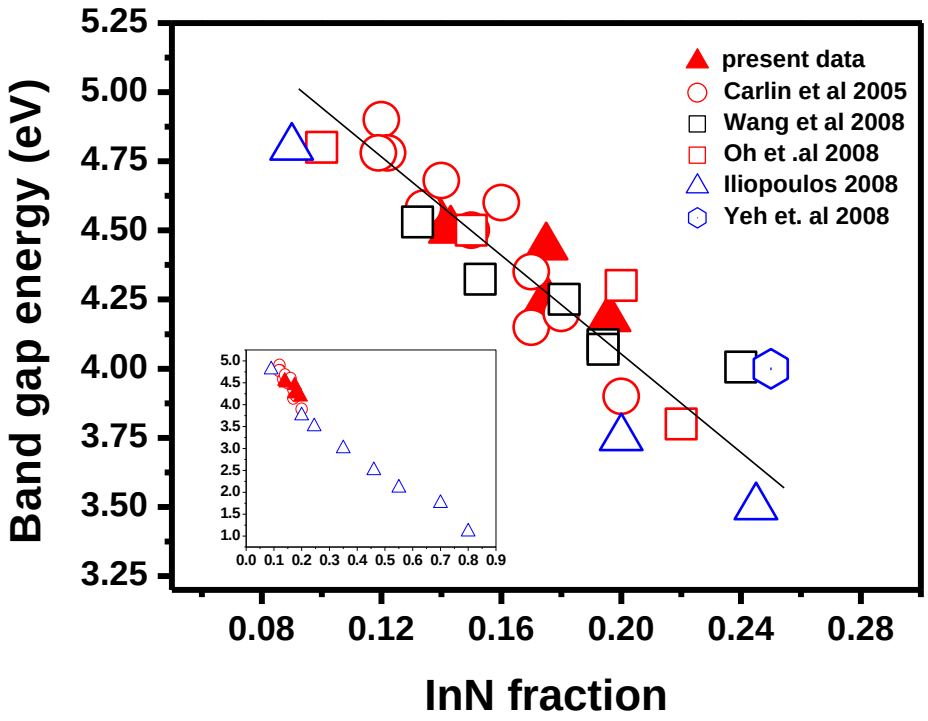

Figure 7.8 Dependence of AlInN bandgap energy on the InN molar fraction. Filled symbols are from the current work whereas open symbols are from the literature. The inset of Fig 7.8 shows the bandgap energy of AlInN for the whole composition range using the literature data [14, 15, 18-20].

The band gap (E_g) of ternary alloys such as $Al_{1-x}In_xN$ is generally fitted using the equation:

$$E_g(x) = 6.28.(1-x) + 0.67.x - b.x.(1-x) \qquad (7.2)$$

where b denotes the bowing parameter. Determination of bowing parameter is important in order to effectively design AlInN devices as it describes the variation in bandgap energy with alloy composition [18]. The estimated bowing parameter is ~ 7 $\pm$ 1 eV. This value of bowing parameter is very close to the value (6 eV) reported by Wang et al [15].

7.3.5 Stokes shift

Spatial fluctuations in the composition of alloy semiconductors can cause inhomogeneous broadening of the exciton density of states. Excitons produced in

such alloy semiconductors are localized at the low energy side of the inhomogeneous broadening because of the excitonic energy relaxation processes. In such cases, an energy difference arises between excitonic absorption and emission and this is defined as a Stokes shift of excitons [21]. Both the inhomogeneous broadening and the Stokes shift of excitons are important parameters to evaluate the degree of exciton localization. A large Stokes shift is one of the common features of lattice relaxation associated with impurities [22, 23].

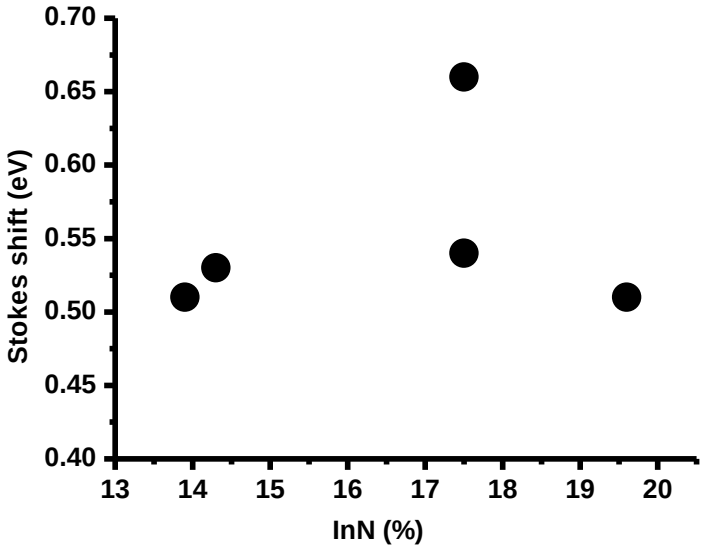

Figure 7.9 Stokes shift of AlInN epilayers as a function of InN fraction.

The Stokes shift is estimated by taking the difference in energy between the effective band gap and the emission peak energy. A plot of the Stokes shift as a function of InN molar fraction is presented in Figure 7.9 for the AlInN epilayers studied in this work. The observed Stokes shift ranges from 0.51 to 0.66 eV for the investigated range of InN composition. Very large Stokes shifts of 0.4–0.8 eV for the composition range x = 0.13 - 0.24 has been reported by Wang et al [15]. Laskar et al [24] recently reported a Stokes shift of 0.85 eV for a-plane AlInN for InN ~ 19%. Kundrotas [25] et al also reported a Stokes shift of 0.4-0.8 eV for InN composition near 18%. Onuma *et al.* [26] reported optical reflectance and PL data over the range $0.07 < x < 0.5$ indicating extremely large Stokes shifts of 1 to 2 eV. Butte *et al* [1] reported a Stokes shift of 0.8 eV for AlInN epilayers nearly lattice

matched to GaN. Such a large energy difference between band edge and luminescence could be possibly ascribed to InN composition fluctuations or to the presence of deep defects or impurities acting as preferential recombination centres. In addition, there is no definite trend in the obtained Stokes shift as a function of InN content observed in AlInN epilayers as shown in Figure 7.9.

Table 7.3 (a) Emission energy, effective band gap and Stokes shift of AlInN/GaN samples

Sample	InN fraction (%)	Effective band gap (E_g)- eV	Broadening Parameter ΔE (meV)	Emission energy (eV) Lamp	CL (low temp) (eV)	Stokes Shift (eV)
C3042A	14.3	4.50	110	3.97		0.53
C3043A	13.9	4.54	110	4.03	3.99	0.51
C3303A	17.5	4.25	102	3.71	3.73	0.54
C3305A	17.5	4.44	110	3.78		0.66
C3622 A	19.6	4.18	119	3.67	3.67	0.51

7.3.6 Cathodoluminescence spectroscopy

Depth resolved CL spectra are useful for identifying the layer of origin of a particular luminescence transition. Figure 7.10 (a)-(c) show the depth resolved CL spectra of three AlInN/GaN heterostructures. The CL spectra are acquired for different electron beam voltages that range from 0.75 to 5 kV. The penetration depth corresponding to each beam voltage is estimated using Monte-Carlo simulation and is shown in Fig 7.10 (d)-(f). For all the three samples, up to a voltage of 2 kV, the electron beam interaction volume is mainly confined within the AlInN epilayers and hardly penetrates the underlying GaN layer. The corresponding CL spectra from the AlInN epilayers (excited using low beam voltages of upto 2 kV) mainly consist of three emission bands. The highest energy emissions at 3.73 eV (C3303A), 3.99 eV (C3043A) and 3.67 eV (C3622 A) are attributed to AlInN emission.

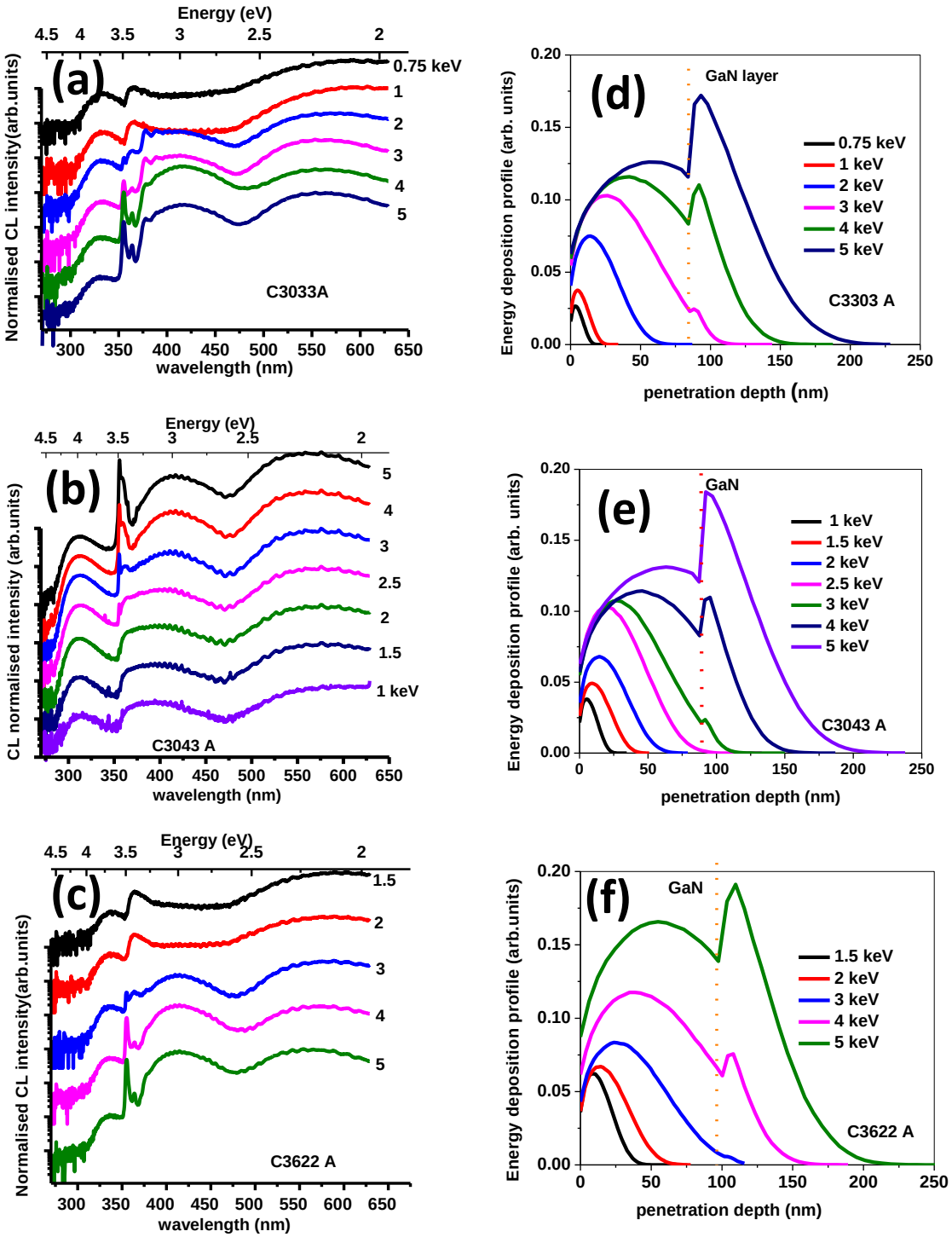

Figure 7.10 Low temperature CL spectra of AlInN/GaN heterostructures as a function of different electron beam energy (a) C3303A (InN ~ 0.18) (b) C3043A (InN ~ 0.14) (c) C3622A (InN ~ 0.20). Monte-Carlo simulation plots showing the electron beam energy deposition profile as a function of depth in AlInN/GaN heterostructures (d) C3303A (e) C3043A (f) C3622A

No peak shift is observed for this emission as a function of electron beam acceleration voltage, possibly suggesting the vertical compositional uniformity of the AlInN epilayers. The lower energy emissions at ~ 3.4 eV (C3303 A and C3622 A) and ~3.2 eV (C3043 A) collected from the AlInN epilayers may be related to defects. The CL emission at a still lower energy of ~ 2.1 eV can be related to the YB defect emission from AlInN epilayers.

On increasing the beam voltage above 2 kV, the interaction volume penetrates to the underlying GaN layer as shown by the Monte-Carlo simulation plots in Fig 7.10 (d)-(f). The corresponding CL spectra show GaN NBE emission at ~ 3.5 eV in addition to the emissions from AlInN epilayer. For all the samples, the CL emission at ~ 3.4 eV gets sharpened with increase in beam voltage. It is worth to note that, this CL emission has two origins, one from the AlInN epilayers (related to defects) and another from GaN. The 3.42 eV emissions from GaN is reported to be related to excitons bound to structural defects in particular to stacking faults and c-axis screw dislocations or some surface related defects [27]. The CL emission spectra of the samples excited using the higher beam voltages (3-5 kV) consist of a blue band emission at ~ 2.97 eV. Since this CL emission peak appears mostly for higher electron beam voltages, its origin is related to the underlying GaN layer. The blue band in unintentionally doped GaN layers are often associated with the acceptor levels; the transition of free electrons in the conduction band combining with the holes in the acceptor levels (eA transitions) [28]. For the sample C3043A, a redshift in blue band emission can be seen with increase in excitation voltage above 2.5 keV. This possibly can be due to the mixing of the blue band defect emission from AlInN epilayers to the blue band emission from the GaN layer. Fujomori et al also reported a defect blue band emission from AlInN epilayers [29].

To study the effect of increased level of excitation on the possibility of state filling, CL spectra of the samples are measured as a function of electron beam currents [Fig 7.11]. No peak shift or line shape change is observed for an order of magnitude increment in excitation level, suggesting carrier filling effects are negligible in these epilayers under the present excitation conditions [30]. No energy shift in AlInN CL emission peak is observed for the CL spectra acquired from

different lateral position of the sample, possibly implying the alloy homogeneity in these epilayers.

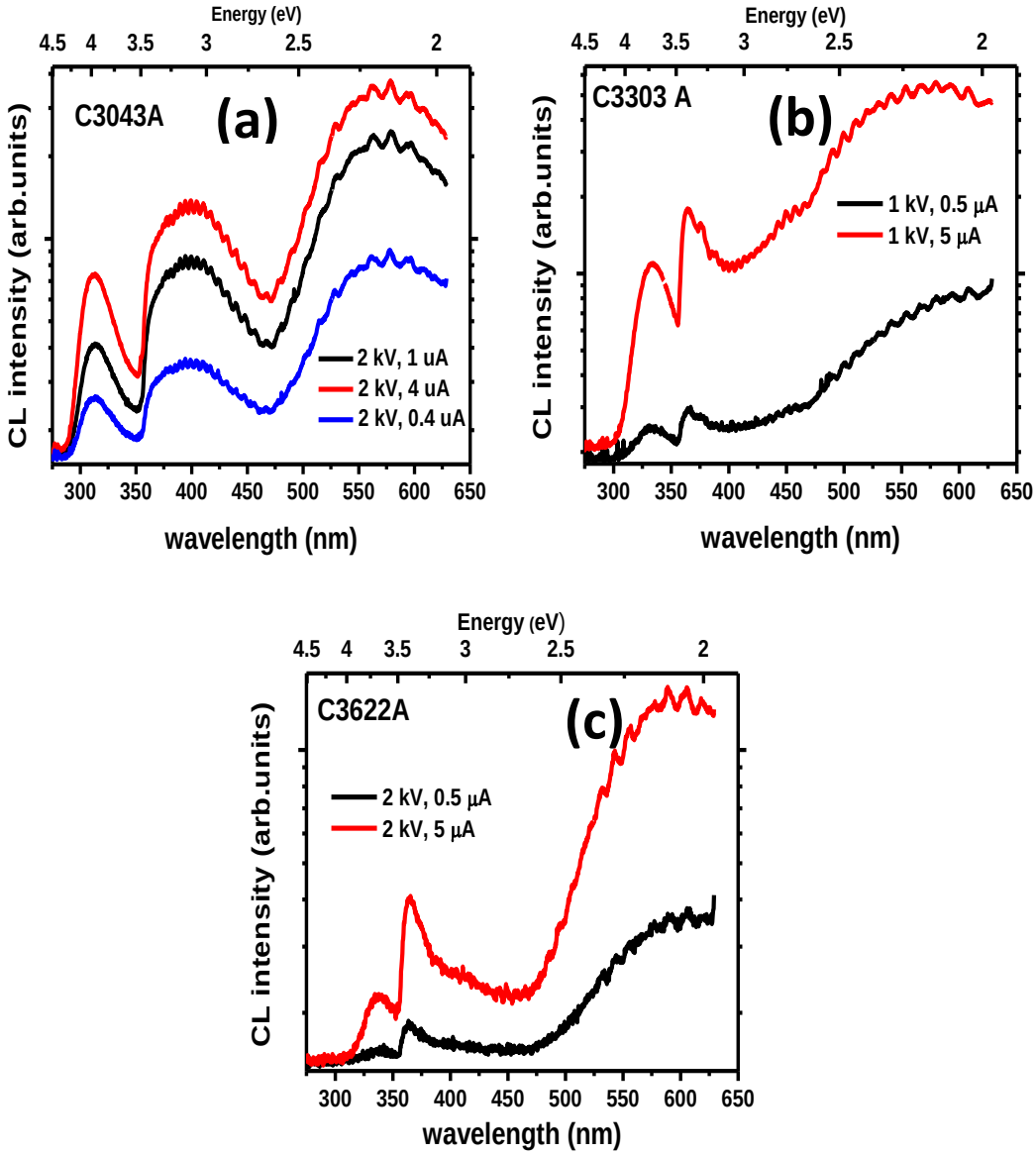

Figure 7.11Current resolved CL spectra of three AlInN/GaN heterostructures for various level of excitation electron beam current (a) C3043A (b) C3303A (c) C3622A

Fig 7.12 shows the CL spectra of the C3622A sample as a function of temperature from 20 to 300 K. The excitation electron beam energy (2 keV) is such that the electron beam interaction volume is mainly confined within the AlInN epilayers. The intensity of CL emission decreases with increase in temperature which can be attributed to an increase of nonradiative transition probability with increasing

temperature. The overall energy shift of the higher energy CL emission at ~3.67 eV is ~ 55 meV and the FWHM of this peak increases from ~ 200 to 280 meV. No strong S-shape dependence as that of InGaN epilayers is observed for this higher energy emission from AlInN epilayers measured as a function of temperature from 20 to 300 K [Fig 7.12 (b)]

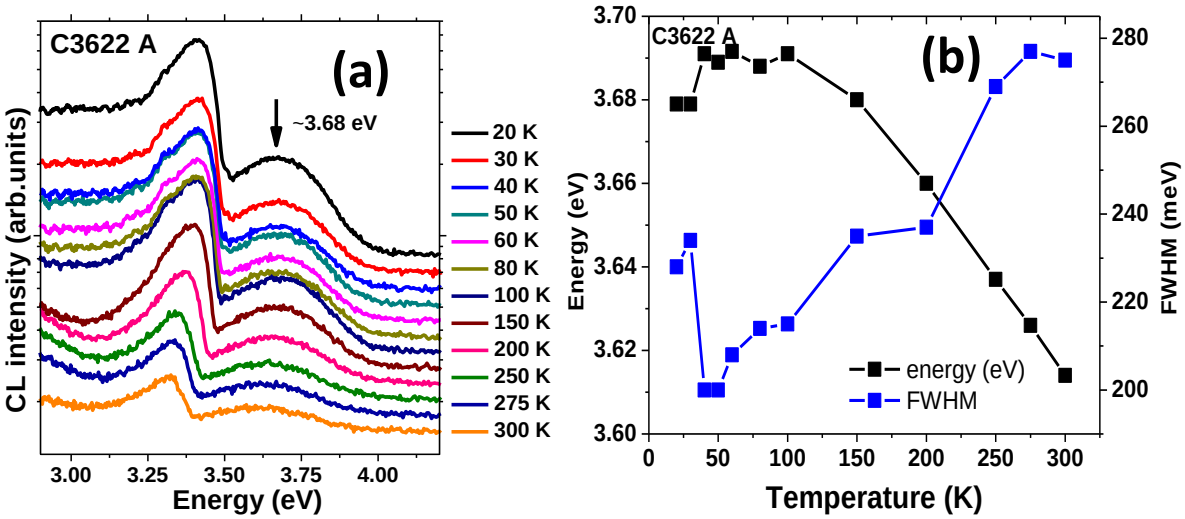

Figure 7.12 (a) Temperature dependent CL spectra of C3622 A AlInN epilayers sample (b) variation of peak position for AlInN emission at ~3.67 eV and its FWHM as a function of temperature

7.5 Polarisation resolved PL measurements

Polarisation resolved PL measurements are performed at ~ 20 K for AlInN/GaN heterostructures using Xe lamp as the excitation source. The different panels of Fig 7.13(a)-(c) compare the PL spectra of three different AlInN epilayers (with InN fraction ranging from 0.14 to 0.20) collected for the light emitted with electric field component (E) perpendicular (red line) and parallel (black line) to the c-axis. Fig 7.13 (d) is a similar plot for GaN epilayer of thickness 3 µm. All the spectra have been corrected for the combined throughput of lamp and the excitation monochromator and for any polariser, depolariser responses. For all three InN composition considered, the intensity of the AlInN as well as GaN NBE emission corresponding to $E \perp c$ polarisation is higher than that for the $E \parallel c$ polarisation.

Moreover, no noticeable energy difference has been observed for AlInN emission peak measured for E∥c and E⊥c orientations. Discussion on this observed behaviour of polarisation resolved PL spectra of both AlInN and GaN are given below.

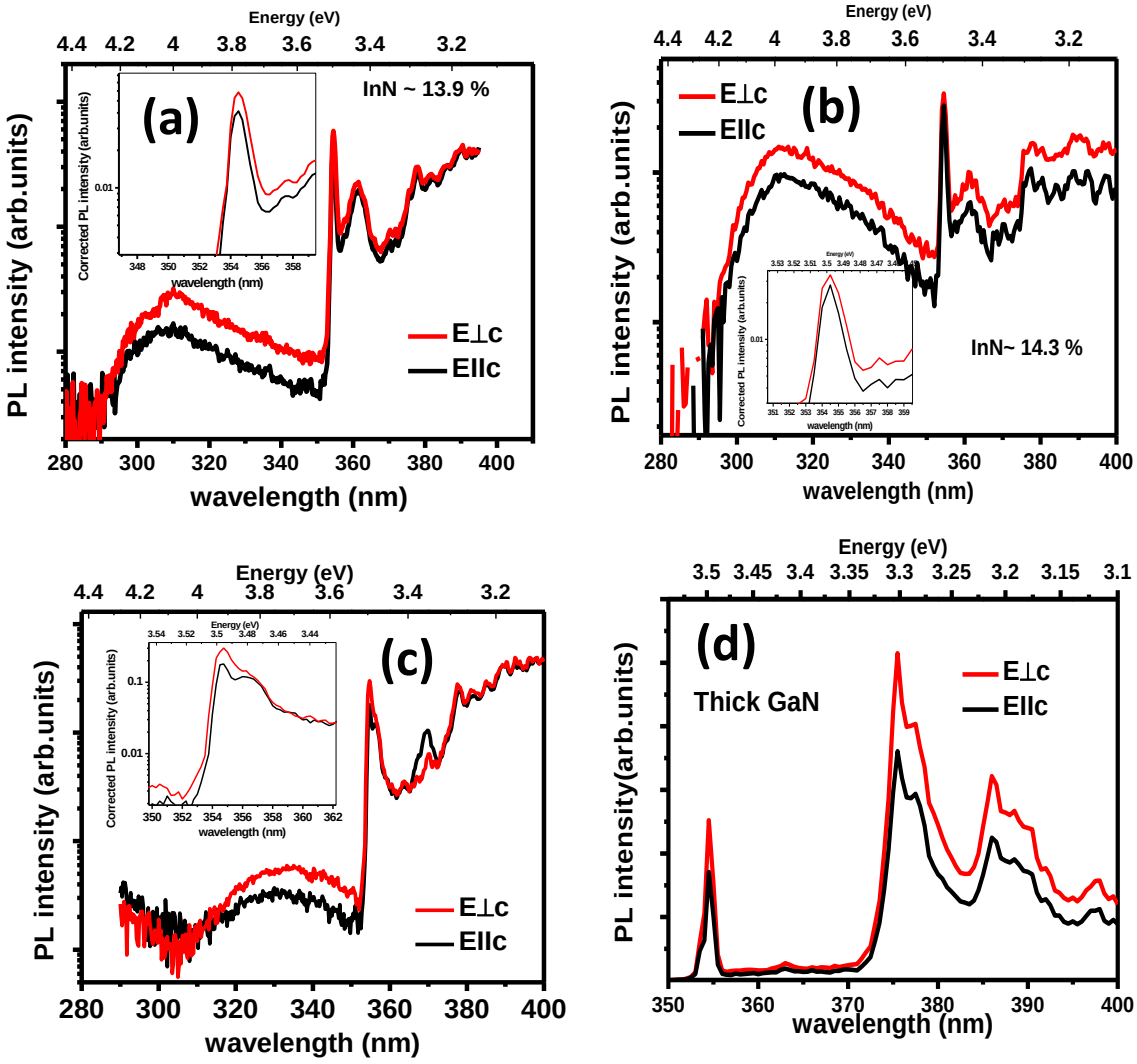

Figure 7.13 (a)-(c) Polarisation resolved PL spectra of the AlInN epilayers as a function of InN composition (a) C3043 A (b) C3042 A (c) C3303 A (d) polarisation resolved PL spectra of the thick (3 µm) GaN layer. Inset of Fig 7.13(a)-(c) show the GaN NBE emission intensity for E⊥ and E∥c orientations.

A brief description on band structure of wurtzite III-nitride can be seen in section 2.2.3 of Chapter 2. The ordering of split VB energy states in AlN, in the order of increasing energy of transition from CB minima is CH, HH and LH bands whilst that for GaN and InN are HH, LH and CH respectively. Figure 7.14 (a) and (b)

illustrates the valence band splitting, mainly allowed optical transition from the bottom edge of the CB to the VB and the ordering of these split valence bands in AlN and GaN respectively [31-33]. The notations Δ_{cr}, Δ_{so}, Γ_{15}, Γ_6 and Γ_1 were already defined in section 2.2.3. This unusual ordering of the valence band in AlN is expected to influence the polarisation resolved optical responses in AlInN epilayers. Fig 7.15 shows a simplified representation of valence band ordering in III-nitride binaries and the A, B and C optical transitions from the CB minimum in the order of their increasing energy.

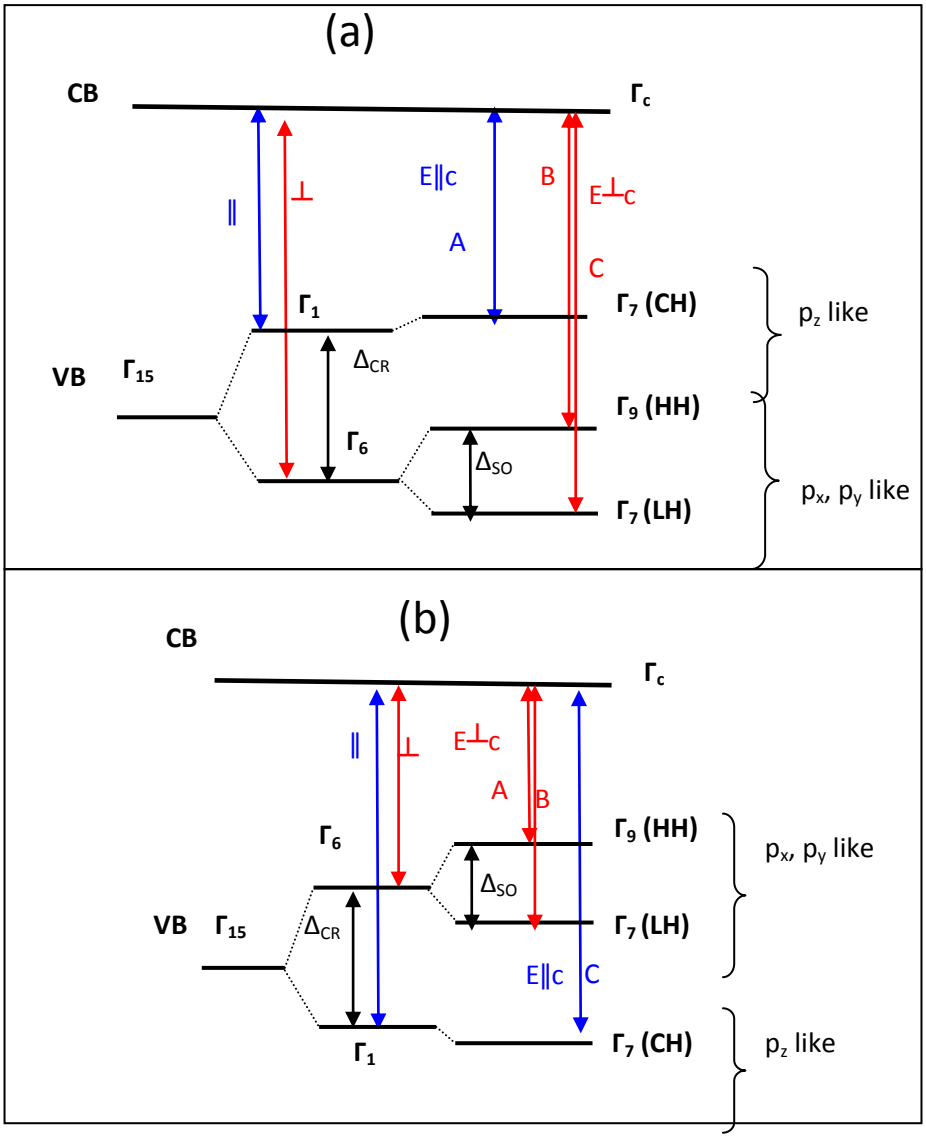

Figure 7.14 Valence band structure and the ordering of different bands in wurtzite (a) AlN and (b) GaN. Only the main allowed transitions corresponding to E∥c and E⊥c orientations are shown in this band diagram [31-33].

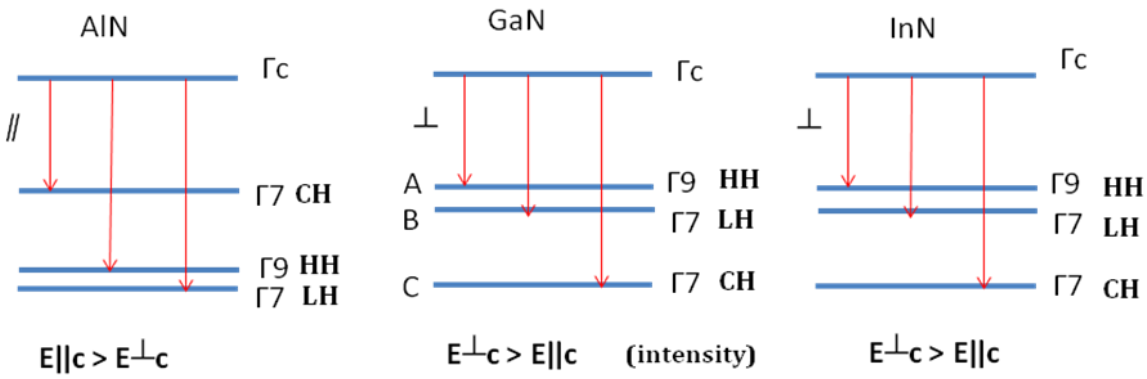

Fig 7.15 The ordering of different energy bands constituting the valence band in binary III-nitrides such as AlN, GaN and InN [31, 33, 34]

Since the valence band of wurtzite III-nitrides is constituted by anisotropic *p*-orbitals, it can be represented by a linear combination of three orbital wave functions, p_x, p_y and p_z. Considering the wavefunctions corresponding to these energy bands, the CH band is more p_z-like whilst the HH and LH bands are p_x and p_y-like states [35-37]. This is based on the assumption that z-axis is along the c-axis of the wurtzite crystal structure. Since the wavefunction representing the HH band has no $|Z\rangle$ component, the transition from conduction band minimum to the HH band is not permitted for light polarised parallel to c-axis (E∥c) orientation but allowed only for light polarised perpendicular to c-axis (E⊥c) orientation. Mixtures of light polarised with electric field orientation parallel and perpendicular to c-axis (E∥c and E⊥c) are possible for optical transitions involving CH and LH bands. Optical transition involving CB minimum and LH band is *mainly* allowed for light polarised perpendicular to the c-axis (E⊥c) and the transition between the CB and CH band is *mainly* allowed for light polarised parallel to the c-axis (E∥c) [32,37].

According to a recent theoretical report by Sakalauskas *et al* [38], for AlN-rich AlInN epilayers, the A transition (transition between CB and top of VB) is strongly allowed for E∥c polarisation and weak for E⊥c (shown in brackets), whereas the B transition is allowed only for the E⊥c orientation as shown in Fig 7.16. Since the top of the VB is constituted by the crystal field split off band (CH) band which favors the E∥c transition, a higher intensity PL emission is expected for E∥c orientation than E⊥c orientation. This is because most of the photogenerated holes

are expected to populate the top valence band at low temperatures [39]. Moreover the transition energy corresponding to AlInN intrinsic PL for E⊥c orientation is expected to be higher than that of E∥c according to Fig 7.16. The PL spectra shown in Figure 7.13 (a) – (c) do not show either of these characteristics of AlInN intrinsic emission. These observations possibly point that, the higher energy PL emission from AlInN epilayers is not the intrinsic emission rather a defect related emission.

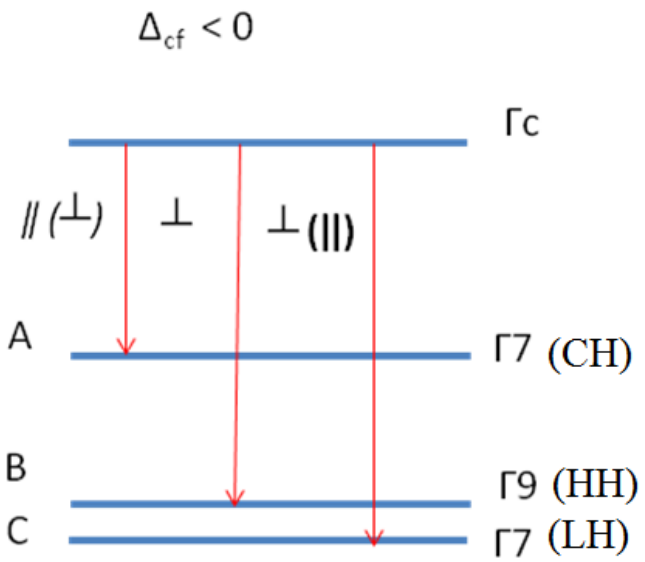

Figure 7.16 Band structure and selection rules for Al rich AlInN epilayers [38]

From Fig 7.13 (a)-(c), the polarisation resolved GaN NBE emission behaviour is consistent for all the samples and E⊥c transition has a higher intensity compared to E∥c. This observation is further confirmed by performing polarisation resolved PL measurements for thick (3µm) GaN epilayers under identical experimental conditions and resulting spectra is shown in Figure 7.13(d). This observation is in agreement with the band structure of GaN given in Figure 7.14 (b). In addition no energy shift between the two polarisation orientations could be resolved for the GaN epilayers. A plot of the integrated intensity of the PL emission for AlInN and GaN as a function of polarisation angle, shown in Figure 7.17, reveals that the polarisation angle dependence of emission intensity follows a similar pattern for both the GaN NBE and the higher energy AlInN emission. This can have another

possible implication; luminescence from AlInN may due to exciton localization and recombination occurring at InN clusters which act as potential minima as in InGaN epilayers; since InN and GaN have similar valence band ordering as discussed above. Further experiments and analysis are needed to obtain more conclusive picture of the above mentioned possible implications regarding the higher energy AlInN emission.

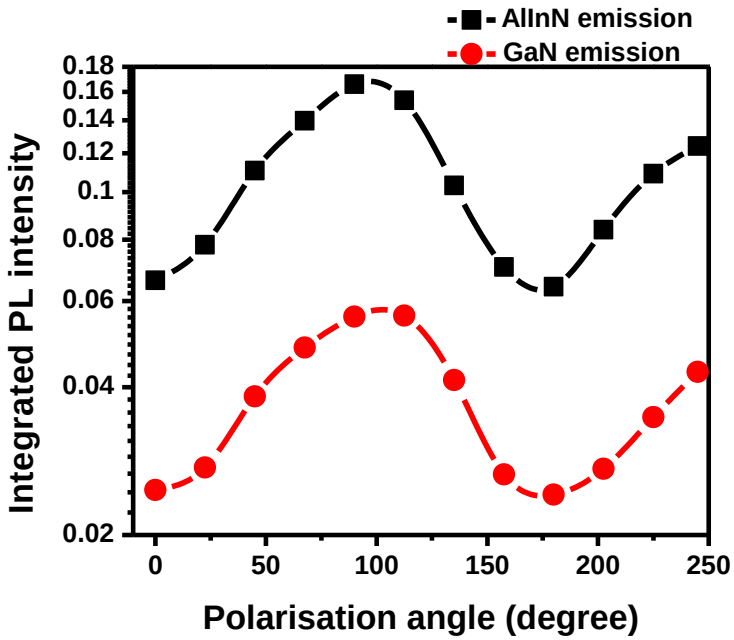

Figure 7.17 Polarisation-angle dependence of the PL peak integrated intensity for both AlInN and GaN emission

7.4 Summary

The composition, surface morphology and luminescence of a range of AlInN epilayers were investigated. The crystalline quality of the samples are analysed based on the χ_{min} values from the RBS measurements. The fraction of InN in AlInN estimated using RBS and HR-XRD measurements range from 0.14 to 0.20. The surface morphology of the AlInN epilayers are investigated using SEM. A crack free and nearly smooth surface with small pits distributed across the surface is seen for all AlInN samples. The luminescence of the AlInN epilayers is studied using PL and CL spectroscopy. Samples are observed to emit AlInN peak on the higher energy side of

the GaN band gap. It is observed that the PL/CL peak emission energies from AlInN epilayers redshift with increasing InN content. The emission energy decreases linearly from 4.03 to 3.67 eV as InN fraction increases from 0.14 to 0.20. PLE is carried out to determine the band gap energies of the AlInN alloys. By fitting the PLE spectra with the sigmoidal function, the effective band gap energy, E_g is determined. It is observed that the E_g decreases linearly with InN fraction for the restricted range of composition studied in this work. By taking the difference between the PL emission energy and the effective band gap determined from the PLE spectra, Stokes shift is obtained and varies between 0.51to 0.66 eV. No clear dependence of the Stokes' shift and InN fraction is seen in this work.

The CL measurements were performed as a function of electron beam energy, temperature, and excitation current on a selected set of AlInN/GaN samples. By confining the excitation volume to the ternary AlInN layer, luminescence peaks originating from the AlInN and GaN were differentiated. The absence of luminescence peak shift associated with the higher energy AlInN as a function of penetration depth and as a function of lateral position suggested the possible compositional homogeneity of the AlInN epilayers. Temperature dependent CL emission studies from AlInN epilayers showed an energy shift of ~ 55 meV as the temperature is increased from 20 to 300 K. No strong S-shape dependence was observed for the AlInN emission energy variation as a function of temperature. Polarisation resolved PL spectra from AlInN/GaN heterostructures were studied for three different InN compositions. For all three samples, the optical transition corresponding to E$\perp$c orientation was higher intense compared to E$\parallel$c orientation for both higher energy AlInN and GaN NBE emission. Polarisation angle dependence of integrated intensity of PL emission shows similar trend of variation for both AlInN and GaN. The obtained results have two possible implications; the observed higher energy AlInN emission is either related to defects or this emission from AlInN epilayers is due to carrier recombination occurring in InN clusters similar to that of InGaN epilayers.

References:

[1] R Butté et al 2007 *J. Phys. D: Appl. Phys.* **40** 6328-6344

[2] Castiglia et al 2009 *Appl Phys Lett* **94** 193506

[3] Carlin J F et al 2005 *Phys stat Sol (b)* **242** 2326

[4] Liberis J et al 2009 *Phys Status Solidi A* **206** 1385- 1395

[5] Sun H, Alt A R, Benedickter H, Bolognesi C R, Feltin E, Carlin J F, Gonschorek M and Grandjean N 2010 *Appl.Phys.Express* **3** 094101

[6] Hovington P, Drouin. D and Gauvin R 1997 *Scanning* **19**, 1

[7] Lorenz K to Martin R W, Private Communication.

[8] Paszkowics W, Podsiadko S and Minikayev R 2004 *J. Alloys Comp*. **382** 100

[9] Bhuiyan A.G, Hashimoto A and Yamamoto A 2003 *J.Appl. Phys*. **94**, 2779

[10] Lorenz K, Franco N, Alves E, Watson I M, Martin R W, O'Donnell K P 2006 *Phys. Rev.Lett.* **97** 085501

[11] Ponce F A, Srinivasan S, Bell A, Geng L, Liu R, Stevens M, Cai J, Omiya H, Marui H and Tanaka S 2003 *Phys. Status Solidi B* **240** 273

[12] Oliver R A, Kappers M J, Sumner J, Datta R and Humphreys C J 2006 J. Cryst. Growth **289** 506

[13] Schenk H P D, Nemoz M, Korytov M, Vennéguès P, Dräger A D and Hangleiter A 2008 *Appl. Phys. Lett.* **93** 081116

[14] Carlin J F, Zellweger C, Dorsaz J, Nicolay S, Christmann G, Feltin E, Butte R and Grandjean N 2005 *Phys. Stat Sol (b)* **242** 2326

[15] Wang K, Martin R W, Amabile D, Edwards P R, Hernandez S, Nogales E, O'Donnell K P, Lorenz K, Alves E, Matias V, Vantomme A, Wolverson D and Watson I M 2008 *J Appl. Phys*. **103** 073510

[16] Cusco R, Pastor D, Hernandez S, Artus L, Martinez O, Jimenez J, Martin R W, O'Donnell K P and Watson I M 2008 *Semicond.Sci.Technol*. **23** 105002

[17] Martin R W, Middleton P G, and O'Donnell K P and Van der Stricht W 1999 *Appl.Phys. Lett.* **74** 263

[18] Iliopoulos E, Adikimenakis A, Giesen C, Heuken M and Georgakilas A 2008 *Appl. Phys. Lett.* **92** 191907

[19] Yeh T S, Wu J M and Lan W H 2008 *J. Cryst. Growth* **310** 5308

[20] Oh T S, Kim J O, Jeong H, Lee Y S, Nagarajan S, Lim K Y, Hong C H and Suh E K 2008 *J Phys D: Appl. Phys* **41** 095402

[21] Yamada Y et al Wide bandgap properties-Fundamental Properties and Modern Photonic and Electronic Devices 2007 (Berlin: Springer)

[22] Jiang H X and Lin J Y III-V 2000 Nitride Semiconductors-Defects and Structural Properties (UK: Elsevier)

[23] Henini M Dilute Nitride Semiconductors 2005 (Oxford: Elsevier)

[24] Laskar M R, Ganguli T, Rahman A A, Arora A, Hatui N, Gokhale M R, Ghosh S and Bhattacharya A *Appl.Phys. Lett.***98**, 181108 2011

[25] Kundratos J et al 2011 *ACTA PHYSICA POLONICA A* **119** 173

[26] Onuma T, Chichibu S F, Uchinuma Y, Sota T, Yamaguchi S, Kamiyama S, Amano H and Akasaki I 2003 *J. Appl. Phys.* **94**, 2449

[27] Reshchikov M A and Morkoç H 2005 *J. Appl. Phys* **97** 061301

[28] Li S et al. 2004 *Journal of Luminescence* **106** 219

[29] Fujimori T *et al* 2004 *J. Cryst. Growth* **272** 381

[30] Zhang X, Rich D H, Kobayashi J T, Kobayashi N P and Dapkus P D *Appl Phys Lett* **73** 1430 (1998)

[31] Sedhain A, Lin J Y, and Jiang H X 2008 *Appl. Phys. Lett* **92** 041114

[32] Taniyasu Y and Kasu M 2011 *Appl. Phys. Lett*. **98** 131910

[33] Chichibu S F, Kawakami Y and Sota T 1999 *Introduction to nitride semiconductor blue lasers and light emitting diode* Edited by Nakamura S and Chichibu S F (New York : CRC Press)

[34] Wang K, Yamaguchi T, Takeda A, Kimura T, Kawashima K, Araki T and Nanishi Y 2010 *Phys. Status Solidi A* 207 1356

[35] Chuang S L 1995 *Physics of Optoelectronic Devices* (USA: Wiley Interscience)

[36] Bhattacharya J 2008 PhD Thesis, Tata Institute of Fundamental Physics, *Optical Polarisation anisotropy in Semiconductor Heterostructures*

[37] Song J –H 2008 *Oxide and nitride semiconductors: processing, properties and applications* (*Editors*: Yao T and Hong S -K) (Berlin: Springer)

[38] Sakalauskas et al 2010 *J.Phys. D Appl. Phys*. **43** 365102

[39] Murotani H et al 2011 *Appl. Phys. Lett*. **98** 021910

Chapter 8

Optical properties of AlInGaN epilayers

8.1 Introduction

AlInGaN alloys are promising as active layers in visible and UV light emitting diodes and laser diodes because of the possibility of almost independent control of the lattice constant and energy bandgap by varying InN and AlN compositions. $In_xAl_yGa_{1-x-y}N$ alloys can be lattice matched to GaN for y = 4.7 *x* [1]. The luminous efficiency of this alloy is expected to be comparable or better to that of the InGaN ternary due to the spontaneous luminescence emission arising from enhanced radiative recombination in nanoscale In-fluctuations or In-segregations acting as potential minima, localising carriers. Advantages of this quaternary alloy in the UV region compared to ternary AlGaN are already discussed in section 2.3.5 of Chapter 2. Now, turning to the InGaN system, though the In-rich InGaN system has been investigated to improve the luminous efficiency of LEDs due to the carrier localisation effect, optoelectronic devices based on In-rich InGaN alloys are subject to problems due to poor crystalline quality. This is due to the much lower growth temperature as well as high defect densities originating from the large lattice mismatch and the low miscibility of InN with other nitrides [2]. Section 2.3.5 of chapter 2 discussed the major applications of the AlInGaN quaternary alloy and discussed the existing research challenges for this material. This chapter is mainly devoted to exploring the optical properties of low InN content thin AlInGaN quaternary alloys fabricated on sapphire and SiC substrates.

AlGaN/GaN based High Electron Mobility Transistors (HEMT) suffer from inherent strain imposed limitations on the device performance especially for AlN> 30 %. Since the $Al_xIn_{1-x}N$ alloy can be lattice-matched to GaN for high Al mole fractions (x = 0.83), the development of AlInN/GaN HEMT structures with AlInN as the barrier layer offers a potential solution to the strain problem [3,4]. One requirement to obtaining AlInN/GaN based HEMTs with excellent characteristics and reliabilities is good crystal quality of the AlInN barrier. The growth of high quality AlInN epilayers is hampered by their poor miscibility and low growth temperature. Matsuoka et al reported that alloying with Ga would reduce the miscibility gap of AlInN and enables higher deposition temperatures [5]. Thus the AlInGaN quaternary system with lattice matching to GaN are a promising barrier layer material for GaN based HEMT devices. Furthermore the electron mobility in such structures can be considerably enhanced by inserting a 0.7-1.5 nm AlN interlayer between the GaN channel and the barrier layer [6, 7]. The set of quaternary AlInGaN samples investigated were from Dr. Lutz Kirste of Fraunhofer Institute for Applied Solid State Physics (IAF) with an InN composition of 2-5 % and Al/In ratio of ~ 4.8 such that the lattice matching condition with GaN is fulfilled. The importance of this InN concentration is that AlInGaN epilayers with a homogeneous composition can be obtained when the composition of InN <5% [8]. The sample set from Lutz Kirste has two kinds of interlayer, (a) a single layer of AlN and (b) a novel triple interlayer AlN/GaN/AlN structure.

8.2 Sample specifications and Experimental details

MBE AlInGaN layers were deposited on highly resistant Metal Organic Chemical Vapour Deposition grown GaN/Al_2O_3 (0001) or GaN/AlN/4H-SiC (0001) templates. The GaN grown on the sapphire substrate is 1-1.5 µm thick while that on the SiC is 1.8 µm thick with a 130 nm AlN starting layer. The MBE growth of nearly lattice matched AlInGaN layers was performed in a VEECO GEN 20A reactor equipped with a nitrogen RF plasma source. Initiating the MBE growth at 740 ^oC with a 60 nm GaN layer, a nominal interlayer of 1.0 nm AlN or 0.7 nm AlN/1.1 nm GaN/0.7 nm AlN were deposited to improve the mobility of the polarisation induced 2 DEG (as these epilayers were intended for the fabrication of barrier layers in

HEMT devices). After a ramp down of the substrate temperature, quaternary AlInGaN layers with an Al/In ratio of about 4.8 and Ga contents up to 50 % were deposited at 580 ^{o}C. Table 8.1 lists the sample details such as sample codes, InN content, thickness of the layers etc. Figure 8.1 shows a schematic structure of a quaternary sample on sapphire substrate having one interlayer of AlN.

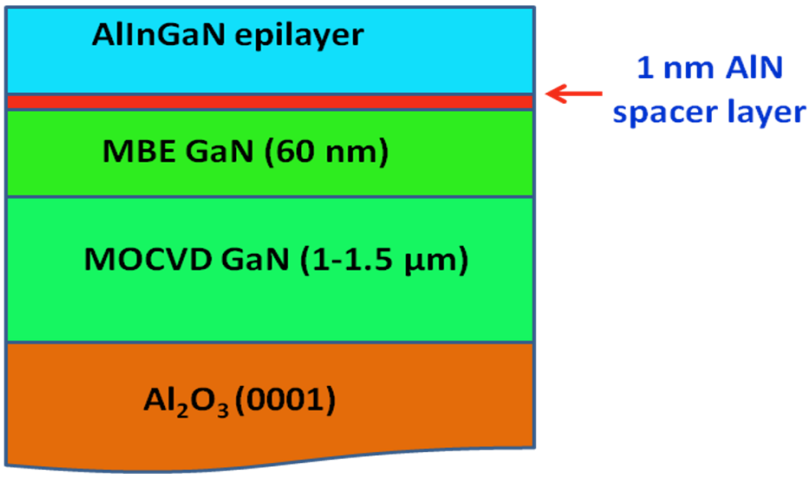

Figure 8.1 Schematic of a quaternary AlInGaN epilayer on sapphire substrate having one interlayer of AlN

Table 8.1 Sample details for AlInGaN epilayers from IAF

Sample code*	InN content	Thickness (nm)	Substrate	Roughness XRR (nm)
Q-3IL-SiC1.8	1.8	42	SiC	0.5
Q-1IL-AlO2.6	2.6	42	c-Al2O3	0.7
Q-3IL-AlO3.2	3.2	41	c-Al2O3	0.6
Q-1IL-SiC4.3	4.3	41	SiC	1.1

1 IL: single interlayer = nominal 1.0 nm AlN

3 IL: triple interlayer = nominal 0.7 nm AlN / 1.1 nmGaN / 0.7 nm AlN

*The number at the end of sample code denote the InN content

High resolution X-ray diffraction (HR-XRD) and X-ray reflectometry (XRR) measurements were performed by Dr. Lutz Kirste of IAF. A brief description of these techniques can be seen in section 3.4 and 3.5 of Chapter 3. They were

performed using (Cu$K_{\alpha 1}$-radiation) with a two –bounce Ge 220 monochromator and a triple axis Ge 220 analyser set up. The nominal InN concentration was determined using the lattice mismatch determined from HR-XRD data. For this they assumed that Al and Ga are preferrentially incorporated in comparison to In during MBE growth due to the higher III-nitride binding energies. The thicknesses of the quaternary epilayers were determined from the HR-XRD and XRR measurements which agree to better than 2 % [9]. Table 8.1 lists the InN composition and quaternary layer thickness as obtained from HR-XRD measurements [9]. Surface roughness values for the AlInGaN epilayers were obtained using the XRR technique. PL measurements were performed using the 1000 W short arc Xenon lamp excitation source combined with a 0.25 m focal length monochromator, as described in Chapter 3**.** For all the PL measurements, the excitation area on the sample is about 2x5 mm^2. The surface morphology was investigated by high resolution scanning electron microscopy at a beam energy of 5 keV. The spatially resolved luminescence properties of the samples were studied using the CL set up attached to the FESEM and employing the CL hyperspectral imaging as described in Chapter 3.

8.3 Results and Discussion

8.3.1 Surface morphology

The surface roughness of the samples was measured using the XRR method and is listed in Table 8.1. The quaternary AlInGaN is smoother when the triple interlayer is used instead of an AlN interlayer. Surface morphology of the quaternary epilayers was also investigated using FESEM. Fig 8.2 shows the surface morphology of the quaternary layers on SiC and sapphire substrates with an AlN interlayer. No hexagonal shaped v-pits are observed on the surface of the samples. Cracks are seen on the surface of the Q-3IL-SiC1.8 sample [Fig 8.8(a)]. Surface undulations and island like nanometer scale clusters possibly related to elastic strain relaxation are seen respectively on the surface of Q-3IL-AlO2.6 and Q-1IL-SiC4.3 quaternary epilayers [10, 11].

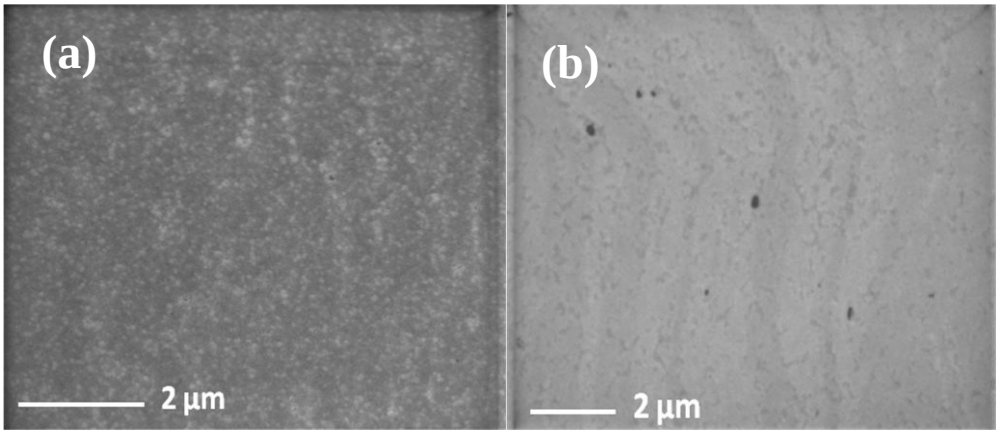

Figure 8.2 Secondary electron image of two AlInGaN epilayers from IAF (a) Q-1IL-SiC4.3 (b) Q-1IL-AlO2.6

8.3.2 Optical properties

8.3.2(a) PL and CL spectroscopy

Low temperature PL spectra of the samples are obtained using Xe lamp as the excitation source. Figure 8.3(a) shows the PL spectra (normalised with respect to the GaN NBE emission intensity) of the quaternary samples for the wavelength range 275 to 400 nm. Two emission bands are clearly seen in each PL spectrum, the higher energy band arising from the quaternary AlInGaN and the longer wavelength band near 360 nm due to GaN near band edge (NBE) emission. The low intensity peaks at ~ 3.35 eV (370 nm) and 3.26 eV (380 nm), which are separated respectively by ~ 90 meV can be attributed to longitudinal optical phonon (LO) replica of the GaN NBE emission peak at ~ 360 nm (3.44 eV). Multiple emission peaks in the shorter wavelength region (280- 330 nm), observed for samples with low indium contents (Q-3IL-SiC1.8 and Q-1IL-AlO2.6) possibly imply the existence of compositional inhomogeneity in the epilayers. Figure 8.3(b) show the room temperature CL spectra of the samples collected from a 3 x 3 µm area of the samples while excited using a 3 keV electron beam energy. AlInGaN emission in the shorter wavelength region, GaN NBE emission at ~ 365 nm and yellow band (YB) emission (for samples on sapphire substrate) are the main emission peaks resolved in the CL spectra. Multiple CL peaks (not so well resolved, as in LT PL spectra) corresponding to quaternary

emission are observed from samples Q-1IL-SiC4.3and Q-1IL-AlO2.6. The YB emission is very weak for AlInGaN samples grown on the GaN/AlN/SiC template possibly implying the reduction of defects in the epilayers. YB emission in undoped GaN is generally attributed to V_{Ga} -containing defects bound to structural defects such as dislocations. In the case of doped GaN layers the YB defect emission band has been associated with Si and Oxygen related defects [12-14]. For the present set of samples, the former statement related to YB emission appears to be more valid than the latter.

Figure 8.4(a) shows the GaN NBE emission from epilayers grown on different substrates. The peak energy difference of GaN NBE emission grown on different substrates of SiC and sapphire indicates the different strain state of the GaN layer. The GaN layers grown on SiC substrates are under slight tensile strain (GaN NBE ~ 3.41 eV) and that grown on sapphire substrate are under compressive strain (GaN NBE emission at ~ 3.44 eV). This is usually attributed to the different signs of lattice mismatch and thermal expansion coefficients of sapphire, 4H-SiC and GaN. GaN layer grown on foreign substrates usually undergoes strain relaxation during growth and cool down after growth by means of introducing misfit dislocations at the interface. The residual strain in the GaN layer is determined by growth conditions, layer thickness and/or layer structures as well as choice of substrate [15]. The different strain conditions prevailing in the GaN buffer layers can influence the structural and optical properties of AlInGaN epilayers grown over them. Figure 8.4 (b) shows the variation in the spectral position of room temperature quaternary CL emission as a function of InN fraction. A red shift in quaternary emission wavelength with increase in InN content is observed.

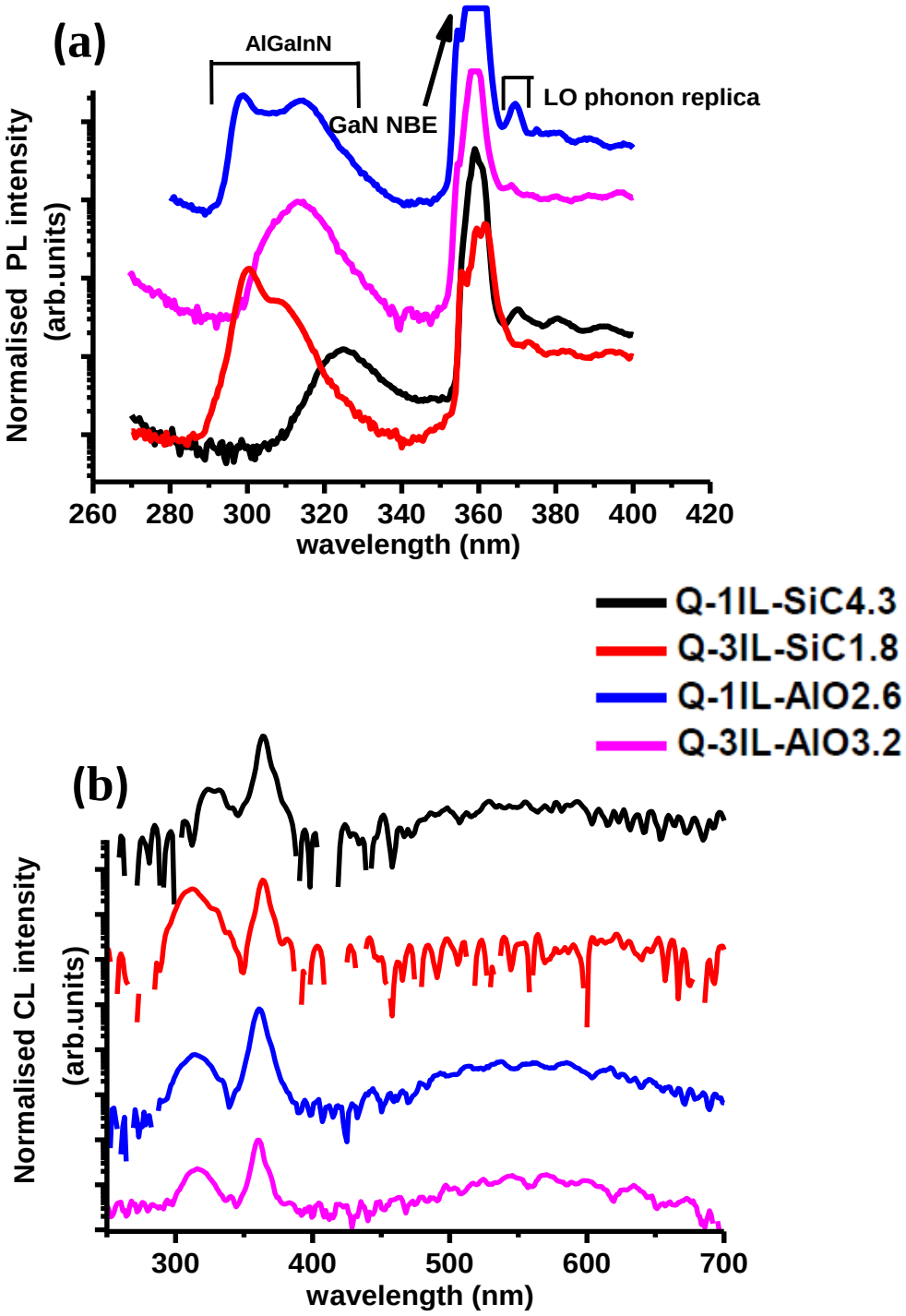

Figure 8.3 (a) Low temperature (20 K) PL spectra (normalised to GaN NBE emission intensity) (b) Room temperature CL spectra (normalised to GaN NBE emission intensity)

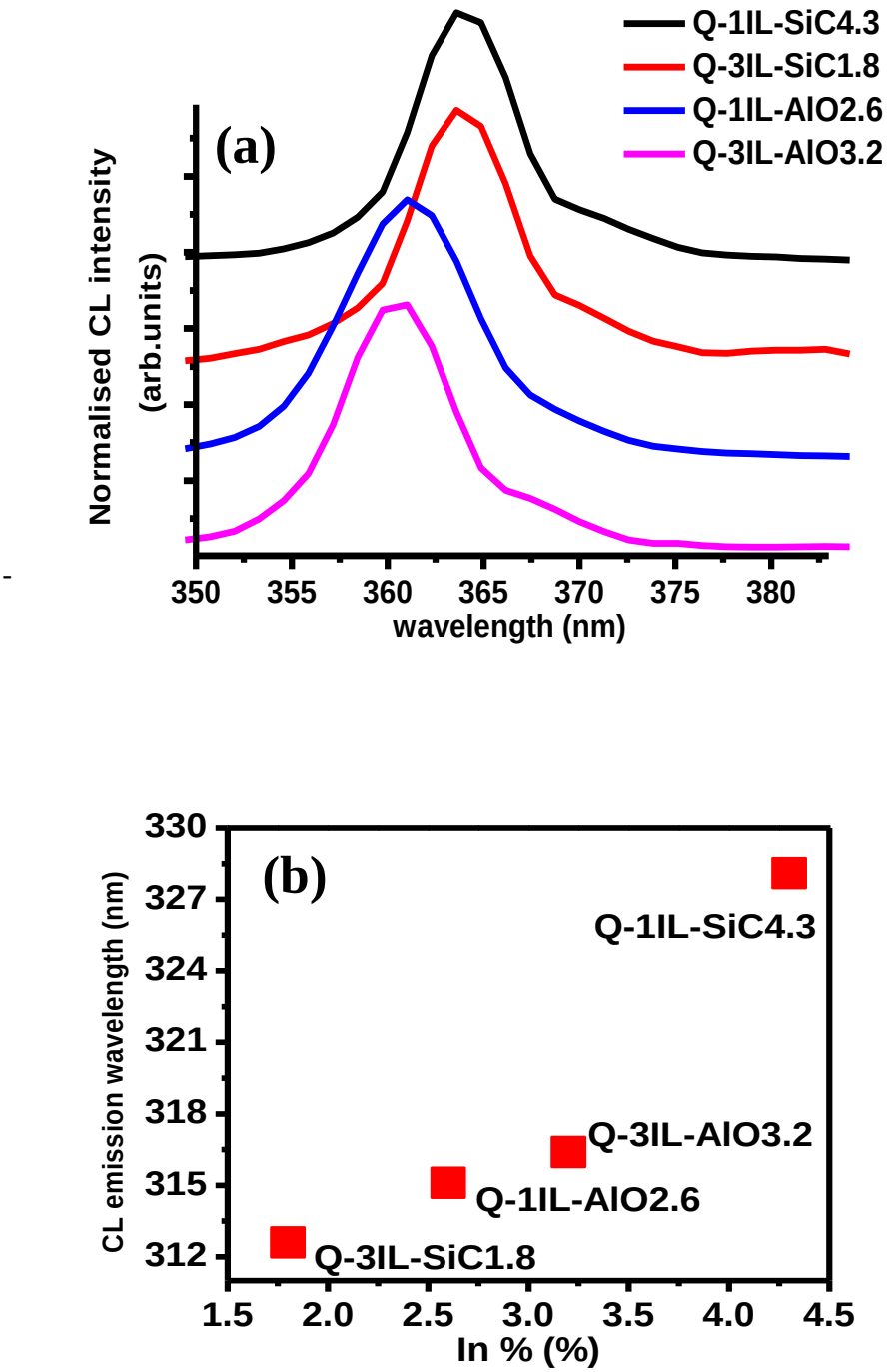

Figure 8.4 (a) GaN NBE CL emission at RT from different samples [obtained from figure 8.3 (b)] (d) The RT CL spectral position of AlInGaN emission *vs* InN fraction.

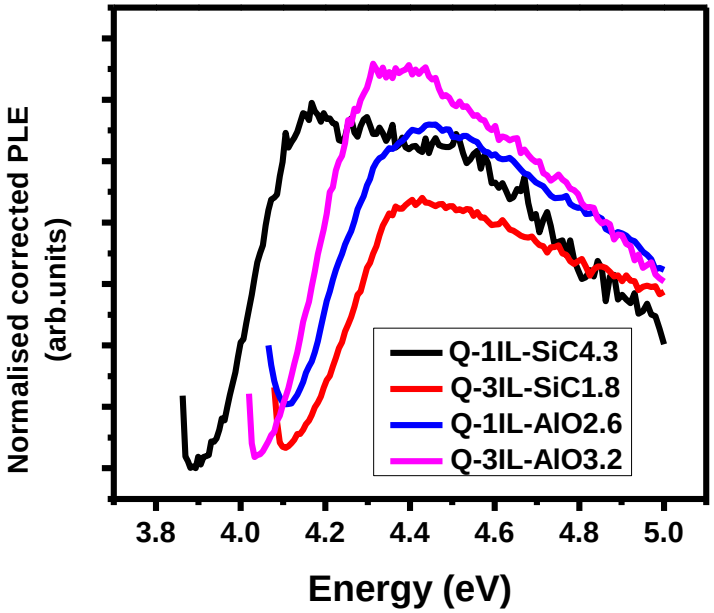

Figure 8.5 Normalised corrected PLE spectra of quaternary AlInGaN epilayers with InN content varying from 1.8 to 4.3 %

To estimate the bandgap energy of these AlInGaN epilayers, PLE measurements are performed as discussed in Chapter 3. Low temperature PLE spectra excited by the Xe-lamp and detected at the AlInGaN emission peak from each of the samples are shown in Figure 8.5. The PLE spectra are acquired by fixing the detection wavelength at the maximum of the respective PL emission bands. All PLE spectra have been corrected for the combined throughput of the Xe-lamp and the detection monochromator. A clear absorption edge can be seen in each of the PLE spectra and is attributed to the band gap absorption in the AlInGaN layer. Each of the PLE spectra has been cut off on the low energy side at the point where the PLE intensity rises again towards the detection emission energy. The effective energy gap can be evaluated by fitting the low energy side of the PLE spectrum to a sigmoidal function as performed earlier for AlInN epilayers in Chapter 7. Table 8.2 summarises the effective bandgap energies, Stokes shift, broadening parameters and the emission energies of AlInGaN epilayers. Similar to the redshift in PL/CL emission wavelength with increasing in InN content, the absorption edge and hence bandgap energy also shows a redshift with an increase in InN content in the quaternary epilayers. The obtained values of Stokes shift (listed in Table 8.2), are of the same order of

magnitude as reported by Feng et al [16] (150 meV, low InN content of ~ 2%) and Nemoz et al [17] (~100 meV, high InN content of 24 %). The broadening parameter is related to the Urbach tail [18, 19]. There can have a number of originating mechanisms for the Urbach tail, including the presence of point defects, extended states at the valence or conduction bands, disordered structure, excitonic transitions or the presence of inhomogeneous strain in the semiconductor [20].

Table 8.2 Sample code, Stokes shift, bandgap energy, broadening parameter and luminescence emission energy of quaternary AlInGaN epilayers

Sample Code	Stokes Shift (meV)	Bandgap energy (eV)	Broadening parameter (meV)	PL emission energy (eV)	RT CL emission energy (eV)
Q-3IL-SiC1.8	185	4.25	58.5	4.1, 4.0	3.97
Q-1IL-AlO2.6	200	4.2	63.7	4.1, 3.9	3.94
Q-3IL-AlO3.2	230	4.18	47.1	3.95	3.93
Q-1IL-SiC4.3	200	4.0	39.9	3.8	3.77

8.3.2(b) Spatially resolved luminescence properties

To obtain highly spatially resolved luminescence information, CL hyperspectral maps are acquired from these quaternary epilayers using the CL set up attached to the FESEM. Electron beam energy resolved CL measurements are also performed wherever necessary to differentiate between the luminescence from the quaternary AlInGaN epilayers and the underlying GaN template layer.

8.3.2(b).i Q-1IL-AlO2.6

CL hyperspectral data are obtained for this sample using electron beam energies of 2 and 3 keV with a beam current of ~3.4 and 1.4 nA respectively**.** Figure 8.6 summarises the results of 2 keV CL hyperspectral imaging performed for the sample

Q-1IL-AlO2.6. Monte Carlo simulation of electron beam depth dose profile for a 2 keV electron beam energy reveals that, 95 % of the electron energy loss occurs within the top AlInGaN layer of Q-1IL-AlO2.6 [Fig 8.7 (a)] and only a very small percentage (less than 5 %) of electrons reach the top layers of GaN.

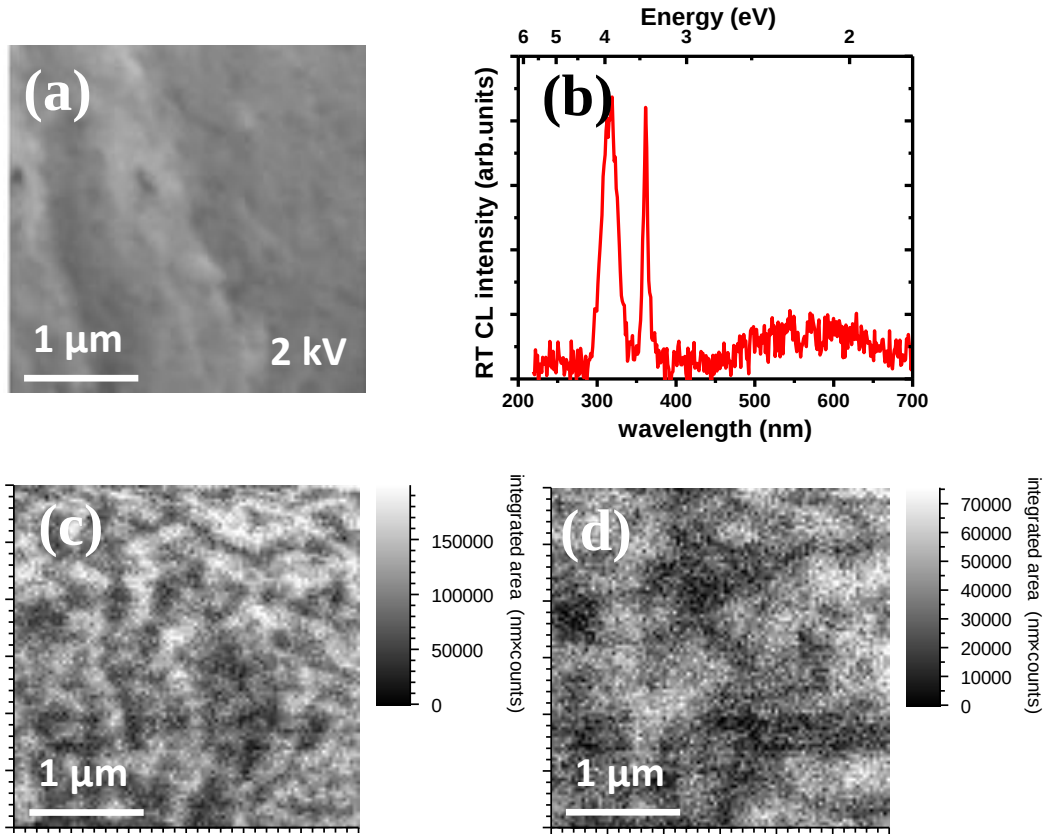

Figure 8.6(a) SEM image of Q-1IL-AlO2.6 showing the CL mapped region (b) spatially averaged CL spectrum from the mapped region (c) integrated intensity CL map for quaternary AlInGaN emission (d) integrated intensity CL intensity map for GaN NBE emission.

The spatially averaged CL spectrum [Fig 8.6(b)] collected from 3 x 3 µm area of the sample, indicated by the SEM image in Fig 8.6(a) is mainly constituted by three emissions; shorter wavelength emission from AlInGaN, GaN NBE emission at ~ 360-365 nm and the defect related YB emission. Surface undulations can be seen from the SEM image of the sample. The CL intensity distribution map corresponding to the quaternary emission [Fig 8.6(c)] clearly shows luminescence emission

intensity fluctuations of sub-µm range. The GaN NBE emission intensity spatial distribution map [Fig 8.6(d)] shows bright regions of µm scale along with the diffused dark regions distributed unevenly across the layer. A close comparison of the integrated intensity CL maps of GaN NBE and AlInGaN reveals that GaN NBE intensity spatial distribution is similar but more diffuse than that of the quaternary emission intensity spatial distribution map. Since the low energy exciting electron beam (2 keV) barely reaches the GaN buffer layer, and the luminescence emission energy of quaternary AlInGaN is greater than that of GaN NBE energy, the spatial intensity distribution of the GaN NBE in Fig 8.6(d) may be due to the secondary emission from the GaN excited by the emission from the quaternary epilayers. This is further supported by a Pearson correlation value of +0.3 between the integrated intensity spatial distribution maps of AlInGaN and GaN NBE.

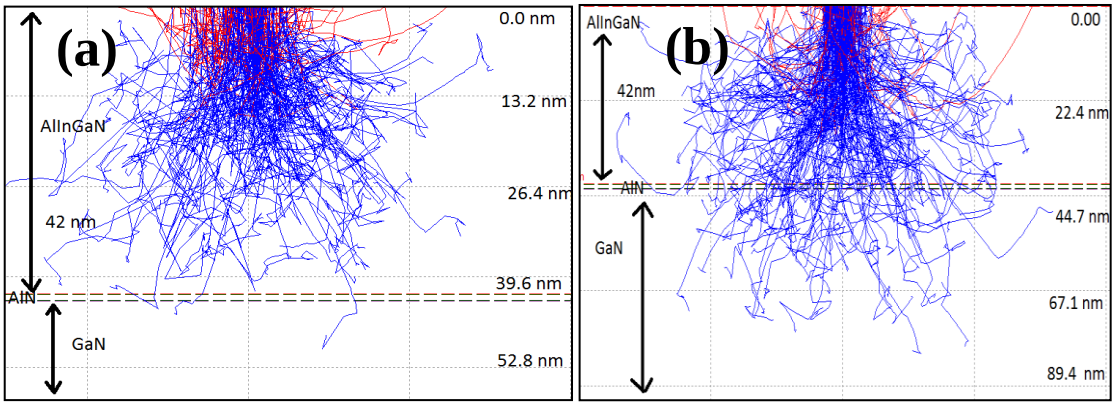

Figure 8.7 Monte Carlo simulated electron beam trajectories in sample Q-1IL-AlO2.6 for electron beam energy (a) 2 keV and (b) 3 keV

The spatial luminescence fluctuations in the sub-micrometer range seen in the CL intensity distribution map of quaternary and ternary III-nitride alloy semiconductors is worthy of discussion. Since the surface roughness of this quaternary epilayer estimated from XRR measurements is 0.7 nm [9], the contribution of surface roughness to this luminescence fluctuation should be minimal. In the case of III-nitride light emitters, the spatial inhomogeneity in the structure of the buffer layer i.e, defects might often be the origin of luminescence inhomogeneities in the layers deposited above the buffer. These structural defects are mostly related to the threading dislocations arising from misfit strain and acting as

non-radiative recombination centres. Another origin of spatial inhomogenities in the luminescence of ternary or quaternary III-nitrides is composition fluctuations expected in alloy III-nitride semiconductors. Since the composition fluctuation results in local variation in bandgap they can cause carrier localisation in small scale potential minima [21]. Localisation of charge carriers can also be caused by strain inhomogenities in the epilayers. To determine the influence of structural defects in the GaN buffer layer to the AlInGaN emission intensity spatial distribution, detailed CL analysis is done for Q-1IL-AlO2.6 using a higher electron beam energy of 3 keV and current of 1.4 nA. Under this electron beam excitation condition interaction volume extends well within the GaN buffer layer as shown by Monte Carlo simulation in Fig 8.7(b).

The integrated intensity spatial distribution of GaN NBE CL emission obtained using 3 keV electron beam energy [Fig 8.8], shows the contrast between dark and bright regions and dark spots related to threading dislocations. A comparison of the GaN NBE and quaternary emission integrated intensity CL maps obtained at 2 and 3 keV electron beam indicate that CL spatial intensity distribution in the AlInGaN do not seem to follow or reflect the threading dislocations in GaN buffer layer. This has two possible implications, (i) the observed spatial fluctuation in AlInGaN CL emission intensity is not largely affected by the structural defects from underlying GaN buffer, but by the InN composition fluctuation causing carriers to be localised in InN segregated regions and/or (ii) the AlN interlayer effectively prevents the structural defects or threading dislocations in the GaN buffer layer from reaching or propagating into the AlInGaN epilayers. This kind of spatial distribution of intensity corresponding to quaternary emission is very similar to that of InGaN epilayers previously reported due to In segregation effects [22]. It is to be noted that both the low temperature PL spectrum [Figure 8.3 (a)] and RT CL spectrum [Figure 8.3 (b)] of this sample exhibited the multiple peaks corresponding to quaternary emission. This also supports that InN composition fluctuations exist in this quaternary layer. A similar CL hyperspectral imaging study of sample Q-3IL-AlO3.2 reveals the same luminescence behaviour as that of Q-1IL-AlO2.6.

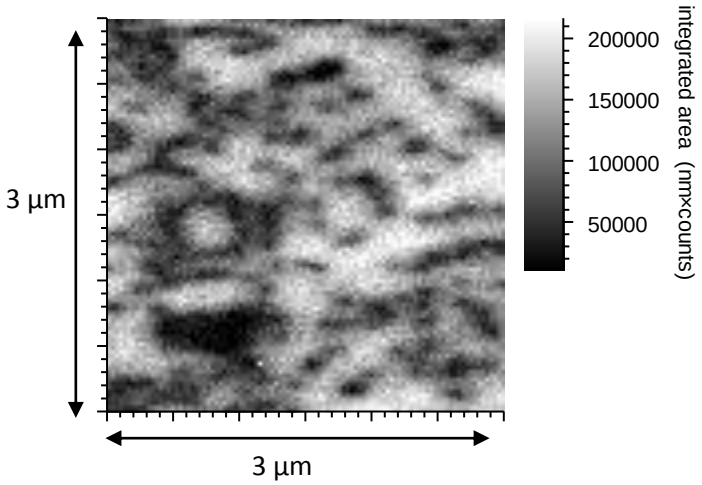

Figure 8.8 Integrated intensity CL intensity map for GaN NBE emission obtained from 3 kV CL hyperspectral imaging.

8.3.2(b).ii. Q-3IL-SiC1.8

The CL hyperspectral imaging is now applied to AlInGaN epilayers grown on SiC substrates. Figure 8.9 shows the CL mapping for the sample Q-3IL-SiC1.8, using electron beam energy of 3 keV. The SEM image of the sample shown in Fig 8.9 (a) reveals cracks on the sample surface. The spatially averaged CL spectra from the mapped region consist of peaks in two wavelength bands corresponding to GaN NBE and AlInGaN emissions.

Considering the spatial distribution of integrated intensity of quaternary and GaN NBE emissions [Fig 8.9 (c) and (d)], the enhanced luminous intensity is observed near the crack region and is associated with quaternary emission. Wang et al previously documented such observation of enhanced quaternary AlInGaN emission intensity near the cracks and pits on the surfaces of epilayers [23]. This may imply In-segregation near the cracks or that the cracks are strain relaxed regions. The GaN NBE emission intensity distribution map [Figure 8.9 (d)] show that the cracks are constituted by very low quality GaN. It is worth to note that contrary to the Q-1IL-AlO2.6 and Q-3IL-AlO samples, dark spots related to threading dislocation are clearly visible on the quaternary spatial intensity distribution map. Also a comparison of Fig 8.9 (c) and (d) reveals more dark spots for the quaternary emission intensity CL map and imply that there is a higher dislocation density for the quaternary epilayer than the underlying GaN layer. This

can be due to the different strain conditions prevailing on the GaN buffer layer and hence on the quaternary epilayers as they are grown on different substrates.

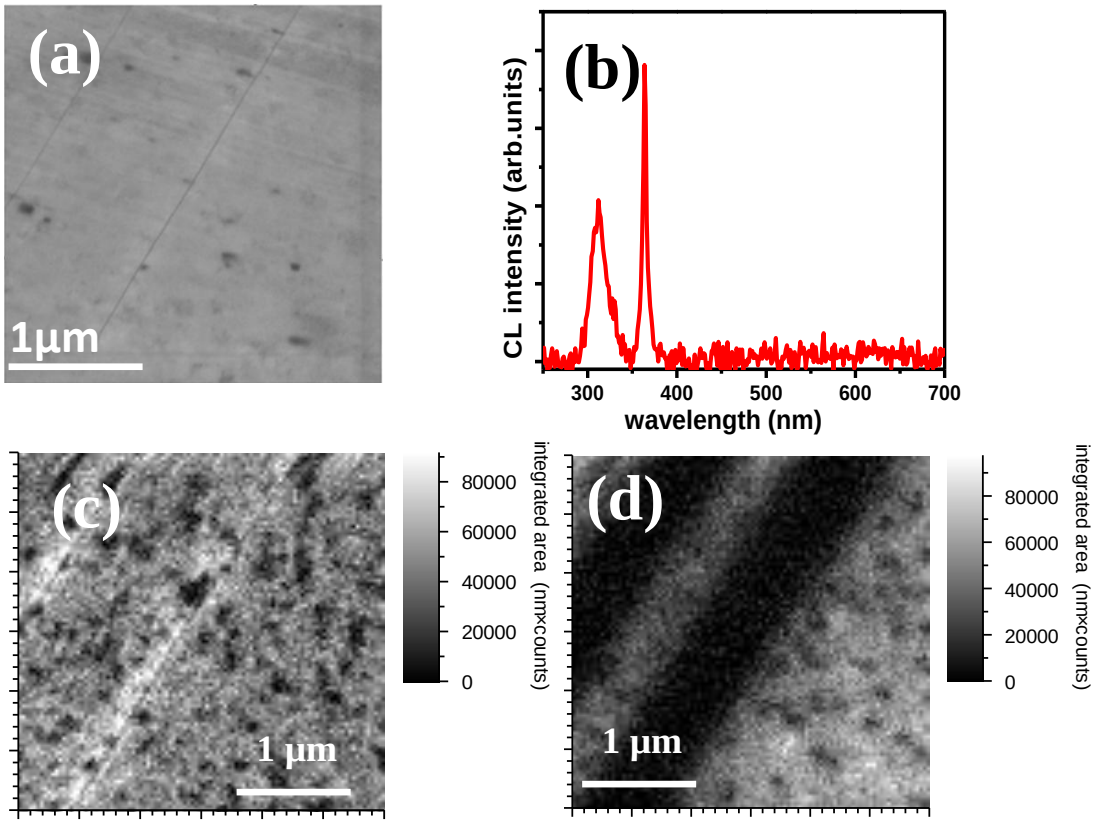

Figure 8.9(a) SEM image of the sample Q-3IL-SiC1.8 showing the CL mapped region (b) spatially averaged CL spectrum from the mapped region (c) spatial distribution of quaternary emission intensity (d) spatial distribution of GaN NBE emission intensity.

8.4 Summary

The optical properties of a set of thin AlInGaN epilayers on sapphire and SiC substrates were investigated. The surface morphology analysis by plan-view SEM revealed some surface undulations and nanoscale clusters on the sample surface. A red shift in quaternary UV emission with increase in InN content is identified by PL and CL spectroscopy. The bandgap energy estimated using PLE measurements also showed a red shift of 220 meV with increase in InN content from 1.8 to 4.3 %.

Spatially resolved optical properties studied using high resolution CL hyperspectral imaging revealed different luminescence behaviour for AlInGaN epilayers grown on sapphire and SiC substrates. Luminescence intensity fluctuations of sub-μm range have been observed for AlInGaN layers grown on sapphire substrate. This is discussed in terms of the InN compositional fluctuations and inhomogeneous strain effects in the epilayers acting as localised carrier recombination centres. Electron beam energy resolved CL hyperspectral imaging showed that AlGaInN epilayers on sapphire substrate did not follow threading dislocations in the underlying GaN buffer layer. CL hyperspectral mapping of the sample Q-3IL-SiC1.8, revealed enhanced emission intensity in the crack regions which might possibly be due to In-segregation and strain relaxation effects.

References:

[1] Tamulaitis G, Kazlauskas K, Zukauskas A, Khan M A et al 2000 *Appl. Phys.Lett* **77** 2136

[2] Che S B, Shinada T, Mizuno T, Wang X, Ishitani Y and Yoshikawa A 2006 *Jpn. J. Appl. Phys.* **45** L1259

[3] Butte et al 2007 *J Phys D Appl Phys* **40** 6328

[4] *Sun H, Alt A R, Benedickter H, Feltin E, Carlin J F, Gonschore M, Grandjean N R and Bolognesi C R 2010 IEEE Electron Device Lett. **31** 292*

[5] Matsuoka T 1997 *Appl. Phys.Lett* **71** 105

[6] Xie J, Ni X, Wu M, Leach J H Ozgur U and Morkoc H 2007 *Appl. Phys.Lett* **91** 132116

[7] Zonato D, Gokden S, Balkan N, Ridley B K and Schaff J 2004 *Semicond Sci Technol* **19** 427

[8] Wu J et al 2004 *J. Cryst. Growth* **273** 79

[9] Kirste L, Lim T, Aidam R, Muller S, Waltereit P and Ambacher O 2010 *Physica Stat. Sol.A-Applications and Material Science* **207** 1338

[10] Chen Y, Takeuchi T, Amano H, Akasaki I, Yamada N, Kaneko Y and Wang S Y 1998 *Appl. Phys. Lett.* **72** 710

[11] Liu J P, Zhang B S, Wu M, Li D B, Zhang J C, Jin R Q, Zhu J J, Chen J, Wang J F, Wang Y T and Yang H 2004 *J. Cryst. Growth* **260** 388

[12] Reshchikov M and Morkoc H 2005 *J.Appl. Phys* **97** 061301

[13] Hwan I, Choi I, Lee C R and Noh S K 1997 *Appl. Phys. Lett.***71** 1359

[14] Slack J A, Schowalter, Morelli D and Freitas Jr J A 2002 *J. Cryst. Growth* **246** 287

[15] Li W and Ni W 1996 *Appl. Phys. Lett.* **68** 2705

[16] Feng S, Cheng Y, Chung Y, Yang C C, Ma K, Yan C C, Hsu C, Lin J Y and Jiang H X 2003 *Appl. Phys. Lett.* **82** 1377

[17] Nemoz M, Beraudo E, Mierry D, Vennegues P and Hirsch L 2007 *Phys. Stat. Sol. (c)* **4** 137

[18] Martin R W, Middleton P G, and O'Donnell K P, Van der Stricht W 1999 *Appl.Phys. Lett.* **74** 263

[19] Urbach F 1953 *Phys. Rev.* **92** 1324

[20] Cremades A, Gorgens L, Ambacher O, Stutzmann M and Scholz F 2000 *Phys.Rev. B* **61** 2812

[21] Tamulaitis G 2011 *Material Science* 17 343

[22] Haffouz S, Tang H, Bardwell J A, Lefebvre P, Bretagnon T, Riemann T and Christen J 2006 *J Appl. Phys* 100 013528

[23] Wang B Z, Wang X L, Wang X Y, Guo L C, Wang X H, Xiao H L and Liu H X 2007 *J. Phys. D: Appl. Phys*. **40** 765–768

Chapter 9
Conclusions and Future Work

9.1 Conclusions

This thesis has presented the results of investigations into the optical, morphological and composition properties of nanostructured III-nitride light emitters, fabricated using binary GaN, the ternaries InGaN and AlInN and the quaternary AlInGaN. The nanostructures studied are coalesced (nano-ELOG) GaN above an array of nanopyramids and nanocolumns, semipolar {10$\underline{1}$1} and nonpolar (11$\underline{0}$0) m-plane InGaN QWs fabricated on the facets of GaN nanopyramids, c-plane AlInN epilayers and c-plane AlInGaN epilayers. Cathodoluminescence hyperspectral imaging is the main characterization tool employed to obtain high quality optical data as described in this thesis. The complimentary optical characterisation techniques of PL and PLE are also used wherever necessary.

Chapter 1 discussed the motivation and objectives of the present study along with an overview of the thesis. **Chapter 2** presented background information on the III-nitrides such as their crystal structure, electronic energy band structure and optical properties. The description of various nanostructured light emitters characterised in this thesis is also outlined in Chapter 2, with details on their background research. **Chapter 3** depicted various experimental techniques used to characterise the III-nitride nanostructures mentioned above. The main techniques used are CL hyperspectral imaging, PL and PLE spectroscopy for investigating the optical properties; SEM for visualisation of the surface morphology; and RBS and HR-XRD to study the compositional properties. The experimental results and their analyses are presented in chapters 4, 5, 6, 7 and 8.

The III-nitride nanostructures investigated in **Chapter 4** are nano-ELOG GaN layers obtained by coalescence overgrowth of GaN nanopyramids. Spatially and spectrally resolved luminescence information from a set of nano-ELOG samples formed under different growth conditions were studied in detail. The observed redshift of the GaN near-bandedge emission with increasing electron beam penetration depth into the coalesced layer is discussed in relation to a carrier induced peak shift, likely to be due to Si out-diffusion from the mask material into the GaN and strain effects. Depth resolved CL measurements are used to quantify the redshift in terms of band-gap renormalisation and strain effects. The redshift due to the bandgap renormalisation is found to account for the large proportion of the measured shift. The energy shift due to strain is estimated and the positive values corresponding to the compressive strain are found to reduce towards the surface as expected. Plan-view CL maps corresponding to GaN NBE peak energy distribution revealed micron-scale domain-like variations in peak energy, most likely related to the effects of local strain.

The optical properties of GaN layers coalesced above an array of nanocolumns investigated using high resolution CL hyperspectral imaging, is described in **Chapter 5.** GaN nanocolumns grown by MBE on Si substrates are coalesced using a nanoscale epitaxial overgrowth technique employing MOCVD. Plan-view microscopy revealed partially coalesced GaN layers with a sub-μm scale domain structure and distinct grain boundaries, which is mapped using CL hyperspectral imaging showing high strain at the grain boundaries. CL spectroscopy and mapping are then used to analyse cross-sectional areas spanning the partially coalesced GaN and underlying nanocolumns. The GaN near bandedge peak is seen to undergo a shift of about 25 meV across the partially coalesced layer of ~ 2 μm thick. The GaN above the nanocolumns remains under tensile strain, probably due to Si out-diffusion from the mask or substrate. The cross-sectional data showed how this strain is reduced towards the surface of the partially coalesced layer, possibly due to misalignment between adjacent partially coalesced regions.

Chapter 6 presented the spatially resolved optical properties of high density arrays of semipolar {10$\underline{1}$1} InGaN QWs fabricated on the nanofacets of GaN pyramids

grown by selective area growth. Three different sample sets differing in pore size and/or shape and QW cap layer thickness are investigated. Using the high spatial resolution CL hyperspectral imaging, the nanoscale spatial dependence of spectral position of the InGaN QW emission across the nanofacets of GaN pyramids were studied. The QW emission energy blueshifts in most of the samples as the electron beam scans from bottom to top of the nanopyramid. The InN incorporation in these InGaN QWs fabricated on the nanofacets of GaN pyramids is thought to be governed by reactor ambient conditions rather than the adatom diffusion lengths. This QW energy blueshift from bottom to top of the nanopyramid is found to follow the release of the tensile strain in GaN towards the top of nanopyramid. The spectral position of InGaN QW emission studied as a function of excitation current density and temperature revealed negligible polarisation - induced internal electric field in these structures. The optical properties of nonpolar InGaN QWs fabricated on nanofacets of GaN 3D structures on a-plane GaN template were also studied. The possibility of the existence of optical modes within the 3D GaN structures is shown by high resolution QW emission CL map from a single 3D nanostructure.

Chapter 7 investigated the composition, surface morphology and luminescence of AlInN epilayers with a range of InN compositions. The fraction of InN in AlInN estimated using RBS and HR-XRD measurements range from 0.14 to 0.20. The surface morphology of the AlInN epilayers investigated using SEM revealed a crack free and nearly smooth surface with small pits distributed across the surface. The luminescence of the AlInN epilayers is studied using PL and CL spectroscopy. The PL and CL peak emission energies from AlInN epilayers redshift with increasing InN content. The band gap energy, E_g of the AlInN alloys determined using PLE spectra decreases linearly with InN fraction for the restricted range of composition studied in this work.

Depth resolved CL measurements are used to differentiate the luminescence peaks originating from the AlInN and GaN. The absence of a luminescence peak shift associated with the higher energy AlInN as a function of penetration depth and as a function of lateral position suggested the possible compositional homogeneity of the AlInN epilayers. Temperature dependent CL emission studies from AlInN epilayers showed an energy shift of ~ 55 meV as the temperature is increased from

20 to 300 K. No strong S-shape dependence was observed for the AlInN emission energy variation as a function of temperature.

Polarization resolved PL spectra from AlInN/GaN heterostructures showed that the optical transition corresponding to E⊥c orientation had higher intensity compared to the E∥c orientation for both higher energy AlInN and GaN NBE emission. The polarisation angle dependence of the integrated PL emission intensity showed a similar trend of variation for both AlInN and GaN. The obtained results have two possible implications: the observed higher energy AlInN emission is either related to defects or this emission from AlInN epilayers is due to carrier recombination occurring in InN clusters similar to those of InGaN epilayers.

Chapter 8 discussed the optical properties of a set of thin AlInGaN epilayers on sapphire and SiC substrates. Plan-view SEM images revealed some surface undulations and nanoscale clusters on the sample surface. A redshift in quaternary UV emission with increase in InN content is identified by PL and CL spectroscopy. The bandgap energy estimated using PLE showed a redshift of 220 meV with increase in InN content from 1.8 to 4.3 %. Spatially resolved optical properties studied using high resolution CL hyperspectral imaging revealed different luminescence behaviour for AlInGaN epilayers grown on sapphire and SiC substrates. Luminescence intensity fluctuations on a sub-μm scale range have been observed for AlInGaN layers grown on sapphire substrate. This is discussed in terms of the InN compositional fluctuations and inhomogeneous strain effects in the epilayers acting as localised carrier recombination centres. Depth resolved CL hyperspectral imaging showed that AlGaInN epilayers on sapphire substrate did not follow threading dislocations in the underlying GaN buffer layer.

9.2 Suggestions for future work

1. The high resolution CL hyperspectral imaging technique offers the important possibility of investigating optical data from high quality III-nitride quantum dots, such as those composed of InGaN or related alloys.

2. Excitation current dependent studies are performed for semipolar {10$\underline{1}$1} InGaN QWs with two different InN contents. However it would be more

interesting to perform similar kind of measurements to a c-plane InGaN QW sample with same growth specifications so that polarisation induced electric field effects can be compared in InGaN QWs grown on polar and semipolar planes.

3. The optical properties of AlInN and AlInGaN epilayers grown on crystal orientations other than the polar (0001) c-axis such as semipolar and non-polar planes would be worth investigating.

4. Fabrication of light emitting devices based on the InGaN QWs on nanopyramids and nano-ELOG GaN (described in chapter 4, 5 and 6) would be an important extension of this work.

5. More measurements on polarisation resolved PL spectroscopy of high material quality and bright luminescent AlInN epilayers are needed to understand the optical anisotropic properties of these ternary III-nitride alloys.

6. Extending the optical anisotropic measurements to quaternary AlInGaN layers would be useful to explore its band structure properties.

Appendix: List of Publications and conference presentations

List of Publications

1. *Light emission from InGaN quantum wells grown on the facets of closely spaced GaN nano-pyramids formed by nano-imprinting*

   Liu C, Satka A, **Lethy K J,** Edwards P R, Allsopp D, Martin R W *et al Applied Physics Express 2 (2009) 121002*

2. *Cross-sectional and plan-view cathodoluminescence of GaN coalesced above a nanocolumn array*
   (Under review in Journal of Applied Physics)

   Lethy K J, Edwards P R, Liu C, W.N. Wang and Martin R W,

3. *High-resolution cathodoluminescence hyperspectral imaging of nitride nanostructures*

   Edwards P R, Liu C, **Lethy K J**, Bruckbauer J, Liu C, Shields P, Allsopp D,Wang T and Martin R W

   (Under review in Journal of Microscopy and Microanalysis)

4. *Cathodoluminescence studies of GaN coalesced from selectively grown nanopyramids*

   Lethy K J, Edwards P R, Liu C, , Shields P, Allsopp D and Martin R W

   (Under review in Journal of Semiconductor Science and Technology)

5. *Cathodoluminescence hyperspectral imaging on the nanometre scale*

   Edwards P R, Liu C, **Lethy K J**, Wark A W and Martin R W
   Proceedings of Hyperspectral imaging 2011 conference , p87-89, Strathclyde, UK

Conference presentations

1. *Synthesis and characterization of MOVPE-grown (11-20) a-plane AlInN epilayers across the composition range*
   Laskar M R, **Lethy K J**, Hatui N, Rahman A A, Gokhale M R, Edwards P R, Martin R W and Arnab Bhattacharya

16th International Conference on Metal Organic Vapor Phase Epitaxy (ICMOVPE –XVI 2012) (*Accepted for Oral presentation*)

2. *Luminescence Anisotropy of AlInN Epilayers* **Lethy K J,** Edwards P R, Sadler T C, Kappers M J, Oliver R A, O'Donnell K P and Martin R W
9th International Conference on Nitride Semiconductors (ICNS-9), Glasgow 2011 *(Oral presentation)*

3. *Cathodoluminescence hyperspectral imaging on the nanometre scale*
Edwards P R, Liu C, **Lethy K J**, Wark A W and Martin R W
Hyper spectral Imaging Conference 2011, Glasgow, UK
(*Oral presentation by Edwards P R*)

4. *Cathodoluminescence studies of coalesced GaN above nanopyramids selectively grown by MOCVD*
Lethy K J, Edwards P R, Martin R W, Duncan A *et al*
UK Semiconductors 2009 Conference July 2009, University of Sheffield
(Poster presentation)

5. *Cathodoluminescence studies of $Al_{1-x}In_xN$ epilayers*
Lethy K J, Trager-Cowan C, Sadler T C, Martin R W et al
8th International Conference on Nitride Semiconductors (ICNS-2009), Korea
(*Poster presentation*)

6. *Cathodoluminescence of Nanostructures*
Martin R W, Edwards P R, **Lethy K J** et al
10th International workshop on beam injection assessment of microstructures in semiconductors- BIAMS 2010. July 4-8 Germany
[Invited talk for Prof Martin R W]

7. *Cross-sectional cathodoluminescence of GaN coaleseced above a nanocolumns array*
Lethy K J, Edwards P R, Liu C et al
10th International workshop on beam injection assessment of microstructures in semiconductors- BIAMS 2010. July 4-8 Germany
(Oral presentation by Prof R W Martin)

8. *Cathodoluminescence hyperspectral imaging of semipolar {10$\underline{1}$1} InGaN/GaN single quantum wells fabricated on nanofacets*
Lethy K J, Edwards P R, Martin R W et al
UKNC conference Sheffield, July 2010 *(Oral presentation)*

9. *Light emission from InGaN quantum wells grown on the facets of closely spaced GaN nano-pyramids*

Edwards P R, **Lethy K J**, Martin R W et al

UKNC conference Cork, January 2010 (*Oral presentation by Edwards P R*)

10. *Intrinsic properties of InN and indium rich nitride alloys- RAINBOW@Strathclyde*

Naresh Kumar, **Lethy K J,** Simon K et al

University Research Day 2009, University of Strathclyde

(*Poster presentation*)